



HAL
open science

A Filtered-Laminar-Flame PDF subgrid scale closure for LES of Premixed Turbulent Flames: Application to a Stratified Bluff-body burner with Differential Diffusion

Suresh Kumar Nambully

► **To cite this version:**

Suresh Kumar Nambully. A Filtered-Laminar-Flame PDF subgrid scale closure for LES of Premixed Turbulent Flames: Application to a Stratified Bluff-body burner with Differential Diffusion. Fluid mechanics [physics.class-ph]. INSA de Rouen, 2013. English. NNT: 2013ISAM0014 . tel-00845904

HAL Id: tel-00845904

<https://theses.hal.science/tel-00845904>

Submitted on 18 Jul 2013

HAL is a multi-disciplinary open access archive for the deposit and dissemination of scientific research documents, whether they are published or not. The documents may come from teaching and research institutions in France or abroad, or from public or private research centers.

L'archive ouverte pluridisciplinaire **HAL**, est destinée au dépôt et à la diffusion de documents scientifiques de niveau recherche, publiés ou non, émanant des établissements d'enseignement et de recherche français ou étrangers, des laboratoires publics ou privés.

THÈSE

Présentée par

Suresh Kumar NAMBULLY

Pour l'obtention du grade de

Docteur de l'Institut National des Sciences Appliquées de Rouen

Discipline : Energétique
Spécialité : Mécanique des Fluides
Formation doctorale : Sciences Physiques, Mathématiques
et de l'Information pour l'Ingénieur
Laboratoire d'accueil : UMR-CNRS-6614-CORIA

A Filtered-Laminar-Flame PDF subgrid scale closure for LES of Premixed Turbulent Flames. Application to a Stratified Bluff-body burner with Differential Diffusion.

Le 18 Mars 2013

Membres du jury

Rapporteurs :

Denis VEYNANTE

Directeur de Recherche, CNRS, Ecole Centrale Paris

Andreas KEMPF

Professeur, Université de Duisburg - Essen

Examineurs :

Simone HOCHGREB

Professeur, Université de Cambridge

Christian ANGELBERGER

Expert, Chef de projet, IFP Energies nouvelles

Pascale DOMINGO

Directrice de Recherche, CNRS, CORIA

Luc VERVISCH

Professeur, INSA de Rouen, CORIA

Vincent MOUREAU

Chargé de Recherche, CNRS, CORIA

Acknowledgement

First and foremost, I acknowledge the confidence shown by Prof. Vervisch and Dr. Domingo to take me as their PhD student in their esteemed research group. This dissertation would not have been possible without their guidance, help and encouragement.

I acknowledge equally the help and guidance Dr. Moureau has provided during the thesis and helped me overcome the steep learning curve of combustion and coding with ease. I would like to express my sincere gratitude to Dr. Lartigue and Dr. Moureau for all the wonderful and enriching YALES2 tutorials which were an indispensable part of the thesis.

Thanks a lot to Prof. Boukhalfa also for giving the opportunity to work at the laboratory of CORIA.

My utmost gratitude to Dr. Vallinayagam Subramanian (Subbu), who introduced me to Prof. Vervisch and helped me kick start my life in France. Equal gratitude to Arnab for being a friend and mentor all throughout. Sincere expression of thanks to Prof. Ramesh of IIT-Madras, India who encouraged me to do a PhD.

Thanks to my amazing office mates Cindy, Nicolas, Francois, Guillaume and Mathias for all the wonderful memories during the PhD. Thanks to all my dear colleagues Xavier, Nico, Benjamin, Lisa, Lola, Pierre, Chloé, Pradeep, Alvin, Alexandre, Aliou, Fon and Mecheline for being good friends. Thanks to Nathalie Fouet of the CORIA library for her help.

I am very much indebted to my parents and relatives who were an everlasting source of encouragement and support all throughout. Last but not the least, my wife Bhagya, without whom this thesis would not have materialized.

Abstract

A sub-grid scale closure for Large Eddy Simulation (LES) of turbulent combustion, based on physical space filtering of laminar flames is presented. The proposed formalism relies on a presumed probability density function (PDF) derived from the filtered laminar flames and flamelet tabulated chemistry. The combustion LES filter size is not fixed in this novel approach when sub-grid scale wrinkling occurs, but calibrated depending on the local level of unresolved scalar fluctuations. The model was validated by simulating 1D filtered laminar flames and 2D Bunsen flames. Subsequently, the model was tested on a 3D turbulent scenario by performing LES of the premixed and stratified configurations of the Cambridge swirl burner, experimentally studied by Sweeney and co-workers. Comparison of simulation and experiments for both the premixed and stratified configurations showed good agreement emphasizing the model characteristics. Instantaneous and time averaged LES data were analyzed to extract information concerning the degree of stratification and the orientation of flame and mixing vectors. A decomposition of the flame response into premixed, diffusion and partially premixed flamelets is performed, to conclude that the premixed mode dominates close to the burner, with some partially premixed burning regime further downstream. Overall, the length scales associated to stratification were found to be much larger than that of the reaction zone and flame, resulting in a quasi-homogeneous propagation, predominantly in a back supported stratified combustion regime. Since this burner also features differential diffusion effects, the numerical model is modified to account for accumulation of carbon in the recirculation zone behind the bluff-body. A differential diffusion number based on the gradient of residence times is proposed, in an attempt to globally quantify differential diffusion effects in burners.

Résumé

Un modèle de sous-maille pour la simulation aux grandes échelles de la combustion turbulente, basé sur le filtrage de flammes laminaires est présenté. Le formalisme repose sur une fonction de densité de probabilité (PDF) présumée construite à partir du filtrage de flammes laminaires 1D et sur une chimie tabulée. La taille de filtre LES appliqué à la combustion n'est pas fixée dans cette nouvelle approche mais est déterminée fonction du niveau local de fluctuations de sous-maille. Le modèle a été validé sur des flammes laminaires 1D filtrées ainsi que sur des flammes de bec Bunsen. Le modèle est ensuite testé sur une configuration 3D turbulente avec la LES d'un brûleur de Cambridge (travaux de Sweeney et al) pour des configurations prémélangées et stratifiées. La comparaison de la simulation avec l'expérience en prémélangé et en stratifié est pleinement satisfaisante confirmant l'intérêt du nouveau modèle. Les résultats instantanés et moyens de la LES sont analysés afin d'extraire des informations sur le degré de stratification et la topologie des zones de combustion. La décomposition de la flamme en flammelettes de prémélange, diffusion et partiellement prémélangées est effectuée. Le mode prémélangé est dominant avec quelques zones en prémélange partiel dans la zone aval. Les échelles spatiales associées à la stratification sont trouvées grandes devant celles associées à la flamme (épaisseurs de zone de réaction et thermique) dont la propagation reste quasi-homogène. Le régime de combustion stratifiée est essentiellement de type "back supported".

Contents

1	Introduction	1
1.1	Context and Motivation	1
1.2	Objectives and Contributions	6
1.3	Thesis structure	7
2	Overview: Bluff body Flow Physics and Modeling of Turbulent flames	9
2.1	Bluff body and annular jet flows	9
	Introduction	9
	Non-reacting annular jet flows	10
	Reacting annular jet flows	13
	Re-laminarisation effects in bluff body combustors	15
2.2	Premixed and stratified combustion modeling in LES	16
	Introduction	16
	Description of chemistry	16
	Turbulent combustion models	19
2.3	Studies on stratified combustion	23
2.4	Differential diffusion studies in combustion	27
3	Governing Equations & Solver Description	33
3.1	General governing equations	33
	Governing equations at the low Mach number limit	34
3.2	LES governing equations	36
	Unresolved Reynolds stress closure	37
3.3	Discretization of the governing equations	39
	Spatial discretization	39
	Solution strategy: Projection method	42
	Time integration scheme	45
3.4	Poisson solver	47
4	FLF-PDF Model and Modeling Differential Diffusion of Mixture fraction	49
4.1	FLF-PDF SGS modeling	49
	Formalism	49
	Balance equations and closures	52
4.2	Filtered laminar flame validation of FLF-PDF	59

1D laminar flame	59
2D laminar Bunsen flame	61
4.3 Modeling differential diffusion of mixture fraction	63
Mixture fraction definition	63
SGS Modeling of mixture fraction differential diffusion	65
A global criterion for differential diffusion in burners	66
5 Experimental configuration and Cold flow simulations	69
5.1 Burner geometry and flow configurations	69
5.2 Numerics and boundary conditions	71
Computational domain	71
Boundary conditions	71
5.3 Non-reacting flow simulations	72
Turbulence resolution parameter and mesh quality	72
Non-reacting flow statistics	73
Mixture fraction fields	77
5.4 Conclusions	77
6 Reacting flow simulations: Premixed Configuration CSWB1	79
6.1 Simulations of CSWB1 with the PCM-FPI model	79
Modeling parameters and test cases	79
Results and discussions	81
Conclusions	83
6.2 Simulations of CSWB1 with the FLF-PDF model	84
Results and flow analysis	86
Summary and conclusions	95
7 Reacting flow simulations: Stratified Configurations CSWB5 & CSWB9	99
7.1 Computational details	99
7.2 Results: Velocity and scalar statistics	100
7.3 Results: Analysis of stratified combustion	110
7.4 Summary and conclusions of CSWB5 and CSWB9 simulations	124
8 Conclusions and Perspectives	127
8.1 Conclusions	127
8.2 Perspectives	128
A Derivation of progress variable diffusivity	131
B Method of tabulation for FLF-PDF	133
C List of Publications	137

C.1 Journal 137
C.2 Conferences 137

References **139**

List of Figures

1.1	Primary energy supply break up extracted from Key World Energy Statistics 2012 published by International Energy Agency	2
1.2	Projected primary energy supply break up extracted from Key World Energy Statistics 2012 published by International Energy Agency	3
1.3	CO ₂ emissions by fuel extracted from Key World Energy Statistics 2012 published by International Energy Agency	4
1.4	Global CO ₂ emissions and the projections for the next 25 years. Extracted from World Energy Outlook 2012 by International Energy Agency	5
2.1	Schematic diagram of the basic annular jet with time averaged flow regions, according to Ko and Chan [1] extracted from the thesis of Lars Blum [2]	11
2.2	Species distribution inside a laminar premixed flame as a function of distance from burner exit.	18
2.3	Temperature as a function of mixture fraction and normalized progress variable . . .	18
2.4	For Class 1 and 2 flames. Premixed: $\alpha = 90^\circ$, Stratified front supported: $\alpha = 0^\circ$, Stratified back supported: $\alpha = 180^\circ$	25
2.5	Mole fraction distribution of few major products of laminar premixed methane air flame at an equivalence ratio of 0.75 showing diffusion of H ₂ and H ₂ O ahead of CO and CO ₂ into the fresh gas.	28
2.6	Diffusivities of major products of laminar premixed methane air flame at an equivalence ratio of 0.75.	28
3.1	Construction of a typical control volume in YALES2 extracted from YALES2 tutorials by Moureau et al. $\bar{\mathbf{x}}_p$ is the barycenter of the control volume. \mathbf{x}_p is the computational node for the control volume	40
4.1	Laminar premixed methane air flame at $\phi = 0.75$. (a) Filtered \tilde{c} profiles at different filter widths (b) S_c profiles for different filter widths. — $\Delta = 5\delta_L$, -- $10\delta_L$, -o- $20\delta_L$, -·◇- $50\delta_L$	50
4.2	Quantities obtained by numerical interpolation. (a) $\tilde{x}^\Delta = \tilde{x}^\Delta(\tilde{c}, S_c)$. (b) $\Delta = \Delta(\tilde{c}, S_c)$. 51	51
4.3	Comparison of source terms of progress variable filtered with Beta-PDF and FLF-PDF for different unmixedness factors S_c for a 1D laminar methane-air flame.	54
4.4	D_{Y_c} [m ² ·s ⁻¹] response <i>vs</i> progress variable for premixed methane-air flame. (a) Various equivalence ratios. - $\phi = 0.5$, -o- 0.75, — 1.0, -□- 1.125. (b) $\phi = 0.75$. -o- Eq. (4.16), -△- ν/S_c	55

4.5	—: $-\nabla \cdot (\bar{\rho} \tilde{\mathbf{u}} \tilde{c})$. --: $\nabla \cdot (\bar{\rho} D_c \nabla \tilde{c})$. - * -: $\bar{\rho} \tilde{\omega}_c$. —○—: $\nabla \cdot \bar{\tau}_c^u$. —△—: $\nabla \cdot \bar{\tau}_c^D$ - · + · -: Total budget, all terms in $\text{kg} \cdot \text{m}^3 \cdot \text{s}^{-1}$	56
4.6	—: $-\nabla \cdot (\bar{\rho} \tilde{\mathbf{u}} \tilde{c}^2)$. --: $\nabla \cdot (\bar{\rho} D_c \nabla \tilde{c}^2)$. —△—: $\nabla \cdot \bar{\tau}_{c^2}^D$. —○—: $\nabla \cdot \bar{\tau}_{c^2}^u$. - · ◇ -: $-\bar{\chi}_c$. - * -: $2\bar{\rho} c \tilde{\omega}_c$. - · + · -: Total budget, all terms in $\text{kg} \cdot \text{m}^3 \cdot \text{s}^{-1}$	57
4.7	D_ϕ^D (Eq. (4.18)) m^2/s for various S_c . (a): $D_{Y_c}^D$. (b): $D_{Y_c^2}^D$	58
4.8	Variation of flame speed as a function of mixture fraction for methane air flame at inlet temperature of 300K and 1 atm pressure	60
4.9	Versus x-coordinate (m): (a) \tilde{c} , (b) \tilde{c}^2 . $\Delta/\delta_L = 5, 10, 20, 50$. —: Filtered 1 D flame solution, -- 1D-LES.	61
4.10	Ratio between computed flame speed and reference ones <i>vs</i> Δ/h . — shows the expected ideal value.	61
4.11	Computational domain for 2D Bunsen flame simulation (coarse mesh) showing the expected flame lengths for the three inlet velocities 1.0 m/s (L1), 2.0 m/s (L2) and 3.0 m/s (L3) respectively.	62
4.12	c -fields for 2D Bunsen flame simulations for different inlet velocities. Top: Refined mesh simulations, D_{Y_c} with differential diffusion. Middle: Refined mesh simulation with $D_{Y_c} = \nu/0.72$, Bottom: Coarse mesh simulation with FLF-PDF. The white line indicates the theoretical flame length.	63
4.13	c -profiles along the axis of the Bunsen burner. 2 m/s case. · · · ·: Expected flame tip location, — Refined mesh simulations, D_{Y_c} with differential diffusion. · - - · Refined mesh simulation with $D_{Y_c} = \nu/0.72$, - - - Coarse mesh FLF-PDF model.	64
4.14	(a) Mixture fraction across the reference flame. (b) Mixture fraction source term across the reference flame (s^{-1}) where — Z_d^{all} , -- Z_d^{maj} , * Z	66
5.1	Cross sectional view of the burner exit showing the bluff body, the two annular jets and the coflow. Also shown is the approximate location of the flame brush and the central recirculation zone (CRZ).	70
5.2	Computational domain for the LES of CSWB experiment with the mesh and instantaneous flame location.	73
5.3	Instantaneous snapshot of the ratio of subgrid kinetic energy to the total kinetic energy. Every major grid line in the figure corresponds to 10 mm.	74
5.4	Instantaneous snapshot of the ratio of turbulent viscosity to molecular viscosity. Every major grid line in the figure corresponds to 10 mm.	75
5.5	Relative orientation of the plane used for comparison to the reference X-axis used in the simulation.	75
5.6	Velocity statistics for non-reacting flow, radial profiles. (a)-(b): Axial component. (c)-(d): Radial. (a)-(c): Mean value. (b)-(d): RMS. Symbols: LDA measurements. LES: — azimuthal averaging, - - - single plane.	76
5.7	Streamlines superimposed on the mean axial velocity field depicting the recirculation zone and the jets.	77

5.8	Instantaneous equivalence ratio fields of the three configurations studied represented with the equivalence ratio distribution. (a) CSWB1 (b) CSWB5 (c) CSWB9. The bold line in (c) is the stoichiometric equivalence ratio contour.	78
6.1	Instantaneous velocity fields of the non-reacting (left) and reacting (right) flow cases.	81
6.2	Ratio of turbulent viscosity to the molecular viscosity in the flame zone	82
6.3	Reynolds averaged statistics (a) Radial profiles of average axial velocity. (b) Radial profiles of axial velocity fluctuations. (c) Radial profiles of average radial velocity (d) Radial profiles of radial velocity fluctuations. Symbol: LDA Measurements. Black line: Linear relaxation model. Red line: Hybrid model. Blue: Modified linear relaxation model	83
6.4	(a) & (b) Radial profiles of average temperature. (c) & (d) Radial profiles of temperature fluctuations. Symbol: Measurements. Black line: Linear relaxation model. Red line: Hybrid model. Blue: Modified linear relaxation model	84
6.5	(a) & (b) Radial profiles of average mixture fraction. (c) & (d) Radial profiles of mixture fraction fluctuations. Symbol: Measurements. Black line: Linear relaxation model. Red line: Hybrid model. Blue: Modified linear relaxation model	85
6.6	Spanwise averaged temperature distribution. (a): $x = 10$ mm. (b): $x = 50$ mm.	86
6.7	Streamlines superimposed on the mean velocity field of the CSWB1 configuration depicting the recirculation zone and the jets.	87
6.8	(a): Instantaneous source term colored by \mathcal{F} (Eq (4.22)). (b): PDF of \mathcal{F} computed over the mesh.	88
6.9	Velocity statistics with flames, radial profiles. (a)-(b): Axial component. (c)-(d): Radial. (a)-(c): Mean value. (b)-(d): RMS. Symbols: LDA. LES: — azimuthal averaging, - - - single plane.	89
6.10	Temperature statistics, radial profiles. (a)-(b): Mean value. (c)-(d): RMS. Symbols: Experiment. LES: — azimuthal averaging, - - - single plane.	90
6.11	Temperature statistics forcing $\mathcal{F} > 1$, radial profiles. (a): Mean value. (b): RMS. Symbols: Experiment. LES: — Azimuthal averaging.	91
6.12	CH ₄ mass fraction statistics, radial profiles. (a)-(b): Mean value. (c)-(d): RMS. Symbols: Experiment. LES: — azimuthal averaging, - - - single plane.	92
6.13	Iso Q-criterion ($Q = 1 \cdot 10^6 \text{s}^{-1}$) with instantaneous velocity and mean mixture fraction (Z_d) fields. Accumulation of the mixture fraction in the re-circulation zone can be seen.	93
6.14	Mixture fraction statistics, radial profiles. (a)-(b): Mean value. (c)-(d): RMS. Open circles: Experiment. Line: LES — Z_d (Eq. (4.25)) azimuthal averaging, - - - Z_d single plane, ■- Z (Eq. (4.6)) azimuthal averaging.	94
6.15	Mean residence time and instantaneous flame location.	95
6.16	CO ₂ mass fraction statistics, radial profiles. (a)-(b): Mean value. (c)-(d): RMS. Symbols: Experiment. LES: — azimuthal averaging, - - - single plane.	96

6.17	CO mass fraction statistics, radial profiles. (a)-(b): Mean value. (c)-(d): RMS. Symbols: Experiment. LES: — azimuthal averaging, - - - single plane.	97
6.18	1D laminar methane-air flame solution as a function of distance from burner exit at equivalence ratio of 0.75 (a) Temperature profiles (b) CO mass fraction profiles. — Unfiltered laminar flame solution, - - - Filtered profiles.	98
7.1	Cross sectional view of the mesh. Left: coarse mesh (50M cells) Right: refined mesh (400M cells)	100
7.2	Cross-sectional planes with mean temperature distribution at 10 mm and 50 mm Left: 10 mm Right: 50 mm a) and b) CSWB5 c) and d) CSWB9	101
7.3	Streamlines superimposed on the mean velocity field of the CSWB5 configuration depicting the recirculation zone and the jets.	102
7.4	Streamlines superimposed on the mean velocity field of the CSWB9 configuration depicting the recirculation zone and the jets.	103
7.5	Axial velocity statistics for CSWB5. Symbols: LDA, LES: — Azimuthally averaged coarse mesh, - - - Single plane coarse mesh, — Azimuthally averaged refined mesh.	103
7.6	Axial velocity statistics for CSWB9. Symbols: LDA. Lines: LES. — azimuthal averaging, - - - single plane.	104
7.7	Radial velocity statistics for CSWB5. Symbols: LDA, LES: — Azimuthally averaged coarse mesh, - - - Single plane coarse mesh, — Azimuthally averaged refined mesh.	104
7.8	Radial velocity statistics for CSWB9. Symbols: LDA. Lines: LES. — azimuthal averaging, - - - single plane.	105
7.9	CSWB5: Mixture fraction statistics, radial profiles. Open circles: Experiment. Line: LES — Z_d (Eq. (4.25)) azimuthal averaging coarse mesh, - - - Z_d single plane coarse mesh, -■- Z (Eq. (4.6)) coarse mesh, — Z_d azimuthal averaging refined mesh.	106
7.10	CSWB9: Mixture fraction statistics, radial profiles. Open circles: Experiment. Line: LES — Z_d (Eq. (4.25)) azimuthal averaging, - - - Z_d single plane, -■- Z (Eq. (4.6)).	107
7.11	Mixture fraction distribution across a laminar premixed flame at equivalence ratios a) $\phi = 1.0$ and b) $\phi = 1.125$, — Z_d^{major} and $\cdots Z$	108
7.12	Mean residence time fields with an instantaneous source term location shown for the two cases a) CSWB5 and b) CSWB9	109
7.13	Temperature statistics for CSWB5, radial profiles. Symbols: Experiment. LES: — azimuthal averaging coarse mesh, - - - single plane coarse mesh. — azimuthal averaging refined mesh.	110
7.14	Temperature statistics for CSWB9, radial profiles. Symbols: Experiment. LES: — azimuthal averaging, - - - single plane.	111
7.15	CH ₄ mass fraction statistics for CSWB5, radial profiles. Symbols: Experiment. LES: — azimuthal averaging coarse mesh, - - - single plane coarse mesh, — azimuthal averaging refined mesh.	112

7.16	CH ₄ mass fraction statistics for CSWB9, radial profiles. Symbols: Experiment. LES: — azimuthal averaging, - - - single plane.	113
7.17	CO mass fraction statistics for CSWB5, radial profiles. Symbols: Experiment. LES: — azimuthal averaging coarse mesh, - - - single plane coarse mesh, — azimuthal averaging refined mesh.	114
7.18	CO mass fraction statistics for CSWB9, radial profiles. Symbols: Experiment. LES: — azimuthal averaging, - - - single plane.	115
7.19	CO ₂ mass fraction statistics for CSWB5, radial profiles. Symbols: Experiment. LES: — azimuthal averaging coarse mesh, - - - single plane coarse mesh, — azimuthal averaging refined mesh.	116
7.20	CO ₂ mass fraction statistics for CSWB9, radial profiles. Symbols: Experiment. LES: — azimuthal averaging, - - - single plane.	117
7.21	LES regime diagrams showing the distribution of flamelets in the computational domain a) CSWB5 b) CSWB9	117
7.22	Instantaneous progress variable source term conditioned on the progress variable ($0.01 < \tilde{c} < 0.99$) colored by equivalence ratio. Left: CSWB5, Right: CSWB9. Every major division of the axis corresponds to 10 mm.	118
7.23	Intersection of the mixing layer and the flame a) CSWB5 b) CSWB9. Every major division of the axis corresponds to 10 mm.	119
7.24	CSWB5 (a): Instantaneous source term colored by \mathcal{F} (Eq (4.22)). (b): PDF of \mathcal{F} computed over the mesh.	120
7.25	CSWB9 (a): Instantaneous source term colored by \mathcal{F} (Eq (4.22)). (b): PDF of \mathcal{F} computed over the mesh.	120
7.26	Probability distribution of equivalence ratio at different heights from the burner exit conditioned on the progress variable($0.01 < \tilde{c} < 0.99$)	121
7.27	Frequency spectra of the axial velocity of a probe place in the shear layer of the inner and outer jet	121
7.28	Probability distribution of instantaneous gradient of equivalence ratio as a function of equivalence ratio gradient at different heights for CSWB5 and CSWB9 conditioned on progress variable ($0.01 < \tilde{c} < 0.99$). Lines with circles: CSWB5 coarse mesh, Dashed line: CSWB5 refined mesh. Line: CSWB9 coarse mesh	122
7.29	CSWB5 flamelets. Left: Premixed flamelets. Middle: Diffusion flamelets. Right: Partially premixed flamelets	123
7.30	CSWB9 flamelets. Left: Premixed flamelets. Middle: Diffusion flamelets. Right: Partially premixed flamelets	124
7.31	Probability distribution plot of θ as a function of θ conditioned over progress variable ($0.01 < \tilde{c} < 0.99$). Left: From instantaneous data. Right: From time averaged data	125

-
- B.1 Laminar premixed methane air flame at $\phi = 0.75$. (a) Filtered \tilde{c} profiles at different filter widths (b) S_c profiles for different filter widths. — $\Delta = 5\delta_L$, -- $10\delta_L$, -o- $20\delta_L$, $\cdot \diamond \cdot$ $50\delta_L$ 133
- B.2 Quantities obtained by numerical interpolation. (a) $\tilde{x}^\Delta = \tilde{x}^\Delta(\tilde{c}, S_c)$. (b) $\Delta = \Delta(\tilde{c}, S_c)$. 134

List of Tables

5.1	Table showing the different configurations studied in this work. In all the cases the inner jet velocity $U_{inner} = 8.31$ m/s and outer jet velocity $U_{outer} = 18.7$ m/s.	70
5.2	Table showing the values used for generating the velocity profiles for the inner and outer jet	71
5.3	Table showing the turbulence injection parameters for Passot-Pouquet spectrum. . .	72

Nomenclature

Roman Symbols

I	Identity tensor or matrix	
n	Normal vector	
u	Velocity vector	[m/s]
\mathcal{G}	Gaussian filter kernel	
\mathcal{O}	of the order of	
\mathcal{V}	Computational cell volume	
S	Control surface	[m ²]
S	Strain rate tensor	[1/s]
T	Shear stress tensor	[N/m ²]
C_s	Smagorinsky model constant	
C_W	WALE model constant	
D_ϕ	Diffusivity of ϕ	[m ² /s]
E	Total energy per unit mass	[J/kg]
e	Internal energy	[J/kg]
h	Characteristic LES mesh size	
P	Pressure	[Pa]
Q	Energy source term	[J/kg/m ³]
r	Specific gas constant	[J/kg/K]
T	Temperature	[K]
t	Time	[s]
Y_c	Progress variable	

Z Mixture fraction

Greek Symbols

Δ	Flame filter width	
Δ_h	Characteristic LES filter width	
δ_{ij}	Kronecker delta	
$\dot{\omega}$	Source term	
γ	Specific heat ratio	
λ	Thermal conductivity	[W/m/K]
μ	Dynamic viscosity	[Ns/m ²]
ν	Kinematic viscosity	[m ² /s]
Ω	Control volume	[m ³]
ϕ	A scalar or the equivalence ratio according to context	

Subscripts

∞	Reference value
0	Value in the reactant stream
e	Internal energy
i	Index
T	Turbulent

Superscripts

'	Derivative
*	Normalized quantity
d	Deviatoric part

n	n^{th} time step	ICS	Incompressible Solver
Non dimensional numbers		IEA	International Energy Agency
Fo	Fourier number	ILDMM	Intrinsic Low Dimensional Manifold
Ma	Mach number	ISAT	In Situ Adaptive Tabulation
Re	Reynolds number	LDA	Laser Doppler Anemometry
Operators		LDV	Laser Doppler Velocitometry
$(\cdot)^T$	Transpose operator	LES	Large Eddy Simulation
\mathcal{C}	Convection operator	LHS	Left Hand Side
\mathcal{D}	Diffusion operator	ODE	Ordinary Differential Equation
∇	Gradient operator	PCG	Pre-conditioned Conjugate Gradient
$\overline{\cdot}$	Filter operator	PCM	Presumed Conditional Moment
$\tilde{\cdot}$	Favre filter operator	PIV	Particle Image Velocimetry
Acronyms		POD	Proper Orthogonal Decomposition
BCG	Bi-Conjugate Gradient	RANS	Reynolds Averaged Navier Stokes equation
CG	Conjugate Gradient		tion
CSWB	Cambridge Swirl Burner	RHS	Right Hand Side
DISI	Direct Injection Spark Ignition	RK	Runge Kutta
DNS	Direct Numerical Simulation	SBB	Sydney Bluffbody Burner
DPCG	Deflated Pre-conditioned Conjugate Gradient	SGS	Sub Grid Scale
F-TACLES	Filtered TABulated Chemistry for LES	TFV4A	Two-step Finite-Volume 4th-order scheme version A
FGM	Flamelet Generated Manifold	TTG	Two Step Taylor Galerkin
FLF	Filtered Laminar Flame	VDS	Variable Density Solver
FPI	Flamelet Prolongation of ILDM	WALE	Wall Adapting Local Eddy viscosity
FVM	Finite Volume Method		
GDI	Gasoline Direct Injection		

Introduction 1

Contents

1.1	Context and Motivation	1
1.2	Objectives and Contributions	6
1.3	Thesis structure	7

1.1 Context and Motivation

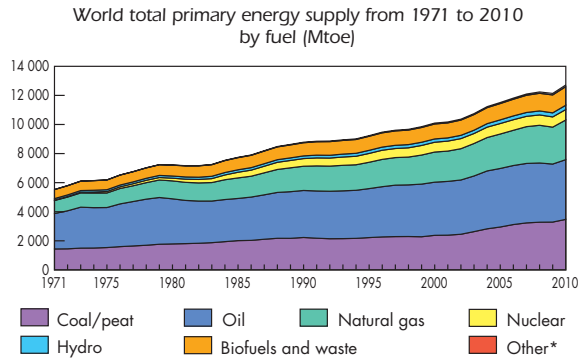
Mankind is facing an ever increasing energy demand for serving a multitude of purposes such as transportation, electricity, manufacturing and heating. Due to growing population and developmental activities, the demand for energy is expected to increase continuously for at least the next coming three decades. Figure 1.1 shows the trend of the total primary energy supply over the last 40 years with its breakup based on the sources supplying it. Similar statistics are frequently published by the International Energy Agency (IEA) to assist policy formations concerning energy. Evidently, the fossil fuels (coal, natural gas and oil) are the highest contributors towards the energy supply with a total contribution of 86.7 % in 1971 and 81.1 % in 2010 respectively. Looking at the projections of the primary energy supply shown in Fig. 1.2 for the coming 20 years, the trend shows a continued dependency on the fossil fuels.

Other sources of energy such as hydroelectricity, biofuels, nuclear energy and renewable sources have increased their contribution over the years but still remains far away from overtaking the fossil fuels. It is noteworthy that the nuclear power has seen a significant growth (4.8%) from 1971-2010. Developing nations like China, India and Brazil are investing large amounts of money and infrastructure on nuclear power to meet their growing energy demands. However in the wake of accidents that happened in Fukushima nuclear power plant on 11 March 2011 in Japan, there is severe pressure on governments to withdraw this source of power and to stop creation of new nuclear power plants. Renewable sources of energy based on solar, wind and geothermal are growing slowly, but presently not enough to meet the industrial demands. Thus the non-renewable sources are expected to remain the primary supplier of our total energy consumption.

Energy extraction from coal, natural gas, oil and biofuels predominantly involves combustion. Consequently the majority of the world's energy demand is met by combustion. Energy from these carbon rich fuels come at the expense of releasing tonnes of CO₂ into the atmosphere often

TOTAL PRIMARY ENERGY SUPPLY

World



1973 and 2010 fuel shares of TPES

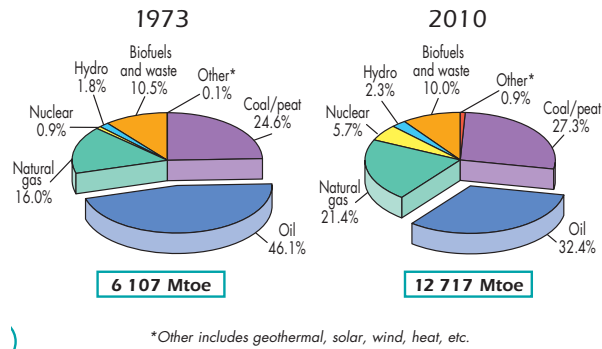


Figure 1.1: Primary energy supply break up extracted from Key World Energy Statistics 2012 published by International Energy Agency

along with other toxic pollutants such as carbon monoxide, oxides of nitrogen and sulphur. This has multiple impacts on health and environment. First of all, the increase in green-house gases like CO_2 and H_2O increases the trapped thermal energy of the sun, resulting in a global rise in temperature. This phenomena is popularly known as global-warming. Secondly, oxides of nitrogen (NO and N_2O) cause ozone depletion resulting in the entry of the carcinogenic solar ultra violet rays. Finally, the partial oxides are known to cause acid rains and several other health problems.

A quantitative view of the CO_2 emissions from 1971-2010 is shown in Fig. 1.3 which is observed to follow the energy supply curves discussed earlier. As expected, the fossil fuels are the major contributors of CO_2 emissions and therefore is predicted to rise in the coming years. This will have a very huge impact on the global temperature resulting in melting of polar ice caps and causing climatic changes through modified ocean currents. The IEA depicts in Fig. 1.4 that if no serious measures are taken by 2017 to reduce CO_2 , the emissions from the existing infrastructure alone is sufficient to cause a global temperature rise of 2°C above the pre-

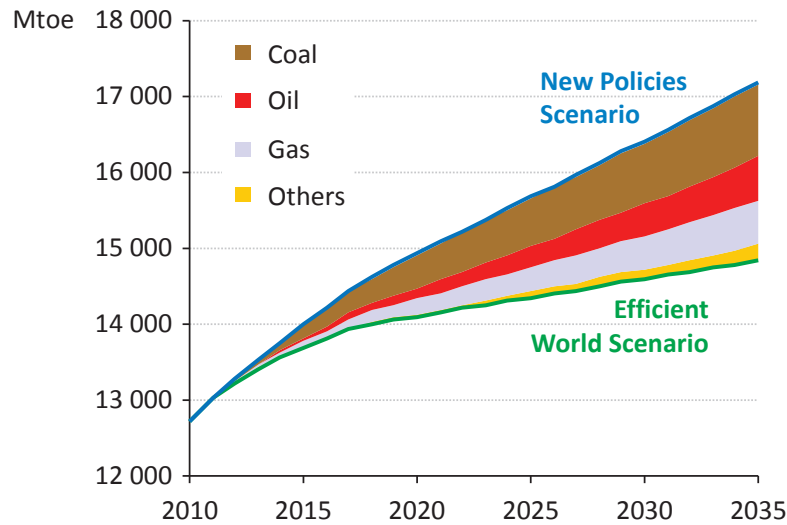


Figure 1.2: Projected primary energy supply break up extracted from Key World Energy Statistics 2012 published by International Energy Agency

industrial levels. These measures addressed towards reduced CO_2 emissions inevitably concerns the optimization of existing combustion systems and development of better technologies for the future.

Different directions are pursued towards optimizing combustion systems and reducing emissions, for e.g. use of alternate fuels, better combustion control and refined combustion techniques. In addition to being efficient, the combustion systems need to satisfy the essential requirements of stability, reliability and long life. To achieve these objectives, researchers resort to different experimental and numerical techniques which help to understand the phenomena occurring within the systems since practical combustion systems are complex, involving several multi physics phenomena such as multiphase flow, heat transfer, reactions and their interactions embedded in turbulent flows.

Measurement of key global quantities such as power output, temperature and pollutants of a practical combustion system can be made with relative ease to characterize the impact of changes made to the system. However, to push the limits of the system, a better understanding of the local phenomena might be required. This often involves isolating fundamental phenomena and developing reduced problems which can be studied extensively using both experimental and numerical techniques. The experiments also form a valuable database for the modeling groups who can develop and validate their numerical models. By working in tandem, the researchers are able to obtain a better understanding of the processes and suggest improvements for the combustion system. Moreover, a well calibrated numerical simulation facility can be used to get a reasonably accurate prediction of a particular change to the combustion system without spending the time, effort and money for manufacturing actual prototypes and testing them.

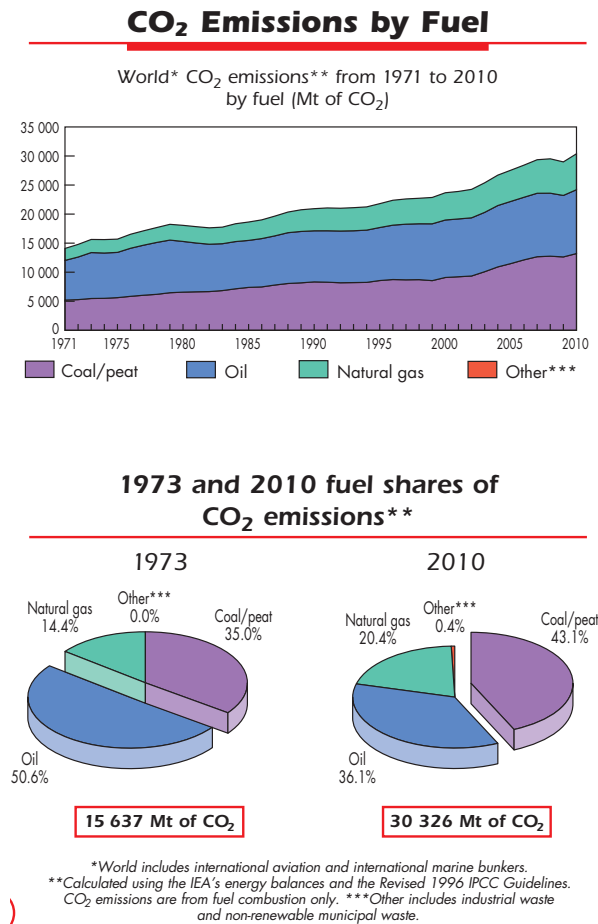


Figure 1.3: CO₂ emissions by fuel extracted from Key World Energy Statistics 2012 published by International Energy Agency

Mathematical modeling of flow systems can involve solving a simple algebraic equation to complex non-linear partial differential equations like the Navier-Stokes equations. Due to the non-linear nature of the Navier-Stokes equations, the existence of an analytical solution is not always guaranteed except for certain canonical flow situations where the equations can be simplified into ordinary differential equations (ODEs) or simple partial differential equations (PDEs) by apriori assumptions and omission of certain terms. These equations can then be solved by known analytical solution methods. Unfortunately, for most of the engineering flow situations these assumptions are invalid and analytical solution does not exist. With the recent advances in computational power, numerical simulation of complex systems has been rendered feasible and is popularly known as computational fluid dynamics (CFD) technique. Three popular approaches exist to solve turbulent fluid flow equations numerically. These are direct numerical simulation (DNS), large eddy simulation (LES) and the Reynolds averaged Navier Stokes equation (RANS) approaches.

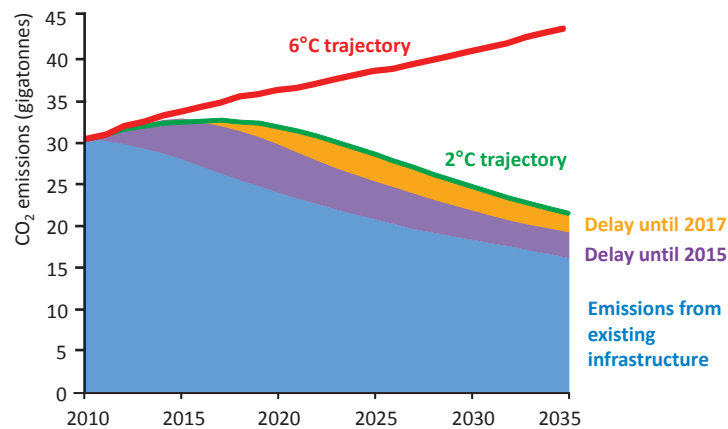


Figure 1.4: Global CO₂ emissions and the projections for the next 25 years. Extracted from World Energy Outlook 2012 by International Energy Agency

DNS involves resolving the smallest possible time and length scales of the flow studied. In a turbulent reactive flow, the smallest length scales are normally associated to the thickness of the radical's evolution inside the flame zone. In very highly turbulent flows, the Kolmogorov length scale might be the lowest length scale to be resolved. These length scales could be of the order of a few micrometres. The smallest time scale on the other hand is governed by the fastest phenomena in the system. For e.g. in a system involving combustion, the smallest time scale is normally governed by the characteristic reaction or diffusive time scale of certain radical species which are of the order of few microseconds. Therefore, a perfect DNS of a large industrial system which is of the order of a few metres can involve billions or even trillions of mesh points with a time step so small that a full flow through time is not feasible to be simulated with the existing computational resources. Therefore, DNS is limited to very small geometries and simplified configurations with low Reynolds number and skeletal reaction mechanisms. This trend is expected to remain so for at least the next 10 years.

RANS and LES evolved as solutions for overcoming this limitation of DNS. In RANS the governing equations are ensemble averaged. This results in the filtering of the small time scale fluctuations and captures only the mean time evolution of the flow. This is computationally less expensive but at the cost of accuracy. From a mathematical point of view, RANS relies heavily on the modeling of certain unclosed terms which appear during the averaging of the NS equations. On the other hand in LES, the governing equations are spatially filtered thus removing the smallest spatial scales. The solutions are then time marched to obtain unsteady flow solutions. It is not as accurate compared to the DNS due to the loss of information associated to spatial filtering but is less costly in terms of computational effort and time. In comparison to RANS, LES is more accurate and ideal for combustion studies where time evolution is critical especially for studying instabilities. It captures the larger unsteady dominant structures of a system giving

a clear upper hand over RANS. Therefore, weighing accuracy and the present computational feasibility, LES is evolving as a promising bargain for the current scenario. In fact, the existing computational resources, code optimizations and declining computational cost make it feasible to perform very highly refined LES of real life burners.

Combustion systems can have premixed, non-premixed or stratified modes of combustion. Lean premixed mode and stratified modes of combustion promises significant efficiency gains and low emissions. Recent aircraft combustion chambers and internal combustion engines exploit this technique and significant amount of research, both experimental and numerical, is dedicated towards understanding these combustion modes. From the numerical simulation perspective, since RANS was the most popular tool for years, most of the LES models were proposed as a direct extension of the RANS models. This approach has a major drawback because of the reason that RANS and LES involve fundamentally different concepts. Therefore, it is essential to develop dedicated combustion models for LES to benefit the computational power available. This forms the basic motivation for this thesis work.

1.2 Objectives and Contributions

The primary objective of the thesis is to develop a dedicated turbulent combustion model for premixed and stratified flames in LES. The secondary objective is to validate the model and to study premixed and stratified combustion by simulating the Cambridge burner (CSWB) studied experimentally by Prof. Hochgreb and co-workers [3, 4] to gain useful insights into premixed and stratified flames. The main contributions of this thesis work are listed below:

- Development and implementation of the filtered laminar flame (FLF) - PDF model for LES in the code YALES2. In this novel approach to combustion in LES, the filter size is not fixed a priori, but calibrated according to the local LES mesh size and subgrid scale scalar fluctuations when the flame wrinkling is not resolved.
- Code development for the FLF-PDF chemical table generation. This involves obtaining laminar flames from Cantera, filtering and interpolating them, and finally storing in look up tables.
- Validation of the model on 1D, 2D and 3D flow cases. Simulation of the non-swirling premixed and stratified cases of the Cambridge swirl burner using the FLF-PDF model. Analysis of stratified flames.
- Analysis of the premixed and stratified configurations by comparing with the experiments and extracting informations such as the validity of flamelet hypothesis, influence of stratification on the flame and model performance.

- Development of a differential diffusion model for addressing the non-passive behaviour of mixture fraction. A differential diffusion number is proposed to predict the presence of this effect in other burners.

1.3 Thesis structure

The thesis is organized as follows:

Chapter 2 briefly reviews the literature existing on reacting and non-reacting annular jet flows, turbulent combustion models for LES (specifically in the flamelet tabulated chemistry context), stratified combustion and differential diffusion studies listing the merits and drawbacks of these models so as to improve upon them in the proposed model.

Chapter 3 details the governing equations solved in the LES at the low Mach number limit. The main features of the YALES2 solver used for the study are described with emphasis on numerical schemes and the time integration.

Chapter 4 gives a detailed description of the derivation of the model and its key features. The method of table generation and the interpolation procedures used are also described. Subsequently, the validation of the model in a 1D laminar flame simulation and a 2D Bunsen flame simulation are also given. The differential diffusion modeling strategy to capture the non-passive behaviour of mixture fraction is described.

Chapter 5 describes the Cambridge swirl burner and the configurations studied in this work. The computational domain, the mesh and the boundary conditions imposed are also discussed. The quality of the velocity boundary conditions are verified by comparison of the non-reacting flow statistics to the experiment.

Chapter 6 discusses the simulation of the fully premixed configuration (CSWB1) using the PCM-FPI model and the FLF-PDF model. The velocity and scalar statistics are compared to the experimental results. Subsequently, the mixture fraction results are also presented emphasizing the impact of differential diffusion modeling.

Chapter 7 discusses the simulation results of the two non-swirling stratified configurations (CSWB5 and CSWB9) of the Cambridge swirl burner. An attempt is made to analyze the results of the stratified flames from the perspective of existing literature and to check the validity of flamelet hypothesis.

Chapter 8 summarizes the main conclusions of the present work and perspectives for further development.

Overview: Bluff body Flow

Physics and Modeling of Turbulent flames

2

Contents

2.1	Bluff body and annular jet flows	9
	Introduction	9
	Non-reacting annular jet flows	10
	Reacting annular jet flows	13
	Re-laminarisation effects in bluff body combustors	15
2.2	Premixed and stratified combustion modeling in LES	16
	Introduction	16
	Description of chemistry	16
	Turbulent combustion models	19
2.3	Studies on stratified combustion	23
2.4	Differential diffusion studies in combustion	27

In this chapter, a brief overview of experimental and modeling studies on annular jet flows, premixed and stratified combustion, and differential diffusion is presented restricting to studies close to the context of this work.

2.1 Bluff body and annular jet flows

Introduction

Bluff bodies are solid bodies stationed across flows which induce certain desirable or undesirable disturbances. The wake of the bluff body normally involves recirculation zones which are caused by the presence of an adverse pressure gradient at certain locations along the bluff body surface. The adverse pressure gradient causes the flow to decelerate suddenly or even reverse, leading to flow separation. The flow separation and resulting vortex shedding were first studied by scientists Strouhal (1878) and Von Karman (1912).

The aerodynamics of bluff body flows is of great importance and has been a subject of study since a long time. To cite a few examples, aircraft, automobile and ship bodies, buildings, flame holders, turbine and compressor blades are all different functional forms of bluff bodies. Based on the roles that they play, bluff bodies may have different names and different design criteria as evidenced in the examples mentioned before.

Single and co-axial annular jet configurations can also be studied under bluff body aerodynamics since they involve a sudden expansion resulting in a low pressure wake, leading to recirculation zones. The annular jet configurations operated with or without swirl are of interest to the combustion community due to its simplicity and flame stability. They find applications in combustion chambers such as aircraft combustors or in academic research for performing fundamental studies on turbulence and flames, and their interactions. A common annular jet configuration is the centre-body configuration consisting of a closed central tube and annular jet(s) around it.

Since this work principally involves large eddy simulation of a centre-body burner (Cambridge swirl burner), attention will be focussed mainly on similar configurations. In the coming sections, a brief literature review of the non-reacting and reacting annular jet studies are reported. They will be sub-divided into experimental and numerical studies. Subsequently, a review on the re-laminarisation effects reported in literature is also made.

Non-reacting annular jet flows

Non reacting flow studies around bluff bodies are essential to gain insights into the flow breakdown mechanisms and for isolating certain flame induced and flow induced phenomena. A brief review of the experimental and numerical studies of non-reacting annular jets are made in this section.

Experimental studies

There are numerous experimental studies on annular jets for different configurations. A comprehensive review of these works can be found in the PhD thesis of Del Taglia [5] and Lars Blum [2].

The first systematic study of non-reacting annular jets was performed by Davies and Beer [6], who divided the flow regions into a recirculation zone, a transition zone and an established flow zone. Later, Ko and Chan [1] proposed a more detailed description in single or coaxial annular jet flows, as shown in Fig. 2.1. They called these regions as the initial merging zone, the intermediate merging zone and the fully merged zone. The initial merging zone extends from the jet exit to the end of potential core of the jet. It is characterized by a central recirculation zone with two counter-rotating vortices. In the intermediate merging zone, the mixing of two coaxial jets or mixing of the single jet with the outer co-flow happens. The jets then merge at a point called the point of reattachment. Ahead of this zone is the fully merged zone, where the behavior was found to be similar to that of a circular jet. Ko and Chan [1] used non-dimensional

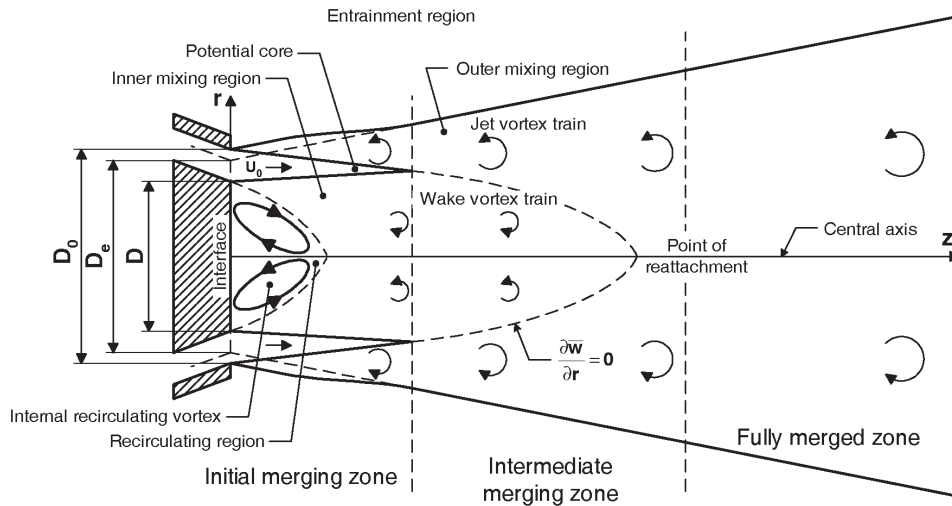


Figure 2.1: Schematic diagram of the basic annular jet with time averaged flow regions, according to Ko and Chan [1] extracted from the thesis of Lars Blum [2]

radial distances to show the similarity between round jets and annular jets in the fully merged zone. They also reported that the recirculation zone causes the jet to develop faster than a similar round jet.

Annular jet studies were based on three main parameters - the blockage ratio, Reynolds number (Re), and the half opening angle of the bluff body. Referring to Fig. 2.1, the blockage ratio is defined as the ratio D^2/D_0^2 where D is the diameter of the bluff body and D_0 is the jet diameter. The Reynolds number based on hydraulic diameter can be expressed as $(D_0 - D)U_0/\nu$. The half opening angle, α depends on the shape of the bluff body. To give an idea, for a cylinder, $\alpha = 0^\circ$ whereas for a circular disk $\alpha = 90^\circ$ and for divergent cones $0 < \alpha < 90^\circ$ (Fig. 2.1) and so on.

Durao and Whitelaw [7] observed that for disk shaped bluff body flows with increasing blockage ratio, the amount of recirculating mass increased but the height of the recirculation zone decreased. They reported an overall anisotropic turbulence in the recirculation zone with an intensity of turbulence close to 30%. They also noticed a discrete frequency in the boundary layer of the annular jet with a Strouhal number of 0.79.

Li and Tankin [8] proposed expressions for the height of the recirculation zone (L_r) in the laminar and turbulent regime by studying annular jet configurations for different blockage ratios at two different half opening angles. According to them, in the laminar regime the height of the recirculation zone is directly proportional to the Reynolds number and blockage ratio ($L_r/D \propto$

Re). In the turbulent regime, this height decreases with Reynolds number and blockage ratio, and is more strongly correlated to the shape of the geometry, which was also observed by Durao and Whitelaw [7] ($L_r/D \propto 1/Re$).

Different experimentalists observed different critical Reynolds number for the laminar to turbulence transition in annular jet flows. Huang [9] reported a transition to turbulence at $Re > 750$ for a blockage ratio of 0.44 similar to the values reported by Li and Tankin [8] which were between 700-800. On the other hand, Sheen *et al.* [10] measured transition to turbulence at a higher value of Reynolds number ($Re = 2000$).

Other major experimental studies include the work of Vanierschot [11] who investigated the influence of swirl on annular jets, LDV measurements on single and double annular jets by Frania *et al.* [12] and Schmitt *et al.* [13] respectively.

Numerical studies

Concerning the numerical simulations of annular jets, the earliest work was that of Pope and Whitelaw [14] who performed steady two dimensional simulations of Durao and Whitelaw [7] experiment. The axial velocities were found to be under predicted and was attributed to the smaller computational domain and lack of higher order turbulence models. Later, Leschziner and Rodi [15] also performed steady two dimensional simulations with a modified $k - \epsilon$ model and reported better prediction of the axial velocities. Other significant early RANS simulations include that of McGuirk [16] and Durao [17], whose velocity and turbulent stress predictions were also not satisfactory. Recently, Del Taglia *et al.* [5] investigated flow asymmetry in annular jets in the laminar regime for various blockage ratios and Reynolds numbers using RANS simulations. The first 3D LES of annular jet was performed by Akselvoll and Moin [18] to match the experiments of Johnson and Bennett [19]. This configuration involved a side recirculation zone. They obtained good results in terms of axial velocity and its fluctuations as well as the passive mixing scalar.

Annular jets operated with swirl is another configuration of interest. Swirling annular jet configurations are marked by a precessing vortex core (PVC), which have a role similar to the recirculation zone. They assist in mixing and enhancing flame stabilization. Due to the inherent unsteady nature of this kind of flows, URANS and LES is preferred over the conventional RANS technique. URANS of swirling jet configurations were performed by [20]. Wegner *et al.* [21] and Dunham *et al.* [22] were able to demonstrate the superiority of LES over URANS for swirl configurations. Other prominent works in LES of non-reacting swirling annular jet flows include that of Garcia-Villalba *et al.* [23], Lu *et al.* [24] and McIlwain and Pollard [25]. The prescription of inlet velocity and fluctuations for the swirl flow were considered critical in these studies. Pierce and Moin [26] and Garcia-Villalba *et al.* [23] had suggested strategies of generating swirling turbulent inflow data. A Smagorinsky model (constant and dynamic) was used in all the studies. However, a consensus regarding the mechanism of PVC and vortex breakdown has not been reached yet. A wide literature exists on the numerical simulation of

swirling annular jet studies. In this work only the non-swirling configuration is studied therefore a comprehensive review of the swirl configurations is not made.

Reacting annular jet flows

On a macroscopic scale the bluff bodies act as flame holders or stabilizers by recirculating the burnt products in its wake and mixing it with the incoming fresh gases. This intensive mixing results in transfer of energy from the burnt gas to the fresh gas causing combustion. The role of bluff bodies as flame-holders in fast flowing environments such as ramjets and afterburners is a topic of constant interest for the combustion community.

Experimental studies

Most of the basic inferences regarding flame stabilization mechanisms were drawn from the pioneering works [27–35] in bluff body flame stabilization and blow off characterization carried out during the period from 1950s to the 80s. Longwell et al. [27] viewed the wake of the bluff body as a homogeneous chemical reactor and attributed the sustenance or extinction of the flame to the residence time of the mixture in the wake. Zukowski and Marble [30] considered the time spent in the shear layer to be the deciding factor for flame stability. The criteria for stability thus depends on the Damköhler number which is the ratio of the residence time to the chemical time. These studies analyzed the maximum flame sustainable velocity and lean blow-off limit for flames stabilized behind a bluff-body in fast flowing environments. Other factors that affect the flame stability are pressure, turbulence, temperature, shape of the bluff body and the type of fuel [36]. Premixed flames stabilized behind bluff bodies were studied by Knikker and Veynante [37] for assessing turbulent combustion models. Sjunnesson and Shepherd [38] conducted studies on the VOLVO burner and reported flame surface density measurements. Recent experiments [39, 40] also studied acoustically excited flames. These are discussed comprehensively by Hussain [41] and S. J. Shanbhogue [42]. All these studies were on simple bluff bodies placed across a wide flow and did not involve jets.

There exists numerous experimental studies on annular jet burners with and without swirl. They were designed to replicate those seen in combustion chamber of aircraft engines, furnaces of glass industries and also to give fundamental knowledge as in academic burners. The Sydney bluff body (SBB) [43, 44] burner, the TECFLAM burner [45, 46], the Cambridge swirl burner (CSWB) [3, 47], the TU Darmstadt (TU-D) stratified burner [48], the PRECCINSTA burner [49] and the turbulent LP (Lean Premixed) combustor [50] are some of the annular jet burner experiments. Sydney bluff body (SBB) burner experiments present a series of non-premixed bluff body stabilized flames. All other mentioned configurations involve premixed and/ or stratified combustion. These experiments give good insight into the fundamental phenomena and also generate valuable database for validation of CFD codes and combustion models.

Numerical studies

Most of the numerical studies were focussed on simulating the experiments mentioned in the previous sections. A brief overview of the main numerical studies are given.

Numerical studies of bluff body stabilized non-premixed flames were mainly restricted to the SBB configuration. RANS [44, 51–55] and LES [56–60] of SBB burner was performed by several researchers. The turbulence model used in the RANS computations were predominantly standard or modified $k - \epsilon$ models with the Reynolds stress model except for Merci et al. [54] who used a cubic non-linear eddy viscosity model. The combustion models used in RANS computations were flame sheet model [44], constrained equilibrium model [54], CMC model [51], flamelet model [55] and PDF models [52, 53]. The temperature and species concentrations were not properly predicted at downstream locations in all of these simulations due to the inability of RANS to capture unsteady mixing phenomena. Most of the combustion models for non-premixed flames developed in RANS context were found to be utilizable for LES as well. LES of the SBB burner by Raman and Pitsch [56, 57] reported a significant improvement in the flow field and scalar prediction over RANS. They used a Smagorinsky model for turbulence closure and a laminar flamelet model for combustion closure. The filtered source terms were closed by presuming Beta-PDF for the mixture fraction and a log-normal distribution for sub filter scalar dissipation rate PDF. In addition they used an adaptive mesh refinement to ensure that the unresolved scalar energy is less than 20%. They attributed the improvement in results with respect to RANS to the ability of LES to capture unsteady large scale mixing and the shear layer interaction with the flame at downstream locations. The prescription of inlet boundary conditions was also reported to be critical. Kempf et al. [58] used a dynamic Smagorinsky model for turbulence closure and a presumed Beta-PDF for mixture fraction with the steady flamelet model for closing the source terms. Navarro-Martinez and Kronenburg [59] projected the ability of LES - CMC model with presumed Beta-PDF for mixture fraction and detailed chemistry to capture finite rate chemistry effects and flame cooling. The most recent work is that of Zhao et al. [60] who performed LES of SBB burner using a multi environment filtered density function and in-situ adaptive tabulation (ISAT) method to capture re-ignition.

Pertaining to numerical simulation of bluff body stabilized premixed flames, most of the configurations mentioned in the section on experimental studies were subjected to numerical simulations. Cannon et al. [61] and Vicente et al. [62] performed RANS of the LP burner [50] using a joint velocity composition PDF and ISAT for chemistry. The species concentrations and temperature were highly over predicted in Cannon's computations at downstream locations whereas Vicente reported better agreement due to a dynamic molecular mixing model. Moller et al. [63] performed LES of the VOLVO burner using three combustion closure approaches :-eddy dissipation model, presumed PDF approach and monotonically integrated LES model (MILES). They reported similar results for the three different sub-grid models. Giacomazzi et al. [64] did LES of the same burner with an eddy dissipation concept implemented in a Fractal model (FM). Manickam et al. [65] used an algebraic flame surface wrinkling model to compare LES and

RANS against measurements for the VOLVO burner. The results showed a superiority of LES over RANS in predicting scalar and velocity fields. Chakravarthy and Menon [66] carried out LES of a confined bluff body flame using a Linear Eddy model (LEM). Boger and Veynante [67] performed LES of a turbulent flame behind a triangular flame holder using a gradient closure. They showed that by using a gradient type closure in LES, counter gradient diffusion at least at the resolved level is captured for which in RANS would require higher order modeling. LES of the PRECCINSTA burner was performed by many researchers [68–71] to validate different combustion models such as the PCM-FPI model [68, 69], thickened flame model [70] and the F-TACLES model [71]. The TECFLAM burner was simulated using a dynamic thickened flame approach by Kuenne et al. [72] and using a G-equation model by Freitag and Janicka [73]. Very good agreement with experiments were reported emphasizing the ability of LES to predict highly turbulent and unsteady flames irrespective of the combustion models.

Recently, the focus has shifted towards the turbulent stratified flame configurations. The CSWB [3] and the TU-D burners [48] were designed specifically to address premixed and stratified flames and their interaction with shear. Except for the work of Kuenne et al. [74] who performed LES of a stratified case in the TU-D burner using a dynamic thickened flame approach combined with FGM, not much work has been reported on these two burners.

Re-laminarisation effects in bluff body combustors

Flame induced effects in flow was found to be significant in bluff body flames. Consequently, the reacting and non-reacting flow fields around a bluff body are completely different from each other. In an isothermal non-reactive flow, asymmetric Von Karman (VK) vortex shedding occurs and a dominant frequency exists. On the other hand, for a reacting flow the VK vortex shedding could be suppressed and only shear instabilities may exist. The turbulence levels in the wake are governed by the right hand side terms of the equation for vorticity (Eq. 2.1). These terms are namely the vortex stretching term (I) due to velocity gradients, the vortex stretching term (II) due to compressibility effects, the baro-clinic torque term (III) and the viscous dissipation term (IV).

$$\frac{\partial \boldsymbol{\omega}}{\partial t} + (\mathbf{u} \cdot \nabla) \boldsymbol{\omega} = \underbrace{(\boldsymbol{\omega} \cdot \nabla) \mathbf{u}}_I - \underbrace{\boldsymbol{\omega} (\nabla \cdot \mathbf{u})}_{II} + \underbrace{\frac{1}{\rho^2} (\nabla \rho \times \nabla P)}_{III} + \underbrace{\nabla \times \left(\frac{\nabla \cdot \mathbf{T}}{\rho} \right)}_{IV} + \nabla \times \mathbf{f}_b \quad (2.1)$$

The kinematic viscosity of a gas increases sharply with temperature and contributes to dampening the vorticity generation by increasing the viscous dissipation term [75]. Studies performed by Mehta and Soteriou [76] show that the balance of baro-clinic torque and the dilatation plays a more important role than the viscosity. They observed that the volumetric expansion during heat release causes the flow to become more symmetric and laminarised. The re-laminarisation of the flow by combustion in bluff body flames was observed in experiments as well as in numerical simulations as reported by Erickson and Soteriou [77]. Shanbhogue et al. [78] gives a comprehensive review of the exothermic influences on the bluff body flow by considering the

influence of exothermicity on the shear layer and bluff body wake. They propose that there exists a significant competition between the shear generated vorticity and the baroclinic torque generated vorticity. This competition may result in complete cancellation of the vorticities or even a domination of the baroclinic vorticity. The baroclinic torque as seen in Eq. 2.1 is a function of the density and pressure gradients and their relative orientation. The density and pressure gradients are found to be related to the gas expansion ratio ρ_b/ρ_u and the flame speed whereas the orientation is a function of the laminar flame speed to the flow velocity. Therefore, the competition of the two vorticity sources is governed by the equivalence ratios and dilution as well. On the other hand for the wake region, exothermicity can lead to suppressing of the Von-Karman instabilities partially or even completely at high density ratios [79].

2.2 Premixed and stratified combustion modeling in LES

Introduction

There are two main parts to simulating reacting flow in LES. They are

- Describing the chemical reactions or addressing chemistry
- Closure of filtered terms (source terms and diffusive terms) or combustion modeling

In subsections 2.2 and 2.2, major works under these two topics are discussed focussing mainly on premixed and stratified combustion.

Description of chemistry

Describing in detail all the reactions and transport occurring within a combustion process mathematically requires solving a large system of highly non-linear stiff species transport equations. This might not be feasible for large geometries due to the tremendous computational cost incurred. Therefore, a lot of attention is focussed in the combustion community to look for strategies which help us overcome this problem. Two commonly applied strategies are to reduce kinetics by developing skeletal mechanisms and by manifold generation. Often a combination of these methods are also employed to achieve the objective of reducing the computational cost.

Reducing kinetics by skeletal mechanisms

Reducing a detailed chemical kinetics scheme to a skeletal mechanism can be performed by omitting certain species or eliminating certain reactions or by doing both such that the global phenomena (flame speed, auto-ignition, major species evolution, etc) of interest is preserved. To identify “unimportant” species one can go about removing a particular species [80] and all associated reactions, and verify if this still preserves the global property. This method could be very time consuming when several species have to be tested. Subsequently, the variation [81] of the property of interest to every species could be determined as a Jacobian quantity to identify

redundant species. Lu and Law [82] proposes a direct relation graph method for the same. To identify redundant reactions Warnatz et al. [83] proposes sensitivity analysis of the reaction rate constant on the species evolution and a reaction flow analysis.

Manifold generation and tabulated chemistry approach

The manifold generation method tries to project the whole system with $N+2$ degrees of freedom (N species, enthalpy and pressure) onto a lower dimensional system by using certain criteria. Towards this direction, Peters [84] proposes to identify very fast evolving species and making the assumption that they are quasi steady and are at equilibrium. Consequently, the system reduces to solving only for the slow evolving species. Similarly the concept can be extended to reactions as well, where certain elementary reactions can be assumed to be in partial equilibrium. Lam [85] suggests the computational singular perturbation method (CSP) to identify such reactions. At low temperatures both these methods may pose problems since the reactions and species might not be in partial equilibrium.

Maas and Pope [86,87] used a more mathematical approach of identifying low dimensional manifolds (ILD^M) in the chemical system towards which the species evolution trajectories converge in time. An eigen value analysis of the species evolution helps to identify the fast and slow evolving species. Using this information, manifolds are built as a function of slow evolving species. In a non diffusing system, at high temperatures (when the system is close to equilibrium) even a single dimensional manifold might be identified thus largely simplifying the system. However this method encounters problems at low temperatures because of the fact that there will be multiple time scales of evolution and the chosen slow species cannot capture the evolution here. Improvements in the approach accounting for transport effects were proposed by Bykov and Maas [88] while the low temperature situation were addressed by Ren and Pope [89].

A less mathematically [90] involved but very practical approach is the Flamelet prolongation of ILDM (FPI) [91] or the flamelet generated manifold (FGM) [92] approach. This approach is based on the flamelet hypothesis which assumes that a flame is made up of smaller elemental laminar flamelets. According to the combustion system and the global behaviour of the combustion involved these flamelets could be assumed to be steady laminar premixed flamelets, perfectly stirred reactors, steady non-premixed flamelets, unsteady non-premixed flamelets or even partially premixed 2D flamelets [93]. In premixed flames usually the steady laminar premixed flamelets are considered. These flamelets can be described on a reduced phase space built from equivalence ratio, enthalpy (h), pressure (P) and a progress variable. The thermo-chemical variables are then tabulated as a function of these phase space variables reducing the number of variables in the system and thus the complexity and computational cost. Usually, a mixture fraction Z , which tracks the fuel-air mixing and has a one to one relation with the equivalence ratio, is used to tabulate the quantities. The three variables Z , h and P completely define the initial and final states of a steady laminar premixed flame. The progress variable, Y_c contains the

¹ILD^M: Intrinsic low dimensional manifold

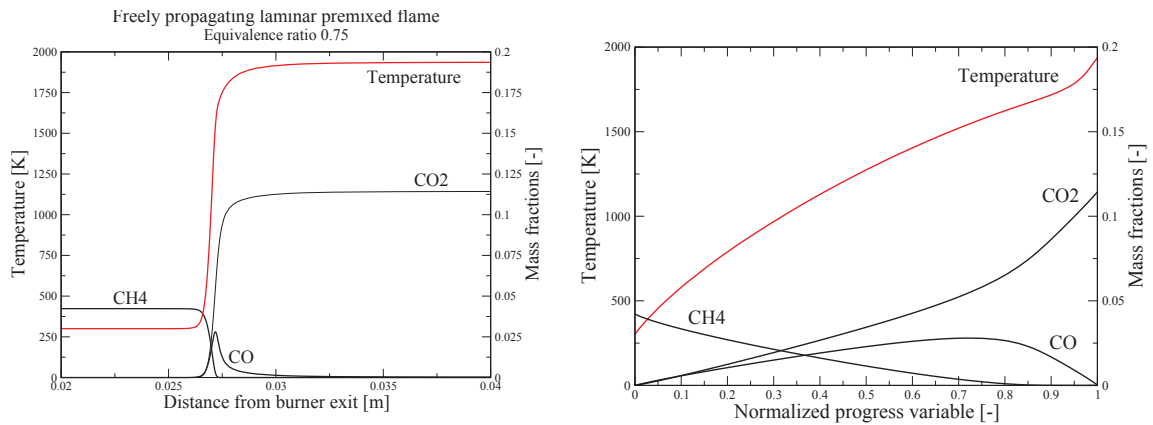


Figure 2.2: Species distribution inside a laminar premixed flame as a function of distance from burner exit.

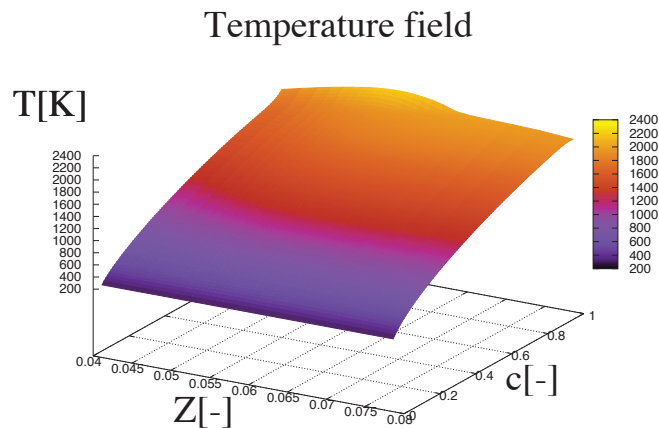


Figure 2.3: Temperature as a function of mixture fraction and normalized progress variable

evolution information of the premixed flame system between the initial and final states. Figure 2.2 (left) shows a typical laminar premixed flame solution of methane air flame depicting a few major species and temperature as a function of distance from burner exit. On the right, the projection of the flame solution onto a normalized progress variable built from $Y_c = Y_{CO} + Y_{CO_2}$ is also shown. Subsequently, extending the procedure to different equivalent ratios (mixture fractions) a map (Fig. 2.3) of the flame solution can be obtained which can be used to represent the flamelets in a combustion system.

Turbulent combustion models

The LES outlook is to resolve the larger scales of the flow and model the sub-grid scales. When it comes to turbulent combustion the flame thickness (order of 100s of microns) is generally much smaller than a typical LES filter size (order of a 1000 microns to few mms). It indicates that combustion essentially exists as a sub-grid phenomena in a typical LES and requires to be modeled. Therefore, combustion modeling needs to be addressed with great care.

Either of the two main strategies described below are normally adopted to develop models for LES of turbulent premixed combustion. The first approach tries to resolve the flame and the second approach tries to capture the flame dynamics without resolving it. Thickened flame models [94] and Linear Eddy Models (LEM) [95, 96] use the former approach whereas the other existing models namely the level set G-equation model [97], Flame Surface Density approaches [98–101] and PCM²-FPI [102] model fall in the latter category. The so-called second approach is strongly based on the flamelet hypothesis which assumes that the flame remains very thin and is unaffected by the turbulent eddies. It is also assumed that the effect of turbulence on the flame is just to wrinkle it without affecting its chemical structure. Recently, an algorithm for CMC³ model [103] was extended to be used in premixed combustion, but has not been tested on an actual LES. Most of these models were developed in a RANS context and there is a very vast literature available. Since this work involves only LES, a review of the models applied in an LES context is only made for brevity.

Thickened Flame model

The thickened flame model tries to resolve the flame on a given LES mesh by artificially thickening it. The initial propositions were made by Butler and O'Rourke [104], and O'Rourke and Bracco [105] to simulate laminar flames on a coarse mesh. They proposed to achieve the artificial flame thickening by enhancing the thermal diffusivity by a factor, while reducing the pre-exponential constant of the reaction term by the same factor to preserve the correct laminar flame speed. Legier et al. [106] proposed a dynamic thickened flame approach where the thickening factor is active only in the vicinity of the flame allowing to capture proper mixing in the non flammable zones. However, in a turbulent flame it was observed [94, 107] that since the thickening of the flame reduced the turbulent length scale to laminar flame thickness ratio, the interaction of turbulence and flame is modified. Therefore, an efficiency factor was proposed by Colin et al. [94] to account for sub-grid wrinkling. Charlette et al. [108] proposed an improved power law wrinkling factor model for the efficiency function which is a key ingredient in the model. Wang et al. [109] suggested a dynamic procedure for obtaining the power law coefficient in LES. Combined with a flamelet hypothesis and using a tabulated chemistry approach, Kuenne et al. [72, 74] used the dynamic thickened flame approach to simulate the TECFLAM burner [45, 46] and the TU-D stratified burner [48]. A typical thickened flame scalar

²Presumed conditional moment

³Conditional Moment Closure

(Y_k) equation reads

$$\frac{\partial(\rho Y_k)}{\partial t} + \nabla \cdot (\rho \mathbf{u} Y_k) = \nabla \cdot (\rho \mathcal{F} \mathcal{E} D_k \nabla Y_k) + \frac{\mathcal{E}}{\mathcal{F}} \rho \dot{\omega}_k \quad (2.2)$$

Here, \mathcal{F} is the thickening factor which is fixed as a constant or determined dynamically whereas \mathcal{E} is the efficiency factor which accounts for sub-grid flame wrinkling. The strengths of this model is that in a laminar flame propagating on a coarse mesh situation it does not require a sub-grid model. Using a reduced chemistry, phenomena like ignition and extinction can be captured with relatively less computational and memory cost in LES using this model. As a consequence, this model is extensively used at CERFACS for simulation of gas turbine burners. However modeling the efficiency function and the thickening factor is a matter of concern and requires strong attention. Moreover, the extension to complex chemistry effects poses many questions.

G-equation model

The G-equation or the level set method was first proposed by Williams et al. [110]. The G-equation is based on the flamelet concept and views the flame as an interface which separates burnt and un-burnt gases. Initially developed in a RANS context, the level set formulation was extended to LES by Pitsch [111] and used for the LES of a turbulent premixed flame stabilized by a triangle flame holder [112, 113] by Moureau et al. [114]. The G-equation model has the advantage that it does not require to resolve the flame on the existing computational mesh, but requires a good estimate of the characteristic propagation speed of the surface and its diffusivity. The coupling of the G-equation model with momentum equation requires careful consideration. In addition, to predict the pollutants an additional progress variable equation with tabulated chemistry may have to be used in tandem with the G-equation.

Flame Surface Density (FSD) approach

Like the other models, the flame surface density approach was also developed initially for RANS by Marble and Broadwell [98], and further studied by several other researchers [115–117]. The feasibility of the concept for LES was studied by Boger et al. [100]. The basic element of the FSD method is to lump together the reaction rate and the diffusive term as a single propagation term and to close it as a product of a propagation velocity and flame surface density. The flame surface density can be defined as the flame surface area per unit volume. The advantage of this method is that the complexity of chemistry, and the interaction of turbulence and chemistry can be decoupled to a certain extent. The propagation velocity takes care of the chemistry and the wrinkling of the flame by turbulence is accounted in the flame surface density term. The FSD term is closed either by using algebraic models [100, 118, 119] assuming an equilibrium between flame surface production and destruction or by solving a separate balance equation [120] for the flame surface density. Recently, Cavallo et al. [121] used the FSD method to simulate the

turbulent stratified burner of Darmstadt. Cross scalar dissipation terms were closed following the approach of Duwig et al. [119].

The FSD method in LES involves a filter size that appears in the closure model which can be used to control the flame thickness thus allowing to resolve the flame on a coarse LES mesh. On the other hand, the disadvantage lies on the fact that all the chemistry information is embedded in the propagation velocity alone.

F-TACLES model

The F-TACLES model by Fiorina et al. [71] uses an explicit filtering method combined with the tabulated chemistry strategy to achieve closure of the filtered source and sub-grid flux terms. The progress variable equation solved in this approach can be written as

$$\frac{\partial(\overline{\rho\tilde{c}})}{\partial t} + \nabla \cdot (\overline{\rho\tilde{\mathbf{u}}\tilde{c}}) = \Xi \nabla \cdot (\alpha_c(\tilde{c}, \Delta) \overline{\rho} D_c \nabla \tilde{c}) + \Xi \Omega_c(\tilde{c}, \Delta) \quad (2.3)$$

where

$$\Omega_c(\tilde{c}, \Delta) = \left(\overline{\rho\dot{\omega}_c} - \nabla \cdot (\overline{\rho(\tilde{\mathbf{u}}\tilde{c} - \tilde{\mathbf{u}}\tilde{c})}) \right)_{(\tilde{c}, \Delta)} \quad (2.4)$$

is the tabulated source term obtained from a 1D laminar flame solution filtered at a filter width Δ . The wrinkling factor, $\Xi = S_t/S_l^0$ is defined as the ratio of turbulent flame speed to the laminar flame speed. The corrective diffusivity

$$\alpha_c(\tilde{c}, \Delta) = \left. \frac{\overline{\rho D_c \nabla \tilde{c}}}{\overline{\rho} D_c \nabla \tilde{c}} \right|_{(\tilde{c}, \Delta)} \quad (2.5)$$

is applied to the filtered equation to compensate the error encountered by filtering of the diffusive term and expressing it in terms of resolved progress variable gradient alone. The filter kernel employed in this method is a Gaussian kernel normalized in physical space. There are two main advantages of this approach.

- Choice of normalized filter in space (Gaussian) ensures that the filtered flame front also propagates at the laminar flame speed for all the filter widths
- The corrective terms and source terms are constructed from the filtered 1D flame solution so that the budget is perfectly closed at all filter widths on a planar laminar flame case

The SGS wrinkling factor looks after the effect of turbulence on the flame. Ξ is modeled following the proposition of Charlette et al. [108].

$$\Xi = \left(1 + \min \left[\frac{\Delta}{\delta_{l(z)}}, \Gamma \frac{u'_{\Delta}}{S_l(z)} \right] \right)^{\beta} \quad (2.6)$$

The formulation was initially applied to study [71] the PRECCINSTA configuration [49]. Subsequently, it was extended to the stratified case [122] by considering a presumed Beta-PDF for the mixture fraction and defining a corrective diffusivity in the mixture fraction and its segregation space. The two major concerns of this model are

- it employs a unity Lewis number assumption which can lead to incorrect prediction of the laminar flame velocity if a special strategy is not adopted
- it uses a fixed filter width and relies heavily on the more or less ad-hoc wrinkling factor model

Similar flamelet models [123] based on physical space filtering were proposed recently by Vreman et al. [123] and Moureau et al. [68] as well. The filtered flamelet model by Vreman et al. [123] also used a fixed filter width to close the filtered source term. It was presumed that the filtered laminar source term directly closes the equation and no attempt to model the sub-grid wrinkling was made. The FLF-PDF model by Moureau et al. [68] forms the basis of this thesis work and will be discussed in detail in the modeling chapter.

PDF Methods

In a premixed flame context the FPI method proposes to tabulate the thermo-chemical quantities (the source terms, species mass fractions, etc) as a function of a mixture fraction, Z and a normalized progress variable, c . Then transport equations for Z and Y_c are solved in the CFD solver which looks up the flamelet table to obtain the source terms or any other property as required. However, when the method is applied in the LES, one encounters two types of problems

- there is access only to the filtered quantities (\tilde{c}, \tilde{Z}) whereas the table has been made as a function of unfiltered quantities
- the LES solver requires a filtered source term $\tilde{\omega}_{Y_c}$ to solve \tilde{Y}_c equation

Unfortunately, due to the non-linear nature of the space filtering operator we have

$$\tilde{\omega}_{Y_c} \neq \omega_{Y_c}(\tilde{c}, \tilde{Z}) \quad (2.7)$$

It is in the spirit of overcoming this problem that the PDF methods arrived on scene. The convolution of the source term with the joint PDF of the variables involved gives directly the filtered source term. If we consider only the independent variables as the mixture fraction and the progress variable once can write

$$\tilde{\omega}_c = \int_0^1 \int_0^1 \omega_c(c, Z) \mathcal{P}(c|Z) \mathcal{P}(Z) dc dZ \quad (2.8)$$

The problem then reduces to determining the PDF. The PDF can be estimated either by solving a PDF transport equation or it can be presumed to follow a specific shape. These two branches form two classes of PDF methods. The former method involves solving all the moments of the PDF is known as the transported PDF approach and the second is called as the presumed PDF or the PCM-FPI approach in the tabulated chemistry context.

PCM-FPI

In the PCM-FPI approach, the shape of the PDFs are presumed a priori. The marginal PDF $\mathcal{P}(c|Z)$ is found to decompose to an independent PDF on c as reported in [102]. The PDFs are normalized and designed to recover the first and second moments of the variable. Mathematically

$$\int_0^1 \mathcal{P}(c)dc = 1 \quad \int_0^1 \mathcal{P}(Z)dZ = 1 \quad (2.9)$$

$$\int_0^1 c\mathcal{P}(c)dc = \tilde{c} \quad \int_0^1 Z\mathcal{P}(Z)dZ = \tilde{Z} \quad (2.10)$$

$$\int_0^1 (c - \tilde{c})^2\mathcal{P}(c)dc = c_v \quad \int_0^1 (Z - \tilde{Z})^2\mathcal{P}(Z)dZ = Z_v \quad (2.11)$$

It can be proved mathematically that the variance is bounded and its maximum value corresponds to $\tilde{c}(1 - \tilde{c})$ and $\tilde{Z}(1 - \tilde{Z})$ for c and Z respectively. It is useful to define normalized variances constrained in $[0,1]$ as

$$S_c = \frac{c_v}{\tilde{c}(1 - \tilde{c})} \quad S_Z = \frac{Z_v}{\tilde{Z}(1 - \tilde{Z})} \quad (2.12)$$

Physically, the PDF represents the sub-grid mixing. For e.g., the PDF of Z represents the mixing of the fuel and oxidizer at the sub-grid scale and the PDF of c that of fresh and burnt gases. By intuition, one can arrive at four elementary shapes of Z that exist corresponding to the mixture in an LES cell being pure fuel, pure oxidizer or a mixture with perfect or imperfect mixing. A Beta-PDF defined in the (\tilde{Z}, S_Z) space recovers all these shapes and is a common choice of the PDF shape for Z . This has been employed widely for non-premixed flames. A Beta-PDF assumption for progress variable has also been employed in literature for simulating premixed flames, even though it is known that the Beta-PDF does not recover the correct flame speed for filtered flame fronts. Other PDF shapes were also investigated such as the FSD-PDF [124]. Lecoq et al. [125] proposed to couple the PCM-FPI technique with the FSD method to achieve better control over the flame speed and thickness.

Once the shape of the PDF is fixed, the laminar flame quantities can be filtered by convoluting with the PDFs as shown in Eq. 2.8 and tabulated a priori as a function of $(\tilde{c}, S_c, \tilde{Z}, S_Z)$. These values obtained from the LES solver at any location at any given time can be used to enter the chemical table and retrieve the required quantities.

The advantage of this method is the relative simplicity and the lesser computational cost. However, as mentioned before presumption of a Beta-PDF might not be suitable for reactive scalars like progress variable.

2.3 Studies on stratified combustion

The typical canonical flames are the premixed and non-premixed flames. However the most frequently encountered situation in industrial burners and internal combustion engines is composed of partially premixed flames. These type of flames are characterized by an incomplete

mixing of the fuel and oxidizer and/or fresh and burnt gases. It is difficult to develop a strict definition for stratified combustion. Pertaining to this work stratified combustion can be viewed as the propagation of flame through fields of premixed fuel-air mixtures of different composition. Stratification is derived from the word *strata* which means layers. In stratified combustion context, the *strata* refers to the layers of equivalence ratio or mixture fraction.

Stratified flames are encountered in gas turbines, internal combustion engines and most of the industrial furnaces. Stratified combustion gains significance because of its ability to maintain high efficiency while producing lesser pollutants like NO_x and CO due to overall lean combustion and consequent diminution of temperature. It allows lean combustion by extending the lean flammability limit as observed by Kang and Kyritsis [126, 127]. Moreover stratification exists in most of the premixed burners involving dilution with coflow air. Stratification can also be caused accidentally due to combustion instabilities as well.

Charge stratification exists in most of the combustion systems and could be inherent, accidental or intentional. For example stratification observed in an unconfined premixed combustion system where the equivalence ratio varies from the premixed value towards zero in the co-flow is inherent to the system. An example of an accidental creation of stratification is when ignition fails in a combustion system leading to accumulation of fuel at some location and resulting in stratification of the fuel-air mixture. Combustion instabilities are largely responsible for such kind of accidental stratification. Stratification is also created intentionally. This technique is used in internal combustion engines (GDI technology) to maintain an overall lean mixture but to ensure complete combustion to reduce emissions. In addition, stratification can also be generated by transient pulsations of the inlet flow.

Based on the mixture fraction distribution across the flame, stratified flames can be classified [48] into three types or classes : 1. lean-lean 2. rich-rich 3. lean-rich. In lean-lean (rich-rich) configuration the mixture fraction values stay lower (higher) than the stoichiometric value throughout the flame whereas in lean-rich case there is a variation of mixture fraction from a lean to rich composition involving stoichiometric values in between. Class 1 and 2 flames can be again sub-divided into back supported and front supported flames. Front supported flames are those in which the reactant mixture fraction is closer to the stoichiometric value and back supported flames have the product mixture fraction closer to the stoichiometry. This classification can be based on the angle subtended between the mixture fraction normal and the flame normal. Front supported and back supported flames can have different speeds of propagation due to the underlying physics and might require separate models to capture them as noted by Richardson et al. [128].

Class 1 and 3 flames are observed in premixed swirl burners and GDI engines, where a fully rich or lean premixed fuel air system flows into a quiescent atmosphere or co-flowing air. At downstream locations due to air entrainment, lean-lean or lean-rich mixtures exist in the flame depending on the initial equivalence ratio of the mixture. Class 2 flames are not very common in industrial systems. Consequently a lot of experimental and numerical studies are devoted

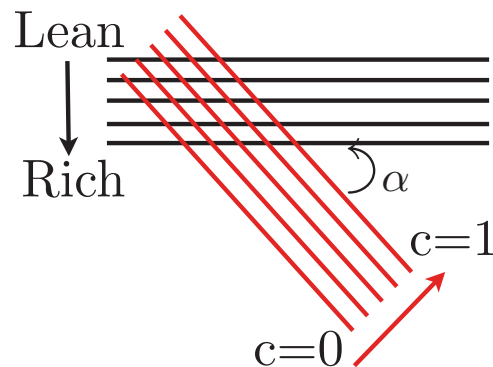


Figure 2.4: For Class 1 and 2 flames. Premixed: $\alpha = 90^\circ$, Stratified front supported: $\alpha = 0^\circ$, Stratified back supported: $\alpha = 180^\circ$

towards the understanding of Class 1 and 3 flames. In Class 3 flames, a staged combustion is predicted to be existing as reported by Hélie and Trouvé [129] and Haworth et al. [130]. In the first stage fully premixed combustion is expected to exist producing partially burnt products which go on to burn completely in the second non-premixed stage. There is a controversy regarding the second stage, whether it is a diffusion flame regime or a distributed flame regime as noted by Jimenez et al. [131]. In the following paragraphs, a review of the experimental and numerical studies in stratified combustion are presented.

Various experimental and numerical studies pertaining to stratified combustion exist in the literature. Most of these studies address the following global topics:

- Enhancement of flammability limit due to "memory" or "history" effect: experimental [127, 132–135] and numerical studies [128, 132, 136, 137] of laminar back supported flames have demonstrated an increase in the flammability limit due to the memory or history effect wherein the propagation history of the flame influences the local flammability limit. The reason for the extension of the flammability was attributed to the diffusion of heat only [127, 132] or radicals only [138] or both heat and radicals [136, 137] from the richer flammable zone to the leaner non flammable regions. An enhanced laminar flame speed was noticed in the stratified mixture in comparison to the propagation in a homogeneous mixture for the same local composition in these studies. This effect was also reported in an experimental study of a low turbulence V-flame experimental by Pasquier et al. [139]. In a time varying composition field, a dynamic flammability limit was observed associated to the mean composition and time scale of the fluctuations [140]. Extension of the flammability limit finds application in direct injection spark ignition (DISI) engines due to their ability to lower NOx emissions [141, 142].
- Validity of flamelet hypothesis in turbulent stratified flames: Direct numerical simula-

tion (DNS) studies performed by Poinso et al. [143], Hélie and Trouvé [129], Haworth et al. [130] and Jiménez et al. [131] on partially premixed combustion have asserted the validity of the flamelet hypothesis for modeling stratified flames. Ramaekers et al. [144] performed DNS studies on stratified Bunsen flame configuration and supports the applicability of the flamelet models for stratified flames. Richardson et al. [128] studied front and back supported flames in a counterflow configuration with product and reactants on either side. Contrary to the DNS studies mentioned before, they reported that a single reaction progress variable was not good at capturing front supported flames. However, the back supported flames were reasonably well represented by the progress variable. Recently, large eddy simulation (LES) of the TU-Darmstadt burner by Kuenne et al. [74] and LES of the stratified configuration of ORACLES rig experiment by Duwig and Fureby [119] were performed successfully by retaining a flamelet hypothesis. Other premixed swirl burners [145] which have small levels of stratification were also successfully simulated retaining the flamelet hypothesis. Sweeney et al. [3] showed in his work that the Cambridge swirl burner (CSWB) statistics were well captured with laminar flame calculations indicating the validity of the flamelet hypothesis on average.

- Presence of staged combustion: In Class 3 flames described earlier the flame encounters a stoichiometric line while propagating from a richer zone to a lean mixture. DNS studies [129–131] reported the presence of a staged combustion in this class of flames. The first stage corresponds to a premixed combustion mode where most of the fuel is consumed and in the second stage a non-premixed combustion of the partially burned products is predicted to exist. The two dimensional DNS by Haworth et al. [130] reported a good representation of the primary combustion by a laminar premixed flamelets. However, the secondary non-premixed combustion stage was not found to be well captured by steady diffusion flamelets because it is non-standard diffusion flame. Galizzi and Escudié [146] also observed the presence of a diffusion branch in the Class 3 configuration.
- Influence of the extent of stratification: Kang and Kyritsis [127] reported a negligible influence of the degree of stratification on flame speed. This is in contrast to the observations made by other studies [135, 139] where a higher intensity of stratification was found to increase the flame speed. Marzouk et al. [137] studied laminar counterflow configuration with propane-air mixture subjected to strain and proposed that the leaner flames are supported by diffusion of heat and radicals from the richer side. The flammability limit was also found to be enhanced if the equivalence ratio gradient was higher. Vena et al. [147] observed that for a large scale mixture fraction gradient the impact on the structure of a locally stoichiometric flame was minimum. Anselmo et al. [148] and Sweeney et al. [47] reported a net increase in flame surface density due to stratification. This is in line with the observations reported by Robin et al. [149] and the studies of Galizzi and Escudié [146]. The increased wrinkling due to stratification was attributed to the variable flame propagation speeds at different equivalence ratios as argued by other researchers [150, 151] as well.

Recently experiments to study interaction of realistic turbulence levels and stratification has been performed which include the ORACLES rig experiment [152], TU-Darmstadt burner [48] and the Cambridge swirl burner (CSWB).

- Modeling stratified combustion: Modeling Class 1 stratified flames was commonly approached by directly extending the existing premixed flame models as seen in the works [74, 119, 144]. On the other hand, there are not too many numerical studies for the Class 3 flames which is expected to have a staged combustion. Multi-regime flamelet models [93, 153] were proposed to account for such scenarios, but they have not been tested on an actual large eddy simulation.

The literature thus gives varying perspectives for important phenomena in stratified combustion such as the memory effect and the influence of stratification on the flame. A consensus is lacking in these cases for explaining the cause and effects [47]. Due to these reasons, a lot of attention has been lately focussed on stratified combustion and interaction of stratified flames and turbulence at realistic turbulence levels. This information is very essential to understand and develop future gas turbine burners and internal combustion engines.

2.4 Differential diffusion studies in combustion

Species are known to have a characteristic diffusive velocity as a function of pressure, temperature, local mixture composition and their molecular weights. Hence in a mixture involving multiple species with varying diffusivities, certain species diffuse faster or ahead of others. This phenomenon is called differential or preferential diffusion. In the context of a flame, premixed or diffusion, which involves different types of chemical species including radicals of varying properties, differential or preferential diffusion is inevitable. Figure 2.5 shows preferential diffusion of H_2 and H_2O ahead of CO and CO_2 in a laminar premixed methane air flame obtained from a Cantera [154] simulation using GRI 3.0 mechanism [155]. In this plot, the progress variable is defined as $Y_c = Y_{CO} + Y_{CO_2}$. Diffusivities of the species obtained from the simulation are also shown in Fig. 2.6 underlining the higher diffusivity of H_2 and H_2O .

For studying a diffusion flame, the common approach is to decouple the reaction and the mixing process. To do that, the mixing process is assumed to be represented by a passive scalar [156, 157] usually called as a mixture fraction and its scalar dissipation rate. By definition the passive scalar does not see the reaction and is directly affected only by convection and diffusion. An equal diffusivity assumption for all species, also represented by a uniform Lewis and Schmidt number assumption, is usually employed to get a perfectly passive scalar. A convenient method is to define mixture fraction as a linear combination of the atomic mass fractions, since there are no source terms associated with them. The Bilger's formula [158] and the Mitchell's [156] formula are examples of it. These definitions are widely used in the combustion community, both by the experimentalists and modeling teams. For a premixed

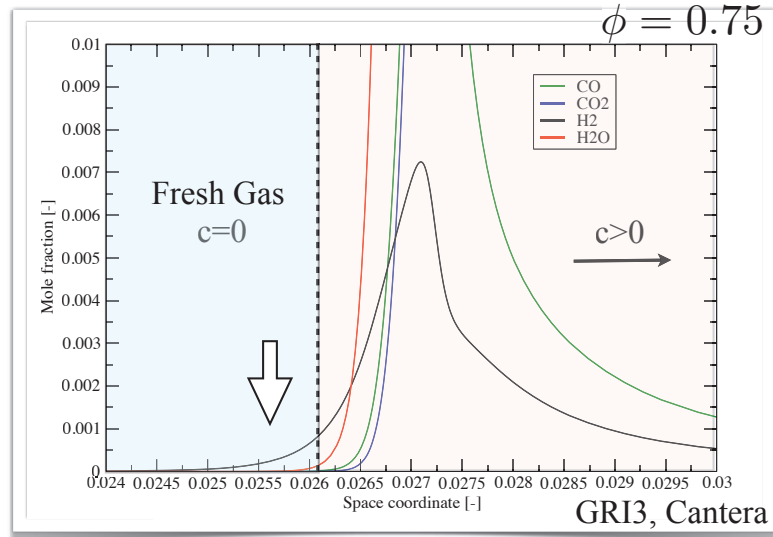


Figure 2.5: Mole fraction distribution of few major products of laminar premixed methane air flame at an equivalence ratio of 0.75 showing diffusion of H₂ and H₂O ahead of CO and CO₂ into the fresh gas.

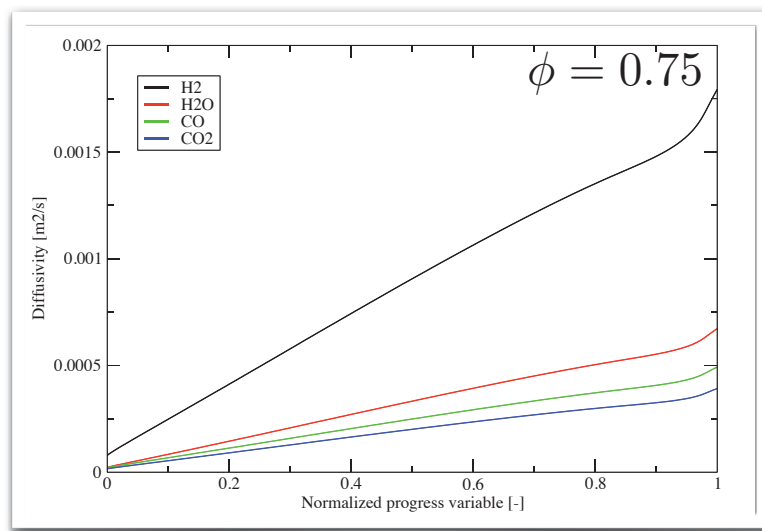


Figure 2.6: Diffusivities of major products of laminar premixed methane air flame at an equivalence ratio of 0.75.

flame generally, a single mixture fraction value is considered to be sufficient to characterize the composition and a progress variable to capture the evolution of reaction. The problem with a mixture fraction defined from atomic ratios is that it can remain a passive scalar only if the atomic mass fractions are conserved across the flame which is not the case in reality.

Inside the flame zone, three main phenomena exist namely convection, diffusion and reaction. Intuitively we know that the convection acts uniformly on all the species and the role of reaction is to just transform the species. Hence the local elemental composition *i.e.* the total number of C, H, O and N atoms at a given location are unaffected by reaction. But differential diffusion of species causes the local atomic concentrations to vary. In short, the atomic ratios are not conserved within the flame zone due to differential diffusion effect. Hence a mixture fraction defined from atomic ratios such as the Bilger's mixture fraction need not yield a passive scalar.

It is interesting to note that in addition to the preferential diffusion of certain species ahead of others there is also the "Lewis number effect" arising from the different diffusivities of species and temperature. The Lewis number effect combined with the preferential diffusion of species is known to exhibit thermo-diffusive instabilities in low Lewis number fuels like hydrogen. They have also the effect of increasing the flame surface area resulting in a net increase in the flame speed as observed [159] in lean hydrogen mixtures. A comprehensive review of these effects on the structure and propagation of premixed flames is given by A.N. Lipatnikov and J. Chomiak [159]. The problem of thermo-diffusive instabilities and higher turbulent flame speeds in the presence of low Lewis number fuels like hydrogen is of great interest and a vast topic on its own. As commented by A.N. Lipatnikov and J. Chomiak [159] it may not be easy to isolate and study the two effects independently. This work involves only methane air flames at atmospheric pressure which have a Lewis number greater than unity and are not known to exhibit thermo-diffusive instabilities under this condition. Attention is therefore mainly restricted on the literature concerning preferential diffusion of species.

Early 80s saw few measurements [160, 161] reported on differential diffusion effects. Bilger and Starner [161] performed Raman measurements to associate a major source of error in Mie experiments to the differential diffusion effects between the particles used for Mie scattering measurements and fuel atoms. Pursuing this fundamental study, a series of non-reactive measurements [162–165] followed to quantify the presence of differential diffusion in non-premixed jets. Kerstein et al. [166] showed through similarity analysis that in a fluid flow involving two differentially diffusing scalars, the time variance of their concentrations scales inversely with the square root of Reynolds number and is a strong function of their respective Schmidt numbers. Other computational studies which include the DNS studies [167–169] provided further quantification of time scales and correlation of scalars involved in differential diffusion. Models [170, 171] to account for diff-diff⁴ in non-reactive flows using transported PDF methods and CMC methods respectively were also proposed. Certain authors [168, 172] consider that since differential diffusion is a molecular process, at high Reynolds number the turbulent diffusion is expected

⁴differential diffusion

to dominate and hence diff-diff can be regarded to be insignificant especially on a statistical sense. But [173] reports diff-diff to be important at all Reynolds numbers and demonstrates the appearance at small length scales for different Reynolds numbers in their DNS. Measurements of Saylor and Sreenivasan [174] also showed the presence of differential diffusion effect at Batchelor scales and on a statistical sense as well. Most of these studies concluded that it is important to include differential diffusion effect in combustion models.

Subsequently, the focus shifted to studying differential diffusion in reacting flows mainly on non-premixed combustion. Several experimental [175–177] and numerical [178–180] studies exist pertaining to diff-diff effects in non-premixed combustion. Smith et al. [175] performed measurements on $\text{H}_2/\text{CO}_2/\text{air}$ non-premixed jet flame configurations for a range of jet Reynolds number varying from 1000 to 30000. Differential diffusion effect was found to be present at all Reynolds numbers. With increasing Reynolds number initially a decrease in the diff-diff effect was observed but then plateaued even though remaining at a significant level. They commented that the Reynolds number based on cold flow conditions could be misleading since reactive flow could have relaminarisation effects leading to lesser turbulence and significant differential diffusion effects. Bergmann et al. [176] studied a non-premixed $\text{CH}_4/\text{H}_2/\text{N}_2$ jet flame and reported an initial laminar potential core region of the jet where the differential diffusion effect was found to be significant for varying Reynolds numbers. Christophe Pope et al. [181, 182] demonstrates this effect in laminar premixed flames for both measurements and experiments for a variety of fuels such as benzene, methane, allene, acetylene, ethylene and propane at different pressures. In all the cases the equivalence ratio defined from atomic mass fractions and the individual elemental mass fractions were found to vary across the premixed flame. The nature of the variation was found to be strongly associated to the molecular weight of the fuel. In the case of pure fuels, the deviation of the equivalence ratio and atomic mass fractions with respect to the inlet value was reported to increase with an increase in molecular weight.

Pitsch and Peters [178] proposed a flamelet formulation for accounting differential diffusion effects in non-premixed flames by defining a conserved mixture fraction scalar not from a combination of reactive scalars but as a purely conserved scalar obtained from a transport equation. This does not involve Lewis number equals to unity assumption. To obtain a simplified flamelet transformation the closure of the scalar dissipation rate as an error function of the mixture fraction is used thus avoiding the use of a mixture fraction diffusivity for modeling scalar dissipation rate. Sutherland et al. [183] observes that this approach is consistent only under the assumption that a conserved mixture fraction definition exists. But no such definition in the presence of differential diffusion has been proposed yet. In [179], Pitsch reported RANS simulation of [176] and observed a significant difference between the chosen conserved mixture fraction and the measured mixture fraction. This was attributed to the differential diffusion effect. In transported PDF methods, micro mixing forms an important component which requires modeling and accounts for the molecular diffusion. A particle formulation for accounting differential diffusion in transported PDF methods was proposed by McDermott and Pope [180]. This model evaluated

on DNS studies has not been tested on an actual LES yet. Richardson and Chen [138] proposed modification of two existing mixing models (IEM⁵ and EMST⁶) by adding correction terms which account for differential diffusion effects in a premixed combustion context. The model involves characteristic constants function of species diffusivities. In the reported study they were closed using the information from the DNS but the evaluation of these constants in an actual LES is not tested yet. Lodier et al. [184] discusses a composition space manifold accounting for the diff-diff effects in a premixed flame context. This work takes into consideration the fact that when premixed flame solution is projected onto a composition space formed by a progress variable, differential diffusion between the composition space and chemical species in the real physical space needs to be taken into account to have accurate representation. As mentioned earlier, choice of different definitions for mixture fraction make comparison of experiments and numerical results ambiguous. Sutherland et al. [183] proposes methods to quantify the impact of differential diffusion effects on the choice of definitions. Recently, tabulated chemistry methods have developed lot of interest due to their simplicity and computational efficiency. Swart et al. [185] used FGM with flamelet dimensions based on atomic mass fractions of C, H and O and a strain parameter to perform DNS study of preferential diffusion effects in H₂ / air flames. This approach is very promising since it can account for both curvature and differential diffusion effects which is essential to capture thermo-diffusive instabilities in H₂ flames. It should be noted that here instead of a single mixture fraction describing the composition three atomic mass fractions are used. Therefore when it comes to LES, this approach can be challenging due to the fact that filtered mass fractions and strain rate terms will be required to enter the table leading to manifold increase in the size of the chemical table. A more efficient two equation model combined with tabulated chemistry was proposed by Regele and Blanquart [186] to account for non-unity Lewis number effect in laminar premixed hydrogen flames. They used a mixture fraction definition avoiding unity Lewis number assumption to tabulate the premixed flame solutions as a function of this mixture fraction and progress variable. An assumption is made that all other species other than the fuel (H₂ in their case) has a unique diffusivity. The solved mixture fraction equation then contains a source term characterized by the Lewis number and the fixed diffusivity of other species. This approach therefore applies importance to the non-unity Lewis number effect rather than the preferential diffusion of species. The origin of differential diffusion is essentially at small length scales characteristic of the diffusivity of the scalar but could appear at larger length scales irrespective of the flow being reactive or non-reactive. The effect could be especially significant when the flow is less turbulent.

To conclude, most of the studies on differential diffusion modeling was focussed around non-premixed configurations essentially due to the a priori knowledge of composition variation across the flame. But the differential diffusion effects was found to be significant in premixed configurations [4] as well and could have implications in the modeling approach. In practice for computations, a conserved mixture fraction is assumed and compared to the experiments which

⁵IEM: Interaction by Exchange with the Mean

⁶EMST: Euclidean Minimum Spanning Tree

uses a definition combining certain reactive scalars. This comparison is not consistent [178] due to two reasons. First of all, the combination of reactive scalars need not yield a passive mixture fraction at all. Secondly, the two definitions of the mixture fraction could be completely different based on its local diffusivity within the flame.

Governing Equations & Solver Description 3

Contents

3.1	General governing equations	33
	Governing equations at the low Mach number limit	34
3.2	LES governing equations	36
	Unresolved Reynolds stress closure	37
3.3	Discretization of the governing equations	39
	Spatial discretization	39
	Solution strategy: Projection method	42
	Time integration scheme	45
3.4	Poisson solver	47

3.1 General governing equations

The general governing equations of fluid flow can be derived by looking at it from a Lagrangian reference or an Eulerian reference. Lagrangian approach follows a parcel of fluid while the Eulerian method focusses on fluid moving in and out of a specific location. The details of the derivation are mentioned in [187]. The relevant equations for this work are described below.

The mass, momentum and energy conservation equations in integral form neglecting body force can be written as

$$\frac{\partial}{\partial t} \int_{\Omega} \rho d\Omega + \int_S \rho(\mathbf{u} \cdot \mathbf{n}) dS = 0 \quad (3.1)$$

$$\frac{\partial}{\partial t} \int_{\Omega} \rho \mathbf{u} d\Omega + \int_S \rho \mathbf{u}(\mathbf{u} \cdot \mathbf{n}) dS + \int_S (\underline{\mathbf{T}} \cdot \mathbf{n}) dS = \int_S (-P\mathbf{n}) dS \quad (3.2)$$

$$\frac{\partial}{\partial t} \int_{\Omega} \rho e d\Omega + \int_S \rho \left(e + \frac{P}{\rho} \right) (\mathbf{u} \cdot \mathbf{n}) dS = \int_{\Omega} Q d\Omega \quad (3.3)$$

Assuming an infinitesimal control volume and employing Gauss theorem for volume to surface integral, the differential form of these equations can be deduced as

$$\frac{\partial \rho}{\partial t} + \nabla \cdot (\rho \mathbf{u}) = 0 \quad (3.4)$$

$$\frac{\partial(\rho\mathbf{u})}{\partial t} + \nabla \cdot (\rho\mathbf{u}\mathbf{u}) = -\nabla P + \nabla \cdot (\underline{\mathbf{T}}) \quad (3.5)$$

$$\frac{\partial(\rho E)}{\partial t} + \nabla \cdot \left(\rho \left(E + \frac{P}{\rho} \right) \mathbf{u} \right) = Q \quad (3.6)$$

where $\underline{\mathbf{T}}$ is the shear stress tensor expressed as

$$\underline{\mathbf{T}} = \mu \left[(\nabla\mathbf{u} + \nabla\mathbf{u}^T) - \frac{2}{3}(\nabla \cdot \mathbf{u})\mathbf{I} \right] \quad (3.7)$$

E is the total energy per unit mass which is the sum of internal energy, e^* and kinetic energy which reads

$$E = e^* + \frac{1}{2}|\mathbf{u}|^2 \quad (3.8)$$

Q is the sum of the work done by external forces on the control volume and the heat released per unit volume per unit time written as

$$Q = \nabla \cdot (\underline{\mathbf{T}} \cdot \mathbf{u}) + \nabla \cdot (\lambda \nabla T) + \rho \dot{w}_e \quad (3.9)$$

These equations are based on the assumptions that the fluid is a continuum. It also assumes that the diffusive fluxes can be written as a product of a diffusivity coefficient and a gradient while satisfying an ideal gas law.

These equations as such are not closed since there are 6 unknowns (ρ , u_i , P and E) and 5 equations. The closure is achieved through the equation of state which relates the pressure, temperature, density and the specific gas constant (r) as

$$P = \rho r T \quad (3.10)$$

The internal energy for an ideal gas in incompressible flow is written as

$$e = \frac{rT}{\gamma - 1} \quad (3.11)$$

Analytical solutions for these equations exist only for very simplified cases. Otherwise due to the highly non-linear nature of these equations, one depends on numerical methods for solution. However, certain simplifications can be made according to the application. In this work, the flow velocity is predominantly weak in comparison to the velocity of sound and it allows to work on simplified low Mach number equations. The details of the governing equations in low Mach limit is discussed in the next section.

Governing equations at the low Mach number limit

The dimensionless form of the governing equations can be obtained by scaling each of the variables with a reference value leading to the following non-dimensional quantities.

$$t^* = \frac{t}{t_0}; x_i^* = \frac{x_i}{L_0}; \rho^* = \frac{\rho}{\rho_\infty}; v_i^* = \frac{v_i}{u_\infty}; P^* = \frac{P}{\rho_\infty c_\infty^2}; \mu^* = \frac{\mu}{\mu_\infty}; E^* = \frac{E}{c_\infty^2} \quad (3.12)$$

The equations in dimensionless form then becomes

$$\frac{\partial \rho^*}{\partial t^*} + \nabla \cdot (\rho^* \mathbf{u}^*) = 0 \quad (3.13)$$

$$\frac{\partial(\rho^* \mathbf{u}^*)}{\partial t^*} + \nabla \cdot (\rho^* \mathbf{u}^* \mathbf{u}^*) = -\frac{\nabla P^*}{Ma_\infty^2} + \frac{\nabla \cdot (\overline{\boldsymbol{\tau}^*})}{Re} \quad (3.14)$$

$$\frac{\partial(\rho^* E^*)}{\partial t^*} + \nabla \cdot \left(\rho^* \left(E^* + \frac{P^*}{\rho^*} \right) \mathbf{u}^* \right) = Q^* \quad (3.15)$$

where the dimensionless numbers namely Mach number, $Ma = u_\infty/c_\infty$ and the Reynolds number, $Re = (\rho_\infty u_\infty L_0)/\mu_\infty$ appear.

Several authors, to quote two examples [188, 189], have used low Mach number asymptotics to simplify Navier-Stokes equations for different situations. The derivation and implications of low Mach number combustion equations using asymptotic analysis derived by Majda et al. [190] are discussed briefly.

The asymptotic analysis involves the following steps

- All variables except for t^* and x^* are expressed as a function of the Mach number. For example, the density is expanded as

$$\rho = \rho_0 + \rho_1 Ma + \rho_2 Ma^2 + \mathcal{O}(Ma^3) \quad (3.16)$$

- The continuity, momentum and energy equations are written in the expanded form as a function of Mach number. This step is not shown here for the sake of clarity.
- Finally terms having the same powers of Ma are collected and equated to zero. Only the first three powers are retained for the analysis which are Ma^{-2} , Ma^{-1} and Ma^0 .

The continuity equation which has only Ma^0 terms yields

$$\frac{\partial \rho_0}{\partial t} + \nabla \cdot (\rho_0 \mathbf{u}_0) = 0 \quad (3.17)$$

The momentum equation gives for the coefficients Ma^{-2} , Ma^{-1} and Ma^0 the following equations respectively

$$\nabla P_0 = 0 \quad (3.18)$$

$$\nabla P_1 = 0 \quad (3.19)$$

$$\frac{\partial(\rho_0 \mathbf{u}_0)}{\partial t^*} + \nabla \cdot (\rho_0 \mathbf{u}_0 \mathbf{u}_0) = -\nabla P_2 + \frac{\nabla \cdot (\mathbf{T}_0)}{Re} \quad (3.20)$$

P_0 and P_1 are the terms appearing in the equations of the form Eq. 3.16 written for pressure. On similar lines, the energy equation gives

$$\frac{\partial(\rho_0 E_0)}{\partial t^*} + \nabla \cdot \left(\rho_0 \left(E_0 + \frac{P_0}{\rho_0} \right) \mathbf{u}_0 \right) = Q_0 \quad (3.21)$$

and finally the equation of state written in terms of internal energy becomes

$$P_0 = \rho_0 e_0 (\gamma - 1) \quad (3.22)$$

These equations [3.17-3.22] form the governing equations at the low Mach number limit ($M \rightarrow 0$) and the following inferences can be made.

1. The absolute pressure, P_0 remains a constant in space. This pressure forms the thermodynamic pressure. For certain flows such as those inside an internal combustion engine, P_0 varies with time. However, for jet flows P_0 can be considered to remain constant in time as well.
2. The density ρ_0 is a function of specific gas constant and the internal energy only, which in turn is a function of temperature.
3. There are no stationary acoustic waves, since P_1 is constant in space.
4. The term P_2 in the momentum equation acts as the hydrodynamic pressure.

In addition it can be noted that, in the low Mach number formulation, the sound velocity $c_\infty \rightarrow \infty$ as $Ma \rightarrow 0$. Consequently, information travels at infinite speed and any change at one point is felt at all other points immediately. This is a typical characteristic of elliptic equation in space. It is also true that when ρ_0 and P_0 are constant in space, the equations reduce to the incompressible Navier Stokes equations satisfying the condition $\nabla \cdot (\mathbf{u}_0) = 0$.

The governing equations for LES are described in the following section.

3.2 LES governing equations

The governing equations for large eddy simulations can be derived by employing a space filtering on the low Mach NS equations described in the previous section. The filtering can be considered as a convolution operation of the LES filter kernel, \mathcal{G} on the governing equations. Typically for any scalar ϕ , the convolution and the consequent filtered scalar $\bar{\phi}$ can be represented as

$$\bar{\phi}(\underline{x}, t) = \iiint_{-\infty}^{+\infty} \phi(\underline{x}^*, t) \mathcal{G}(\underline{x}^* - \underline{x}, \Delta) d\underline{x}^*. \quad (3.23)$$

where Δ is the filter size and the \underline{x} denotes the space vector. The LES filter, \mathcal{G} should ideally satisfy the condition that

$$\iiint_{-\infty}^{+\infty} \mathcal{G}(\underline{x}, \Delta) d\underline{x} = 1 \quad (3.24)$$

A density weighted filtering or Favre filtering is usually employed (refer [191]) to avoid the appearance of a mass source term in the filtered continuity equation. A Favre filtered scalar $\tilde{\phi}$ is defined as

$$\tilde{\phi}(x, \Delta) = \frac{\overline{\rho\phi}}{\bar{\rho}} \quad (3.25)$$

Performing the LES Favre filter operation on the governing equations yields for the mass, momentum and a general scalar the following equations respectively ¹

$$\frac{\partial \bar{\rho}}{\partial t} + \nabla \cdot (\bar{\rho} \tilde{\mathbf{u}}) = 0 \quad (3.26)$$

$$\frac{\partial (\bar{\rho} \tilde{\mathbf{u}})}{\partial t} + \nabla \cdot (\bar{\rho} \tilde{\mathbf{u}} \tilde{\mathbf{u}}) = -\nabla \bar{P} + \nabla \cdot (\bar{\mathbf{T}}) - \nabla \cdot (\bar{\rho} (\tilde{\mathbf{u}} \tilde{\mathbf{u}} - \tilde{\mathbf{u}} \tilde{\mathbf{u}})) \quad (3.27)$$

$$\frac{\partial (\bar{\rho} \tilde{\phi})}{\partial t} + \nabla \cdot (\bar{\rho} \tilde{\mathbf{u}} \tilde{\phi}) = \nabla \cdot (\bar{\rho} D_\phi \nabla \tilde{\phi}) - \nabla \cdot (\bar{\rho} (\tilde{\mathbf{u}} \tilde{\phi} - \tilde{\mathbf{u}} \tilde{\phi})) + \bar{\rho} \tilde{\omega}_\phi \quad (3.28)$$

where the stress term is written as

$$\bar{\mathbf{T}} = \mu \left[\overline{(\nabla \mathbf{u} + \nabla \mathbf{u}^T) - \frac{2}{3} (\nabla \cdot \mathbf{u}) \mathbf{I}} \right] \approx \mu \left[(\nabla \tilde{\mathbf{u}} + \nabla \tilde{\mathbf{u}}^T) - \frac{2}{3} (\nabla \cdot \tilde{\mathbf{u}}) \mathbf{I} \right] \quad (3.29)$$

and the filtered diffusive term in the scalar equation is usually approximated as

$$\nabla \cdot (\bar{\rho} D_\phi \nabla \tilde{\phi}) \approx \nabla \cdot (\bar{\rho} D_\phi \nabla \tilde{\phi}) \quad (3.30)$$

While deriving these equations, commutativity of the filtering and gradient operators were assumed. In the numerical simulation only the quantities $(\tilde{\mathbf{u}}, \bar{\rho}, \nabla \bar{P}$ and $\tilde{\phi})$ are solved and the remaining terms are modeled. The assumptions in Eq. 3.29 and Eq. 3.30 could have significant implications in reactive flow situations as will be shown later. However, a general practice in LES is to assume that the error induced by these assumptions are accounted for within the modeled terms.

There are three terms in the above equations which need to be modeled namely

1. Unresolved Reynolds stress tensor term $\mathbf{T}_{ij}^{SGS} = (\tilde{\mathbf{u}} \tilde{\mathbf{u}} - \tilde{\mathbf{u}} \tilde{\mathbf{u}})$
2. Unresolved scalar flux term $(\tilde{\mathbf{u}} \tilde{\phi} - \tilde{\mathbf{u}} \tilde{\phi})$
3. Filtered source term $\bar{\rho} \tilde{\omega}_\phi$

Out of these terms, only the closure of the Reynolds stress term is discussed in this chapter. The closure of the sub-grid scalar fluxes and the filtered source term will be described in detail in Chapter 4.

Unresolved Reynolds stress closure

The unresolved stress term or the sub-grid stress term is closed following a Boussinesq approximation [192, 193] where the deviatoric part of the SGS stress tensor is modeled as

$$\mathbf{T}_{ij}^{SGS} - \frac{\delta_{ij}}{3} \mathbf{T}_{kk}^{SGS} = -\nu_T \left(\frac{\partial \tilde{\mathbf{u}}_i}{\partial \mathbf{x}_j} + \frac{\partial \tilde{\mathbf{u}}_j}{\partial \mathbf{x}_i} - \frac{\delta_{ij}}{3} \frac{\partial \tilde{\mathbf{u}}_k}{\partial \mathbf{x}_k} \right) = -2\nu_T \left(\tilde{\mathbf{S}}_{ij} - \frac{\delta_{ij}}{3} \tilde{\mathbf{S}}_{kk} \right) \quad (3.31)$$

¹without the subscripts

where $\tilde{\mathbf{S}}$ is the resolved strain tensor. The symmetric part of the SGS tensor is assumed to be accounted by the pressure term, $\nabla\bar{P}$.

In Eq. 3.31, an unknown term in the form of ν_T appears which is generally called as turbulent viscosity. Several closure strategies exist to model the turbulent viscosity. Only two of them namely the dynamic Smagorinsky model and the wall adapting local eddy viscosity model (WALE) used in this work are described below.

Dynamic Smagorinsky model

The dynamic Smagorinsky model [194, 195] proposes to calculate the turbulent viscosity as

$$\nu_T = (C_s\Delta)^2|\tilde{\mathbf{S}}| \quad (3.32)$$

The Smagorinsky constant, C_s is estimated in a dynamic manner following Germano's scale similarity hypothesis [195]. It states that the unresolved stresses are controlled largely by the large scale resolved structures. When expressed mathematically

$$\underline{\mathbf{T}}_{ij}^{SGS} = (\underline{\mathbf{u}}_i\underline{\mathbf{u}}_j - \underline{\mathbf{u}}_i\underline{\mathbf{u}}_j) \quad (3.33)$$

The unresolved fluxes at the test level can be expressed as

$$T_{ij}^{SGS} = (\widehat{\underline{\mathbf{u}}_i\underline{\mathbf{u}}_j} - \widehat{\underline{\mathbf{u}}_i\underline{\mathbf{u}}_j}) \quad (3.34)$$

where $\widehat{\cdot}$ represents filtering at a test filter $\hat{\Delta}$ larger than the LES filter size (Δ).

Filtering the SGS stress tensor at the test filter width $\hat{\Delta}$ yields a second equation as

$$\hat{\mathbf{T}}_{ij}^{SGS} = (\widehat{\underline{\mathbf{u}}_i\underline{\mathbf{u}}_j} - \widehat{\underline{\mathbf{u}}_i\underline{\mathbf{u}}_j}) \quad (3.35)$$

Taking the difference of these two equations one can write

$$\underbrace{(\widehat{\underline{\mathbf{u}}_i\underline{\mathbf{u}}_j} - \widehat{\underline{\mathbf{u}}_i\underline{\mathbf{u}}_j})}_{\underline{\mathbf{L}}_{ij}} = T_{ij}^{SGS} - \hat{\mathbf{T}}_{ij}^{SGS} \quad (3.36)$$

Here $\underline{\mathbf{L}}_{ij}$ is generally called as the Leonard's stress tensor.

To determine the constant of Eq. 3.32, each of the stress terms in Eq. 3.35 and Eq. 3.33 are expressed using the Smagorinsky model as

$$\underline{\mathbf{T}}_{ij}^{SGS} - \frac{\delta_{ij}}{3}\underline{\mathbf{T}}_{kk}^{SGS} = -2(C_s\Delta)^2|\tilde{\mathbf{S}}|\tilde{\mathbf{S}}_{ij} \quad (3.37)$$

$$T_{ij}^{SGS} - \frac{\delta_{ij}}{3}T_{kk}^{SGS} = -2(C_s\Delta)^2|\hat{\mathbf{S}}|\hat{\mathbf{S}}_{ij} \quad (3.38)$$

Taking the difference of the above two equations yields the Leonards stress term on the LHS while the RHS has only the constant C_s as the unknown. This model is over-specified since there are five independent equations for determining the constant C_s . Therefore, usually a least squares method is employed to determine C_s or the minimum value among the coefficients is chosen which is the case in YALES2.

WALE model

The WALE model [196] proposes to calculate the turbulent viscosity, μ_t as

$$\mu_T = \rho(C_W \Delta)^2 \frac{(\underline{\mathbf{S}}_{ij}^d \underline{\mathbf{S}}_{ij}^d)^{3/2}}{(\tilde{\underline{\mathbf{S}}}_{ij} \tilde{\underline{\mathbf{S}}}_{ij})^{5/2} + (\underline{\mathbf{S}}_{ij}^d \underline{\mathbf{S}}_{ij}^d)^{5/4}} \quad (3.39)$$

where the model constant C_W is 0.4929 and $\underline{\mathbf{S}}_{ij}^d$ is given as

$$\underline{\mathbf{S}}_{ij}^d = \frac{1}{2} (\tilde{\underline{\mathbf{g}}}_{ij}^2 + \tilde{\underline{\mathbf{g}}}_{ji}^2) - \frac{1}{3} \delta_{ij} \tilde{\underline{\mathbf{g}}}_{kk}^2 \quad (3.40)$$

and $\tilde{\underline{\mathbf{g}}}_{ij}$ is the velocity gradient tensor

$$\tilde{\underline{\mathbf{g}}}_{ij} = \nabla \tilde{\mathbf{u}} \quad (3.41)$$

In comparison to the dynamic Smagorinsky model, the WALE model takes into account the strain rate and the rotation while simultaneously reducing to a desired near wall behaviour.

3.3 Discretization of the governing equations

Once the governing equations have been established, the next task is to convert them into computer solvable algebraic equations. This involves spatially and temporally discretizing the partial differential equations and integrating. The discretization and integration of the governing equations derived based on low Mach number formalism are discussed in this section.

Spatial discretization

A finite volume method is adopted here where the spatial discretization involves dividing the domain of interest into smaller geometric elements. YALES2 accommodates tetrahedral, pyramidal and prism elements in 3D, and triangular and rectangular elements in 2D. Control volumes are constructed from these elements and computational nodes are decided. The governing equations are solved for values of the variables at these computational nodes. The governing equations are therefore expressed or discretized in terms of the values of the variables at computational nodes alone. A typical construction of control volume in a 2D situation with triangles is shown in Fig. 3.1. YALES2 uses a **node centered** scheme². A **collocated** arrangement of variables is adopted where all the variables including the pressure and velocity are stored at the nodes.

The integral form of the governing equations acts as the starting point for the finite volume method. This requires that the convective, diffusive and source terms are approximated by appropriate and sufficiently accurate algebraic expressions in space. An overview of the discretization of the convective, diffusive and source terms are described in the next section. In

²The control volume can be constructed in two ways:- (1) By using the finite volumes themselves as the control volume and assigning a computational node at the centre, known as cell centered scheme (2) By defining the common vertices of the volumes as computational node and developing the control volumes around it, called as the node centered scheme.

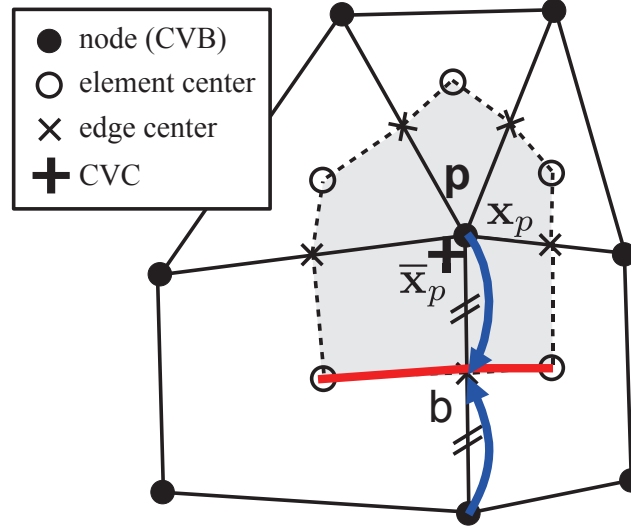


Figure 3.1: Construction of a typical control volume in YALES2 extracted from YALES2 tutorials by Moureau et al. $\bar{\mathbf{x}}_p$ is the barycenter of the control volume. \mathbf{x}_p is the computational node for the control volume

effect, it breaks down finally to discretizing the volume integrals, spatial gradients and Laplacian operators. The complete derivation and details are given in the thesis of Stijn Vantiegheem [197].

Source term discretization

Source terms can be discretized by assuming that the value of the source term at the computational node is a good representative average value of the source term distribution in the control volume. Consequently, we can write for a control volume centred around point P as,

$$\int_{\Omega} \dot{\omega}_{\phi} d\Omega = (\bar{\omega}_{\phi})_P d\Omega_{CV} \quad (3.42)$$

where $(\bar{\omega}_{\phi})_P$ is the value of the source term at the node, P and $d\Omega_{CV}$ is the control volume around it.

Convective and Diffusive term discretization

The convective and diffusive terms appear as fluxes integrated over the surface in the conservation equation after applying the Gauss theorem (Eqs. 3.1 - 3.3). The scalar convective flux term can be written as

$$\int_S \rho \phi (\mathbf{u} \cdot \mathbf{n}) dS = \sum_{i=1}^N (\rho \mathbf{u} \phi)_i \cdot d\mathbf{S}_i \quad (3.43)$$

where $i=1, N$ represent the control volume surfaces forming the control volume. $(\rho \mathbf{u} \phi)_i$ is the value of the flux evaluated at the control volume surface and $d\mathbf{S}_i$ is the control volume surface vector formed by a node pair.

Similarly, the scalar diffusive flux term can be written as

$$\int_S \rho D_\phi \nabla \phi \cdot \mathbf{dS}_i = \sum_{i=1}^N (\rho D_\phi \nabla \phi)_i \cdot \mathbf{dS}_i \quad (3.44)$$

For the momentum equation, the strategy is the same where instead of a scalar, the concept of an advected velocity is used.

Thus the problem of spatial integration comes down to determining the variables at the control volume surface. In Fig. 3.1, \mathbf{b} is a point on the control volume surface where the flux ψ (convective or diffusive) has to be evaluated. A straightforward method is to approximate the flux at \mathbf{b} as

$$\psi_b = \frac{\psi(\bar{\phi}_{\Omega_p}) + \psi(\bar{\phi}_{\Omega_q})}{2} \quad (3.45)$$

where

$$\bar{\phi}_{\Omega_p} = \frac{1}{V_p} \int_{\Omega_p} \phi d\Omega \quad (3.46)$$

This scheme is second-order accurate for a regular mesh and is only first-order accurate for an irregular mesh. It is desirable to have higher order schemes to be more accurate but is difficult to implement in an unstructured mesh since it requires to embed a second level of connectivity information of neighbours not immediate to a node. Therefore, a less expensive scheme can be developed which uses the points around \mathbf{b} but inside the control volume. Pursuing this direction, Moureau and Lartigue [198] have developed a fourth order scheme. The development of the scheme involves expressing the nodal values as a function of the volume averages calculated at the barycenter of the control volume by deconvolution operation. From the nodal values, the values at the control volume surface is calculated. The complete details of the derivation can be found in the thesis of Kraushaar [199].

Since the derivative operator basically involves a deconvolution first and then interpolation of the solution from the barycenter of the control volume to the node, a large skewness in the mesh can lead to a big difference between the barycenter and the node. This increases the error of interpolation and hence it is desirable to have skewness kept to the minimum. Recommended maximum value of skewness is 0.8.

Code parallelisation

YALES2 performs a double decomposition of the computational domain. It uses the METIS library [200] to first decompose the computational domain among the processors. The divided domain is then further divided into cell groups to achieve double decomposition. The use of cell groups provides few advantages. Cell groups enable efficient use of the cache, making operations faster. It also helps to build a more optimized Poisson solver by solving the implicit Poisson in the cell groups and then in the whole domain which converges faster [201]. Finally, the cell groups make it easy to repartition the domain relatively easily aiding in dynamic load balancing.

Solution strategy: Projection method

In the low Mach number formulation for a non-reacting constant density flow, the equations reduce to the incompressible Navier-Stokes equation. For incompressible flows, $\partial\rho/\partial t = 0$ which yields $\nabla \cdot (\rho\mathbf{u}) = 0$ as the continuity equation. Since the continuity equation does not involve a time derivative, it is implied that the time stepping of the momentum equation should satisfy momentum conservation while simultaneously satisfying mass continuity. On the other hand for reacting variable density flows, the equations remain in a compressible form but within the low Mach assumption.

Consequently, there exists two types of solvers in YALES2, an incompressible solver (ICS) and a variable density solver (VDS) for low Mach number flows. The time advancement in both the solvers are based on the fractional time stepping method of Kim and Moin [202] developed for constant density flows which has been extended to variable density flows by Pierce and Moin [26]. The velocity is solved at integral time steps ($n, n+1$, etc) whereas the scalars, density and pressure are solved at staggered half time steps ($n+1/2, n+3/2$, etc). The method is explained briefly in the subsequent paragraphs.

Incompressible solver (ICS)

The fractional time stepping strategy inherently uses a modified version of the projection method proposed by Chorin [203] for solving NS equations in finite-difference schemes. The projection method is based on the Helmholtz Hodge decomposition which states that a vector field on a simply connected domain can be split uniquely into a divergence free field and an irrotational field. In this context, the divergence free field is the velocity at the next time step and the irrotational field is the pressure gradient term.

As mentioned before, in the incompressible formulation only a momentum equation which ensure mass continuity needs to be solved. The following steps are involved in the ICS.

1. Predictor step

$$\frac{\hat{\mathbf{u}} - \mathbf{u}^n}{\Delta t} + \mathcal{C}_u^n = \mathcal{D}_u^n - \frac{1}{\rho} \nabla P^{n-1/2} \quad (3.47)$$

where \mathcal{C}_u^n and \mathcal{D}_u^n are the convective and diffusive terms respectively, appearing in the conservative form as given in Eq. 3.2 without the density term evaluated at time step n . In this step, the predictor velocity, $\hat{\mathbf{u}}$ is calculated by time integrating the Eq. 3.47 with the appropriate boundary conditions for $(n+1)^{th}$ time step. This preserves the large structures without inducing unphysical splitting. The time integration scheme is described in subsection 3.3.

2. Intermediate velocity correction step:

$$\frac{\mathbf{u}^* - \hat{\mathbf{u}}}{\Delta t} = \frac{1}{\rho} \nabla P^{n-1/2} \quad (3.48)$$

This step calculates a corrected velocity \mathbf{u}^* by removing the pressure influence of the previous time step.

3. Corrector step :

$$\frac{\mathbf{u}^{n+1} - \mathbf{u}^*}{\Delta t} = -\frac{1}{\rho} \nabla P^{n+1/2} \quad (3.49)$$

In the corrector step, the velocity \mathbf{u}^{n+1} at time step (n+1) is determined by time integrating Eq. 3.49 where the pressure at (n+1/2) is found from the solution of a Poisson equation which reads

$$\nabla \cdot (\nabla P^{n+1/2}) = \frac{1}{\Delta t} \nabla \cdot (\mathbf{u}^*) \quad (3.50)$$

The Poisson equation for the pressure Eq. 3.50 is derived by differentiating equation Eq. 3.49 and setting the mass continuity constraint on \mathbf{u}^{n+1} field. To determine $P^{n+1/2}$ a linear system of equation with a dimension as large as the number of nodes has to be solved. This step is an important entity of the solver and consumes the maximum amount of time. Therefore significant CPU time can be gained at this step and this will be addressed in section 3.4. It is interesting to note that the two previous steps (Eq. 3.48 and Eq. 3.49) can be combined together and be viewed as a single pressure correction step also.

Variable density solver (VDS)

Unlike the ICS, in the variable density solver, an explicit continuity equation appears and requires time integration. A time staggered discretization [26] is used and the steps involved in the variable density solver are described below.

1. Density predictor step:

$$\frac{\rho^* - \rho^{n+1/2}}{\Delta t} + \mathcal{C}_u^n = 0 \quad (3.51)$$

A first approximation of the density, ρ^* is obtained by advancing the continuity Eq. 3.51 in time. It is worth noting the time staggered nature of density calculated at (n+1/2).

2. Scalar predictor step:

A predictor step for scalars (calculated at staggered time steps) are also carried out as

$$\frac{(\rho\phi)^* - (\rho\phi)^{n+1/2}}{\Delta t} + \mathcal{C}_\phi^{n+1/2} = \mathcal{D}_\phi^{n+1/2} + \mathcal{S}_\phi^{n+1/2} \quad (3.52)$$

where $\mathcal{S}_\phi^{n+1/2}$ is the source term of the scalar ϕ evaluated at n+1/2. The time integration scheme used in this step is similar to the scheme explained in subsection 3.3.

3. Evaluation of density, ρ^{n+1} :

The density at (n+1)th step is evaluated as

$$\rho^{n+1} = \frac{\rho^{n+1/2} + \rho^{n+3/2}}{2} \quad (3.53)$$

In the above equation, $\rho^{n+3/2}$ is obtained as

$$\rho^{n+3/2} = \alpha_{relax} * \rho_{eos} + (1 - \alpha_{relax})\rho^* \quad (3.54)$$

where

$$\rho_{eos} = \frac{P_0}{rT} \quad (3.55)$$

Throughout this thesis work, an energy equation is not solved explicitly. The temperature T and the specific gas constant r are obtained from flamelet libraries or look up tables, the details of which are mentioned in chapter 4. The term α_{relax} represents a relaxation coefficient to accommodate sudden changes in density, especially when the flow is highly unsteady and is developing. A good value for the relaxation factor $\alpha_{relax} = 0.7$ for an established configuration while for the transient states a value of 0.5 can be used.

4. Velocity predictor step :

In this step the velocity is first advanced in time in the conserved form with an RHS calculated from the previous time step as

$$\frac{(\rho\mathbf{u})^* - (\rho\mathbf{u})^n}{\Delta t} + C_u^n = D_u^n - \nabla P^{n-1/2} \quad (3.56)$$

It should be noted that this predicted velocity $(\rho\mathbf{u})^*$ does not satisfy the continuity equation.

5. Velocity corrector step:

$$\frac{(\rho\mathbf{u})^{n+1} - (\rho\mathbf{u})^*}{\Delta t} + \nabla P^{n-1/2} = \nabla P^{n+1/2} \quad (3.57)$$

The influence of the previous pressure is removed and the velocity is corrected with the new pressure. The pressure at time step $(n+1/2)$ is obtained by imposing the mass continuity by differentiating Eq. 3.57 yielding a Poisson equation of the form

$$\nabla \cdot (\nabla P^{n+1/2}) = \frac{\rho^{n+3/2} - \rho^{n+1/2}}{\Delta t^2} - \frac{1}{\Delta t} \nabla \cdot (\rho\mathbf{u})^* \quad (3.58)$$

While deriving the above equation, it was considered that the velocity field at $(n+1)^{th}$ time step satisfies the continuity equation as

$$\nabla \cdot (\rho\mathbf{u})^{n+1} = - \left(\frac{\partial \rho}{\partial t} \right)^{n+1} \approx \frac{\rho^{n+3/2} - \rho^{n+1/2}}{\Delta t} \quad (3.59)$$

The staggered time step helps to yield a second order accuracy in time for density evaluated at $(n+1)$.

6. Scalar corrector step:

Subsequently all the scalars are also advanced in time following an equation similar to 3.52 with RHS terms evaluated at $(n+1)^{th}$ time step with the velocities and pressure evaluated in the previous steps.

Time integration scheme

In order to perform the time integration, a suitable time step that ensures stable code performance needs to be determined. In the low Mach limit since the acoustics are not resolved the size of the time step is not limited by the sound speed. The time steps are based on the convective and diffusive velocities. In YALES2, the convective time step is evaluated from a CFL number, C specified by the user as

$$\Delta t_{conv} = C \frac{\delta x \|\mathbf{A}_p\|}{|(\mathbf{u} \cdot \mathbf{A}_p)|} \quad (3.60)$$

where $\mathbf{u} \cdot \mathbf{A}_p$ represents the flux across the control surface \mathbf{A}_p and δx is a distance calculated as the norm of the distance matrix to each neighboring node. $\|\cdot\|$ represents the norm and $|\cdot|$ represents the absolute value.

Similarly, a diffusive time step is evaluated based on the Fourier number, Fo specified by the user as

$$\Delta t_{diff} = Fo \frac{(\delta x^2)}{\nu} \quad (3.61)$$

where ν is the effective viscosity evaluated as the sum of the molecular, turbulent and artificial viscosities. The time step of computation is then evaluated as $\Delta t^{Comp} = \min(\Delta t_{diff}, \Delta t_{conv})$.

For a typical LES mesh, the diffusive time step is an order of magnitude smaller than the convective time step meaning that the time step of computation is governed by diffusion. To advance the code faster in time, YALES2 allows the user to enable an implicit diffusion scheme. When the implicit diffusion scheme is enabled, the convective and source terms are advanced over a convective time step with the scheme described in the coming section while the diffusion terms are advanced separately using an RK4 scheme over the convective time step and added to the original variable. When the implicit diffusion is disabled, both convective and diffusive terms are advanced together over the time step Δt^{Comp} . The time advancement scheme in YALES2 is discussed below.

The choice of time advancement schemes are governed by the required accuracy and stability. YALES2 uses centered schemes in space which are known to be oscillatory [204]. A direct combination with Runge-Kutta (RK) schemes could render it unstable and therefore as a strategy to stabilize, artificial or numerical diffusion is introduced to the scheme. This can be achieved in two ways

- Adding artificial viscosity explicitly
- Incorporating numerical diffusion in the scheme

The code gives facility for both. A Cook and Cabot 4th order artificial viscosity [205] is implemented in the code falling under the first category. Pertaining to the second, a suitable scheme is chosen which ensures the presence of numerical diffusion ensuring stability without the necessity to add an explicit artificial viscosity term.

Even though the code YALES2 provides several time advancement schemes, throughout this work only the TFV4A (Two-step Finite-Volume 4th-order version A) scheme was used and the discussion will be restricted to this particular case. This scheme is obtained from a linear combination of the two step Runge Kutta scheme and the two step Taylor-Galerkin (TTG4-A) scheme of Semin and Quartappel [206]. To illustrate, consider an unsteady incompressible scalar advection problem which reads

$$\frac{\partial \phi}{\partial t} + \mathbf{u} \cdot \nabla \phi = 0 \quad (3.62)$$

The fourth order two step RK scheme which can be obtained combining every two steps of the RK4 scheme [199] reads

$$\phi^{(2)} = \phi^n - \frac{\Delta t}{3} \mathcal{C}(\phi^n, \mathbf{u}) + \frac{1}{12} \nabla t^2 \mathcal{C}^2(\phi^n, \mathbf{u}) \quad (3.63)$$

$$\phi^{(n+1)} = \phi^n - \Delta t \mathcal{C}(\phi^n, \mathbf{u}) + \frac{1}{2} \nabla t^2 \mathcal{C}^2(\phi^{(2)}, \mathbf{u}) \quad (3.64)$$

where $\mathcal{C}(\phi^n, \mathbf{u}) = \mathbf{u} \cdot \nabla(\phi^n)$ is the convective term and $\mathcal{C}^2(\phi^n, \mathbf{u}) = \mathbf{u} \cdot \nabla(\mathbf{u} \cdot \nabla \phi)$.

On the other hand, the TTG4-A scheme reads

$$\phi^{(2)} = \phi^n - \frac{\Delta t}{3} \mathcal{C}(\phi^n, \mathbf{u}) + \frac{1}{12} \nabla t^2 \mathcal{D}(\phi^n, \mathbf{u}) \quad (3.65)$$

$$\phi^{(n+1)} = \phi^n - \Delta t \mathcal{C}(\phi^n, \mathbf{u}) + \frac{1}{2} \nabla t^2 \mathcal{D}(\phi^{(2)}, \mathbf{u}) \quad (3.66)$$

TTG4-A is similar to the Lax-Wendroff scheme, which consists of higher order diffusive terms ensuring numerical stability. In Eq. 3.66, \mathcal{D} is the discretization operator of the diffusion term similar to that appearing in Lax-Wendroff schemes. Since its a diffusion term, the stencil of \mathcal{D} and \mathcal{C} are different and forms the main difference between the two step RK method and the TTG4-A scheme.

The TTG4-A scheme is incorporated with numerical diffusion for stability whereas the RK4 scheme is more accurate but less stable. Considering the close similarity of the equations of the two methods, a linear combination of these two schemes can therefore be considered to obtain accuracy and stability simultaneously. This leads to

$$\phi^{(2)} = \phi^n - \frac{\Delta t}{3} \mathcal{C}(\phi^n, \mathbf{u}) + (1 - \alpha) \frac{1}{12} \nabla t^2 \mathcal{C}^2(\phi^n, \mathbf{u}) + \alpha \frac{1}{12} \nabla t^2 \mathcal{D}(\phi^n, \mathbf{u}) \quad (3.67)$$

$$\phi^{(n+1)} = \phi^n - \Delta t \mathcal{C}(\phi^n, \mathbf{u}) + (1 - \alpha) \frac{1}{2} \nabla t^2 \mathcal{C}^2(\phi^n, \mathbf{u}) + \alpha \frac{1}{2} \nabla t^2 \mathcal{D}(\phi^n, \mathbf{u}) \quad (3.68)$$

where α is the relaxation parameter between the two schemes. Evidently, when $\alpha = 0$ it becomes a RK-4 scheme and when $\alpha = 1$ the method reduces to a TTG4-A scheme. During this thesis, the velocity time integration was carried out with $\alpha = 0.2$ while the scalars were advanced in time with a pure RK4 scheme.

3.4 Poisson solver

As mentioned before, advancing the momentum equation in time requires solving a linear system of equations for the Poisson equation. For a system of linear equations of the form $AX = B$, there exists several class of methods for solution such as the Gauss-Seidel method, LU decomposition method and the Conjugate Gradient (CG) methods. It is essential that these solutions are accurate and fast. Since in practical LES situations, the matrix A to be inverted is very large (as big as the number of nodes in the domain), iterative fast converging and accurate methods are preferred rather than a direct matrix inversion method due to the lower storage required. Conjugate gradient methods and its derivatives are very useful in this direction and are used in YALES2.

Conjugate Gradient Methods

Conjugate gradient algorithms are particularly suitable for symmetric and positive definite³ matrices whereas bi-conjugate gradient methods (BCG) are more generalized and suitable for non-symmetric matrices. The discretized form of the Poisson Eq. 3.50 are symmetric and hence both of these methods work.

For an N dimensional system of equations $AX = B$, the direct conjugate gradient method approaches the solution X^* by sequentially taking orthogonal directions in the N dimensional space such that a direction is never repeated. This approach takes exactly N steps to determine the solution which is very expensive since in a typical CFD problem N is of the order of few millions. Since the N directions of descent can be taken in any order to reach the solution, a cheaper and faster iterative version of the conjugate gradient method could be developed. In this approach an initial solution and an initial direction is chosen to start. The descent is then made continually along orthogonal directions without repetition but in such a way that the value of the function

$$f(X) = \frac{1}{2}X^TAX - BX \quad (3.69)$$

decreases at every step. By using this metric, indirectly, we are trying to find a X^* such that the derivative of the function, $f(X)$ is minimized or $f'(x) = AX - B = 0$ which is the final system to be solved. Due to numerical difficulties, it might be difficult to achieve the exact solution of the system. Therefore, a threshold or a minimum residual, ϵ is prescribed by the user as a convergence criteria and the descent is stopped when $f'(x) = AX - B < \epsilon$. This iterative method requires far less steps than the direct method and is used in YALES2.

The iterative form of the CG method can be made to converge faster by pre-conditioning the matrix A. This choice of pre-conditioner can be made by making use of a previous solution matrix. This gives to the class of conjugate gradient methods called the Pre-conditioned conjugate gradient methods (PCG) and deflated conjugate gradient methods (DPCG). The reader is

³A given matrix A is said to be positive definite if for another matrix $z \in R$, zAz^T is positive for all non-zero elements

referred to the book by Golub and vanLoan [207] for details. Throughout this work, DPCG is used for solving the Poisson equation. Details of the algorithms implemented in YALES2 can be obtained in [208].

FLF-PDF Model and Modeling

Differential Diffusion of

Mixture fraction 4

Contents

4.1	FLF-PDF SGS modeling	49
	Formalism	49
	Balance equations and closures	52
4.2	Filtered laminar flame validation of FLF-PDF	59
	1D laminar flame	59
	2D laminar Bunsen flame	61
4.3	Modeling differential diffusion of mixture fraction	63
	Mixture fraction definition	63
	SGS Modeling of mixture fraction differential diffusion	65
	A global criterion for differential diffusion in burners	66

In this chapter, the Filtered Laminar Flame PDF (FLF-PDF) model is described. 1D and 2D validation of the model by simulating unfiltered and filtered laminar flames are also presented. Subsequently, a strategy to model differential diffusion of mixture fraction is discussed. A global differential diffusion number based on the gradient of residence times in fresh and burnt gas is proposed as a criterion to identify the presence of differential diffusion effect of mixture fraction in burners.

4.1 FLF-PDF SGS modeling

Formalism

The transport equations used for LES of turbulent premixed flame can be derived by convoluting the conservation equations with the LES filter operator \mathcal{G} , defined in the physical space as

$$\mathcal{G}(x, \Delta) = \sqrt{\frac{6}{\pi\Delta^2}} \exp\left(-6(x/\Delta)^2\right) . \quad (4.1)$$

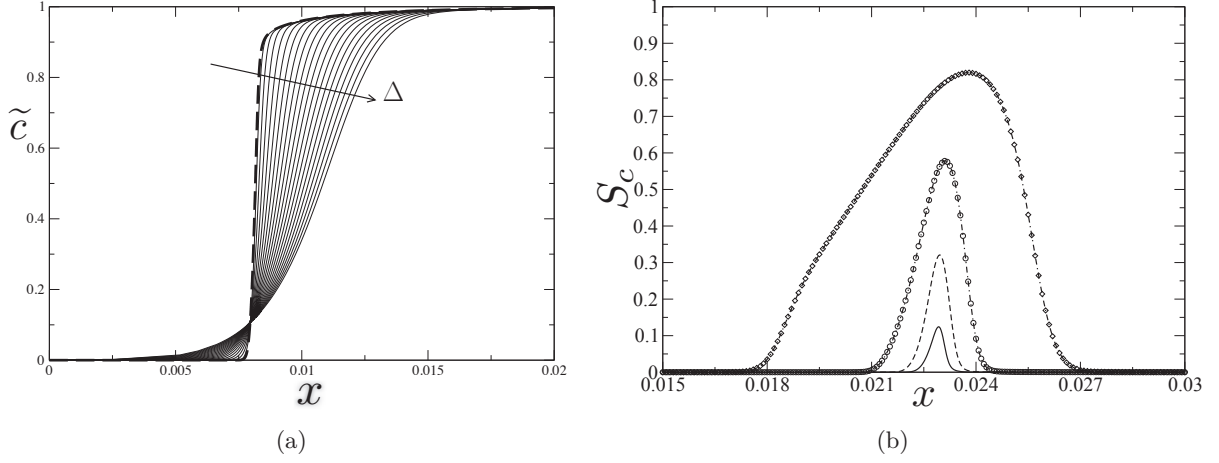


Figure 4.1: Laminar premixed methane air flame at $\phi = 0.75$. (a) Filtered \tilde{c} profiles at different filter widths (b) S_c profiles for different filter widths. — $\Delta = 5\delta_L$, --- $10\delta_L$, -o- $20\delta_L$, -·◇- $50\delta_L$.

The Favre filtering operation is then expressed with

$$\tilde{\phi}(x, \Delta) = \frac{\overline{\rho\phi}}{\bar{\rho}} = \frac{1}{\bar{\rho}(x, \Delta)} \int_{-\infty}^{+\infty} \rho(\xi)\phi(\xi)\mathcal{G}(x - \xi, \Delta)d\xi, \quad (4.2)$$

where Δ is the filter width. It is assumed that the reaction zones can be described with a reaction progress variable, Y_c and $c = Y_c/Y_c^{Eq}$ ($Y_c = c = 0$ in fresh gases and $Y_c = Y_c^{Eq}$ and $c = 1$ in burnt gases).

In a one-dimensional flamelet, $c(x)$ is monotonically evolving when progressing from fresh to burnt gases, then it can be uniquely inverted to form $x(c)$. Similarly, $\phi(x)$ is known and $\phi(x(c))$ is available and denoted $\phi(c)$. The relation (4.2) becomes:

$$\tilde{\phi}(x, \Delta) = \frac{1}{\bar{\rho}(x, \Delta)} \int_0^1 \rho(c)\phi(c)|\nabla c|^{-1}\mathcal{G}(\tilde{x}^\Delta(\tilde{c}, \Delta) - x(c), \Delta)dc. \quad (4.3)$$

where $\tilde{x}^\Delta(\tilde{c}, \Delta)$ denotes the x -position in the one-dimensional flame where the \tilde{c} -value is found for the filter width Δ . Equation (4.3) reads in a PDF context as:

$$\tilde{\phi}(\tilde{c}, S_c) = \int_0^1 \phi(c)\tilde{P}(c; \tilde{c}, S_c)dc, \quad (4.4)$$

Comparing Eqs. 4.3 and 4.4 we can write the filtered laminar flame PDF (FLF-PDF) as

$$\tilde{P}(c; \tilde{c}, S_c) = \frac{1}{\bar{\rho}(\tilde{c}, S_c)} \rho(c)|\nabla c|^{-1}\mathcal{G}(\tilde{x}^\Delta(\tilde{c}, \Delta) - x(c), \Delta). \quad (4.5)$$

In this work, the tabulation of thermo-chemical quantities are performed as a function of (\tilde{c}, S_c) and not directly as a function of the filter width Δ which is done in the F-TACLES method. Therefore, the PDF needs to be expressed as a function of (\tilde{c}, S_c) which essentially requires establishing the relation $\tilde{x}^\Delta(\tilde{c}, S_c)$ and $\Delta(\tilde{c}, S_c)$.

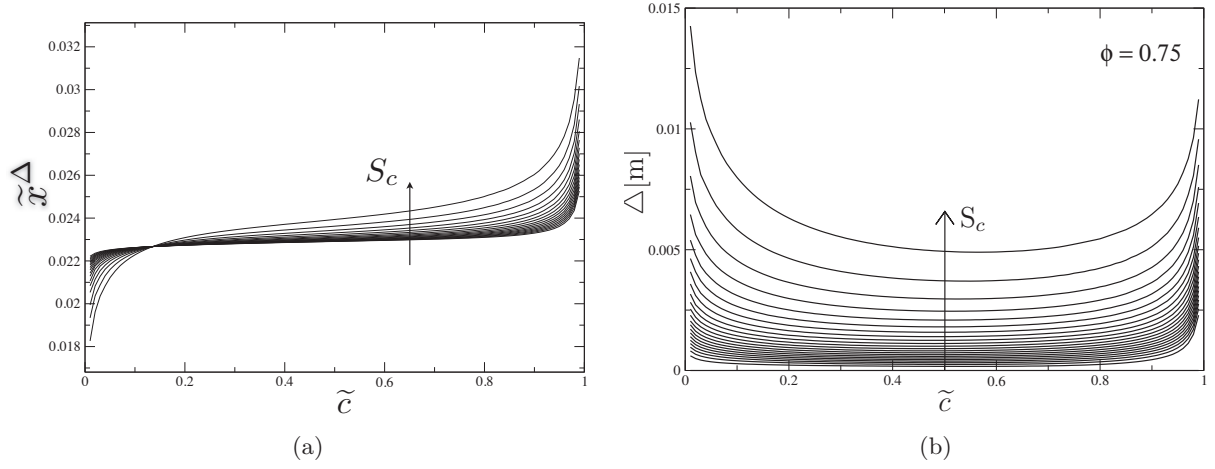


Figure 4.2: Quantities obtained by numerical interpolation. (a) $\tilde{x}^\Delta = \tilde{x}^\Delta(\tilde{c}, S_c)$. (b) $\Delta = \Delta(\tilde{c}, S_c)$.

To obtain these quantities, consider a laminar premixed flame solution obtained from a Cantera [154] simulation of methane-air mixture. The GRI 3.0 mechanism [209] with 53 species and 325 reactions and differential diffusion [210] was used. By using Eq. 4.2, the filtered progress variable $\tilde{c}(x, \Delta)$ can be obtained along with $\tilde{c}^2(x, \Delta)$ and the unmixedness $S_c(x, \Delta) = (\tilde{c}^2 - \tilde{c}^2) / [\tilde{c}(1 - \tilde{c})]$ (which is zero when $\Delta \rightarrow 0$ and increases up to unity when $\Delta/\delta_L \gg 1$, where δ_L is the characteristic flame thickness). For an equivalence ratio of 0.75, which will be the one of the turbulent burner studied subsequently, the plots of $\tilde{c}(x, \Delta)$ and $S_c(x, \Delta)$ are shown in Figs. 4.1a and 4.1b. Figures 4.2a and 4.2b give $\tilde{x}^\Delta(\tilde{c}, S_c)$ and $\Delta(\tilde{c}, S_c)$ for the same simulation. In order to obtain these plots, a deconvolution of the filter has to be performed which is not straightforward using a pure analytical method. To circumvent this problem, a fully numerical method based on interpolation is used to arrive at these quantities which is described in Appendix B. Now, a FLF-PDF defined in (\tilde{c}, S_c) has been established which is equivalent to a Gaussian filter in physical space. This PDF is such that it preserves the laminar flame speed for any given filter width (see Eqs. 13-17 of [71] for mathematical proof) and is an important characteristic for coarse mesh LES of a laminar flame.

However, for a turbulent reacting flow simulation in LES, using a fixed filter width is not suitable following the DNS results of Moureau et al. [68]. It was found that even if the sub-grid wrinkling is modeled perfectly, to have a filtered laminar flame statistically equivalent to a filtered DNS flame (i.e. having the same \tilde{c}, S_c values), the laminar flame has to be filtered with a filter size (Δ) smaller than the characteristic mesh size (h) (see Figs. 24 and 25 of [68]). This filter width is then a function of the SGS fluctuations. To incorporate this knowledge, during this work the PDF is built based on the local grid point values of (\tilde{c}, S_c) which are obtained by solving balance equations for \tilde{Y}_c and \tilde{Y}_c^2 . This indirectly allows for finding the actual filter size that needs to be applied to the flame at a given position in the turbulent flow and for a mesh

size h . This is an advantage over the F-TACLES model which uses an explicit fixed filter width combined with a SGS wrinkle factor model to simulate a turbulent flame.

To summarize, for simulating laminar flame propagation on a coarse mesh, a FLF-PDF built from fixed filter width is suitable since it preserves the correct flame speed, whereas for modeling the turbulent flame propagation on an LES mesh, FLF-PDF built on variable filter width has to be used (based on [68]) to account for the SGS fluctuations [68]. A switching type model appears useful to satisfy both these criteria and is used in this work, the description of which is given in subsection 4.1.

The next section deals with the LES scalar transport equations solved in this work and the closure of the SGS terms appearing these equations. It also describes the way by which the switching is achieved.

Balance equations and closures

The following scalar transport equations are considered in this study, along with the usual filtered Navier-Stokes equations in the low-Mach number limit:

$$\frac{\partial(\bar{\rho}\tilde{Z})}{\partial t} + \nabla \cdot (\bar{\rho}\tilde{\mathbf{u}}\tilde{Z}) = \nabla \cdot (\bar{\rho}D_Z\nabla\tilde{Z}) + \nabla \cdot (\bar{\tau}_Z^D + \bar{\tau}_Z^u), \quad (4.6)$$

$$\frac{\partial(\bar{\rho}\tilde{Z}^2)}{\partial t} + \nabla \cdot (\bar{\rho}\tilde{\mathbf{u}}\tilde{Z}^2) = \nabla \cdot (\bar{\rho}D_Z\nabla\tilde{Z}^2) + \nabla \cdot (\bar{\tau}_{Z^2}^D + \bar{\tau}_{Z^2}^u) - \bar{\chi}_Z, \quad (4.7)$$

$$\frac{\partial(\bar{\rho}\tilde{Y}_c)}{\partial t} + \nabla \cdot (\bar{\rho}\tilde{\mathbf{u}}\tilde{Y}_c) = \nabla \cdot (\bar{\rho}D_{Y_c}\nabla\tilde{Y}_c) + \nabla \cdot (\bar{\tau}_{Y_c}^D + \bar{\tau}_{Y_c}^u) + \overline{\rho\dot{\omega}_{Y_c}}, \quad (4.8)$$

$$\frac{\partial(\bar{\rho}\tilde{Y}_c^2)}{\partial t} + \nabla \cdot (\bar{\rho}\tilde{\mathbf{u}}\tilde{Y}_c^2) = \nabla \cdot (\bar{\rho}D_{Y_c}\nabla\tilde{Y}_c^2) + \nabla \cdot (\bar{\tau}_{Y_c^2}^D + \bar{\tau}_{Y_c^2}^u) - \bar{\chi}_{Y_c} + 2\overline{\rho\tilde{Y}_c\dot{\omega}_{Y_c}}, \quad (4.9)$$

where the SGS transport by velocity/diffusive contributions and the scalar dissipation rate read:

$$\bar{\tau}_\phi^u = - \left(\overline{\rho\mathbf{u}\phi} - \bar{\rho}\tilde{\mathbf{u}}\tilde{\phi} \right), \quad (4.10)$$

$$\bar{\tau}_\phi^D = \left(\overline{\rho D_\phi \nabla \phi} - \bar{\rho} D_\phi \nabla \tilde{\phi} \right), \quad (4.11)$$

$$\bar{\chi}_\phi = \overline{2\rho D_\phi |\nabla \phi|^2}. \quad (4.12)$$

Twelve terms require closure, namely the eight $\bar{\tau}_\phi$ subgrid flux, the two sources involving the chemical rate $\dot{\omega}_{Y_c}$ and the two $\bar{\chi}_\phi$ scalar dissipation rates.

To model differential diffusion effects, an additional passive scalar and residence time equations are also solved, the details of which will be mentioned in the section on modeling of differential diffusion.

Source terms

Throughout this paper, the progress variable definition $Y_c = Y_{\text{CO}_2} + Y_{\text{CO}}$ is used. The source terms defined in one-point are computed by convoluting a tabulated flamelet response, $\dot{\omega}_{Y_c}(c, Z)$, with the FLF-PDF for c (Eq. (4.5)) and a usual Beta-PDF for mixture fraction, by considering

flamelets at different equivalence ratios. Because only dilution by air in burnt gases and weak stratification will be studied, SGS fluctuations of c and Z are considered statistically uncorrelated, moreover it will be seen below that fluctuations of Z will be almost fully resolved by the mesh, leading to very small $S_Z = (\tilde{Z}^2 - \tilde{Z}^2)/(\tilde{Z}(1 - \tilde{Z}))$ levels, with thus a weak contribution of the Beta-PDF to the modeling. The sources then read:

$$\overline{\rho\dot{\omega}_{Y_c}}(\tilde{c}, S_c, \tilde{Z}, S_Z) = \bar{\rho} \int_0^1 \left[\int_0^1 \dot{\omega}_{Y_c}(c, Z) \tilde{P}(c; \tilde{c}, S_c) dc \right] \tilde{P}(Z; \tilde{Z}, S_Z) dZ, \quad (4.13)$$

$$\overline{\rho Y_c \dot{\omega}_{Y_c}}(\tilde{c}, S_c, \tilde{Z}, S_Z) = \bar{\rho} \int_0^1 \left[\int_0^1 c \dot{\omega}_{Y_c}(c, Z) \tilde{P}(c; \tilde{c}, S_c) dc \right] Y_c^{Eq}(Z) \tilde{P}(Z; \tilde{Z}, S_Z) dZ, \quad (4.14)$$

where $\tilde{c} = \tilde{Y}_c / \tilde{Y}_c^{Eq}$ and $S_c = (\alpha_c Y_{c_v} + (\alpha_c - 1) \tilde{Y}_c \tilde{Y}_c) / [\tilde{Y}_c (\tilde{Y}_c^{Eq} - \tilde{Y}_c)]$ with $\alpha_c = (\tilde{Y}_c^{Eq})^2 / \tilde{Y}_c^{Eq^2}$, the filtered equilibrium values are computed with the Beta-PDF of the mixture fraction. All these quantities are accessible after solving the above balance equations. The organization of these quantities into a database is detailed in Appendix B.

The advantage of using the FLF-PDF over Beta-PDF is that since the FLF-PDF is derived from a normalized space filter, it always ensures that the filtered flame front propagates at the laminar flame speed for all filter widths [71]. In other words,

$$\rho_0 S_L = \int_{-\infty}^{+\infty} \rho \dot{\omega}_c dx = \int_{-\infty}^{+\infty} \overline{\rho \dot{\omega}_c}^\Delta dx \quad (4.15)$$

Figure 4.3 gives a comparison of the source terms filtered with the FLF-PDF and Beta-PDF for different unmixedness factors. A difference in the two profiles is notable especially towards the burnt gas side. For the stoichiometric mixture, the difference is more pronounced with the filtered source terms of FLF-PDF dropping far ahead of the Beta-PDF profiles. It should be noted that fixed segregation does not mean a fixed filter width or in other words, a fixed segregation will not yield the correct laminar flame speed. However to form a common ground of comparison for the two PDFs, the progress variable unmixedness space is chosen and hence shown here.

Molecular diffusivity and SGS scalar diffusive fluxes

The molecular diffusivity D_{Y_c} should take into account the differential diffusion of the species CO and CO₂. For a 1D premixed flame, a general expression for the molecular diffusivity, which takes into account the differential diffusion of species involved, was derived in [184] and is also detailed in Appendix A. We obtain

$$D_{Y_c} = -\frac{1}{\nabla Y_c} (V_a Y_c + V_{CO} Y_{CO} + V_{CO_2} Y_{CO_2}), \quad (4.16)$$

where V_{CO} and V_{CO_2} denote the diffusive speeds of CO and CO₂ respectively and $V_a = -\sum_i V_i Y_i$ is a corrective velocity introduced to ensure mass conservation, with

$$V_i = -D_i \frac{\nabla(Y_i \bar{W})}{Y_i \bar{W}}, \quad (4.17)$$

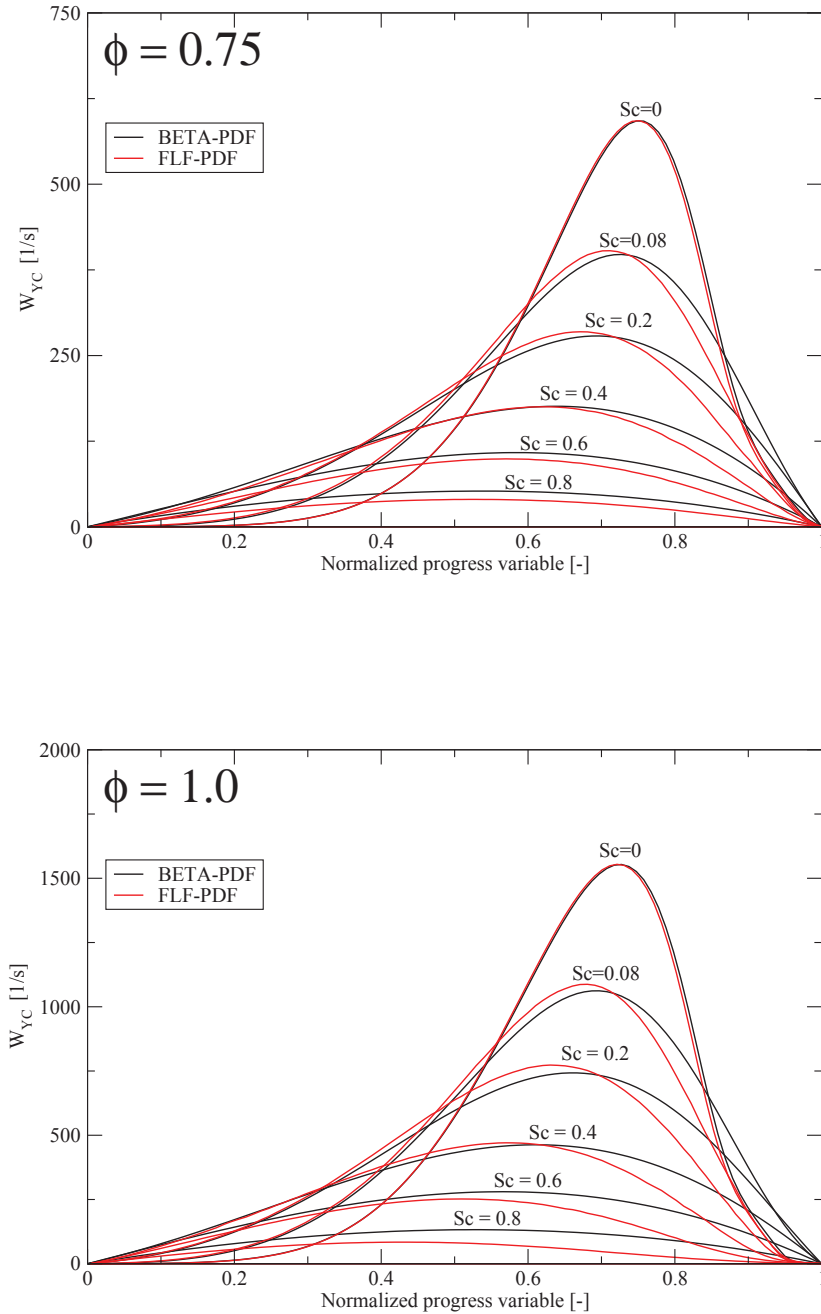


Figure 4.3: Comparison of source terms of progress variable filtered with Beta-PDF and FLF-PDF for different unmixedness factors S_c for a 1D laminar methane-air flame.

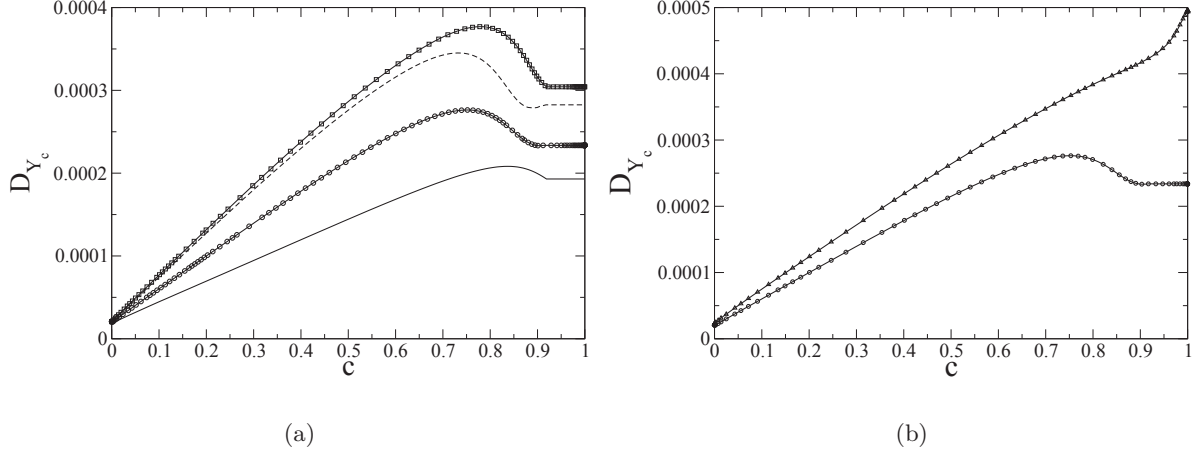


Figure 4.4: D_{Y_c} [$\text{m}^2 \cdot \text{s}^{-1}$] response *vs* progress variable for premixed methane-air flame. (a) Various equivalence ratios. $- \phi = 0.5$, $-o- 0.75$, $- - 1.0$, $- \square - 1.125$. (b) $\phi = 0.75$. $-o-$ Eq. (4.16), $-\triangle-$ ν/Sc .

\bar{W} is the mean molecular weight. In the calculation of the reference one-dimensional flame, methane-air chemistry is described with the fully detailed GRI 3.0 mechanism [209] and the Curtiss and Hirschfelder [210] expressions are used for D_i . In the LES solver, the molecular diffusivity, D_{Y_c} is obtained from the relation 4.16 and it is tabulated with the laminar flamelets $D_{Y_c}(c, Z)$ (Fig. 4.4(a)), to ensure correct flame speed. Figure 4.4(b) displays the diffusivity response *vs* the progress variable, calculated using Eq. (4.16) and the basic relation based on kinematic viscosity $D_{Y_c} = \nu/Sc$, with the Schmidt number $Sc = 0.72$ and ν varying with temperature according to the Sutherland's law. Sc was here defined to match the fresh gas value, the departure between the two definitions starts very early when progressing from fresh gases towards burnt ones, to reach its maximum of about 50% in burnt gases, motivating the need for Eq. (4.16).

The SGS diffusive term $\bar{\tau}_\phi^D$ appears during the filtering operation on the governing equations. In analysis of swirling flame DNS at quite high Reynolds number (about 40,000), it was found that the divergence of this term can be of the same order of $\nabla \cdot \bar{\tau}_\phi^u$, the SGS convective contribution (see Fig. 5 of [211]). Except for two recent publications [71, 122], the general practice in LES has been to neglect the term $\nabla \cdot \bar{\tau}_\phi^D$ or assume it to be accounted overall by the modeling of the other fluxes. It can be seen in Figs. 4.5 and 4.6, showing all the terms contributing to the budget of the filtered progress variable in a premixed flamelet, that at high filter widths, this SGS diffusive term can become very large. Therefore, it is proposed to accommodate it by

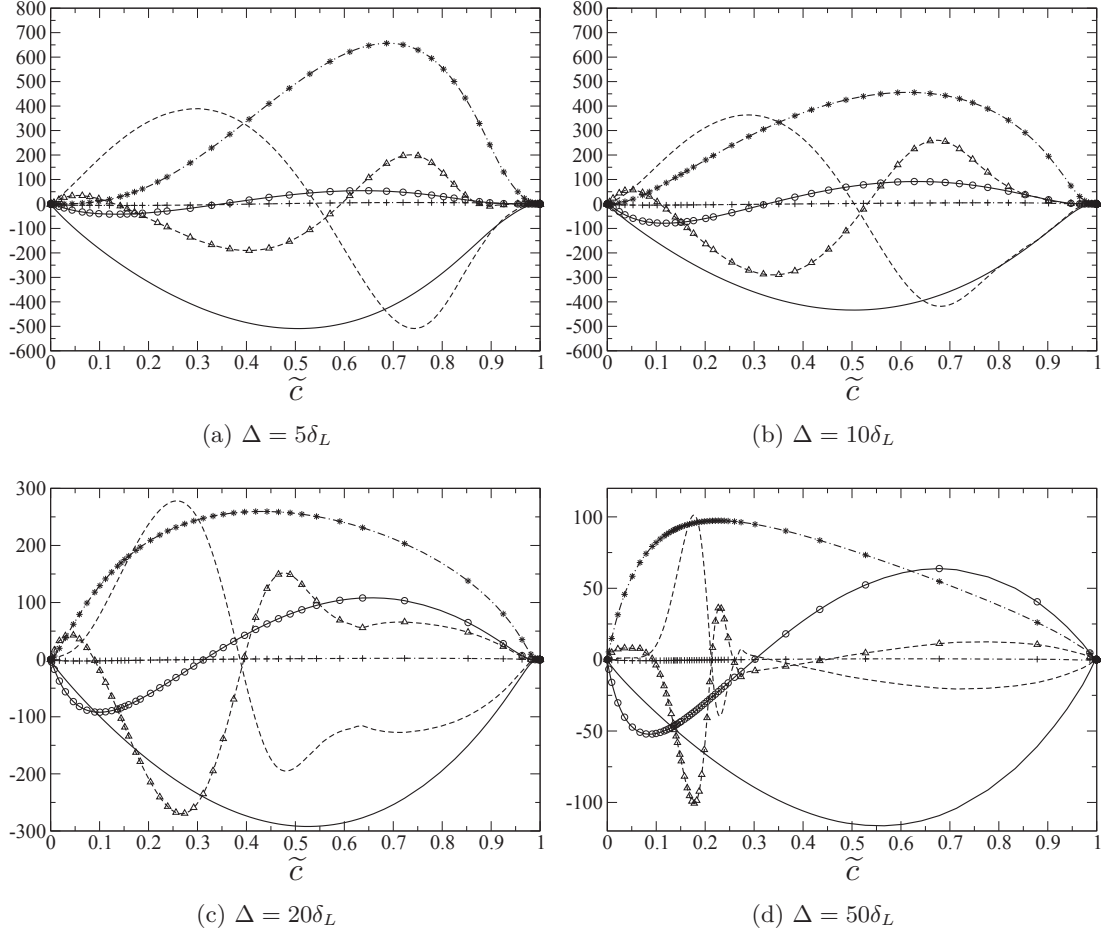


Figure 4.5: $-\cdot$: $-\nabla \cdot (\bar{\rho} \tilde{\mathbf{u}} \tilde{c})$. $-\cdot-$: $\nabla \cdot (\bar{\rho} D_c \nabla \tilde{c})$. $- * -$: $\bar{\rho} \tilde{\omega}_c$. $- \circ -$: $\nabla \cdot \bar{\tau}_c^u$. $- \triangle -$: $\nabla \cdot \bar{\tau}_c^D$. $- \cdot + \cdot -$: Total budget, all terms in $\text{kg} \cdot \text{m}^3 \cdot \text{s}^{-1}$.

defining a SGS molecular diffusivity, $D_\phi^D(\tilde{c}, S_c, \tilde{Z})$ from a filtered 1D laminar flame equation as:

$$D_\phi^D(\tilde{c}, S_c, \tilde{Z}) = \frac{\overline{\rho D_\phi(c, Z) \nabla \phi} - \bar{\rho} D_\phi(\tilde{c}, S_c, \tilde{Z}) \nabla \tilde{\phi}}{\bar{\rho} \nabla \tilde{\phi}} \Big|_{1D}, \quad (4.18)$$

which leads to $\bar{\tau}_\phi^D = \bar{\rho} D_\phi^D(\tilde{c}, S_c, \tilde{Z}) \nabla \tilde{\phi}$, where fluctuations of mixture fraction have been neglected and ϕ denotes Y_c or Y_c^2 . $D_{Y_c}^D$ and $D_{Y_c^2}^D$ could be negative as observed in Fig. 4.7, then $\nabla \cdot \bar{\tau}_{Y_c}^D$ and $\nabla \cdot \bar{\tau}_{Y_c^2}^D$ could also be negative, as seen in Figs. 4.5 and 4.6. But it should be noted that the effective diffusivity,

$$D_\phi^E(\tilde{c}, S_c, \tilde{Z}) = D_\phi(\tilde{c}, S_c, \tilde{Z}) + D_\phi^D(\tilde{c}, S_c, \tilde{Z}), \quad (4.19)$$

actually used in above balance equations, never goes negative. With those relations, the response of filtered laminar premixed flames are exactly reproduced by the simulations whatever the filter size, as discussed below. Notice also that D_ϕ^D is calibrated from a one-dimensional flame, to be

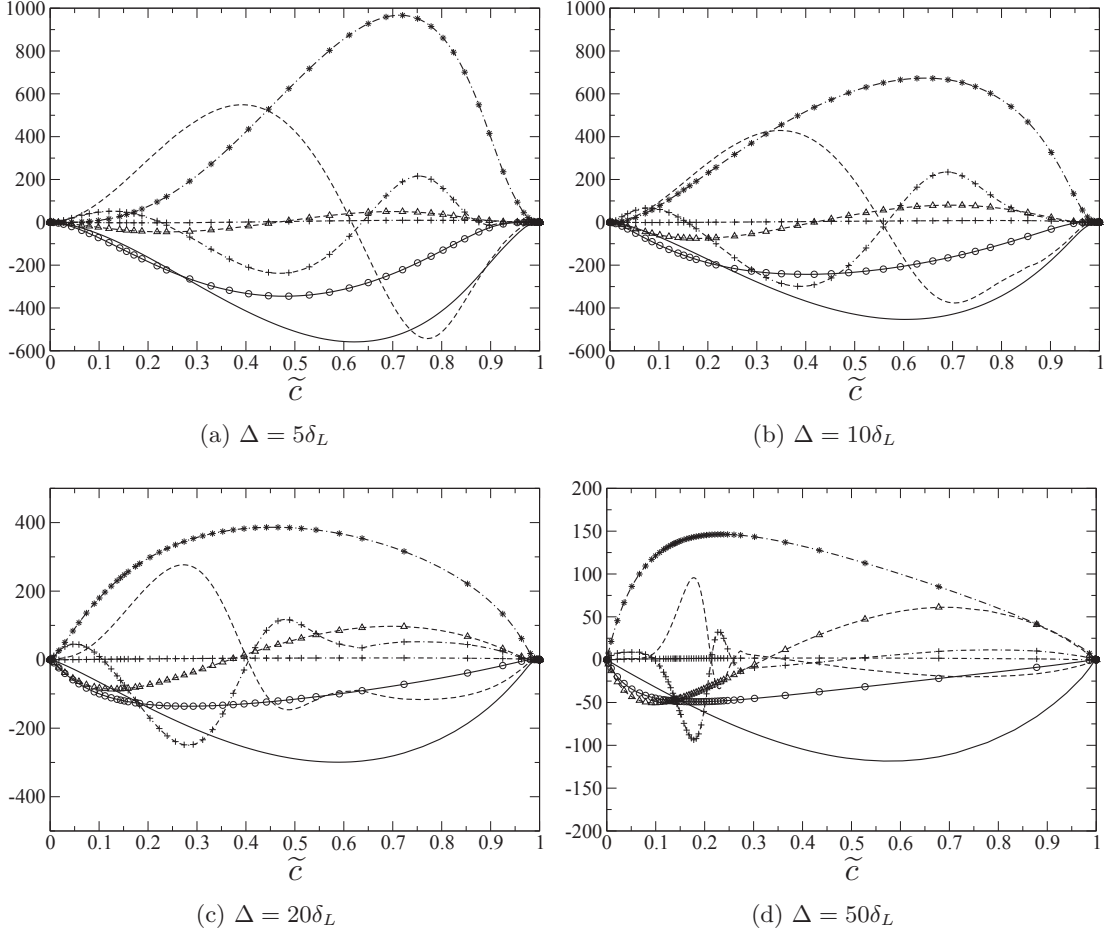


Figure 4.6: $-\cdot$: $-\nabla \cdot (\tilde{\rho} \tilde{\mathbf{u}} \tilde{c}^2)$. $-\cdot-: $\nabla \cdot (\tilde{\rho} D_c \nabla \tilde{c}^2)$. $-\triangle-$: $\nabla \cdot \tilde{\tau}_{c^2}^D$. $-\circ-$: $\nabla \cdot \tilde{\tau}_{c^2}^u$. $-\cdot\diamond-$: $\bar{\chi}_c$. $-\ast-$: $2\tilde{\rho} c \dot{\tilde{c}}$. $-\cdot+$: Total budget, all terms in $\text{kg} \cdot \text{m}^3 \cdot \text{s}^{-1}$.$

then applied to a three-dimensional flux in LES, which accounts for scalar field curvature effects through the divergence of the gradients of \tilde{Y}_c and \tilde{Y}_c^2 . This approach for closing the sub-grid diffusive flux term is very close to the strategy adopted in the F-TACLES method [71].

SGS scalar convective fluxes

In this study, the turbulent viscosity used in the momentum equation, ν_T is expressed by a localized dynamic Smagorinsky model [195]. For the passive scalars, a usual gradient assumption is formulated:

$$(\tilde{\mathbf{u}}\phi - \tilde{\mathbf{u}}\tilde{\phi}) = -\frac{\nu_T}{Sc_T^\phi} \nabla \tilde{\phi}. \quad (4.20)$$

This class of subgrid models were found to work well for capturing subgrid flux of passive scalars in mixing problems [212, 213], here $Sc_T = 0.9$ is used. However for the progress variable in premixed flames, the unresolved scalar fluxes could be of counter-gradient type as reported at

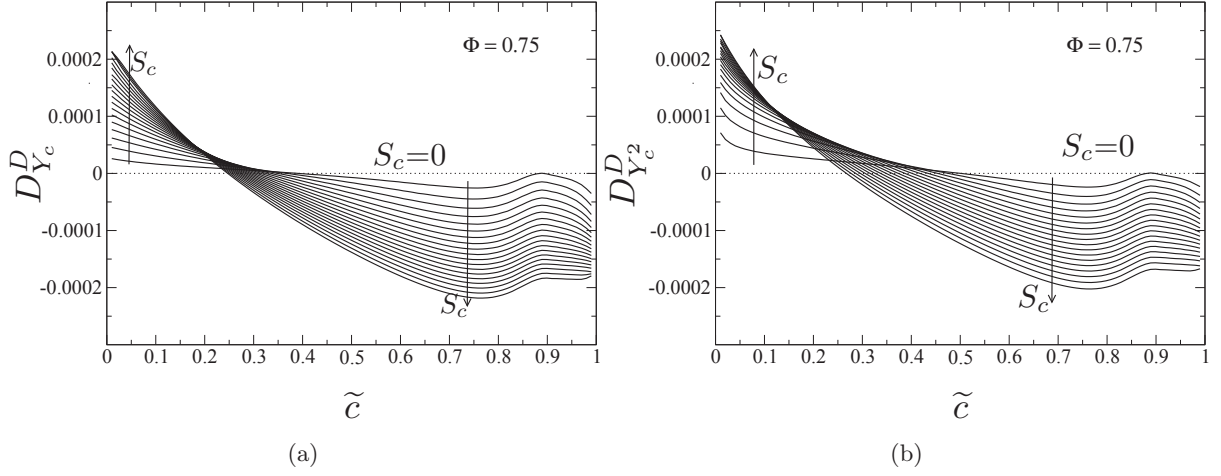


Figure 4.7: D_{ϕ}^D (Eq. (4.18)) m^2/s for various S_c . (a): $D_{Y_c}^D$. (b): $D_{Y_c^2}^D$.

many places in the literature [214,215]. The profiles of this term in a 1D laminar premixed flame for different filter widths are shown for progress variable (\tilde{c}) and its square (\tilde{c}^2) in Figs 4.5 and 4.6, depicting its counter-gradient nature, its amplitude non-negligible compared to all other terms of the balance equation can also be seen.

The gradient assumption is retained for mixture fraction, while for the reactive scalars \tilde{Y}_c and \tilde{Y}_c^2 , the SGS convective transport is closed directly from the filtered 1D laminar flame response. A lookup table of $\nabla \cdot \bar{\tau}_{\phi}^u(\tilde{c}, S_c, Z)$ is built and this term added to the respective source terms of the balance equations. It was tried to tabulate only $\bar{\tau}_{\phi}^u$ from the one-dimensional flame and not its divergence, a procedure which is fine to simulate a one-dimensional filtered flame, but that was found unstable when applied to three-dimensional LES, thereby the term was treated instead as a direct source in the equations.

SGS scalar dissipation rate and unmixedness

The filtered scalar dissipation rate, $\bar{\chi}_{\phi}$ appears in the transport equations for \tilde{Z}^2 and \tilde{Y}_c^2 . A closure based on linear relaxation hypothesis [216] is used for both the scalars, where the filtered scalar dissipation rate is expressed as the sum of resolved and unresolved parts:

$$\bar{\chi}_{\phi} = \overline{2\rho D_{\phi} |\nabla\phi|^2} = 2\bar{\rho}D_{\phi}|\nabla\tilde{\phi}|^2 + 2\bar{\rho}\frac{\phi_v}{\Delta_h^2/(\nu_T/S_{cT})}, \quad (4.21)$$

with $\Delta_h = \mathcal{V}^{1/3}$ the implicit filter width based on an estimation of the local cell characteristic length, where \mathcal{V} is the mesh cell volume [217]. Obviously, this closure based on the subgrid turbulent scalar cascade cannot be justified when the level of SGS velocity fluctuations is very small, in other words when the flame wrinkling is resolved by the LES mesh (*i.e.* an unsteady laminar flame simulated over a coarse grid). $\bar{\chi}_{\phi}$ enters the $\tilde{\phi}^2$ budget, which is used for computing S_c , the unmixedness, a quantity that was also related to the filter size $\Delta = \Delta(\tilde{c}, S_c)$ in above

FLF-PDF modeling. It is then proposed to directly define S_c from the filter size and \tilde{c} in the case of weak SGS velocity fluctuations and to use the information from the $\widetilde{\phi^2}$ balance equation, at locations where flow turbulence is unresolved by the grid.

To dynamically determine the local level of flame resolution, as usually done in turbulent combustion-regime diagram [218–220], the subgrid kinetic energy k_{SGS} is compared with S_L the flame speed, leading to the factor \mathcal{F} :

$$\mathcal{F} = \frac{((2/3)k_{SGS})^{1/2}}{S_L}, \quad (4.22)$$

with $k_{SGS} = \nu_T^2 / (C_y \Delta_h)^2$ where the Yoshizawa [221] expression $C_y = \sqrt{2/3} A / (\pi K_o^{3/2})$ with $C_y = 0.086$ is used. Then, the following procedure is applied to delineate between the level of SGS flame wrinkling:

- When $\mathcal{F} \leq 1$, the subgrid velocity fluctuations are less than the flame speed implying that the wrinkling is resolved on the LES mesh. In this case, to ensure the correct laminar propagation speed, $S_c = S_c(\tilde{c}, \Delta)$ is obtained directly from the FLF-PDF formalism, as a function of the filter width and the LES resolved progress variable; the filter width is chosen as $\Delta \approx 5 h$, so as to resolve the flame on the LES mesh of characteristic size h .
- If $\mathcal{F} > 1$, subgrid flame wrinkling requires to be modeled and S_c is computed from the variance of the progress variable, obtained from the $\widetilde{Y_c^2}$ balance equation.

The FLF-PDF closure is first tested in the simulations of unresolved laminar flames, before being applied to a turbulent burner.

4.2 Filtered laminar flame validation of FLF-PDF

The testing and validation of the model is performed on the in-house low-Mach number finite volume solver for unstructured grids developed by Moureau et al. [68, 222] called YALES2 which was described earlier in Chapter 3. The energy equation is not solved, instead the temperature and the specific gas constants are read directly from the chemical table.

1D laminar flame

The ability of the proposed PDF to yield the proper filtered flame front for different filter widths is tested by solving the full set of transport equations with their modeled terms. The reference laminar premixed flame at an equivalence ratio of 0.75 is used. The diffusive flame thickness, $\delta_L = \nu_0 / S_L$ at this equivalence ratio is approximately 68 μm and the thermal thickness defined as $\delta_{th} = 1 / |\nabla c|_{max}$ is approximately 475 μm . The laminar flame speed, S_L is about 0.244 m/s. The laminar flame solution was then filtered at four different filter widths $5\delta_L$, $10\delta_L$, $20\delta_L$ and $50\delta_L$ to generate reference solutions for the four test cases. The unmixedness factor profiles for these filter widths are shown in Fig. 4.1b.

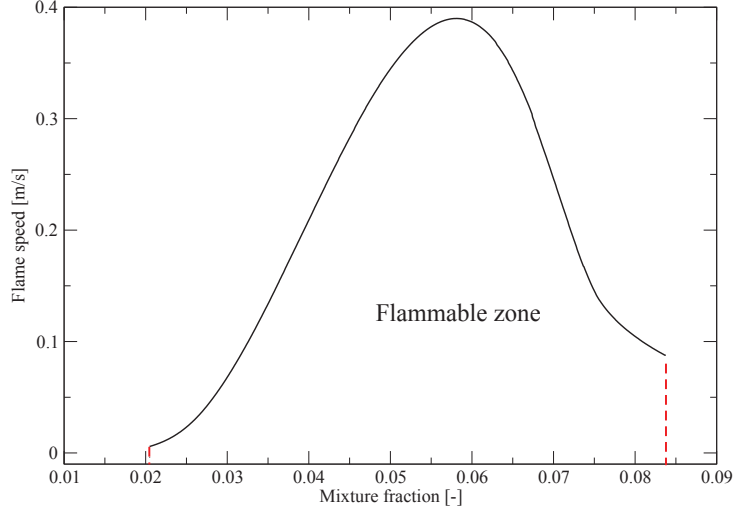


Figure 4.8: Variation of flame speed as a function of mixture fraction for methane air flame at inlet temperature of 300K and 1 atm pressure

A plot of the flame speed as a function of mixture fraction for premixed methane air flame obtained using Cantera is shown in Fig. 4.8. It also indicates the flammability limits with the rich flammability limit around $Z = 0.082$ and lean flammability limit around $Z = 0.02$.

The ability of the model to propagate the flame at the correct flame speed at all filter widths is first evaluated. The inlet velocity is set as the flame speed, S_L and a uniform mesh distribution with local mesh size, $h = 25 \mu\text{m}$ is used for the simulation. The time period of simulation is $\tau = 100\delta_L/S_L$. By definition of the model, the filtered flame front should match the filtered reference flame solutions and should propagate at the laminar flame speed at all filter widths. This was verified for both \tilde{c} and \tilde{c}^2 (Figs. 4.9a and 4.9b). The perfect agreement between the reference solution and the LES simulations shows that the FLF-PDF is able to recover the filtered flame front propagating at the correct laminar flame speed, with the proper expected thickness, *i.e.* the one obtained with the Gaussian filter applied to the flame.

The minimum number of points required in LES to obtain the correct flame speed for a given filter width is then checked. For this test case, the filter width is fixed at a large value $\Delta = 20\delta_L$. The filtered thermal flame thickness, $\tilde{\delta}_{th} = 1/|\nabla\tilde{c}|_{max}$ is then about $943 \mu\text{m}$. Tests are performed varying the mesh resolution, *i.e.* various $\tilde{\delta}_{th}/h$ and Δ/h ratios. A plot of the ratio between the obtained flame speed and its reference value is given in Fig. 4.10. To attain reasonable accuracy in flame speed prediction, it is seen that $h < \Delta/5 = 272 \mu\text{m}$ must at least be verified, stating that about 5 points should be within the reaction zone. As tests do not include curvature of the front, a second laminar canonical problem is now considered including

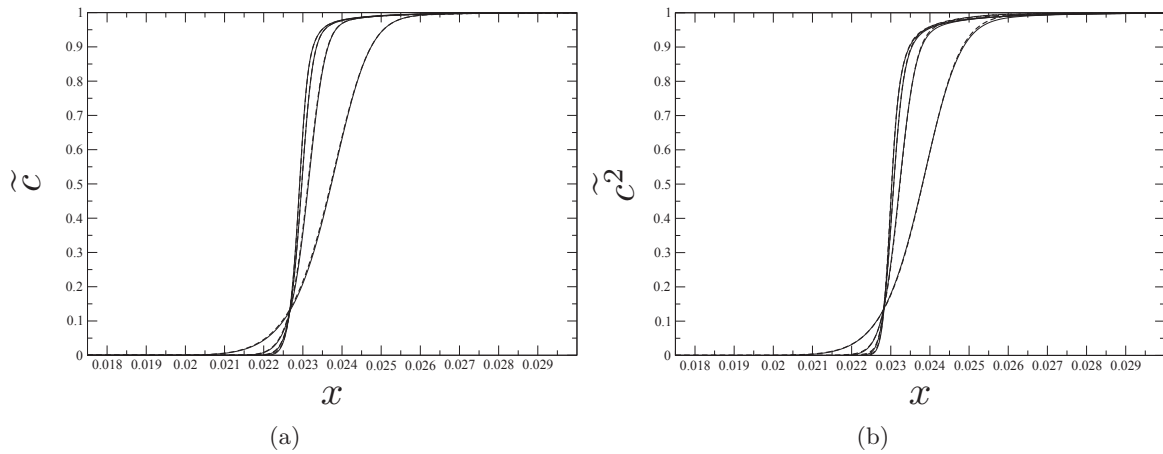


Figure 4.9: Versus x -coordinate (m): (a) \tilde{c} , (b) \tilde{c}^2 . $\Delta/\delta_L = 5, 10, 20, 50$. —: Filtered 1 D flame solution, -- 1D-LES.

flame tip effects.

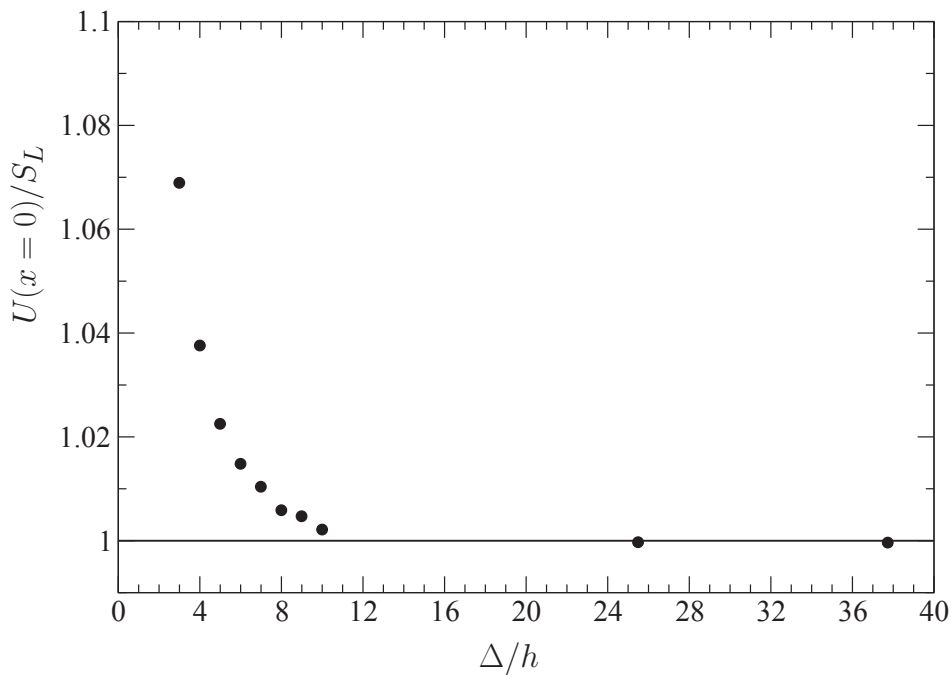


Figure 4.10: Ratio between computed flame speed and reference ones *vs* Δ/h . — shows the expected ideal value.

2D laminar Bunsen flame

The model validation on a 2D laminar Bunsen flame case is presented in this section. The computational domain and the local LES filter width for the coarse mesh simulations are shown in Fig. 4.11, in the flame zone the characteristic mesh resolution is of the order of $200 \mu\text{m}$. A

refined mesh simulation is performed in which the flame front is fully resolved, each of the triangle in the coarse mesh is refined homogeneously into 16 more triangles, leading to a resolution below $50 \mu\text{m}$ in the flame zone. A premixed methane-air mixture at an equivalence ratio of 0.75 ($S_L = 0.244 \text{ m/s}$) issues into the domain through a jet of diameter, $D_0 = 5.0 \text{ mm}$. The mixture fraction is set constant throughout the domain to ensure a fully premixed situation. Tests were performed for three inlet bulk velocities: 1.0 m/s, 2.0 m/s and 3.0 m/s. The corresponding theoretical flame length may be calculated as $L_{th} = D_0/(2\tan(\alpha))$, where α is the semi flame-cone angle expressed as $\alpha = \sin^{-1}(S_L/U_{inlet})$. The expected flame lengths for the three inlet velocities in the increasing order are then obtained as $L1 = 9.94 \text{ mm}$, $L2 = 20.34 \text{ mm}$ and $L3 = 30.64 \text{ mm}$, respectively.

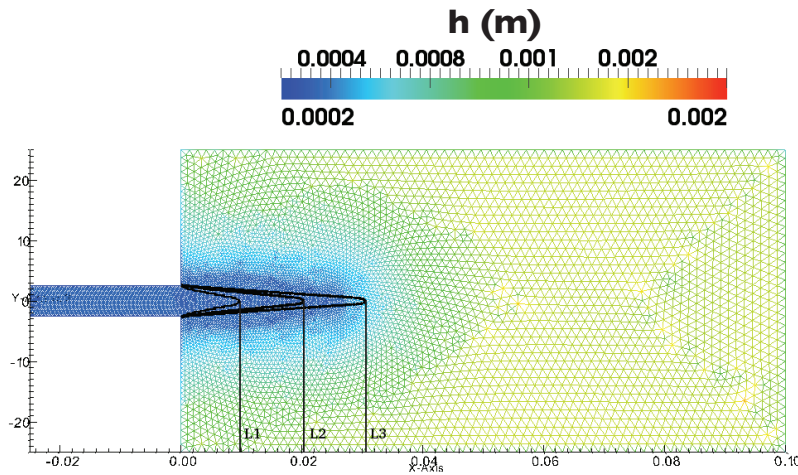


Figure 4.11: Computational domain for 2D Bunsen flame simulation (coarse mesh) showing the expected flame lengths for the three inlet velocities 1.0 m/s (L1), 2.0 m/s (L2) and 3.0 m/s (L3) respectively.

Three simulations were performed for each inlet velocity in order to assess the role of the various model ingredients:

1. Refined mesh simulation (fully resolved thermal flame thickness) with D_{Y_c} defined with differential diffusion (Eq. (4.16)).
2. Refined mesh simulation where $D_{Y_c} = \nu/Sc$, with $Sc = 0.72$.
3. Coarse mesh simulation (LES) with FLF-PDF modeling.

In these simulations, the flame tip is highly curved and features non-trivial propagation properties [223], which are not that easy to capture over a coarse mesh, modeling the under-resolved transport acting on the laminar flame solution. The results of these tests are shown in Fig. 4.12. In terms of flame length, refined simulations with the proper diffusivity for the progress variable gave results very close to theoretical values. With the same mesh, but using a constant

Schmidt number for the progress variable, the flame lengths were under predicted, emphasizing the importance of proper molecular diffusivity of the progress variable controlling the flame speed. Coarse mesh simulations carried out with all the FLF-PDF modeled terms discussed in above section, gave very close agreement to the expected flame length for all the inlet velocities (Fig. 4.12); this is confirmed in Fig. 4.13, showing details of the c -profiles on the axis of symmetry of the Bunsen burner in the 2 m/s case. It should be noted that since the flow is laminar, $\mathcal{F} = 0$ (Eq. (4.22)) in all these cases with $\Delta = 1.5$ mm used. In the turbulent burner simulations discussed hereafter, all the range of \mathcal{F} values will be encountered.

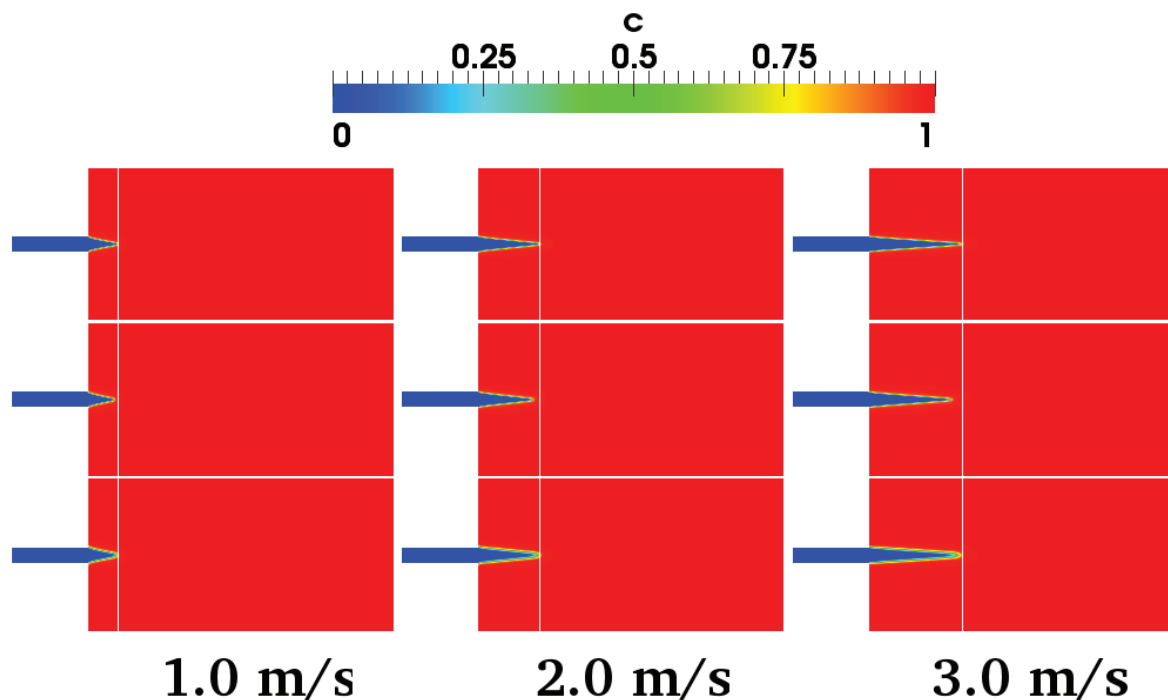


Figure 4.12: c -fields for 2D Bunsen flame simulations for different inlet velocities. Top: Refined mesh simulations, D_{Y_c} with differential diffusion. Middle: Refined mesh simulation with $D_{Y_c} = \nu/0.72$, Bottom: Coarse mesh simulation with FLF-PDF. The white line indicates the theoretical flame length.

4.3 Modeling differential diffusion of mixture fraction

Mixture fraction definition

It is a common practice to employ a Zeldovich variable (conserved or passive scalar) type definition of mixture fraction to track the mixing of fuel and oxidizer [224]. Its definition assumes

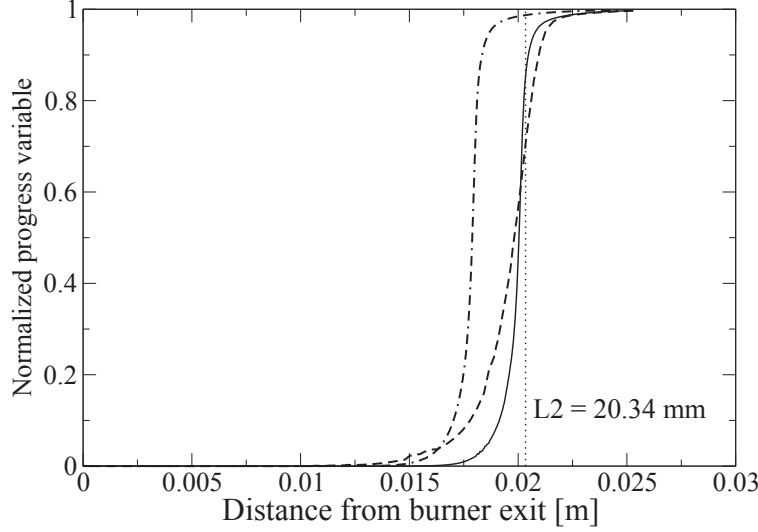


Figure 4.13: c -profiles along the axis of the Bunsen burner. 2 m/s case. \cdots : Expected flame tip location, $-$ Refined mesh simulations, D_{Y_c} with differential diffusion. $-\cdot-\cdot$ Refined mesh simulation with $D_{Y_c} = \nu/0.72$, $- - -$ Coarse mesh FLF-PDF model.

the same uniform diffusivity for the fuel and oxidizer (usually the thermal one) and it does not see the chemical reaction. Therefore, across a 1D laminar premixed flame a Zeldovich mixture fraction is constant and can be uniquely related to the equivalence ratio. On the other hand, passive scalars may also be defined from atomic concentrations of carbon, hydrogen or oxygen, which they are then free from chemical source, but sensitive to differential diffusion and will thus vary across a premixed flame front.

Experimentalists frequently resort to a mixture fraction defined from measured species mass fractions employing Bilger's formula [158]:

$$Z_B = \frac{2(Y_C - Y_{C,2})/M_C + (Y_H - Y_{H,2})/(2M_H) - (Y_O - Y_{O,2})/M_O}{2(Y_{C,1} - Y_{C,2})/M_C + (Y_{H,1} - Y_{H,2})/(2M_H) - (Y_{O,1} - Y_{O,2})/M_O}, \quad (4.23)$$

where M_C , M_H and M_O are the atomic weights of carbon, oxygen and hydrogen atoms, subscripts 1 and 2 denoting fuel and oxidizer stream respectively. In order to study the behavior of mixture fraction, the one-dimensional laminar methane-air premixed flame at an equivalence ratio of 0.75 is considered. Shown in Fig. 4.14a are two mixture fractions, Z_d^{all} and Z_d^{maj} , calculated using Bilger's formula. Z_d^{all} considers all the species of the GRI 3.0 mechanism whereas Z_d^{maj} uses only six major species (CH_4 , CO , CO_2 , H_2 , H_2O and O_2). The ideal expected passive scalar behavior Z is also shown in Fig. 4.14a. First, there exists significant difference between the mixture fraction calculated considering all the species of GRI mechanism (Z_d^{all}) and the mixture fraction profile calculated using the 6 major species (Z_d^{maj}). Second, both the mixture

fraction profiles are not conserved across the flame (Z_d^{all} being closer to be conserved). Third, towards the burnt gas there is an enhancement of the mixture fraction, Z_d^{maj} , due to a deficiency of H atoms and an accumulation of C atoms.

The reason behind this behavior of mixture fraction is the differential (or preferential) diffusion of certain species ahead of others. The atomic concentration ratios C/H and C/O vary across a laminar premixed flame affecting the mixture fraction defined from atomic mass fractions, similarly the equivalence ratio cannot be uniform even in premixed flames. This differential diffusion effect in mixture fraction exists in a laminar premixed flame at length scales smaller than the flame thickness. However in a turbulent burner, if the conditions are conducive, this effect generated at lower scales can be amplified and appear at larger scales as recently reported in a bluff-body burner by Barlow et al. [4]. The mixture fraction in the re-circulation zone of this fully premixed burner (calculated from the measured major species of above list) was found to be 10% higher than the expected inlet value due to the differential diffusion effect. The burner consists of a central closed tube bluff body, which traps the burnt gas and continuously mixes it with the incoming fresh gas ensuring flame stabilization. On either sides of the flame brush, there exists zones of different residence times - a low residence time in the incoming jet region and a high residence time in the recirculation zone. The fast diffusing species (products from burnt gases and intermediates from reaction zone) reach the fresh gases ahead of the heavier slowly diffusing species and are carried downstream by the incoming jet stream. Unable to reach the fresh gas, the slower species are trapped in the recirculation zone resulting in an accumulation of C atoms in the recirculation zone. This burnt gas in the recirculation zone deficient in H atoms and retaining a larger amount of C atoms gives mixture fraction values higher than the expected inlet values as seen for Z_d^{maj} in the laminar premixed flame case.

SGS Modeling of mixture fraction differential diffusion

Since the typical LES mesh size is much larger than the flame thickness, differential diffusion is essentially a subgrid scale phenomena for LES. To simulate differential diffusion of mixture fraction from resolved scales, the following procedure is attempted:

- First, the mixture fraction profile, $Z_d(x)$, using Bilger's definition (Eq. (4.23)), is collected through the one-dimensional laminar flame. Here, x is a physical space coordinate varying across the flame. This $Z_d(x)$ provides a way to construct a globalized differential diffusion source from its budget equation as:

$$\dot{\omega}_{Z_d}(x) = \rho_o S_L \frac{dZ_d(x)}{dx} - \frac{d}{dx} \left(\frac{\mu}{Sc} \frac{dZ_d(x)}{dx} \right). \quad (4.24)$$

Here, the dynamic viscosity μ and Schmidt number Sc are chosen so that they take exactly the same expression as they have in the LES solver. ρ_o is the density in fresh gases and S_L is the premixed laminar flame speed. Introduced into a three-dimensional Z_d balance equation, $\dot{\omega}_{Z_d}$ ensures that the Z_d profile computed in the normal direction to reaction

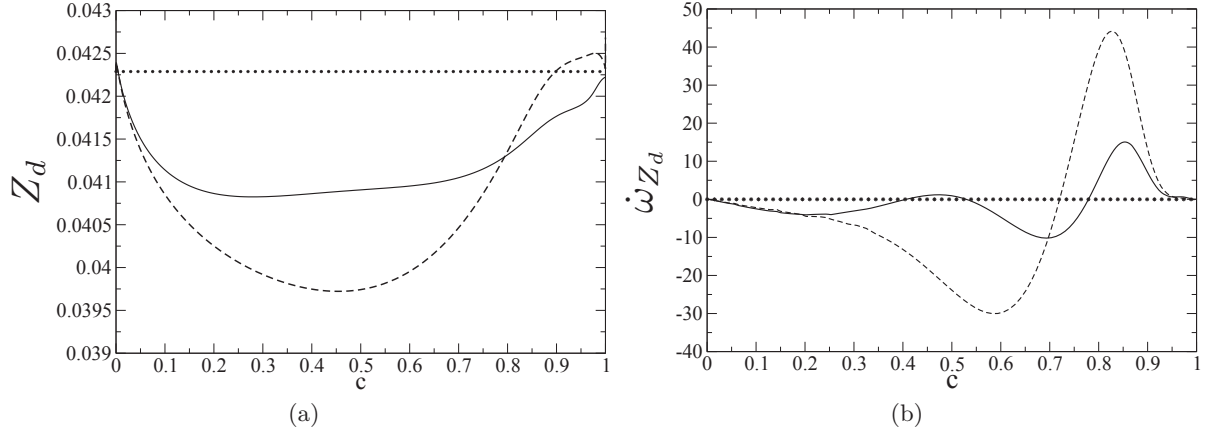


Figure 4.14: (a) Mixture fraction across the reference flame. (b) Mixture fraction source term across the reference flame (s^{-1}) where $- Z_d^{all}$, $-- Z_d^{major}$, $\star Z$

zones, with μ/Sc as the diffusion coefficient, would match exactly the one observed with detailed chemistry in the laminar flame.

- Second, the source term is remapped from the physical space, x onto the progress variable c space as $\dot{\omega}_{Z_d}(c)$ and filtered following the FLF-PDF procedure, to yield $\tilde{\omega}_{Z_d}$.

Figure 4.14b shows $\dot{\omega}_{Z_d}(c)$ for the two mixture fractions, Z_d^{all} and Z_d^{major} . As expected, it is positive in the burnt gas side to represent the fast diffusion of light species towards fresh gases and thus the relative increase of Z_d in burnt gases. It can also be seen that the source term of Z_d^{all} is much smaller than Z_d^{major} . With this approach, the source of SGS differential diffusion, $\tilde{\omega}_{Z_d}$ can be added to the usual space-filtered mixture fraction, $\tilde{Z}_d(\underline{x}, t)$, in the LES transport equation as:

$$\frac{\partial \tilde{\rho} \tilde{Z}_d}{\partial t} + \nabla \cdot (\tilde{\rho} \tilde{\mathbf{u}} \tilde{Z}_d) = \nabla \cdot \left(\left[\frac{\mu}{Sc} + \frac{\mu_T}{Sc_T} \right] \nabla \tilde{Z}_d \right) + \tilde{\omega}_{Z_d}, \quad (4.25)$$

where Sc_T is the turbulent Schmidt number, as defined in the above section. In this work two mixture fractions are transported: \tilde{Z} , a passive mixture fraction and \tilde{Z}_d , the non conserved mixture fraction with source term to compare with experimental results obtained with the 6 major species considered in the experiment. For the purpose of accessing the chemical table, the passive mixture fraction is used, because the variation of Z was not found large enough to modify significantly the LES burning rate. This SGS modeling of differential diffusion transport will be assessed against experiments in the next section.

A global criterion for differential diffusion in burners

Differential diffusion of mixture fraction being modeled as an additional source $\dot{\omega}_{Z_d}$, let us first consider an infinitesimal element of a shear layer transporting the mixture fraction with the initial condition $Z_d(x_0)$ in both sides ‘A’ and ‘B’ of the velocity gradient and featuring the same progress of reaction (i.e. $\dot{\omega}_{Z_d}$ is uniform). The velocities of this canonical problem are U^A and

U^B with $U^A > U^B$. Over the elementary streamwise length δx , the variations of Z_d in the two streams read:

$$Z_d^A(x_0 + \delta x) = Z_d(x_0) + \dot{\omega}_{Z_d} \delta t^A, \quad (4.26)$$

$$Z_d^B(x_0 + \delta x) = Z_d(x_0) + \dot{\omega}_{Z_d} \delta t^B, \quad (4.27)$$

where $\delta t^A = \delta x / U^A$ and $\delta t^B = \delta x / U^B$ and with $\delta t^A < \delta t^B$. Introducing $\Delta Z_d = Z_d^B(x_0 + \delta x) - Z_d^A(x_0 + \delta x)$, the following relation holds:

$$\Delta Z_d = (\delta t^B - \delta t^A) \dot{\omega}_{Z_d} = \frac{(\delta t^B - \delta t^A)}{\tau_Z} = N_d, \quad (4.28)$$

with $\tau_Z = 1 / \dot{\omega}_{Z_d}$ and N_d is a differential diffusion number representative of the mixture fraction variation induced by the shear layer. Now, let us consider the case where the progress variable is not the same in both the streams. Then, $\dot{\omega}_{Z_d}$ is not uniform anymore and rewriting relation 4.28:

$$\Delta Z_d = (\delta t^B - \delta t^A) \dot{\omega}_{Z_d}(c^B) + \delta t^A (\dot{\omega}_{Z_d}(c^B) - \dot{\omega}_{Z_d}(c^A)). \quad (4.29)$$

If we consider ‘A’ and ‘B’ as the fresh and burnt gas locations (with $\delta t^A \ll \delta t^B$) i.e the residence time in the fresh gas being much smaller than the residence time in the burnt gas, the expression for ΔZ_d can be written as

$$\Delta Z_d \approx (\delta t^B - \delta t^A) \dot{\omega}_{Z_d}(c^B) = N_d. \quad (4.30)$$

This suggests that it is the value of $\dot{\omega}_{Z_d}$ in burnt gases that should be used to calibrate N_d , which is positive as shown in Fig. 4.14b for major species. To define a global number indicative of the maximum deviation in the mixture fraction, one could compute in the reference laminar flame the averaged contribution:

$$\langle \dot{\omega}_{Z_d} \rangle = \frac{1}{x_b - x_f} \int_{x_f}^{x_b} \dot{\omega}_{Z_d}(x) dx, \quad (4.31)$$

where x_f is the fresh gas limit located as the point where $\dot{\omega}_{Z_d}$ changes sign (Fig. 4.14b) and x_b is the burnt gas limit ($c = 0.99$), leading to

$$N_d = \frac{\tau_b - \tau_f}{\tau_{Z_d}}, \quad (4.32)$$

with $\tau_{Z_d} = 1 / \langle \dot{\omega}_{Z_d} \rangle$; τ_b and τ_f are the maximum residence times in burnt gas and the fresh gas sides of the flame respectively. To evaluate this expression against experiments from LES, an equation for the residence time [225] of the following form

$$\frac{\partial \bar{\rho} \tau_{res}}{\partial t} + \nabla \cdot (\bar{\rho} \tilde{\mathbf{u}} \tau_{res}) = \nabla \cdot (\bar{\rho} D_{res} \nabla \tau_{res}) + \bar{\rho}, \quad (4.33)$$

is also solved, where the diffusivity, D_{res} is chosen equal to the mixture fraction diffusivity.

Experimental configuration and Cold flow simulations 5

Contents

5.1	Burner geometry and flow configurations	69
5.2	Numerics and boundary conditions	71
	Computational domain	71
	Boundary conditions	71
5.3	Non-reacting flow simulations	72
	Turbulence resolution parameter and mesh quality	72
	Non-reacting flow statistics	73
	Mixture fraction fields	77
5.4	Conclusions	77

In this chapter initially the geometry of the Cambridge burner configuration studied in this work is discussed. Subsequently, the computational details regarding the mesh and information concerning the boundary and initial conditions for the flow and flame are described. Finally, the non-reacting flow results are presented and discussed.

5.1 Burner geometry and flow configurations

The Cambridge swirl burner was designed to study turbulent premixed and stratified flames by Prof. Hochgreb and co-workers [3, 47]. The front and cross sectional views of the burner are shown in Fig. 5.1. As depicted in Fig. 5.1, the burner consists of two concentric annular flow passages, with a ceramic central bluff body to secure flame stabilization [47]. The inner jet has a gap of 5.46 mm and is always operated with a bulk velocity of 8.31 m/s. The Reynolds number based on the hydraulic diameter is 5960. The outer annulus has a 4.70 mm gap, a bulk velocity of 18.7 m/s and Reynolds number of 11540. The burner is designed to operate with swirl as well. In this work, only the cases without swirl are studied and hence details of the swirl are omitted. Both the jets provide flows of premixed CH₄/air mixture. A large annular laminar air co-flow of diameter 19.2 cm and bulk velocity of 0.4 m/s surrounds the fuel/air streams, to secure the lateral boundary condition by preventing environmental air entrainment. Three configurations

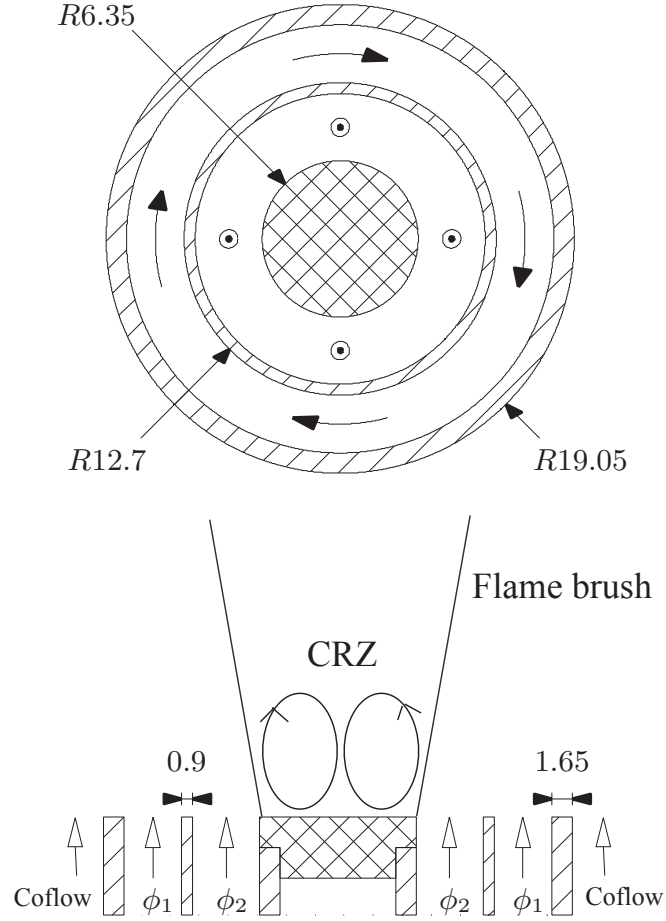


Figure 5.1: Cross sectional view of the burner exit showing the bluff body, the two annular jets and the coflow. Also shown is the approximate location of the flame brush and the central recirculation zone (CRZ).

Case	ϕ_{inner}	ϕ_{outer}	Z_{inner}	Z_{outer}	$\phi_{inner}/\phi_{outer}$
CSWB1	0.75	0.75	0.0423	0.0423	1
CSWB5	1.0	0.5	0.055	0.0291	2
CSWB9	1.125	0.375	0.061	0.021	3

Table 5.1: Table showing the different configurations studied in this work. In all the cases the inner jet velocity $U_{inner} = 8.31$ m/s and outer jet velocity $U_{outer} = 18.7$ m/s.

Jet	U_0	r_1	r_2	α
Inner jet	8.31 m/s	0.00635	0.0118	6.1
Outer jet	18.7 m/s	0.0127	0.0174	6.2

Table 5.2: Table showing the values used for generating the velocity profiles for the inner and outer jet

of the burner were studied, where only the equivalence ratios of the CH₄/air mixture emanating from the jets are changed.

These configurations are summarized in table 5.1. The nomenclature is based on the experimental results published in [47]. For the non-reacting cases, only the velocity measurements (LDA and PIV) are available. For the reacting flow, both scalar and velocity measurements are available. The scalar measurements involve temperature, mixture fraction and species data available at every 10 mm from burner exit up to 80 mm. The experimental data is available online at the Cambridge website¹.

5.2 Numerics and boundary conditions

Computational domain

The cylindrical domain spanning 38 cm in diameter and 46 cm in height is decomposed over an unstructured mesh composed of 50 million tetrahedral elements (8.73 million computational nodes), with a resolution varying between 300 μm and 400 μm in the flame zone. The computational domain, mesh and instantaneous flame location for CSWB1 is shown in Fig. 5.2. A refined mesh simulation involving 400M tetrahedra (71.8 million computational nodes) of the CSWB5 case was also performed by homogeneously refining the coarse mesh homogeneously in all directions. This gives a mesh resolution of the order of 150 to 200 μm in the flame zone.

Boundary conditions

The velocity boundary conditions were the same for all the three test cases. The actual length of the two pipes is around 285 mm upstream of the burner jet. To capture the proper evolution of the flow and turbulence in the pipe 70 mm length of the pipes upstream is simulated. A compromise is made here to reduce the computational cost incurred. A power law profile was specified at the inlet of both the pipes for the axial velocity. The profile follows the equation

$$U(r) = U_0 \left(1 - \frac{r}{0.5(r_2 - r_1)} \right)^{\frac{1}{\alpha}} \quad (5.1)$$

where r_1 and r_2 are the inner and outer radius of the two jets such that $r_1 \leq r \leq r_2$. The values of the parameters used for the profiles are summarized in table 5.2. The radial velocities were

¹<http://www.dspace.cam.ac.uk>

Jet	u'	L_{ref} (m)	U_x	U_y	U_z
Inner jet	0.0831	0.00136525	0.0	0.0	8.31
Outer jet	1.87	0.001175	0.0	0.0	18.7

Table 5.3: Table showing the turbulence injection parameters for Passot-Pouquet spectrum.

initialized as zero. A flat velocity profile was imposed for the co-flow at 0.4 m/s. Homogeneous isotropic turbulence is injected at the inlet of the pipes and the flow is allowed to evolve over the pipe to ensure fully developed flow. The homogeneous isotropic turbulence injection was based on the Passot-Pouquet spectrum [226]. The Passot-Pouquet spectrum requires a length scale for the eddy, a velocity fluctuation (turbulence intensity) and the reference velocity values in three directions. The values used for the two jets are specified in table 5.3. No slip wall boundary conditions are set at the burner lips and the bluff body. The co-flow boundary is defined as a slip wall. Convective outflow boundary condition is used at the domain outlet.

All simulations in this work were carried out using the solver YALES2 which was described earlier in Chapter 3. All the simulations were run for 2 flow through times initially and then statistics accumulated over 3 flow through times based on the inner jet velocity of 8.3 m/s. The non-reactive flow simulations were carried out on the IBM cluster available at CRIHAN, Saint Etienne du Rouvray. A single flow through time simulation (which is approximately 55 ms) takes about 15 hours of CPU time on 128 processors. Most of the reactive flow simulations were performed on the IBM Blue Gene machines (Babel, IDRIS), except for the refined mesh simulation which was performed on the new generation IBM machines (Turing, IDRIS). The coarse mesh reacting flow simulations consumes about 90 hours of CPU time on 2048 processors. This increase in time can be attributed to the time lost in accessing the values from the look up tables and the increased time for solving Poisson equation due to the variable density. On the other hand, the refined mesh simulations takes up 162 CPU hours on 8192 processors for the same simulation. In the refined simulations, considerable time is consumed on loading the mesh on each of the processors in addition to the other factors discussed before.

5.3 Non-reacting flow simulations

For the non-reacting flow simulations a constant density, incompressible formulation was solved using the incompressible solver (ICS) of YALES2. The kinematic viscosity in this case was fixed at $1.517e-5$ m^2/s . The dynamic Smagorinsky model [194, 195] was used to model the turbulent viscosity $\mu_T(\underline{x}, t)$.

Turbulence resolution parameter and mesh quality

To quantify minimum mesh resolution required for a good LES, Pope proposed to have at least 80% of the total kinetic energy to be resolved. To verify the quality of the computations

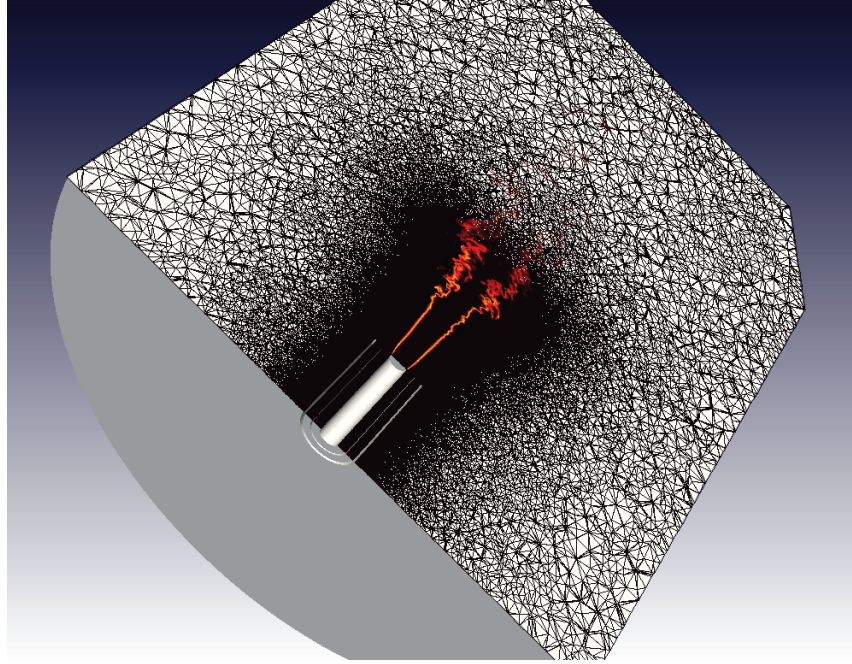


Figure 5.2: Computational domain for the LES of CSWB experiment with the mesh and instantaneous flame location.

performed, the sub-grid kinetic energy can be computed as

$$k_{SGS} = \frac{\nu_T^2}{(C_y \Delta_h)^2} \quad (5.2)$$

where Δ_h is the LES filter size calculated from the computational cell volume as $(\mathcal{V})^{1/3}$ and C_y is considered from the Yoshizawa expression [221] as 0.086.

Based on the SGS kinetic energy, a resolution parameter [227] can be defined as

$$M(\underline{x}, t) = \frac{k_{SGS}(\underline{x}, t)}{K(\underline{x}, t) + k_{SGS}(\underline{x}, t)} \quad (5.3)$$

where K represents the resolved kinetic energy. An LES computation with $M \leq 0.2$ is considered as a good LES according to Pope's criteria. Fig. 5.3 shows that this criteria is almost satisfied in most of the flow locations.

In addition, the ratio of turbulent to molecular viscosity (ν_T/ν) can also be considered as a measure of the mesh resolution since nu_T is directly linked to the SGS kinetic energy. Figure 5.4 shows the ratio ν_T/ν indicating high values in the shear layer depicting a higher SGS kinetic energy whereas the ratio is smaller in the potential core of the jets. In general, the smaller the value of ν_T/ν , the better the resolution of the LES.

Non-reacting flow statistics

Non-reacting flow measurements are available for the CSWB1 case. It should be noted that the velocity boundary conditions are the same for all the three cases and only the mixture fraction

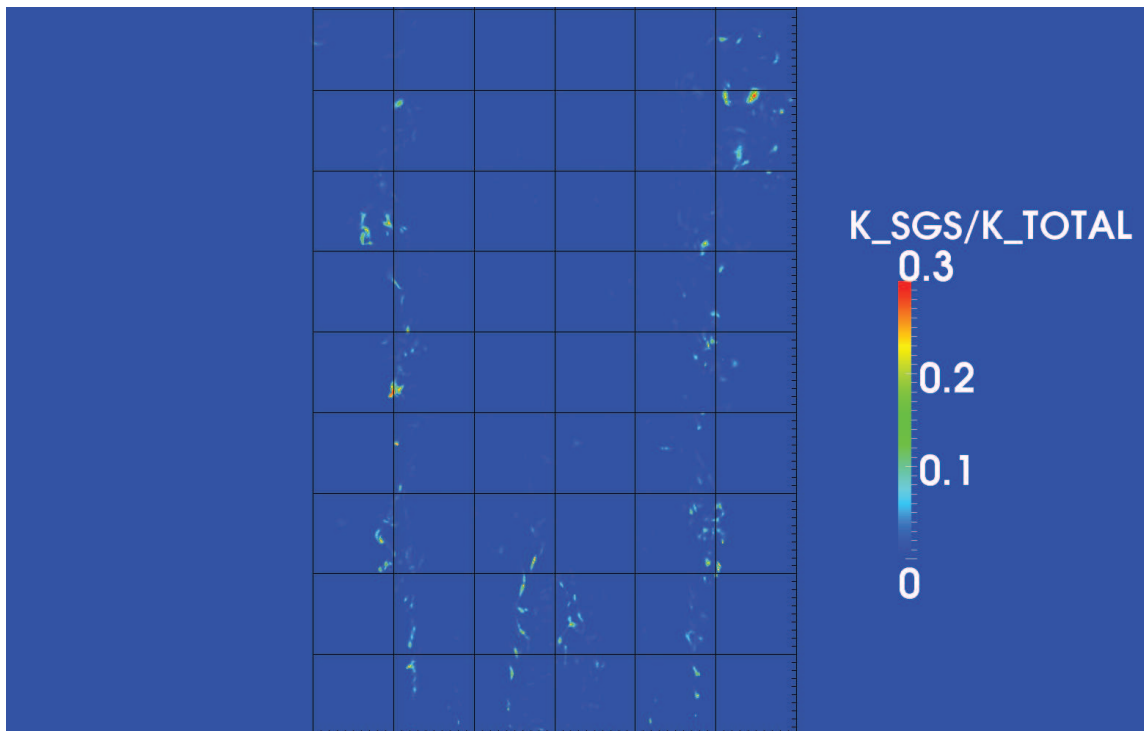


Figure 5.3: Instantaneous snapshot of the ratio of subgrid kinetic energy to the total kinetic energy. Every major grid line in the figure corresponds to 10 mm.

boundary conditions are different. The non-reacting LES velocity statistics are compared with the LDA measurements. Comparison of the Reynolds averaged axial and radial velocity profiles, and their fluctuations are shown in Fig. 5.6. Reasonable agreement was obtained between the experiment and the simulations. A certain extent of asymmetry was observed in the mean velocity fields (Fig. 5.7) as well as in the mean LDA profiles of the experiment. This effect was found to be much more enhanced in the reacting flow. Therefore, while comparing the statistical results with the experiments, a single plane profile of the average velocities are also shown. This plane was chosen based on the closeness to the experimental results from the reactive flow simulations and is fixed for all the results reported. The relative position of the chosen plane with respect to the reference X-axis used in the simulation is shown in Fig. 5.5. The difference between the azimuthally averaged profiles and the single plane profile is also an indication of the difficulty incurred in comparing experiments and LES solely based on 1D profiles. Axial and radial velocity fluctuations is under estimated for the outer jet close to the burner exit but attains good agreement later on. This possibly arises from the artificial turbulence injection at the inlet and the shorter length of the pipe (70 mm), used for the simulation in comparison to the actual length of the pipes in the experiment (280 mm) leading to the lack of proper prediction of the shear induced instabilities between the outer jet and the coflow.

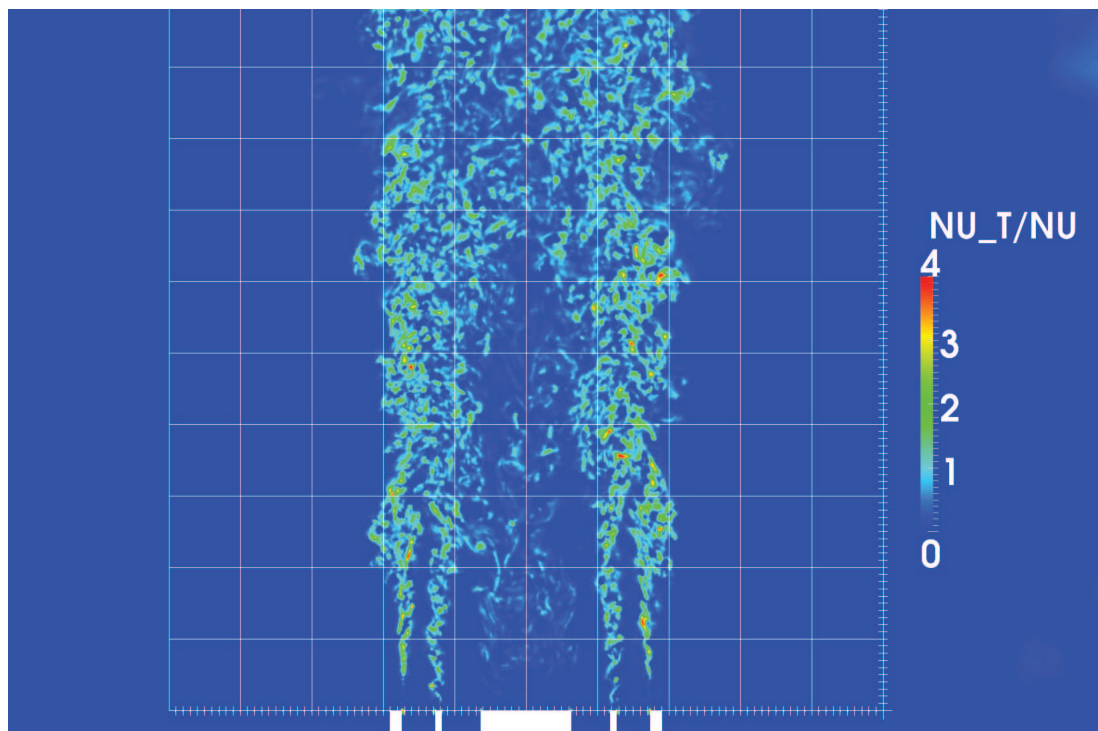


Figure 5.4: Instantaneous snapshot of the ratio of turbulent viscosity to molecular viscosity. Every major grid line in the figure corresponds to 10 mm.

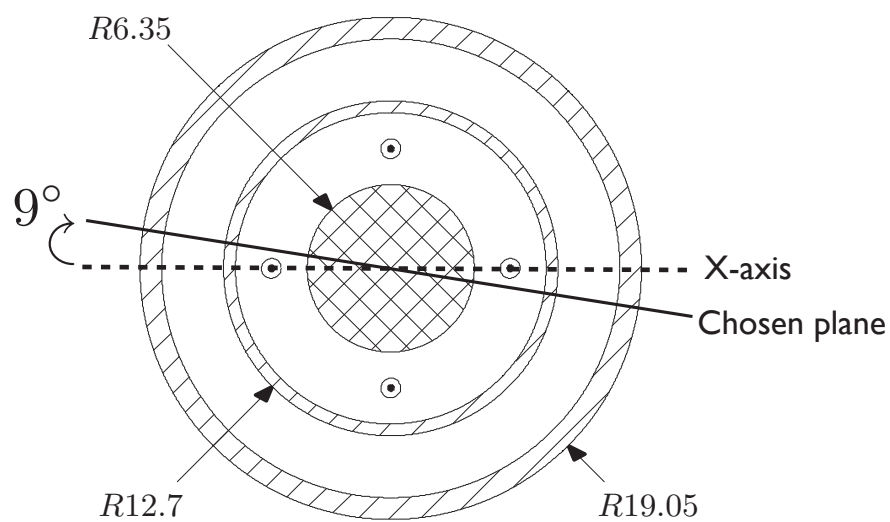


Figure 5.5: Relative orientation of the plane used for comparison to the reference X-axis used in the simulation.

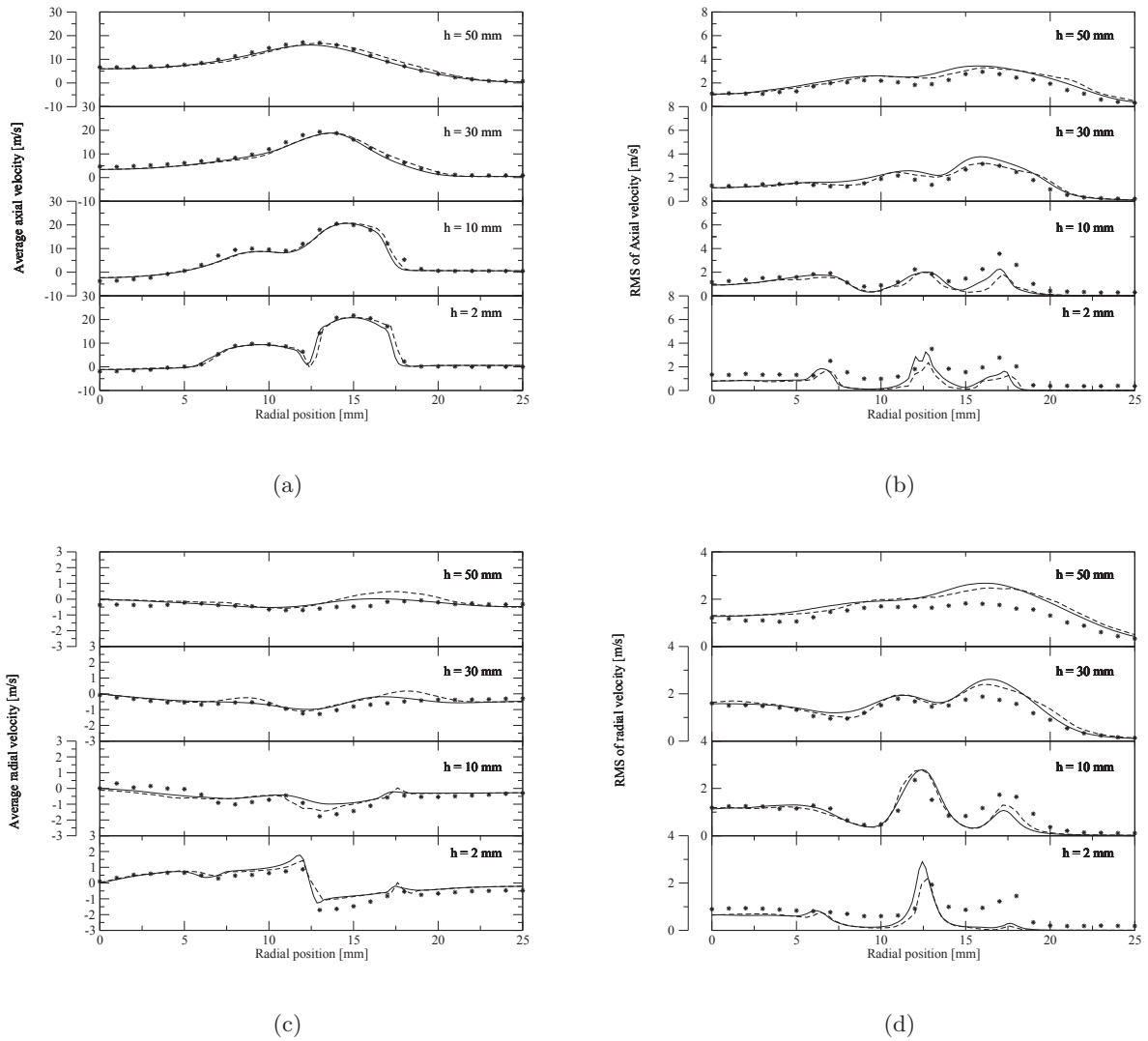


Figure 5.6: Velocity statistics for non-reacting flow, radial profiles. (a)-(b): Axial component. (c)-(d): Radial. (a)-(c): Mean value. (b)-(d): RMS. Symbols: LDA measurements. LES: — azimuthal averaging, - - - single plane.

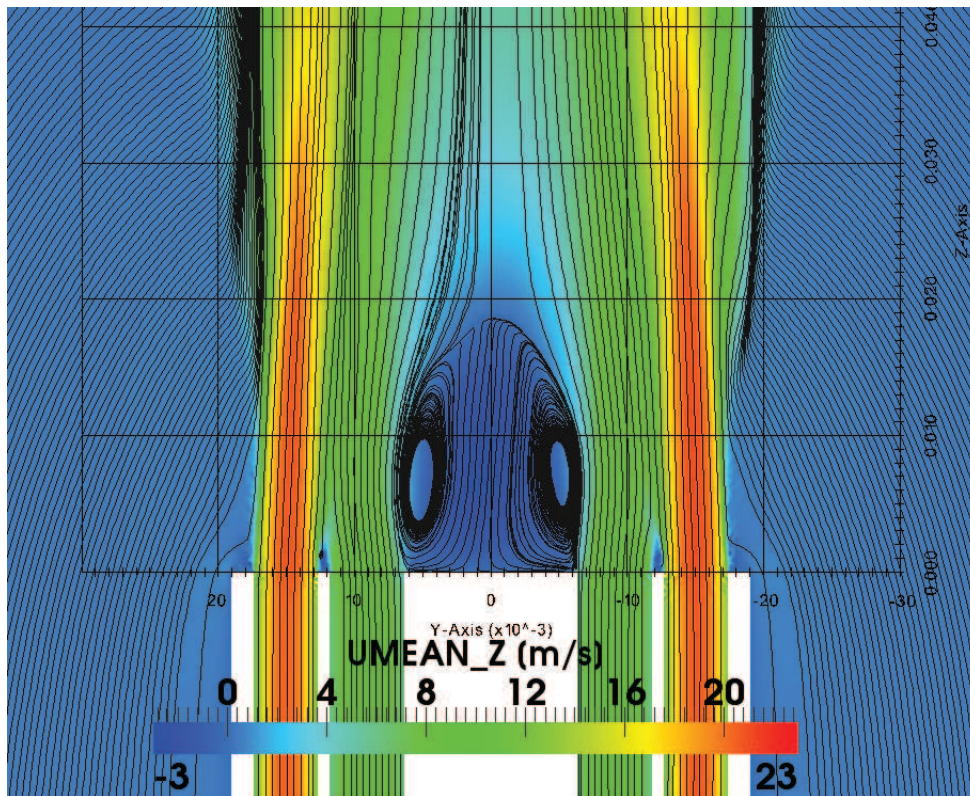


Figure 5.7: Streamlines superimposed on the mean axial velocity field depicting the recirculation zone and the jets.

Mixture fraction fields

The mixing fields of the three configurations studied in this work are shown in Fig. 5.8. The first case (CSWB1) is a completely premixed configuration where both the jets operate with an equivalence ratio of 0.75. In the CSWB5 configuration, the inner jet operates with a stoichiometric mixture while the outer jet supplies a lean mixture at an equivalence ratio of 0.5. On the other hand, the CSWB9 configuration has a rich mixture exiting at an equivalence ratio of 1.125 from the inner jet and a very lean mixture of equivalence ratio 0.375 from the outer jet. The outer jet operating equivalence ratio in CSWB9 is 0.375 which is below the lean flammability limit of methane-air mixture equal to 0.47 reported in literature [228].

5.4 Conclusions

In this chapter, the geometry of the Cambridge burner configuration studied in this work was presented in the beginning. The computational details, the mesh, boundary and initial conditions were described subsequently. The non-reacting flow results for all the three cases studied were presented and discussed by plotting the velocity statistics and mixture fraction fields.

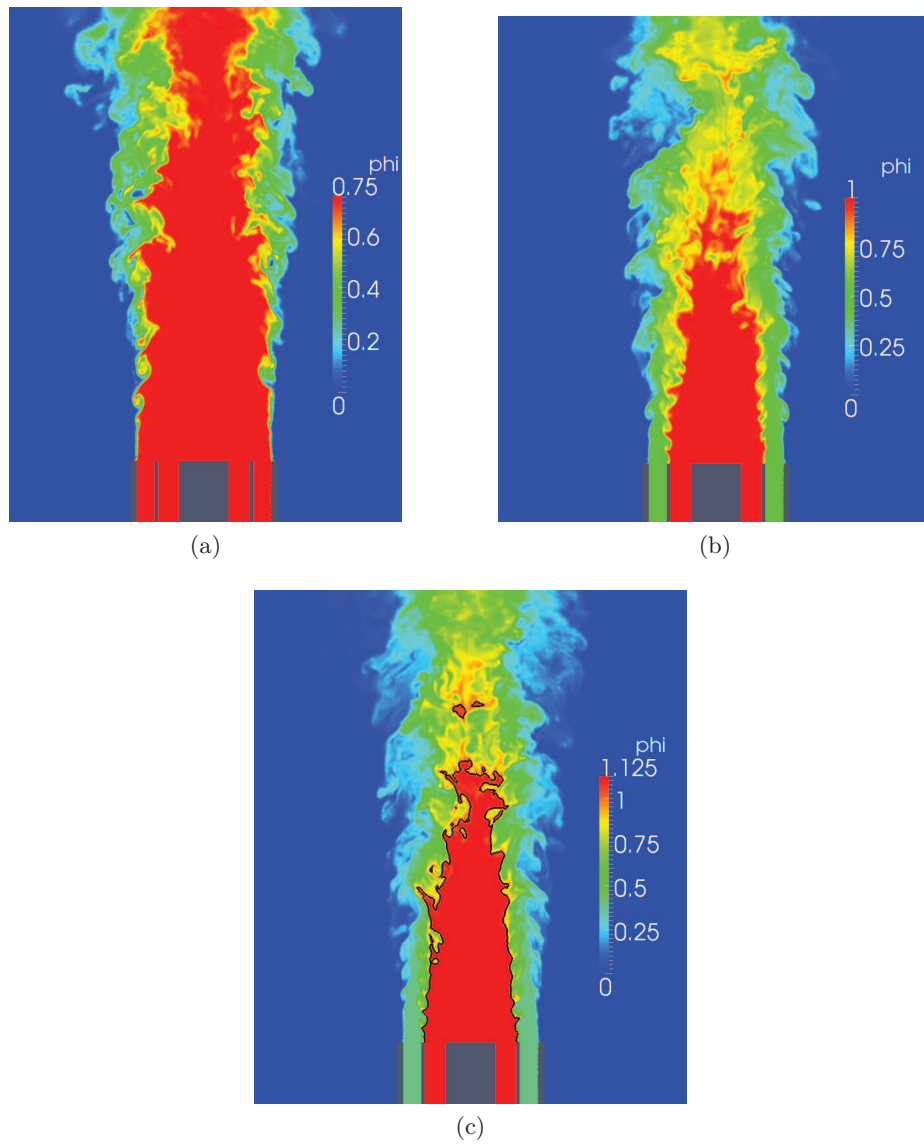


Figure 5.8: Instantaneous equivalence ratio fields of the three configurations studied represented with the equivalence ratio distribution. (a) CSWB1 (b) CSWB5 (c) CSWB9. The bold line in (c) is the stoichiometric equivalence ratio contour.

Reacting flow simulations: Premixed Configuration

CSWB1 6

Contents

6.1 Simulations of CSWB1 with the PCM-FPI model	79
Modeling parameters and test cases	79
Results and discussions	81
Conclusions	83
6.2 Simulations of CSWB1 with the FLF-PDF model	84
Results and flow analysis	86
Summary and conclusions	95

In this chapter, large eddy simulation of the fully premixed configuration CSWB1 of the Cambridge burner is discussed. In the first section, simulation with the PCM-FPI model and different scalar dissipation rate closures are presented. In the second section, the simulation of the CSWB1 using the FLF-PDF model is given with discussions on velocity and scalar statistics.

The reacting flow simulations are performed starting from an established non-reacting flow solution. Combustion is initiated by putting a pocket of burnt gas in the recirculation zone. This burnt gas mixes continuously with the fresh gas and continues the combustion process. After a few flow through times a flame is stabilized around the central tube.

6.1 Simulations of CSWB1 with the PCM-FPI model

In this section, the simulations of the CSWB1 configuration with the PCM-FPI model using different strategies for scalar dissipation rate closure are discussed.

Modeling parameters and test cases

The basic concepts behind the PCM-FPI model were described earlier (§ 2.2). To simulate the CSWB1 configuration using PCM-FPI model, the four balance equations (Eqs. 4.6 - 4.9) are solved. A filtered chemical table consisting of 70 x 21 x 50 x 21 points in $(\tilde{c}, S_c, \tilde{Z}, S_Z)$ directions

respectively was used. To generate the filtered lookup table, a Beta-PDF was presumed for both the mixture fraction and the normalized progress variable. The progress variable definition $Y_c = Y_{CO} + Y_{CO_2}$ is retained for all the cases.

As described earlier, the scalar dissipation rate closure forms the modeling bottleneck for the PCM-FPI approach. The filtered scalar dissipation rate is split into an LES resolved dissipation rate term and a subgrid contribution (see Eq. 4.21) which requires to be modeled.

Three different strategies were tested in this work to close the SGS dissipation rate of the progress variable. These three strategies are

1. Linear relaxation

$$\chi_{SGS}^{Lin} = C_D 2\bar{\rho} \frac{D_T Y_{c_v}}{\Delta_h^2}; \quad C_D = 1.0 \quad (6.1)$$

2. Hybrid SGS dissipation

$$\chi_{SGS}^{Hyb} = (1 - S_c) C_D 2\bar{\rho} \frac{D_T Y_{c_v}}{\Delta_h^2} + S_c (-2\bar{\rho} D_{Y_c} |\nabla \widetilde{Y_c}| + 2\overline{\rho Y_c \omega_{Y_c}} - \overline{Y_c^{Eq} \rho \omega_{Y_c}}); \quad C_D = 1.0 \quad (6.2)$$

3. Modified linear relaxation

$$\chi_{SGS}^{Lin+} = C_D 2\bar{\rho} \frac{(D_{Y_c} + D_T) Y_{c_v}}{\Delta_h^2}; \quad C_D = 0.085 \quad (6.3)$$

These strategies are adopted usually for the PDF methods, both transported and presumed. Studies on partially premixed and non-premixed combustion involving these closures are available in literature [216, 229–231].

The sub-grid scalar dissipation rate closures discussed above has two characteristic parameters namely, the constant C_D and the turbulent diffusivity D_T . The turbulent diffusivity of the scalar is normally defined as $D_T = \nu_T / Sc_T$, a ratio of the turbulent viscosity, ν_T and a turbulent Schmidt number Sc_T . The turbulent viscosity comes from a SGS turbulent viscosity model such as the Smagorinsky or the WALE model. However, the choice of the turbulent Schmidt number is more or less uncertain, with values ranging from 0.4 to 1.0 found in literature as observed by Kemenov and Pope [231]. A dynamic closure can also be considered for the turbulent Schmidt number following the lines of scale similarity. The constant C_D on the other hand is normally retained as unity even though a dynamic model can be imagined as seen in [216]. Certain authors [232, 233] tried to calibrate the model constant to match the experimental scalar dissipation rate on an average sense. To summarize, there is a certain level of uncertainty involved in the choice of C_D and Sc_T .

In the following paragraphs, the simulations of the CSWB1 case performed using the three closures are discussed. The turbulent Schmidt number for all the scalars was fixed as 0.9 in these simulations. The constant C_D used in each of the cases are shown along with the equations. The reason behind the choice of $C_D = 0.085$ will be discussed in the coming paragraphs. The D_{Y_c} in this case was defined as ν / Sc where a value of $Sc = 0.72$ was used for all the scalars.

Re-laminarisation effects

An analysis of the instantaneous axial velocity fields for the reacting and non-reacting cases revealed significant re-laminarisation effects for all the three closures discussed. Fig. 6.1 shows the comparison of instantaneous axial velocity fields of the non-reacting and the reacting cases for the CSWB1 configuration. As discussed previously in Chapter 2 (§ 2.1), bluff body flows show significant relaminarisation effects which are observed in this case as well. Evidently, the central recirculation zone of the reacting flow is laminarised in comparison to the non-reacting flow which can be attributed to an increased viscosity and thermal dilatation effects.

Consequently, the turbulent viscosity coming from the SGS models also tend to zero. In Fig. 6.2, a snapshot of the ratio of turbulent viscosity to the molecular viscosity in the flame zone is given. Clearly, close to the burner exit the turbulent viscosity values can be observed to be close to zero. It means that the flow is more or less laminar close to the burner exit and is resolved on the LES mesh. However, the flame remains unresolved since the typical flame thickness is much smaller than the LES mesh. In other words, the LES combustion model has to solve for a laminar flame propagation on a coarse mesh close to the burner, but capture wrinkling effects downstream.

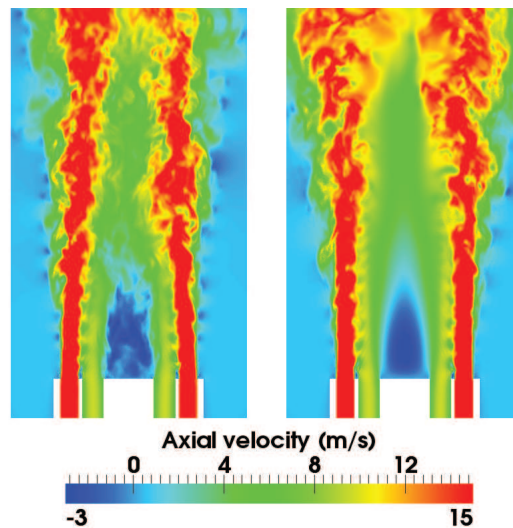


Figure 6.1: Instantaneous velocity fields of the non-reacting (left) and reacting (right) flow cases.

Results and discussions

The time averaged statistics of the velocity, temperature and mixture fraction statistics are compared to the experiments. Since the objective of this section is to project the impact of the different scalar dissipation rate closures, the results of the differential diffusion modeling of mixture fraction and the impact of flow and scalar asymmetry are omitted. Therefore, only the azimuthally averaged results are presented for comparing the different models.

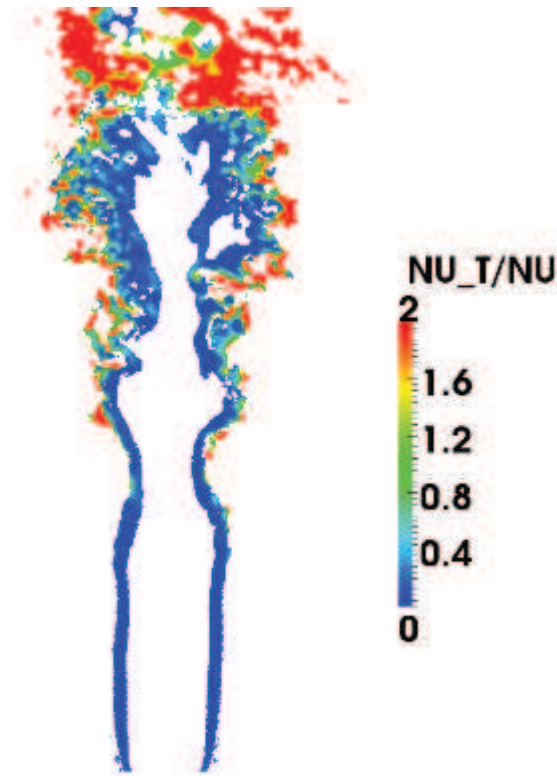


Figure 6.2: Ratio of turbulent viscosity to the molecular viscosity in the flame zone

Fig. 6.3 shows the average axial and radial velocity statistics compared to the experiments. On a whole, a fair agreement can be seen between the linear relaxation model (black) and the modified linear relaxation model (blue) whereas the hybrid model (red) tends to predict higher velocities and fluctuations at downstream locations.

Looking at the scalar statistics of temperature (Fig. 6.4), obvious deviation between the models can be seen. Clearly, the simple linear relaxation model (black) predicts a lower laminar flame speed close to the burner exit up to 30 mm where the re-laminarisation effects discussed previously is significant while the hybrid model (red) over predicts the flame speed resulting in a wider opening. The modified relaxation model (blue) was built with a constant $C_D = 0.085$ so as to yield a progress variable variance predicting the proper flame speed on the given mesh. As a result of the specific choice of the constant, a very close agreement is seen with the experiments both in average and fluctuations.

The mixture fraction statistics (Fig. 6.5) results show almost the same predictive capabilities for both the linear relaxation models but is far off for the hybrid model. This is expected from the observations made in the velocity field statistics.

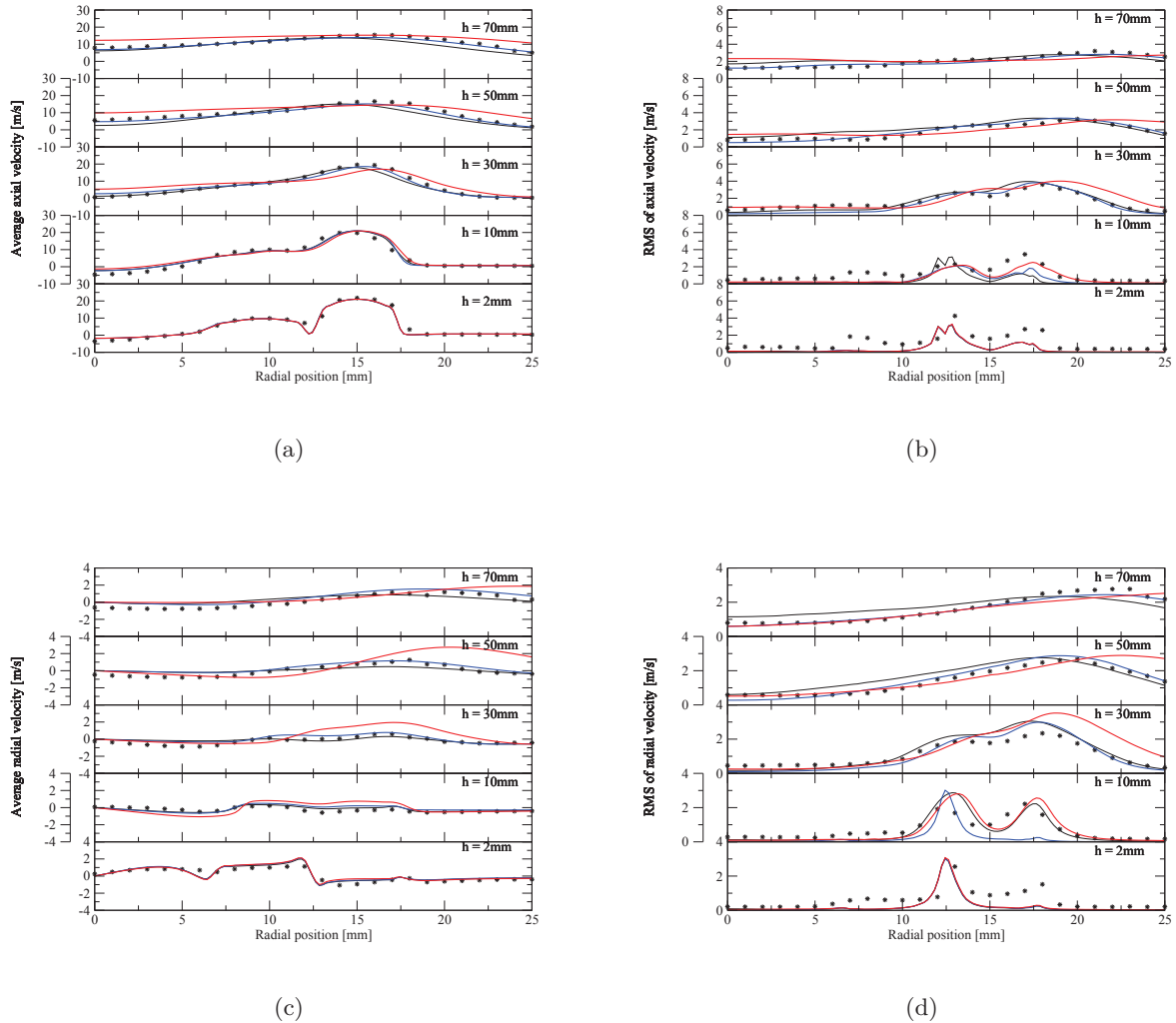


Figure 6.3: Reynolds averaged statistics (a) Radial profiles of average axial velocity. (b) Radial profiles of axial velocity fluctuations. (c) Radial profiles of average radial velocity (d) Radial profiles of radial velocity fluctuations. Symbol: LDA Measurements. Black line: Linear relaxation model. Red line: Hybrid model. Blue: Modified linear relaxation model

Conclusions

The main conclusions of the simulation with the PCM-FPI model is that the scalar dissipation rate modeling of progress variable has a strong impact on the flame evolution. The normal scalar dissipation rate closures based on linear relaxation hypothesis and the hybrid variant may have to be adapted for the given LES mesh and the experiment being simulated. This adaptation in the form of the constant or the Schmidt number was demonstrated to improve the predictive capabilities here. However, a more robust approach is desired which will conserve the flame

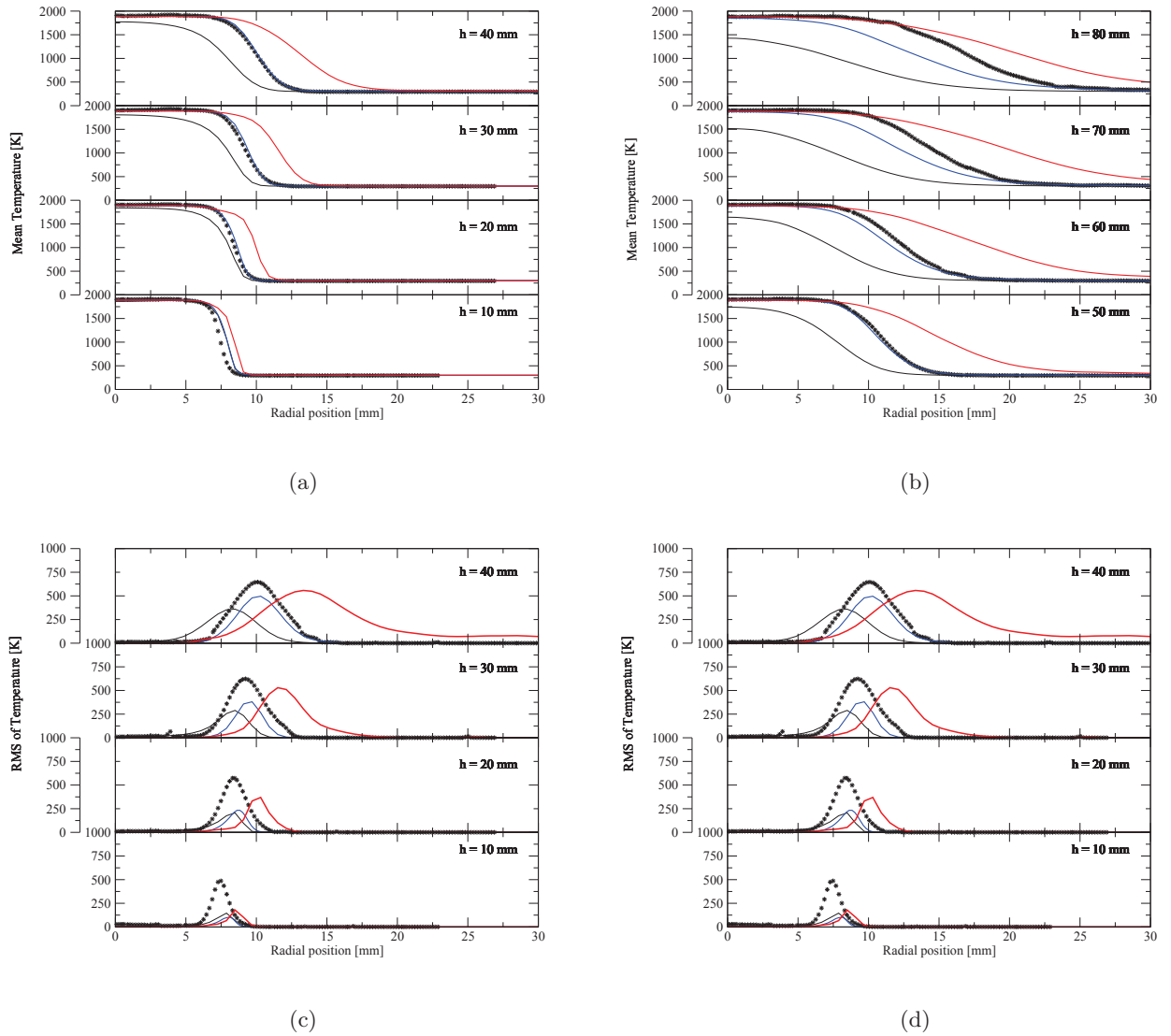


Figure 6.4: (a) & (b) Radial profiles of average temperature. (c) & (d) Radial profiles of temperature fluctuations. Symbol: Measurements. Black line: Linear relaxation model. Red line: Hybrid model. Blue: Modified linear relaxation model

invariants (the flame speed and the internal structure) on a coarse mesh. This forms the main motivation for using a switching model combined with the FLF-PDF introduced in Chapter 4.

6.2 Simulations of CSWB1 with the FLF-PDF model

In this section, simulation of the CSWB1 configuration using the FLF-PDF model is discussed. The importance of differential diffusion modeling is projected and eventually used to calculate a global differential diffusion number for the burner studied. The computational domain and the

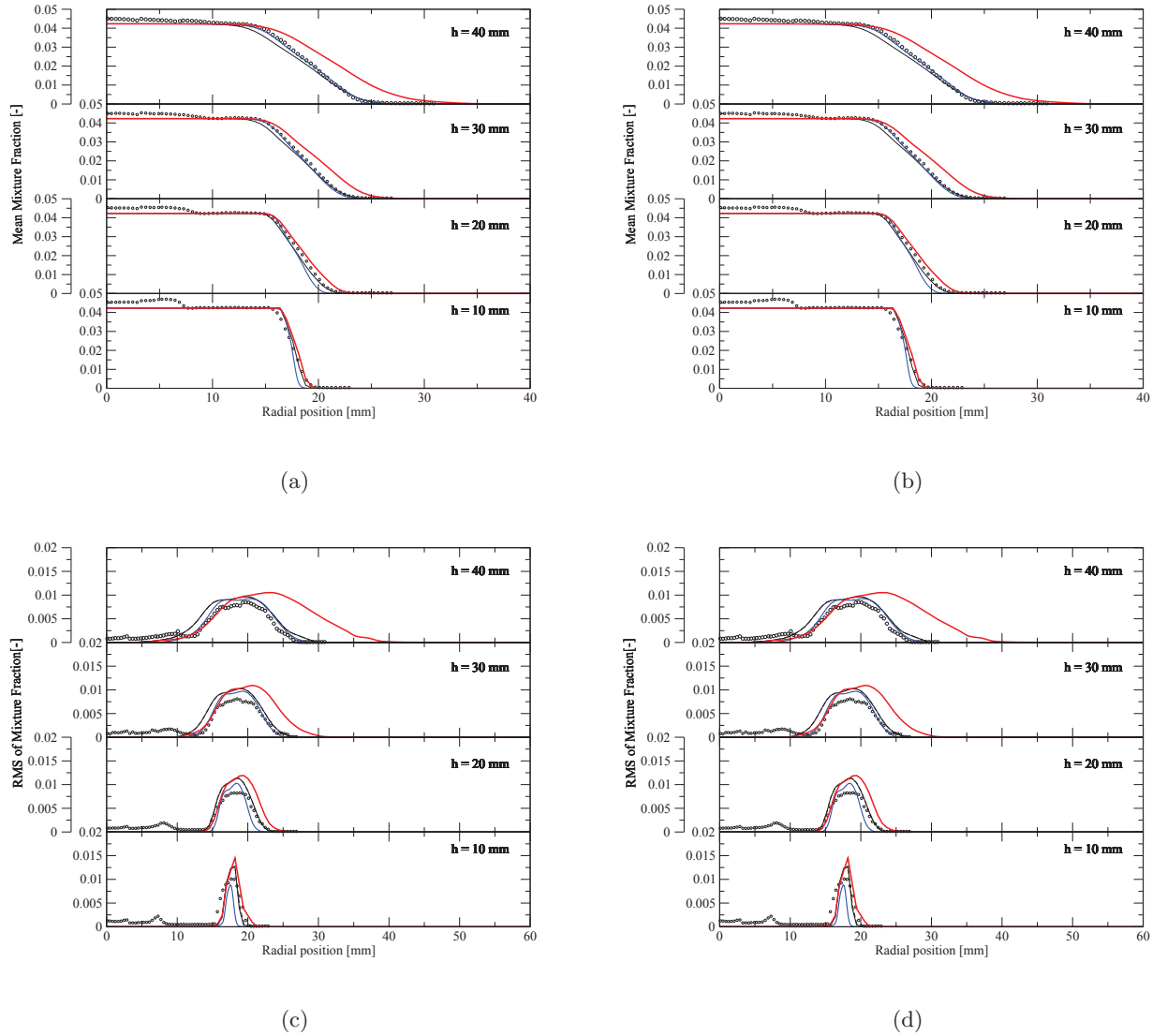


Figure 6.5: (a) & (b) Radial profiles of average mixture fraction. (c) & (d) Radial profiles of mixture fraction fluctuations. Symbol: Measurements. Black line: Linear relaxation model. Red line: Hybrid model. Blue: Modified linear relaxation model

mesh (described in 5.2) are the same as those used for simulations with the PCM-FPI model discussed earlier. When the flame wrinkling is resolved ($\mathcal{F} < 1$), the proposed model requires an explicit flame filter width, Δ which is fixed as 2 mm. The choice of this value is based on the fact that the lowest mesh resolution in the flame zone is around $400 \mu\text{m}$ which requires a flame filter width five times larger than it to have around 4-5 points within the flame.

As previously discussed, annular bluff body flows are known to show asymmetric behaviour, even in the mean flow [234, 235]. This was also observed in the LDA and PIV experimental database of this burner. Similarly, the scalar fields are also asymmetric in their average distri-

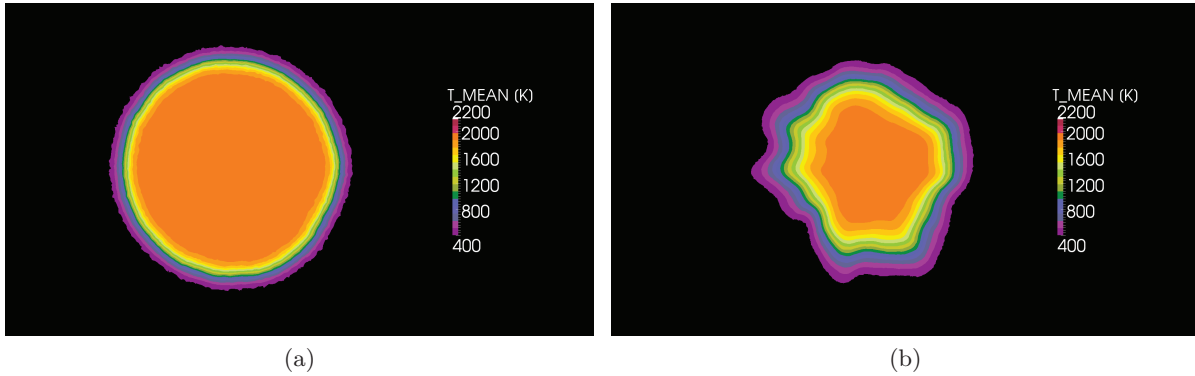


Figure 6.6: Spanwise averaged temperature distribution. (a): $x = 10$ mm. (b): $x = 50$ mm.

bution, especially at downstream locations. Figure 6.6 shows the time averaged temperature field at 10 mm and 50 mm from the burner exit. Clearly a loss of symmetry is seen at 50 mm, which renders it difficult to compare LES statistics against experiments, due to the lack of a fully homogeneous azimuthal direction. A preferential orientation of the re-circulation zone described in [234, 235] can also be seen in the reacting case shown in Fig. 6.7. This loss of symmetry might also be related to very low frequency structures present in the system which would require very long times of simulation rendering it computationally very expensive. Also, the asymmetry associated to the mesh itself which could play a role in the generation of asymmetry in solution. In this thesis work, to make the comparison between the LES and experimental results, after building statistics of 3D-fields by time averaging, results are shown for both azimuthal averaging and a given plane (see Fig. 5.5) that is retained the same for all the plots, whatever the stream-wise position. The choice of this plane has negligible effect close to the burner, but it impacts slightly on the comparison when traveling further downstream; nevertheless, results shown in this manner again illustrates the difficulty of comparing only 1D-profiles in flows featuring some asymmetric behaviour.

Results and flow analysis

In comparison to the non-reactive flow, the reactive flow field was found to be less turbulent even for the simulations with FLF-PDF model. As depicted by the instantaneous axial velocity fields in Fig. 6.1. Figure 6.8a displays the instantaneous source term of progress variable colored by \mathcal{F} (Eq (4.22)), the subgrid wrinkling factor. At locations close to the burner exit, \mathcal{F} is less than unity indicating that the flow and subgrid flame wrinkling are actually resolved. At downstream locations, where the turbulent shear layer interacts with the flame, the subgrid flame wrinkling is not resolved on the LES mesh ($\mathcal{F} > 1$). As confirmed by the PDF of \mathcal{F} and its cumulative function computed at a given instant in time (Fig. 6.8b), 50% of burning locations feature a resolved wrinkling, whereas the remaining part needs SGS dissipation rate information. As

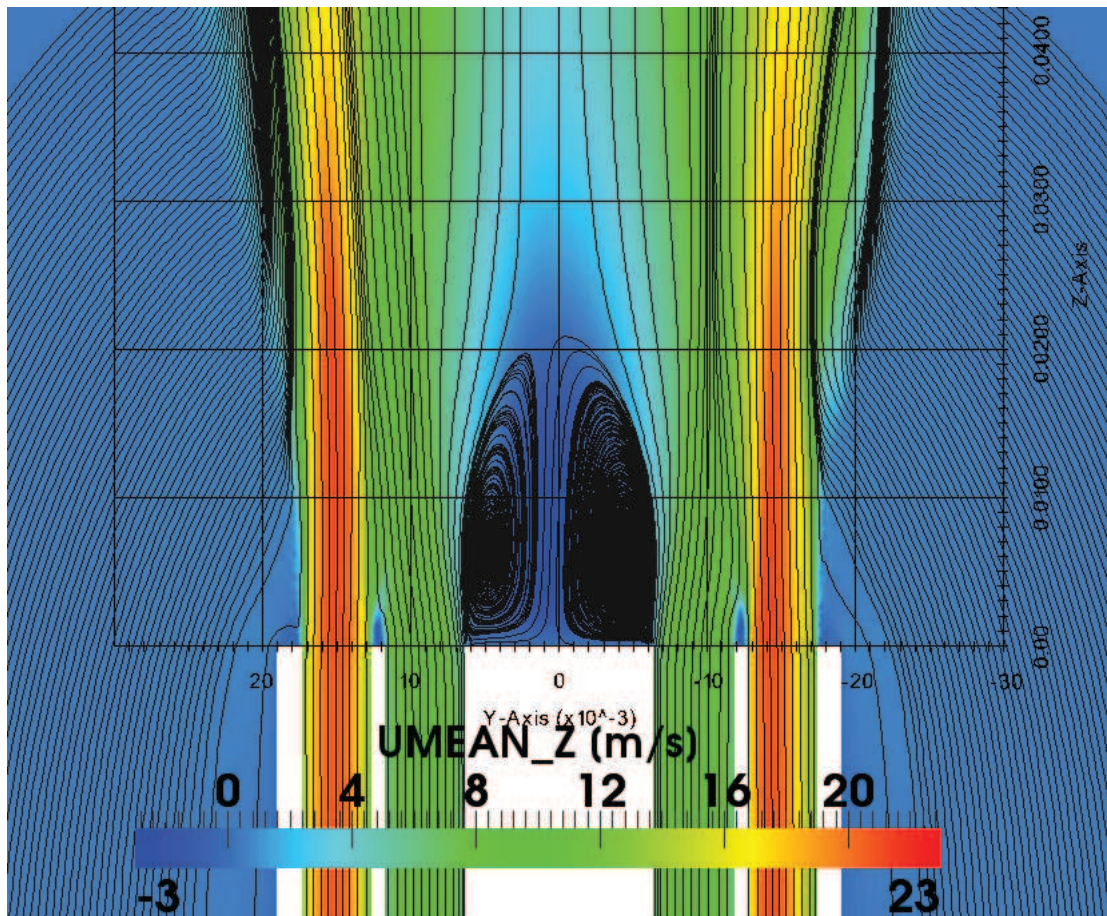


Figure 6.7: Streamlines superimposed on the mean velocity field of the CSWB1 configuration depicting the recirculation zone and the jets.

discussed above (§ 4.1), the modeling dynamically accounts for this change in the combustion LES regime, by using two different definitions of S_c , the unmixedness.

In the burning case, averaged axial and radial velocities (Fig. 6.9) are found to be in good agreement with the LDA data. Close to the jet exit, the fluctuations in the shear layer of the outer jet and the co-flow are slightly smaller relative to the experimental data, but follows the experimental trend at downstream locations, similar to the observations in the cold flow case. The temperature statistics (Fig. 6.10) are well predicted up to 50 mm from the burner exit by both the azimuthally averaged data and the single plane one. Above this height, there is dilution of the fuel air mixture by the co-flow air, which in turn is controlled by the instabilities arising from jet shear layers. Beyond 50 mm, the single plane data is found to have good agreement with the measurements. To visualize the impact of the procedure used to determine the unmixedness, the same simulation was performed forcing $\mathcal{F} > 1$, therefore imposing a modeling based on a usual SGS variance closure. The results are shown in Fig. 6.11, the flame spreading is underpredicted along with the temperature fluctuations, the filtered flame thickness

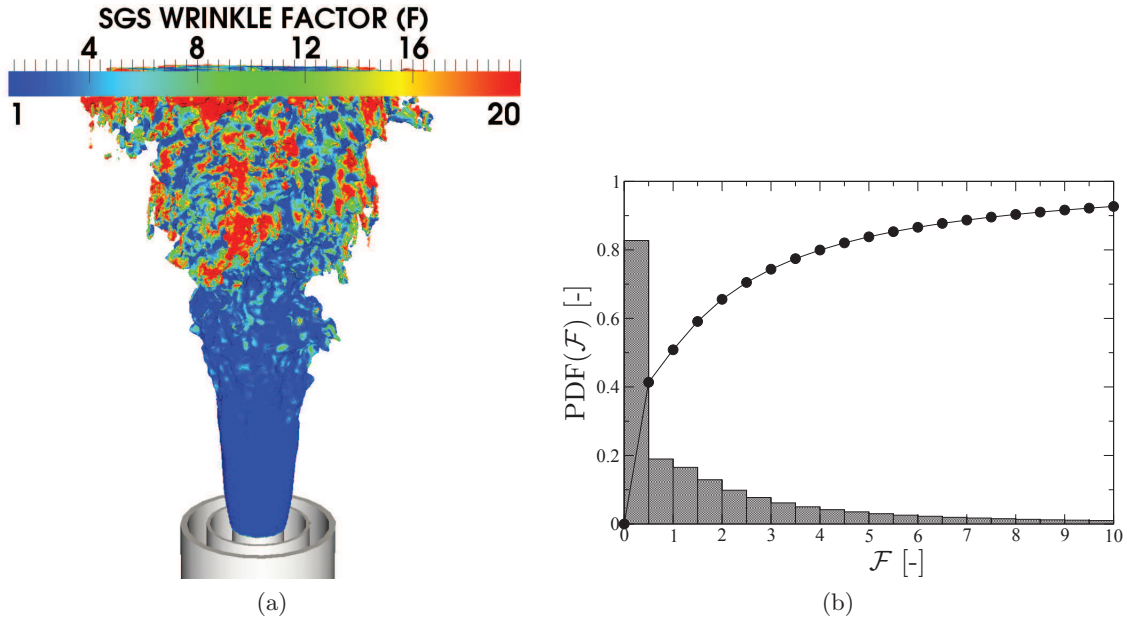


Figure 6.8: (a): Instantaneous source term colored by \mathcal{F} (Eq (4.22)). (b): PDF of \mathcal{F} computed over the mesh.

being in fact overestimated in these simulations. Back to the FLF-PDF modeling (*i.e.* \mathcal{F} set free), looking at the mean profiles of CH_4 (Fig. 6.12) a trend similar to the temperature statistics are seen. The fluctuation profiles for the temperature and CH_4 mass fraction is found to be under predicted in the flame zone close to the burner exit. In a refined mesh simulation of the same burner, but for a stratified configuration analyzed in a companion paper, the fluctuations were properly recovered, suggesting that some SGS fluctuations may need to be added when comparing with experiments for the resolution considered in this paper.

While looking at the mixture fraction profiles with the differential diffusion effect modeled as a source term, the mixture fraction variations are correctly captured with respect to the experiment. The accumulation of mixture fraction in the recirculation zone due to the differential diffusion effect is well reproduced by Z_d (Eq. (4.25)), as observed in Fig. 6.13. Comparison of the statistics of mixture fraction with experimental profiles are also given in Fig. 6.14, where the bold line shows Z_d and the dotted line shows the passive mixture fraction, Z . The graphs confirms that Z_d evolves correctly and compares well to the experiment, while the standard mixture fraction misses carbon accumulation within the recirculation zone. In the shear layer where the outer jet interacts with the coflow, there is no flame and hence no differential diffusion. In this zone both Z_d and Z evolve identically.

To better understand the differential diffusion phenomena, Eq. (4.33) providing an estimation of flow residence time was also solved and the result is shown in Fig. 6.15. As expected, there is a high residence time in the central recirculation zone and a lower one in the jet stream. Comparing Figs 6.13 and 6.15 it can be seen that the accumulation of mixture fraction correlates well with

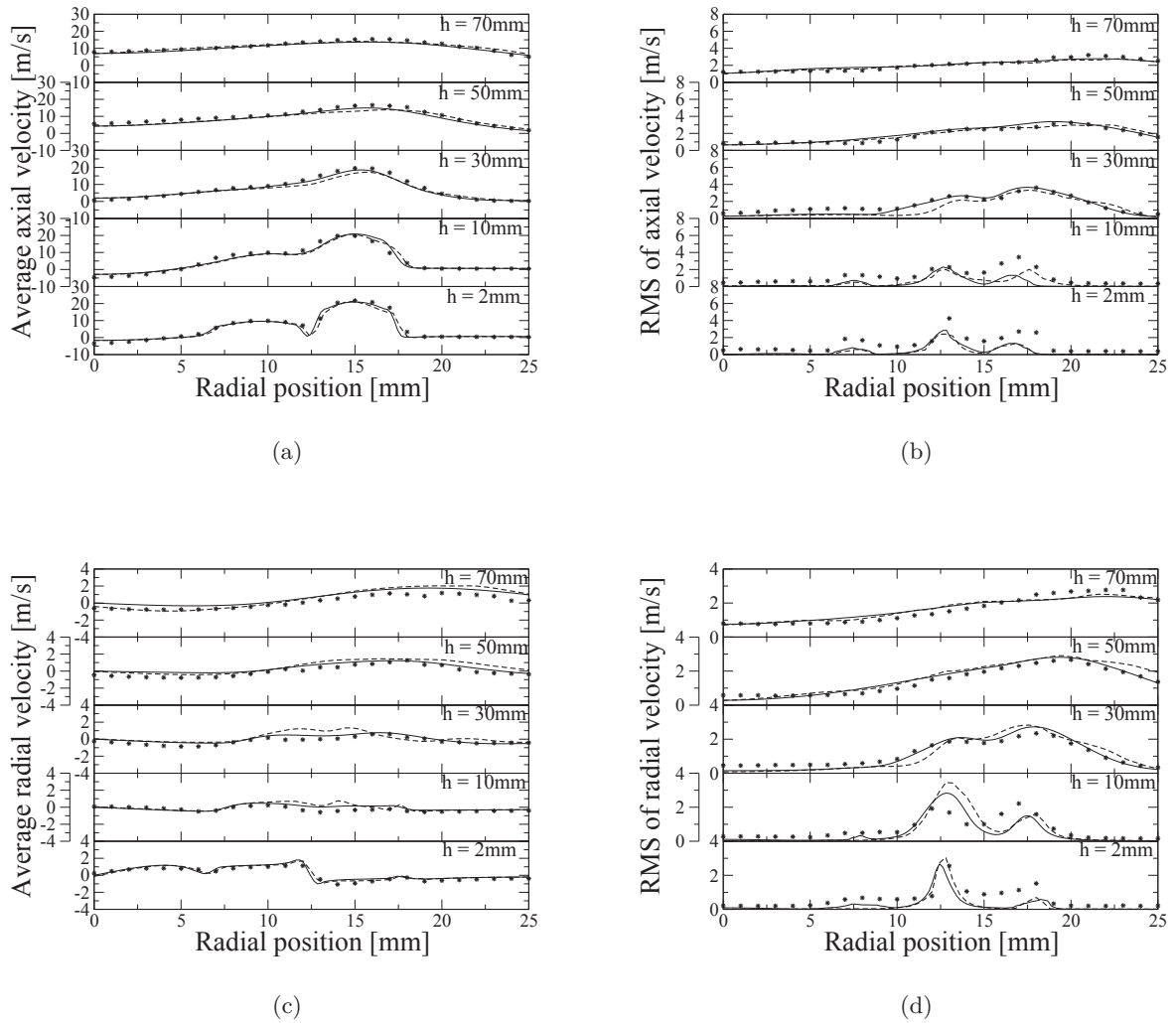
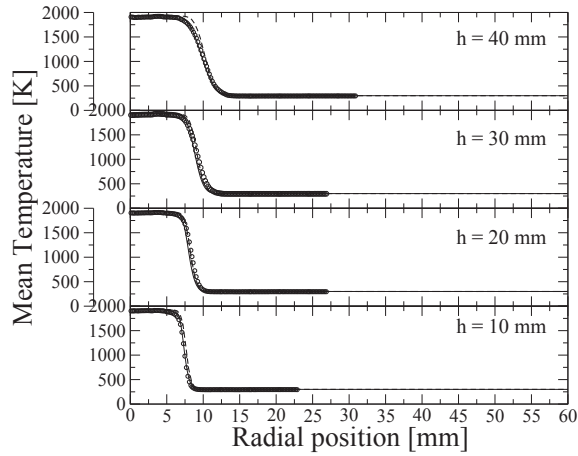
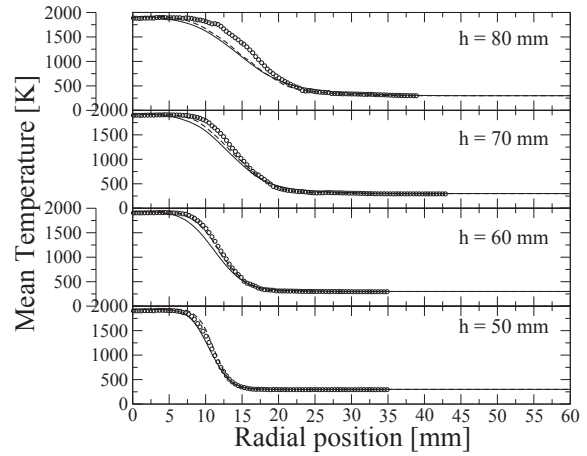


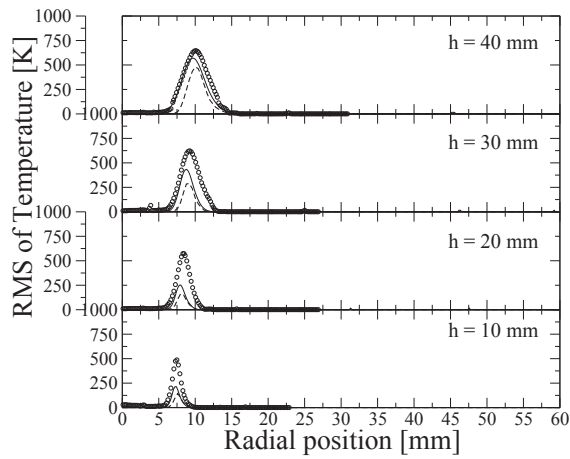
Figure 6.9: Velocity statistics with flames, radial profiles. (a)-(b): Axial component. (c)-(d): Radial. (a)-(c): Mean value. (b)-(d): RMS. Symbols: LDA. LES: — azimuthal averaging, - - - single plane.



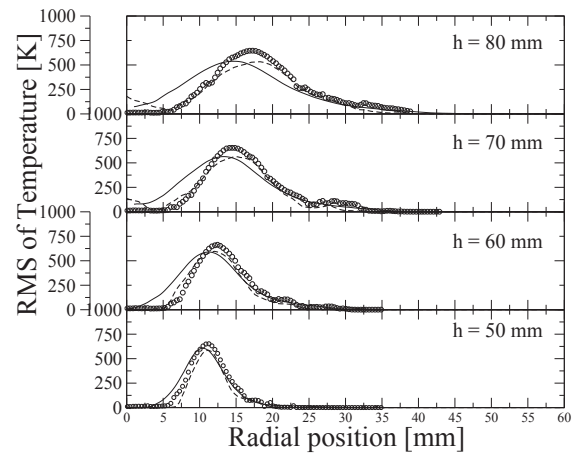
(a)



(b)



(c)



(d)

Figure 6.10: Temperature statistics, radial profiles. (a)-(b): Mean value. (c)-(d): RMS. Symbols: Experiment. LES: — azimuthal averaging, - - - single plane.

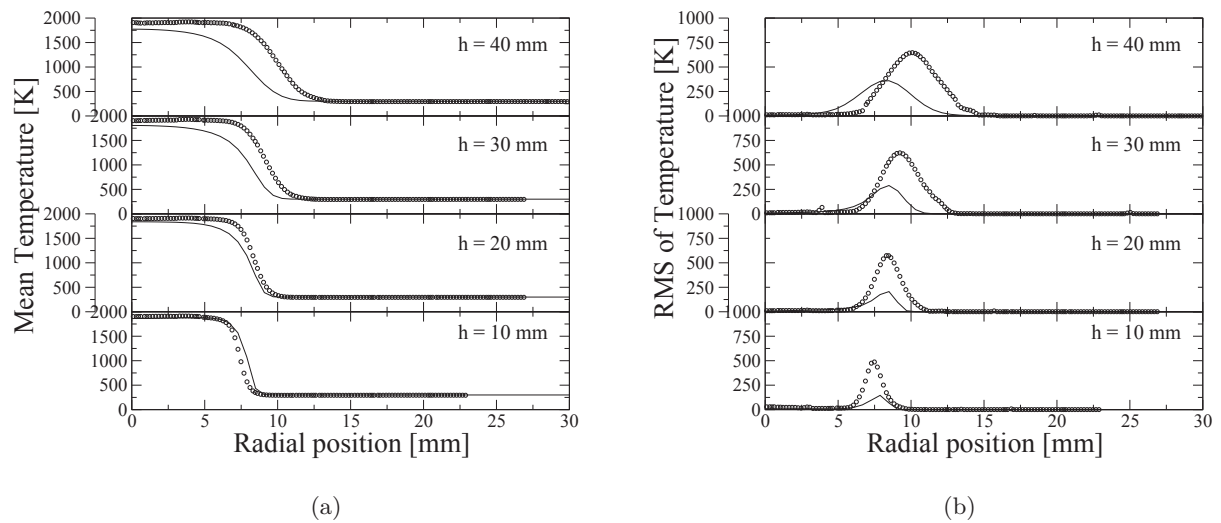
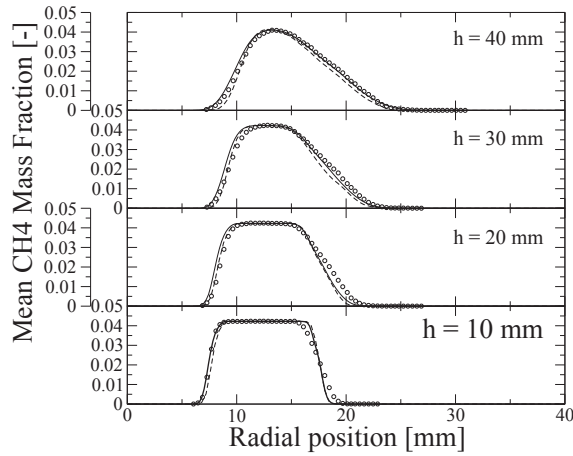


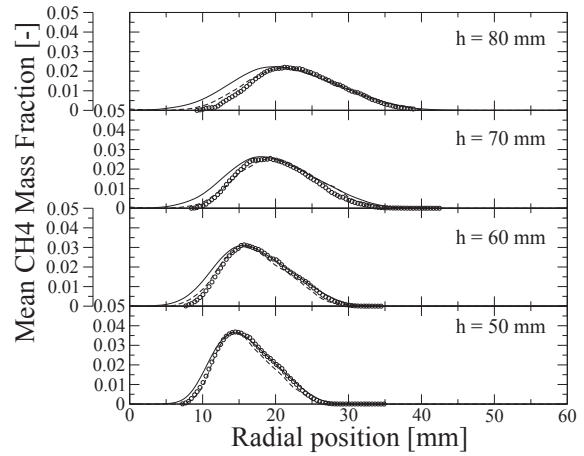
Figure 6.11: Temperature statistics forcing $\mathcal{F} > 1$, radial profiles. (a): Mean value. (b): RMS. Symbols: Experiment. LES: — Azimuthal averaging.

the higher residence time. In other words, the increase in equivalence ratio due to the differential diffusion effect is seen in the zone where the difference in residence time on either sides of the flame brush is high. From the simulations, the maximum value of the mean residence time in fresh gas is obtained as $\tau_f = 0.002$ s and the maximum value of the mean residence time in burnt gas, $\tau_b = 0.018$ s. The averaged contribution of the source term, $\langle \dot{\omega}_Z \rangle = \tau_Z^{-1}$ is obtained as 0.32 s $^{-1}$. From these values, $\Delta Z = N_d = (\tau_b - \tau_f)/\tau_Z$, the differential diffusion number defined in relation (4.32) leads to an estimated global deviation of mixture fraction due to differential diffusion of 12%. This global estimation is close to the experimentally observed increase in the recirculation zone, which is about 10%. To further anticipate the validity of the N_d definition, two situations are envisioned.

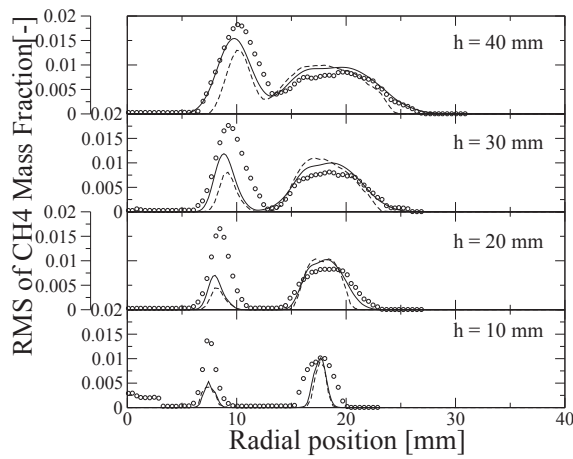
1. The Reynolds number is increased progressively in the same burner. With increasing Reynolds number both τ_f and τ_b decreases. However, τ_f decreases sharply with increasing Reynolds number as it is directly a function of the jet velocity, whereas the decrease of τ_b is governed by the intensity of turbulence and speed of rotation inside the recirculation zone. This turbulence intensity in turn is governed by the re-laminarisation effects due to the combustion and the bluff body geometry. Therefore, the decrease in τ_b with Reynolds number will be much slower and reaches a saturation above a certain Reynolds number. Consequently for a given equivalence ratio, N_d increases initially with increasing Reynolds number and then saturates. This behavior of N_d is in agreement with experimental observation by Dunn and Barlow [236], who varied Reynolds number in their burner.
2. In swirling flows with a central bluff body, with increasing swirl number larger amounts of incoming fluid is recirculated at frequency similar to the burnt gas thus reducing the



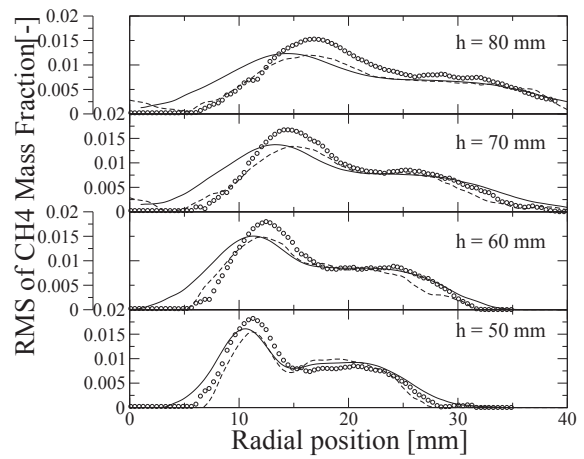
(a)



(b)



(c)



(d)

Figure 6.12: CH_4 mass fraction statistics, radial profiles. (a)-(b): Mean value. (c)-(d): RMS. Symbols: Experiment. LES: — azimuthal averaging, - - - single plane.

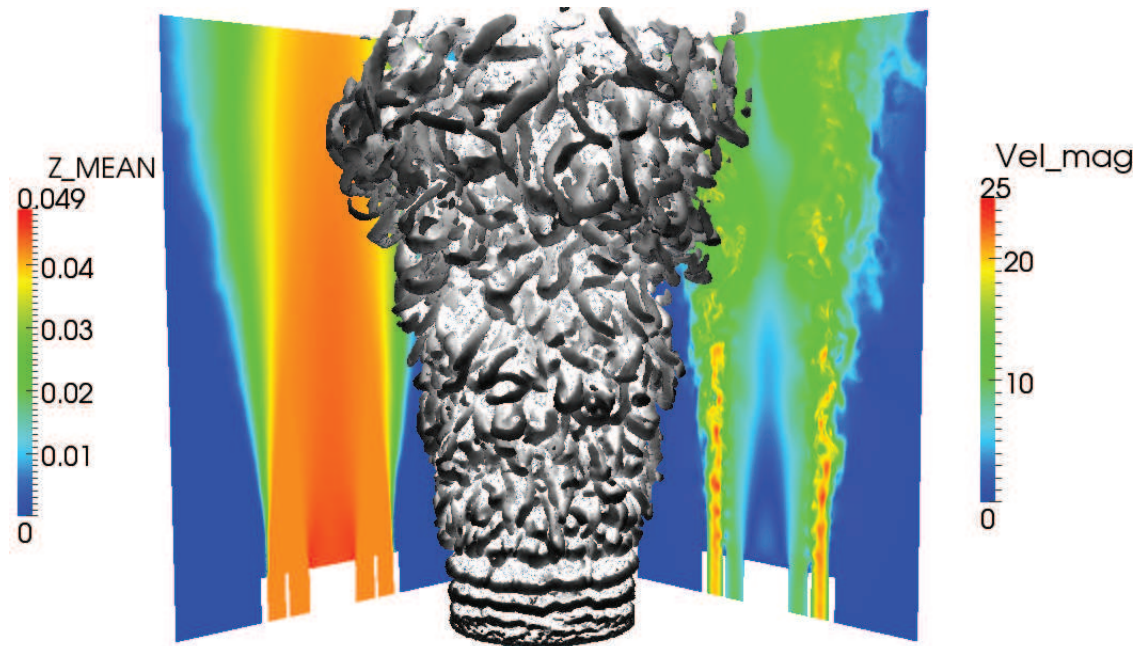


Figure 6.13: Iso Q-criterion ($Q = 1 \cdot 10^6 \text{s}^{-1}$) with instantaneous velocity and mean mixture fraction (Z_d) fields. Accumulation of the mixture fraction in the re-circulation zone can be seen.

difference in residence times. Therefore, at higher swirl numbers the differential diffusion effect is expected to vanish. At low swirl numbers, there could exist a higher value of N_d , because of a relatively lower residence time in the un-burnt gas. Consequently, the differential diffusion effect can be expected to appear, which is in accordance to what was observed in the TU Darmstadt burner experiment studied by Kuenne et al. [72]. Indeed, the mixture fraction statistics of this burner shows an accumulation in the recirculation zone.

The comparison of the statistics between the experiment and LES is however not straightforward for the product species such as CO and CO_2 , because balance equations affected by differential diffusion are not specifically solved for these species. Therefore results can only be used to illustrate the limit of tabulation techniques using a single equivalence ratio in the presence of differential diffusion. In Fig. 6.16, CO_2 mass fraction is properly predicted in the flame zone but is under estimated in the recirculation zone (radial location < 6.35 mm). The standard flamelet hypothesis does not see the accumulation of CO_2 in the recirculation zone caused by the diff-diff interaction with flow time scales and therefore predicts a mass fraction of Y_{CO_2} at equilibrium for the equivalence ratio of the incoming stream. However, the measured Y_{CO_2} in the re-circulation zone is greater than $Y_{\text{CO}_2}^{Eq}(Z_d)$ due to the differential diffusion effects discussed earlier leading to the accumulation of CO_2 . The measured CO_2 value seen in the plot approximately follows the relation $Y_{\text{CO}_{2d}}/Y_{\text{CO}_2} \approx Z_d/Z$.

Looking at the CO profiles in Fig. 6.17, no accumulation is seen in the recirculation zone.

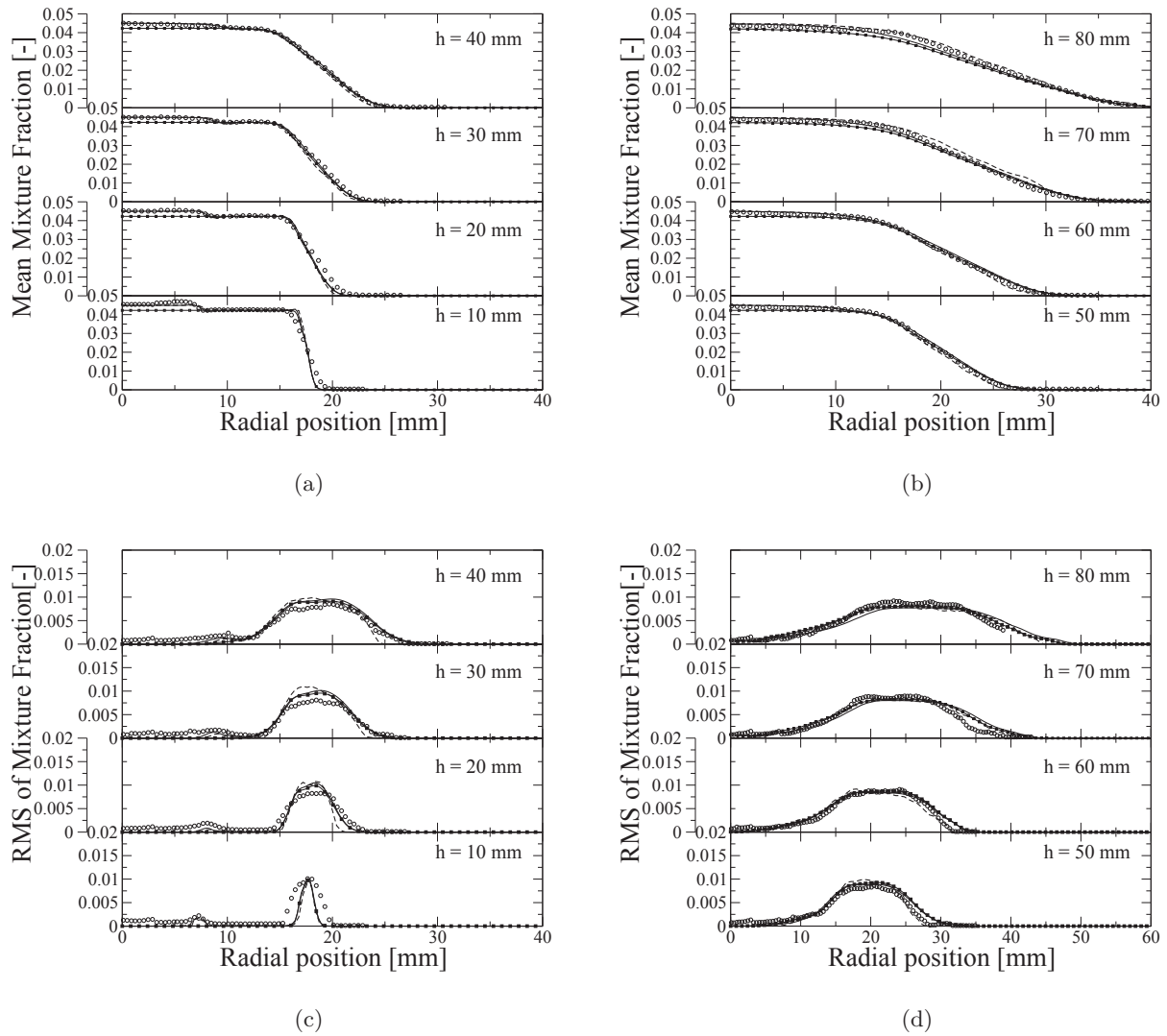


Figure 6.14: Mixture fraction statistics, radial profiles. (a)-(b): Mean value. (c)-(d): RMS. Open circles: Experiment. Line: LES — Z_d (Eq. (4.25)) azimuthal averaging, - - - Z_d single plane, -■- Z (Eq. (4.6)) azimuthal averaging.

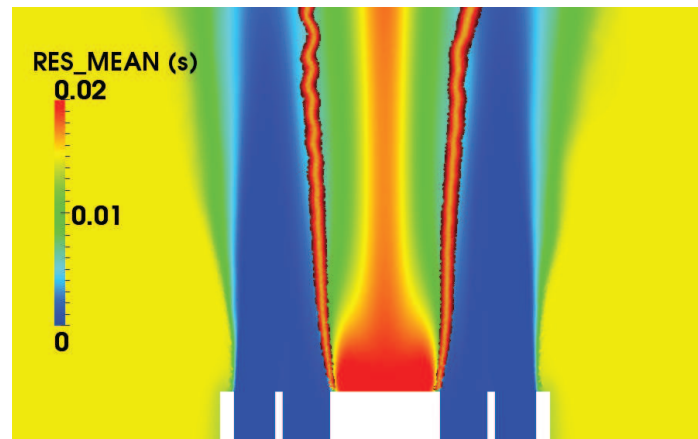


Figure 6.15: Mean residence time and instantaneous flame location.

It could be due to the conversion of CO into CO₂ in the recirculation zone. On the other hand, the measured CO mass fractions are much higher than the predicted ones. This large difference between the measurement and simulation profiles arises from the fact that they involve CO mass fractions which are filtered at different filter widths. On one hand, the measurements involve CO data which is unfiltered or filtered at a length scale corresponding to the measurement pixels whereas the LES solution has a filtered profile with a filter width, Δ controlled by the SGS variance of the progress variable. In fact, this problem of comparison arising due to the difference in filter width exists for all the scalars. But the impact of filtering is more pronounced in non-monotonically evolving scalars like CO, H₂, etc. In Fig. 6.18, comparison of filtered temperature profiles and CO profiles of a 1D laminar methane-air flame is shown. For monotonically evolving scalars like temperature, filtering does not alter the maximum value of the filtered profiles. The variation is still between the same minima and maxima as the unfiltered profile but with a smoother gradient. On the other hand for non-monotonically evolving scalars like CO, filtering (Fig. 6.18) reduces the maximum value significantly at every increasing filter width spreading the profiles on either sides. Due to the reason evidenced above, comparison of CO profiles between the experiment and simulation show large difference. One method to overcome this difficulty is to perform a deconvolution of the simulation profiles to get the unfiltered solution and then make comparison to the measurement results at the same filter width basis. In addition to the impact of the filter width, presence of heat loss effects or extinction can also affect the CO mass fractions. Laminar premixed flamelets alone cannot capture these effects properly and requires additional parameters.

Summary and conclusions

LES of the Cambridge burner using the FLF-PDF model was discussed. Since the model conserves the flame invariants (flame speed and internal structure) when the flame wrinkling is resolved on the LES mesh, a good prediction of scalar and velocity profiles was obtained. The differential diffusion modeling strategy was found to capture the accumulation of the mixture

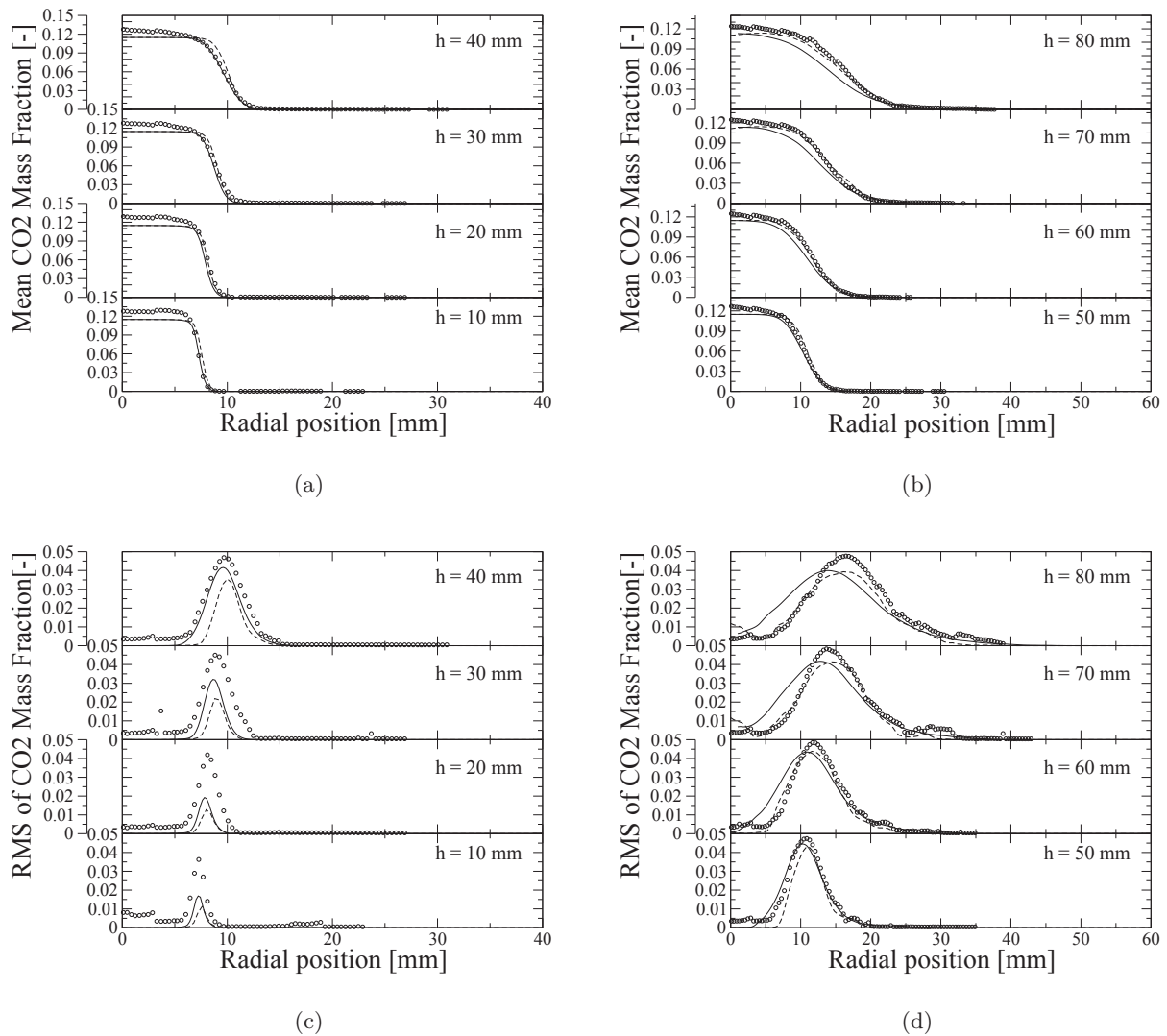


Figure 6.16: CO₂ mass fraction statistics, radial profiles. (a)-(b): Mean value. (c)-(d): RMS. Symbols: Experiment. LES: — azimuthal averaging, - - single plane.

fraction in the recirculation zone. The LES analysis showed that the difference in residence times across the flame is a good marker of this diff-diff effect. The global differential diffusion number based on the residence times was found to give a quantitative value for the extent of accumulation expected for the mixture fraction in the recirculation zone.

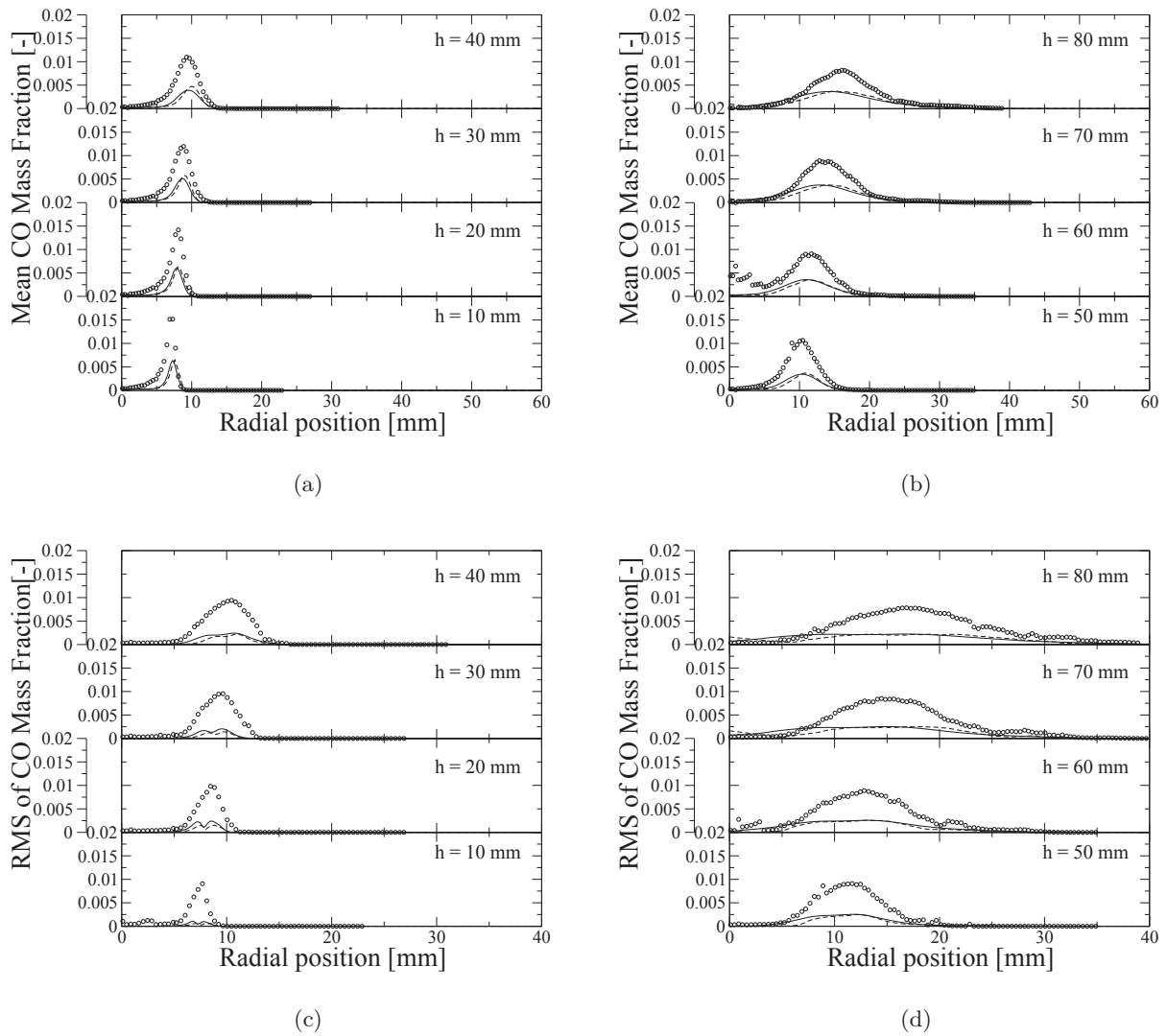


Figure 6.17: CO mass fraction statistics, radial profiles. (a)-(b): Mean value. (c)-(d): RMS. Symbols: Experiment. LES: — azimuthal averaging, - - - single plane.

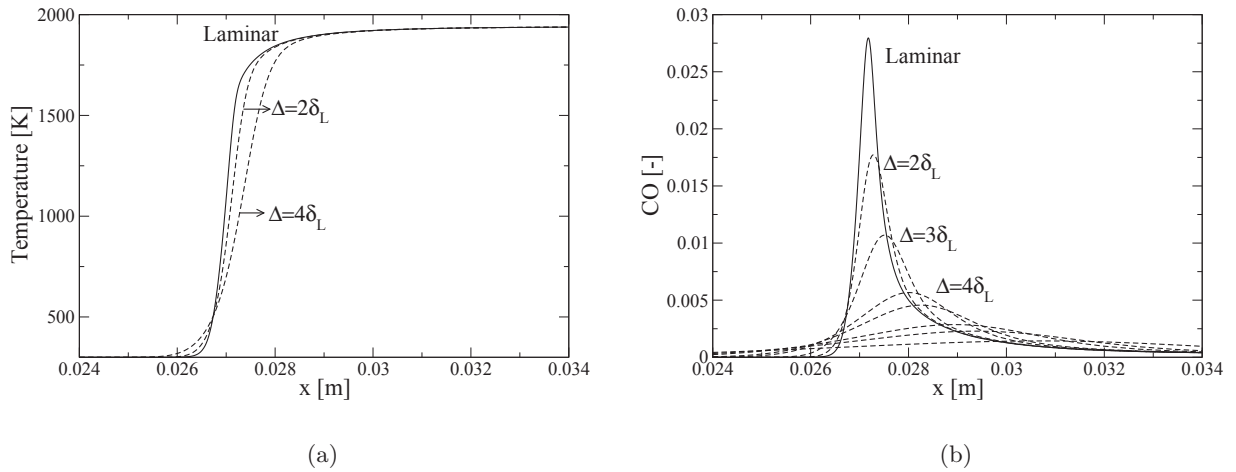


Figure 6.18: 1D laminar methane-air flame solution as a function of distance from burner exit at equivalence ratio of 0.75 (a) Temperature profiles (b) CO mass fraction profiles. — Unfiltered laminar flame solution, - - - Filtered profiles.

Reacting flow simulations: Stratified Configurations CSWB5 & CSWB9

7

Contents

7.1	Computational details	99
7.2	Results: Velocity and scalar statistics	100
7.3	Results: Analysis of stratified combustion	110
7.4	Summary and conclusions of CSWB5 and CSWB9 simulations	124

In this chapter, large eddy simulation of the turbulent stratified configurations (CSWB5 and CSWB9) of the Cambridge swirl burner using the FLF-PDF model is presented. A comparison of the experimental and simulation results are initially given. Once the overall validity of the numerical results are assessed, various aspects of the stratified combustion in the burner are analyzed and described in terms of the length scales, intensity of stratification and mode of combustion from instantaneous and time averaged LES data.

7.1 Computational details

The operating conditions for the two configurations were described already in Chapter 5. They constitute the stratified operations of the CSWB at moderate and high global stratification ratios ($\phi_{inner}/\phi_{outer}$) of 2 and 3 respectively (see Table 5.1). The outer jets of CSWB5 and the CSWB9 operate at equivalence ratios of 0.5 and 0.375 respectively while the lower flammable limit of methane is reported to be around 0.47 in literature [228]. Evidently, the CSWB9 configuration involves an outer jet mixture below the lean flammable limit. The mixture fraction boundary conditions for each case are given in Table 5.1 with the coflow mixture fraction set as zero.

Coarse mesh simulations were performed for both CSWB5 and CSWB9 on the unstructured mesh composed of 50 million tetrahedra discussed for the CSWB1 case previously. For the CSWB5 case, a refined mesh simulation involving about 400M cells was also performed to study the impact of grid resolution on the results, the resolution for which varies between 150 μm and 300 μm in the reaction zone. This mesh was obtained by performing a homogeneous refinement of the 50M mesh. A cross-sectional view of the two meshes are shown in Fig. 7.1 for comparison.

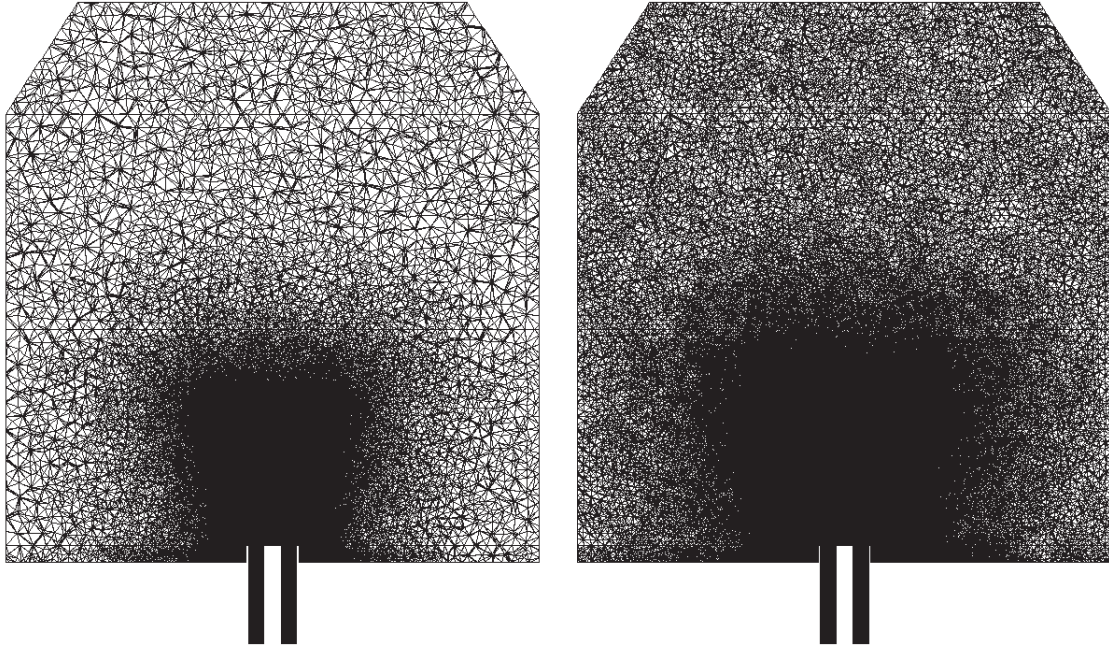


Figure 7.1: Cross sectional view of the mesh. Left: coarse mesh (50M cells) Right: refined mesh (400M cells)

As mentioned earlier, when the flame wrinkling is resolved ($\mathcal{F} < 1$), the proposed model requires an explicit flame filter width, Δ . For the coarse mesh simulations a value of 2 mm is used (same as that for the CSWB1 case). For the refined mesh simulations, $\Delta = 0.6$ mm was used which gives a Δ/h ratio of 2.

7.2 Results: Velocity and scalar statistics

In this section, the numerical results are evaluated on a statistical basis by comparing the Reynolds averaged profiles and their fluctuations with those of the measurements.

As discussed previously (§ 6.2), the time averaged LES field was not symmetric especially at locations downstream of 30 mm. Figure 7.2 depicts the asymmetry by showing the Reynolds averaged temperature profiles for CSWB5 and CSWB9 at 10 mm and 50 mm. Close to the burner exit, the mean temperature is more or less symmetric, however at 50 mm the symmetry is completely destroyed. This was observed for the refined mesh simulations as well (not shown here). Three dimensional time averaged statistics are presented with data obtained by azimuthal averaging and from a specific plane data for all the statistics.

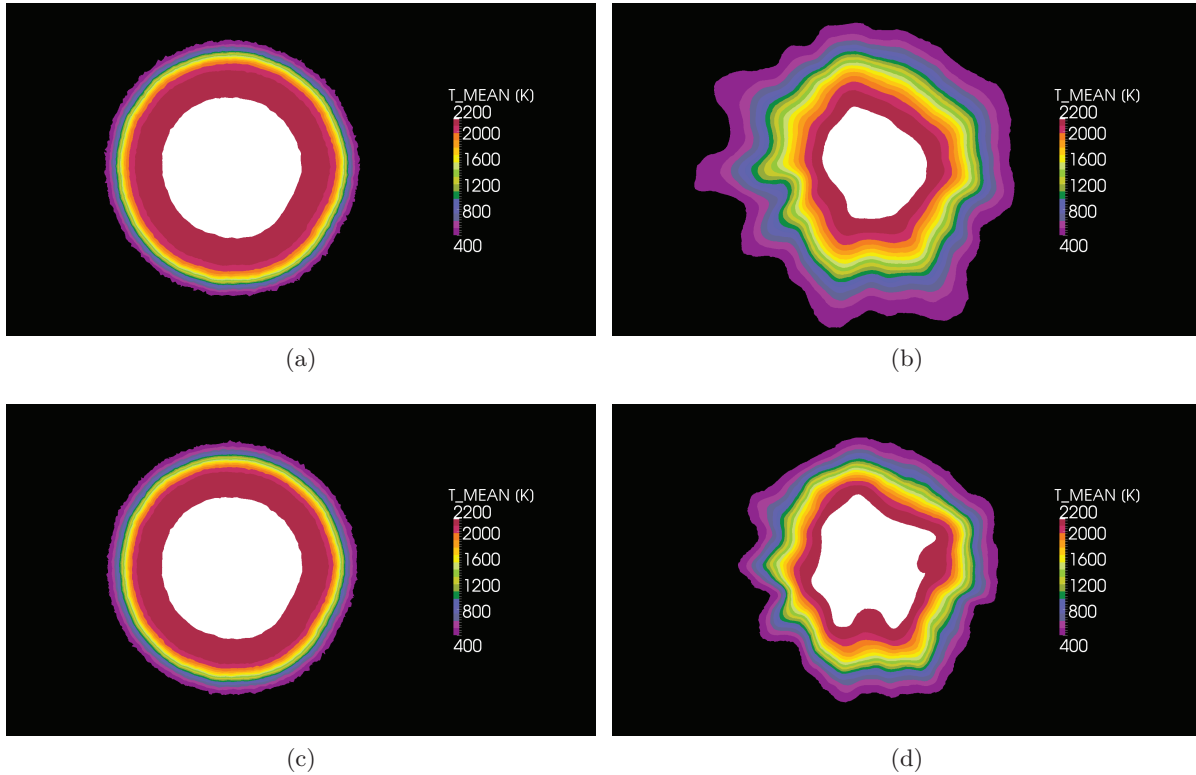


Figure 7.2: Cross-sectional planes with mean temperature distribution at 10 mm and 50 mm Left: 10 mm Right: 50 mm a) and b) CSWB5 c) and d) CSWB9

Axial velocity statistics

The comparison of the axial velocity statistics of LES with the LDA measurements are shown in Figs. 7.5 and 7.6. The LES data has an overall good agreement with the LDA data. It can be seen that the predicted axial velocity in the central recirculation zone is however higher than the measurements. A possible explanation for this observation is the heat transfer to the ceramic bluff body. Since the model does not account for the presence of heat losses, the predicted temperature (see Figs. 7.13 and 7.14) near the bluff body is higher than the measured temperature. The calculated density is therefore lower, and hence the velocities tend to be higher in comparison to the situation where the heat loss effects would have been taken into account. The axial velocity fluctuations in the flame zone (radial locations between 6.35 mm and 10 mm) are under predicted by the coarse mesh. The proper level of fluctuations cannot be recovered by adding the SGS contribution, because in this zone due to re-laminarisation effects the subgrid viscosity is almost zero. Therefore, it is believed that the large filter size of the coarse mesh is responsible for damping of the fluctuations. In the refined mesh simulations, the filter size decreases resolving smaller length scales and the right level of fluctuations are recovered emphasizing the need for performing LES on more than a single mesh resolution. The mean

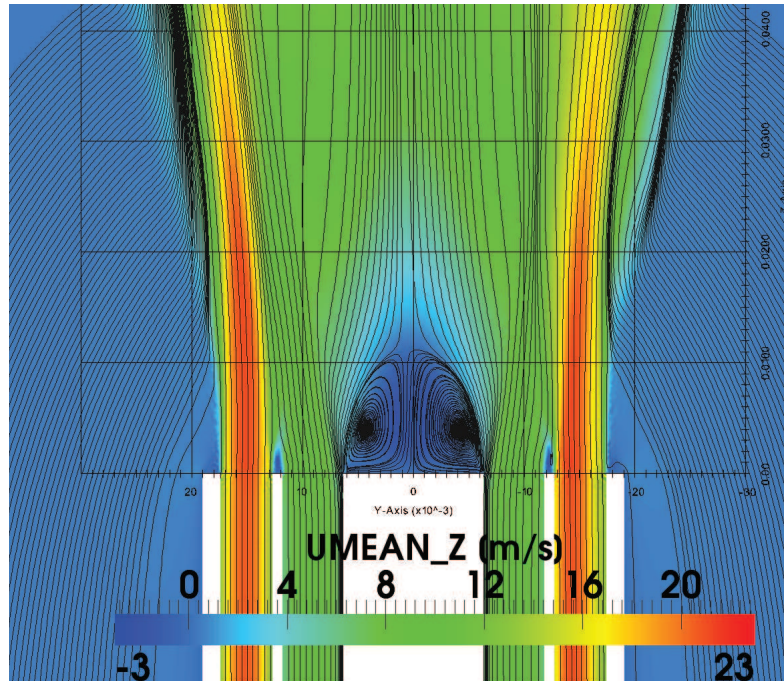


Figure 7.3: Streamlines superimposed on the mean velocity field of the CSWB5 configuration depicting the recirculation zone and the jets.

axial velocity plot with the streamlines are shown in Figs. 7.3 and 7.4. The re-circulation zone of CSWB5 is slightly smaller than CSWB9 owing to the higher flame opening angle because of the higher flame speed for the stoichiometric mixture.

Radial velocity statistics

The comparison of the radial velocity statistics are presented in Figs. 7.7 and 7.8. Similar to the axial velocity profiles, the mean radial velocity profiles of CSWB5 and CSWB9 also resemble each other very closely. An under prediction of the fluctuations is seen in the flame zone for the coarse mesh, while a proper level is recovered in the refined mesh.

Mixture fraction statistics

The Reynolds averaged profiles of the mixture fraction for CSWB5 and CSWB9 are shown in Figs. 7.9 and 7.10. The salient features to be noted are the three steps in the profile close to the burner exit for either cases. The two steps at radial locations beyond 6 mm represent the two equivalence ratios of the pipes. The third step at radial locations below 6 mm is caused by the differential diffusion effect discussed earlier in section 6.2. As mentioned before in the section on differential diffusion modeling (§ 4.3) two mixture fractions are solved; the passive \tilde{Z} and the non-passive \tilde{Z}_d . The passive scalar completely misses the accumulation as expected, whereas the mixture fraction with the source term (\tilde{Z}_d) in the flame follows the accumulation

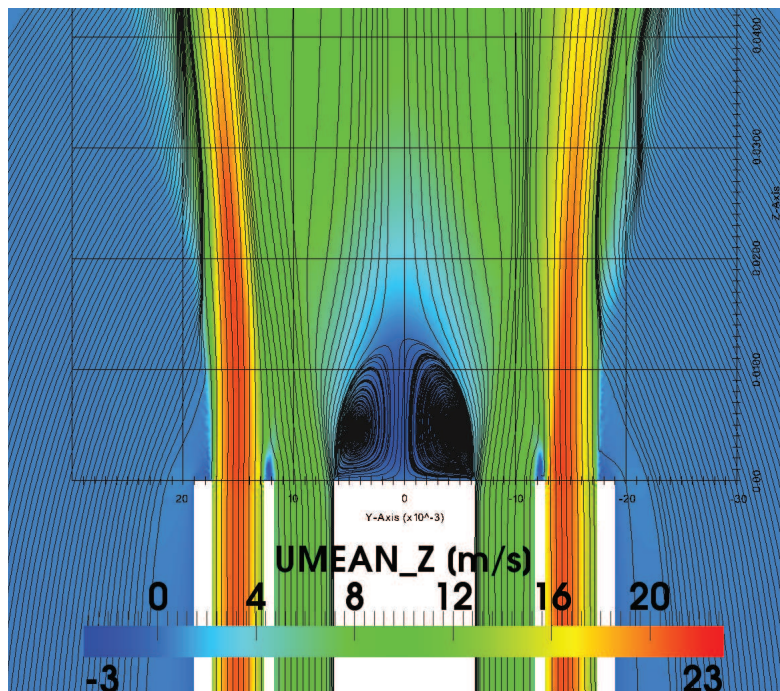


Figure 7.4: Streamlines superimposed on the mean velocity field of the CSWB9 configuration depicting the recirculation zone and the jets.

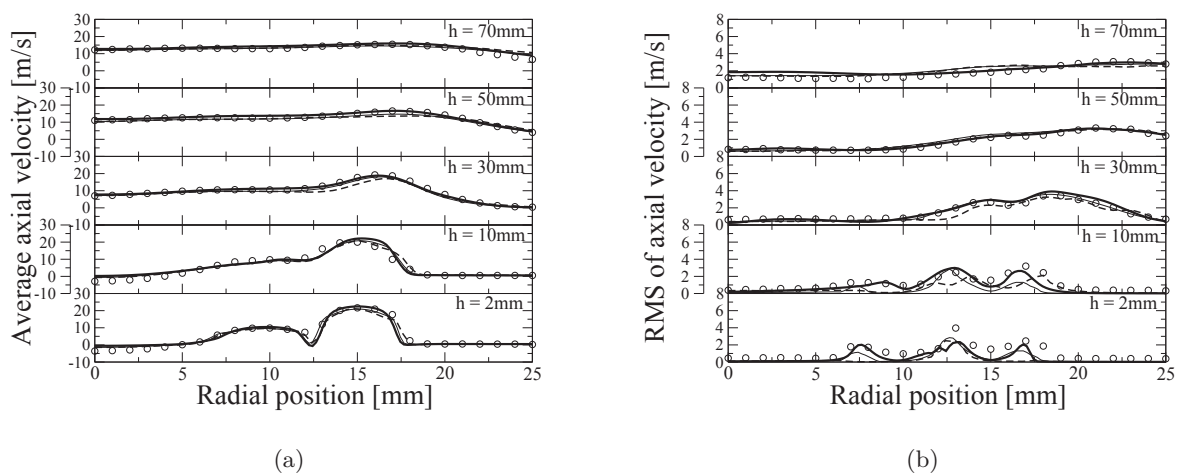


Figure 7.5: Axial velocity statistics for CSWB5. Symbols: LDA, LES: - - Azimuthally averaged coarse mesh, - - - Single plane coarse mesh, — Azimuthally averaged refined mesh.

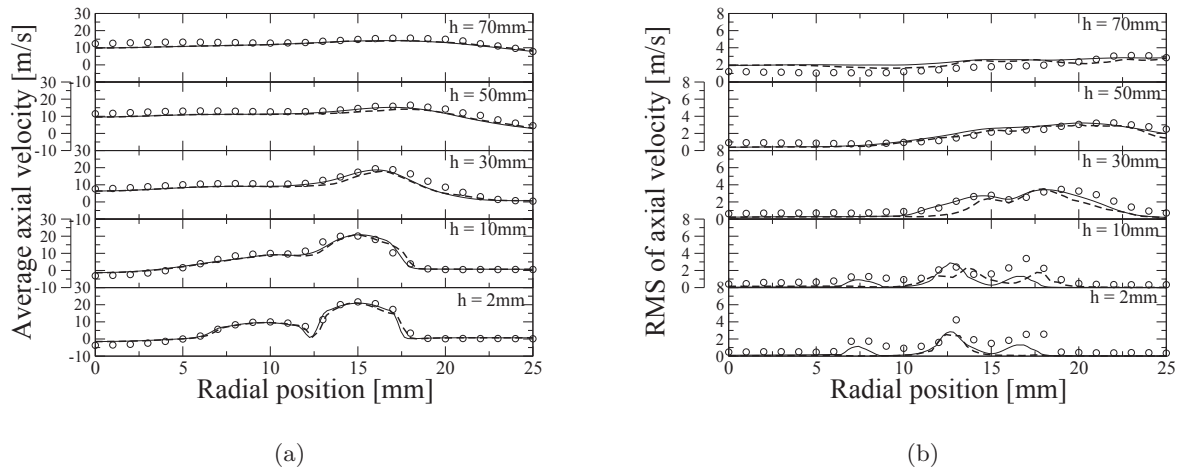


Figure 7.6: Axial velocity statistics for CSWB9. Symbols: LDA. Lines: LES. — azimuthal averaging, - - single plane.

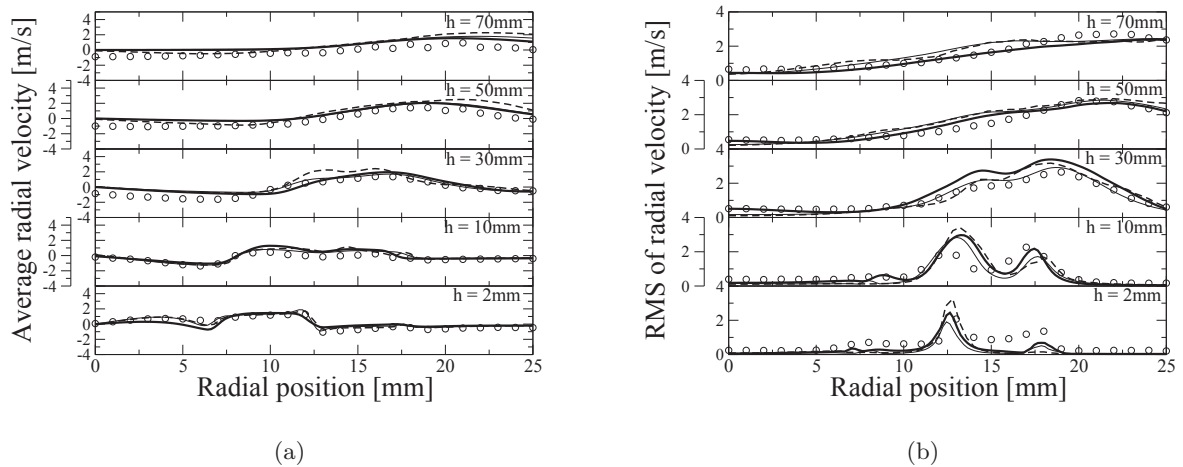


Figure 7.7: Radial velocity statistics for CSWB5. Symbols: LDA, LES: — Azimuthally averaged refined mesh, - - Single plane coarse mesh, - . Azimuthally averaged coarse mesh.

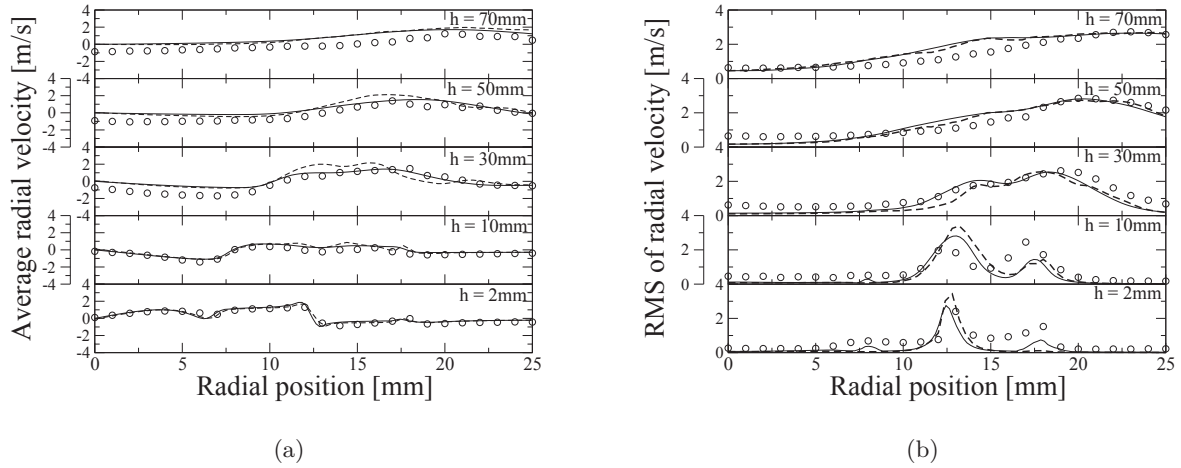


Figure 7.8: Radial velocity statistics for CSWB9. Symbols: LDA. Lines: LES. — azimuthal averaging, - - single plane.

seen in the experiment. In comparison to the measurements at 10 mm for the premixed CSWB1 case, the accumulation is much lower for the two stratified cases. This can be attributed to a combination of two factors:

- First and foremost, in comparison to the lean premixed equivalence ratio of 0.75 seen in the CSWB1 case, the Bilger mixture fraction profiles for the stoichiometric and the richer equivalence ratios show very negligible accumulation of the mixture fraction in the burnt gas ($c > 0.8$) across the laminar flames. This is seen in Fig. 7.11 that the Bilger mixture fraction (Z_d^{maj}) defined from the six major species as utilised by the experimentalists undergoes variation across the laminar flame but shows very little accumulation or enhancement over the expected passive value in the burnt gas ($c > 0.8$) and it was shown in the definition of the differential diffusion number N_d (Eq. 4.32) that it is the source term in the burnt gas which promotes the accumulation effect.
- Secondly, the flame opening angle of the two stratified cases are wider due to the higher flame speeds associated with the inner jet equivalence ratios, resulting in a shorter recirculation zone compared to the premixed case. The height of the re-circulation zone for the CSWB5 and CSWB9 is around 11 mm and 13 mm respectively (see Figs. 7.3 and 7.4) whereas for CSWB1 it is around 20 mm (see Fig. 6.7). Extending the residence time (Eq. 4.33) concept here, it means that there is a lesser gradient in residence times between the burnt and fresh gas in the CSWB5 and CSWB9 configuration which results in lesser accumulation. This can be seen by comparing the residence time plots of the two stratified cases shown in Fig. 7.12 with that of the CSWB1 case given in Fig. 6.15.

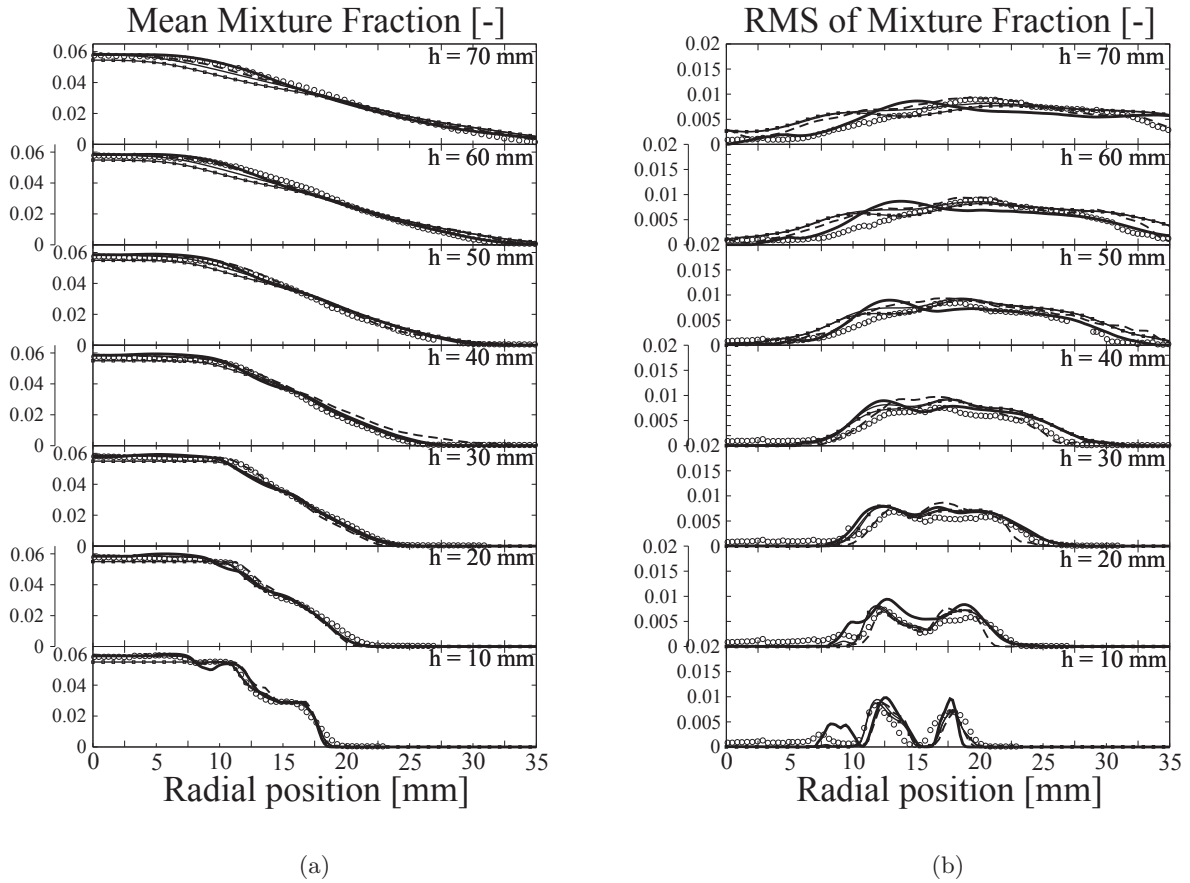


Figure 7.9: CSWB5: Mixture fraction statistics, radial profiles. Open circles: Experiment. Line: LES — Z_d (Eq. (4.25)) azimuthal averaging coarse mesh, - - - Z_d single plane coarse mesh, -■- Z (Eq. (4.6)) coarse mesh, — Z_d azimuthal averaging refined mesh.

Looking at the RMS profiles, at 10 mm from the burner exit three peaks are distinguishable in the measurements. The coarse mesh simulations capture the two peaks away from the flame (> 10 mm) while missing the peak in the flame zone caused by the differential diffusion effect, even though the mean profiles are in good agreement with the experiment. On the other hand, the refined mesh simulation reproduces all the three peaks with the fluctuations inside the flame zone radially shifted outwards and slightly higher in magnitude. It could therefore be inferred that, on the coarse mesh there is a larger damping effect by the larger flame filter which fails to account for the fluctuations within the flame zone. When the mesh is refined, the influence of the filter on the flame is reduced and the proper level of fluctuations are recovered. As we move further downstream, the three peaks reduce to two and finally to one as the flow becomes more turbulent and mixing is enhanced.

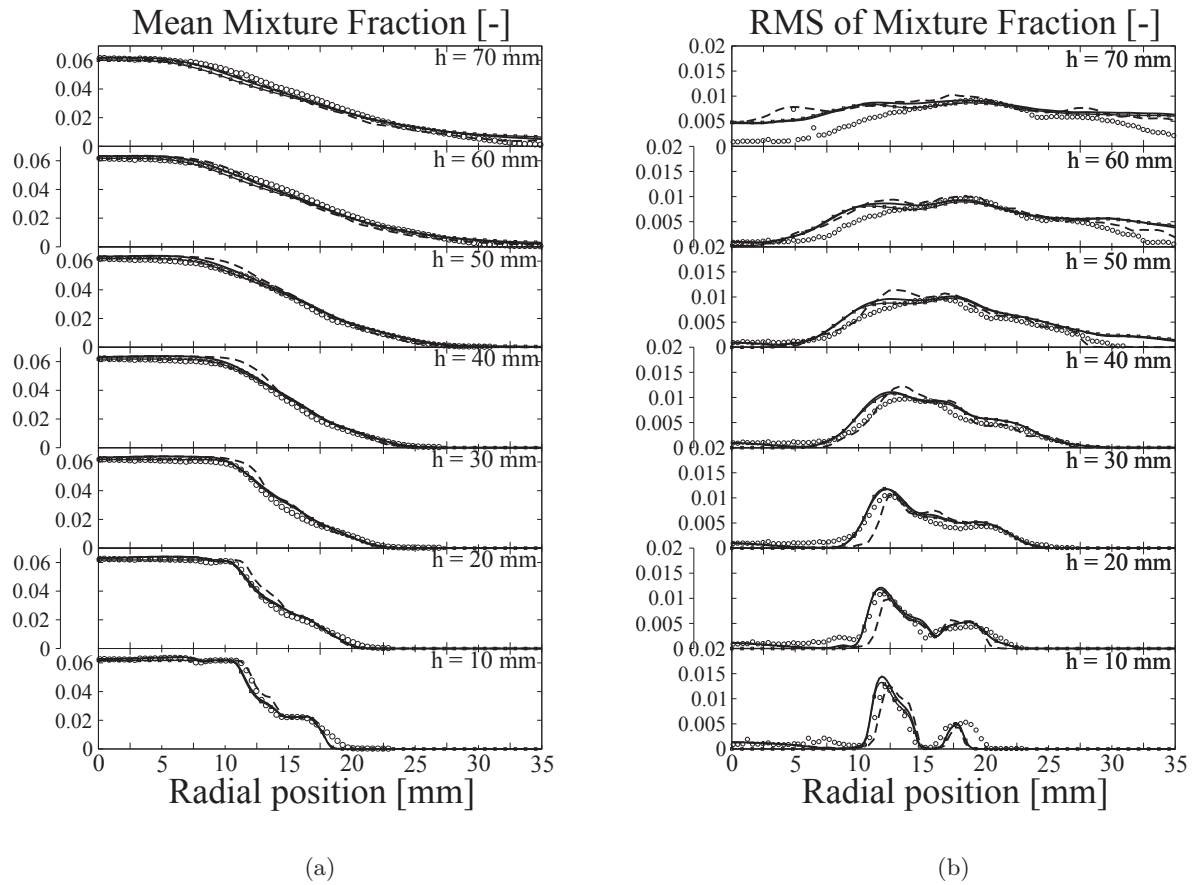


Figure 7.10: CSWB9: Mixture fraction statistics, radial profiles. Open circles: Experiment. Line: LES — Z_d (Eq. (4.25)) azimuthal averaging, - - Z_d single plane, -■- Z (Eq. (4.6)).

Temperature statistics

Figures 7.13 and 7.14 show the Reynolds averaged temperature statistics for CSWB5 and CSWB9 simulations. In both cases, the mean predicted temperature along the axis, especially in the recirculation zone is higher than the experimental values. In fact, the predicted temperature is close to the adiabatic temperature in the recirculation zone since it is composed purely of burnt gases. Therefore, a lower measured temperature indicates possible heat loss at the walls of the bluff body. In this work no heat loss model is included even though strategies for including it in tabulated chemistry methods have been proposed [237–239] which could lead to a dramatic increase in the size of the database and hence the memory overhead on the processors. In addition, heat loss can also have the effect of reducing the flame speed as mentioned by [74]. Therefore, the simulated temperature and species profiles are slightly radially shifted outwards compared to the experiments. The azimuthally averaged profile and the single plane profile remain close to each other up to 30 mm from the burner exit. Beyond this height, the

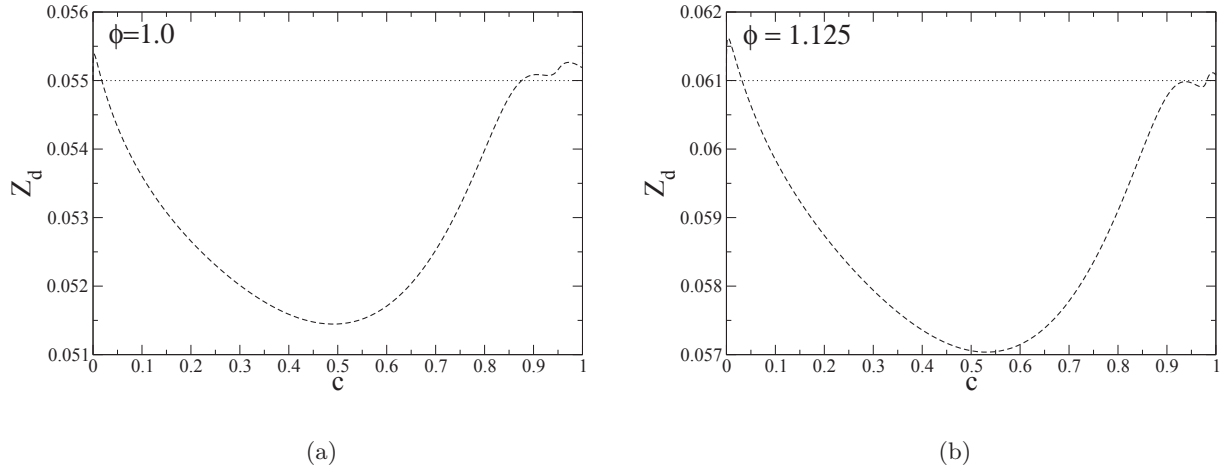


Figure 7.11: Mixture fraction distribution across a laminar premixed flame at equivalence ratios a) $\phi = 1.0$ and b) $\phi = 1.125$, $-- Z_d^{major}$ and $\dots Z$

shear layer intersects the flame due to which the flame becomes more wrinkled. The loss of symmetry thus becomes more pronounced above 30 mm. At far downstream locations (>50 mm), an azimuthally averaged data does not compare well with the experiments whereas the single plane data agrees well with the measurements. Looking at the RMS profiles of temperature in Figs. 7.13 and 7.14, it can be seen that the fluctuations of temperature in the flame zone are under predicted on the coarse mesh in comparison to the experiments especially close to the burner exit. The RMS profiles of temperature are linked to the small scale variations which are damped on the coarse mesh however recovered in the refined mesh simulations. This may be due to the fact that the flame is almost laminar in this zone marked by sharp temperature gradient.

Species statistics

The time averaged radial profiles and RMS of only the major species CH_4 , CO and CO_2 are presented here for brevity even though measurements for other species such as H_2 , H_2O and O_2 are also available. The radial profiles of CH_4 (Figs. 7.15 and 7.16) show two step profiles close to the burner exit as expected and then reduces to a smooth single peak profile downstream. It can also be noted that the wake of the bluff body in CSWB9 case does not show the presence of CH_4 in time averaged sense. This in turn could mean that there is no leakage of CH_4 across the premixed combustion zone as reported by Haworth et al. [130]. The mean profiles of CO are shown in Figs. 7.17 and 7.18 and those of CO_2 in Figs. 7.19 and 7.20 respectively. In comparison to the premixed case (CSWB1), the CO_2 mass fraction statistics shows negligible or no accumulation in the recirculation zone for the stratified configuration. On the other hand the

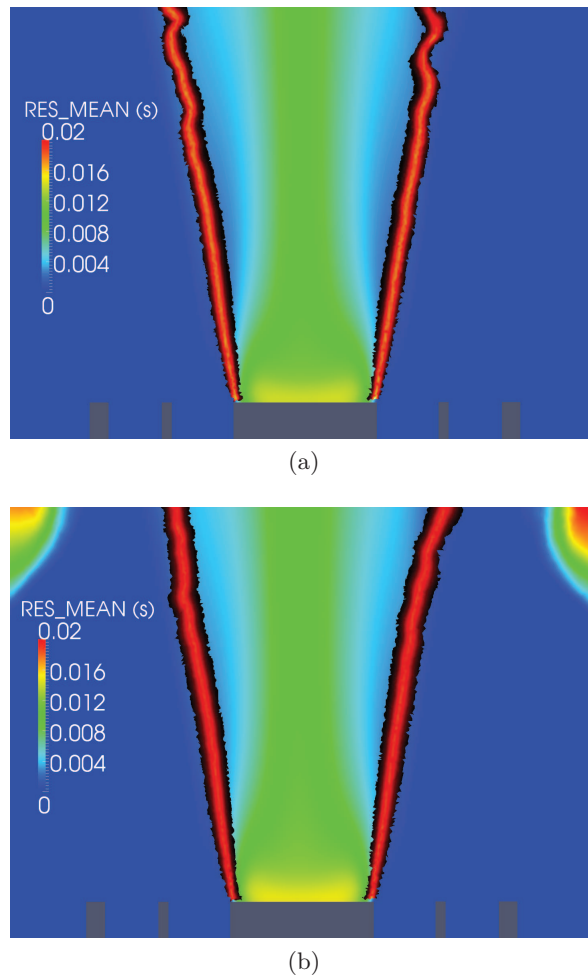


Figure 7.12: Mean residence time fields with an instantaneous source term location shown for the two cases a) CSWB5 and b) CSWB9

accumulation of CO is high in the recirculation zone for the stratified configuration in comparison to negligible presence of CO for the premixed case CSWB1. This could be due to the fact that the premixed configuration involves a lean mixture and therefore sufficient oxygen is available to convert the accumulated CO to CO₂. While in the stratified configuration, because of the rich mixtures of the inner jet an oxygen deficiency prevents conversion of CO to CO₂. The deviation between the CO measurement and LES profiles in the flame zone (radial locations between 6 mm - 10 mm) for both CSWB5 and CSWB9 can be explained by the same argument of having larger filter on simulation in comparison to a smaller filter width in measurements discussed in 6.2. It is also noteworthy that in Fig. 7.17 the CO profile of the refined mesh case is found to approach closer to the measurements as expected, due to the smaller filter width in comparison to the coarse mesh.

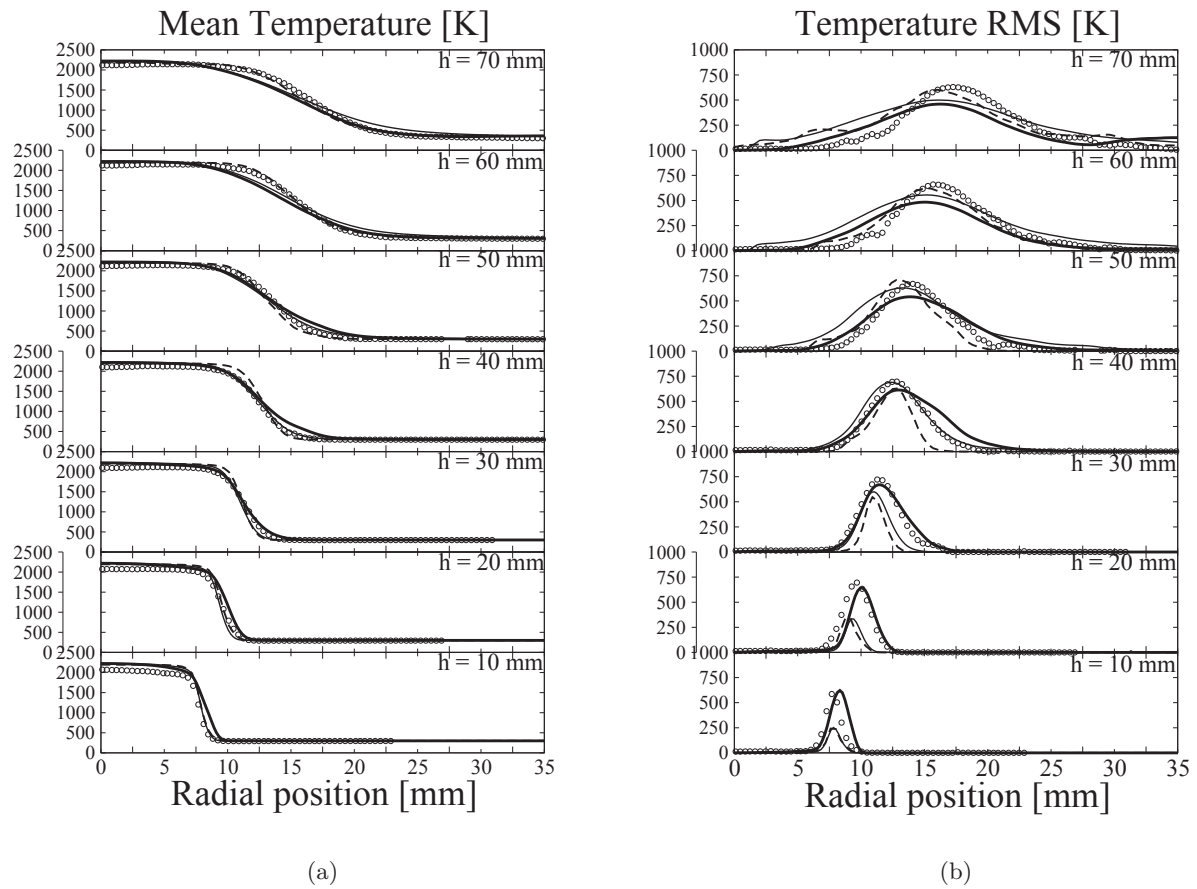


Figure 7.13: Temperature statistics for CSWB5, radial profiles. Symbols: Experiment. LES: — azimuthal averaging coarse mesh, - - - single plane coarse mesh. — azimuthal averaging refined mesh.

7.3 Results: Analysis of stratified combustion

In this section, salient features of the mode of combustion in the burner is presented by using the LES regime diagram, quantification of the intensity of stratification, determining the relative orientation of the flame and mixing vectors, and performing a hybrid flamelet combustion regimes analysis.

LES regime diagram

Figure 7.21 shows the LES regime diagram proposed by Pitsch and Duchamp de Lageneste [240] for the two cases studied here. It is seen that for both cases, points exist for all the major flame combustion regimes. The various regimes arise due to the varying interactions of the flame and the shear which will be discussed in the coming sections.

In this diagram, the ordinate axis gives the ratio of the flame filter width to the laminar flame

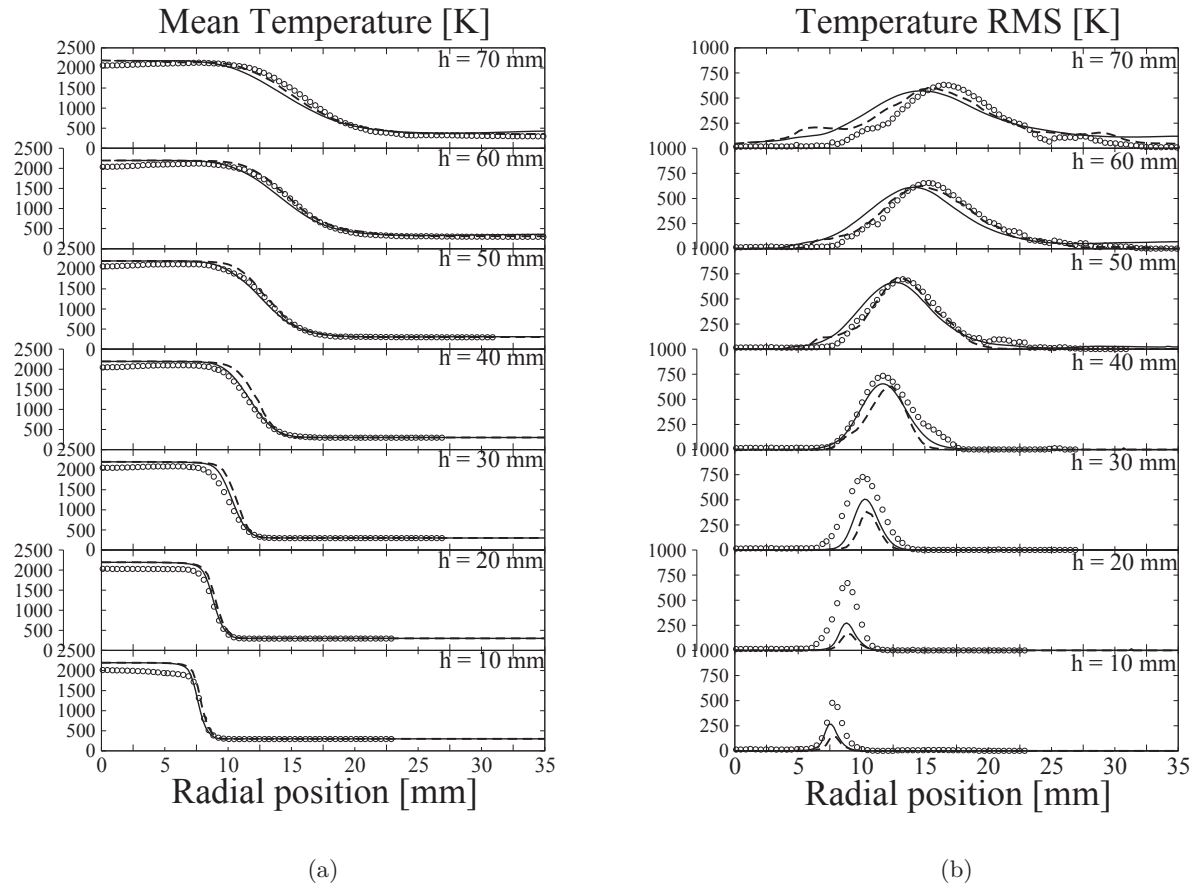


Figure 7.14: Temperature statistics for CSWB9, radial profiles. Symbols: Experiment. LES: — azimuthal averaging, - - - single plane.

thickness. The flame filter width in the wrinkled flamelets regime is Δ , the one used to filter the laminar flame with the FLF-PDF model. In the thin reaction zones regime, it is usually assumed in literature that the filter width is the LES mesh characteristic filter $\Delta = \nu^{1/3}$. However, if the sub-grid mixture fraction fluctuations S_z is negligible as seen for the simulations here, it is also possible to extract the explicit filter width $\Delta(\tilde{c}, S_c, \tilde{Z})$ from the solution field assuming that the LES imposes a Gaussian filter on the flame. Since the present model gives the possibility to extract the exact flame filter size at any point, to plot the regime diagram the flame filter width Δ is used. The flame thickness used here is the diffusive flame thickness calculated as $\delta_L = \nu_0/S_L$, where ν_0 is the kinematic viscosity of fresh gas. Along the X axis, the Karlovitz number is considered which is obtained from the LES as

$$Ka^2 = \left(\mathcal{F}\right)^3 \frac{\delta_L}{\Delta} \quad (7.1)$$

The scatter plot superimposed on the regime diagram is conditioned on the progress variable such that $0.01 < \tilde{c} < 0.99$. When the flame is within the wrinkled flamelet regime, the flame

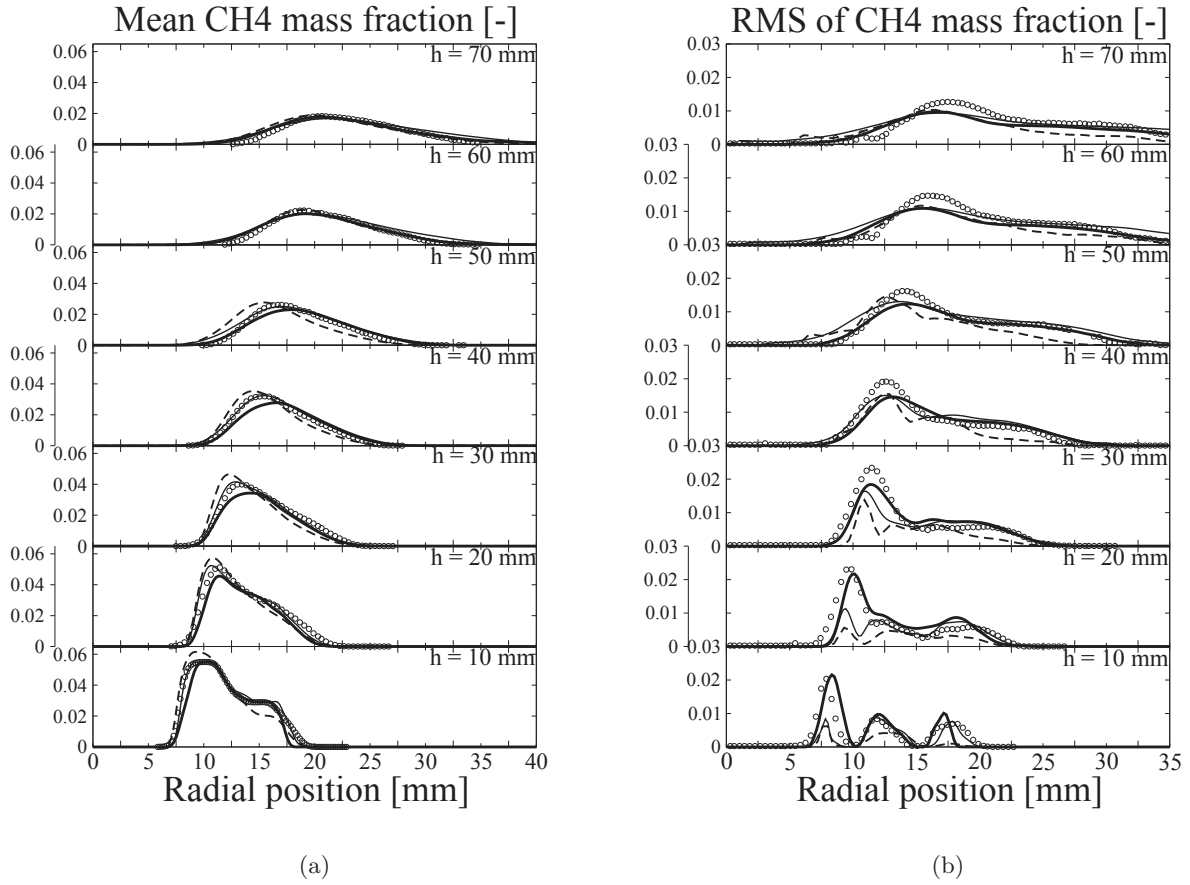


Figure 7.15: CH₄ mass fraction statistics for CSWB5, radial profiles. Symbols: Experiment. LES: — azimuthal averaging coarse mesh, - - - single plane coarse mesh, — azimuthal averaging refined mesh.

wrinkling is resolved on the LES mesh leading to $\mathcal{F} < 1$. In the wrinkled flamelet regime, the flame thickening is controlled by the explicit filter width Δ specified, ensuring sufficient number of points inside the flame zone. In the corrugated flamelets and the thin reaction zones $\mathcal{F} > 1$ and S_c is evaluated as a function of \widetilde{Y}_c and \widetilde{Y}_c^2 . In this zone the Karlovitz number and the flame wrinkling are relatively high, and the latter is unresolved on the coarse mesh but accounted for in the PDF (Eq. 4.5). In these zones, the flame filtering is governed implicitly by the actual LES mesh since the values of \widetilde{Y}_c and \widetilde{Y}_c^2 are dependent on the mesh.

The observed combustion regimes may be linked to the particular stratified flame topologies. Looking at 7.22, we can identify an initial premixed zone up to 30 mm. Between 30 mm and 40 mm, the flame intersects the mixing layer as shown in Fig. 7.23. As we move downstream (> 40 mm) there exists stratified combustion characterized by varying equivalence ratios in the progress variable source term. Since the inner jet is not as turbulent as the outer jet as depicted by their Reynolds numbers in section § 5.1, the LES mesh resolves the flame wrinkling where

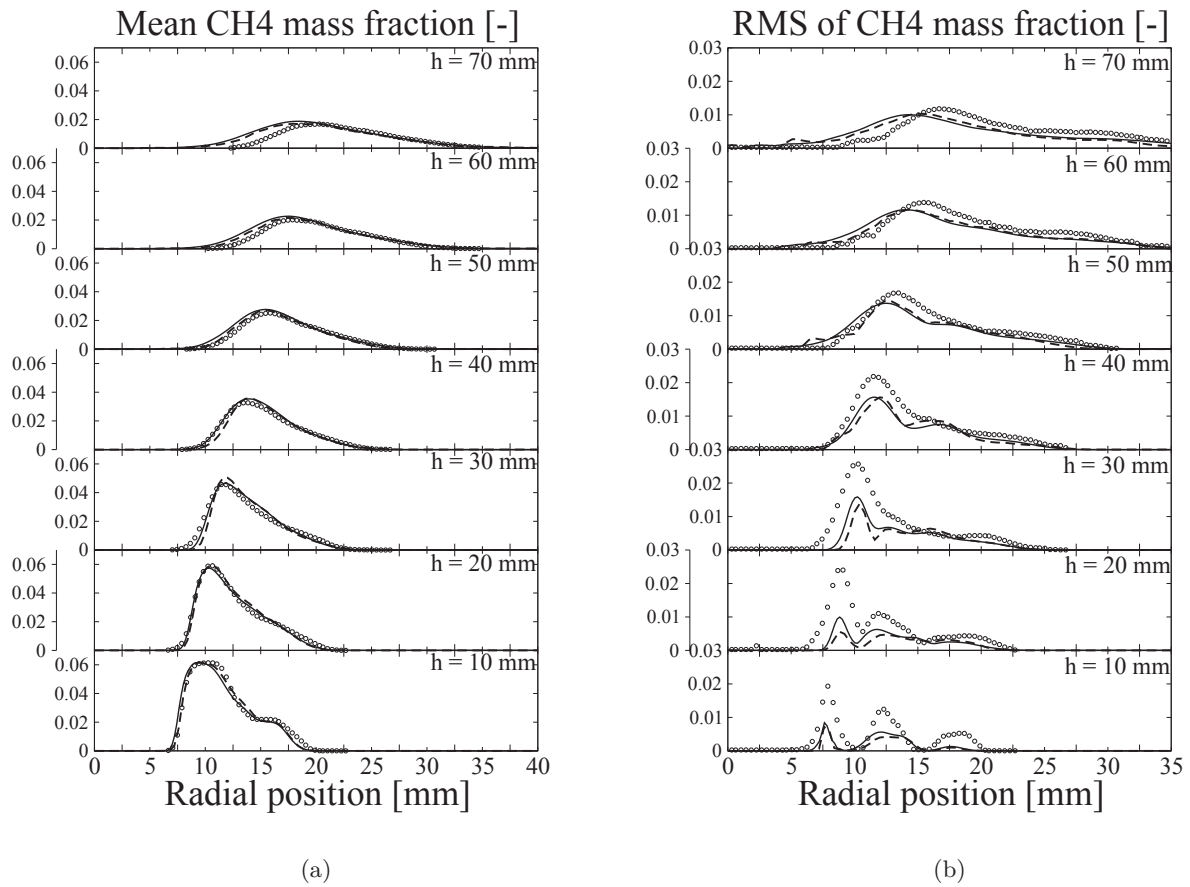


Figure 7.16: CH_4 mass fraction statistics for CSWB9, radial profiles. Symbols: Experiment. LES: — azimuthal averaging, - - - single plane.

the flame is premixed. Therefore, in this part of the flame, $\mathcal{F} < 1$ and predominantly lies in the wrinkled flamelet regime of the LES diagram. This was observed for both the cases. When the shear layer of the inner and outer jets intersects the flame, presence of smaller structures increases the wrinkling and leads to \mathcal{F} going greater than 1 and the model shifts accordingly. Figures 7.24a and 7.25a show the instantaneous source term colored by \mathcal{F} depicting the behavior discussed above. Also shown are the cumulative distributions of the PDF(\mathcal{F}) versus \mathcal{F} in Figs. 7.24b and 7.25b.

Degree of stratification

In order to quantify the extent of stratification in the two cases, it is useful to look at two quantities; the probability distribution of equivalence ratio and the probability distribution of the gradient of equivalence ratio across the flame at different heights from the burner exit. Figure 7.26 shows the distribution of equivalence ratios for CSWB5 and CSWB9 at heights ranging from 20 mm - 70 mm conditioned in the flame zone ($0.01 < \tilde{c} < 0.99$). It is evident

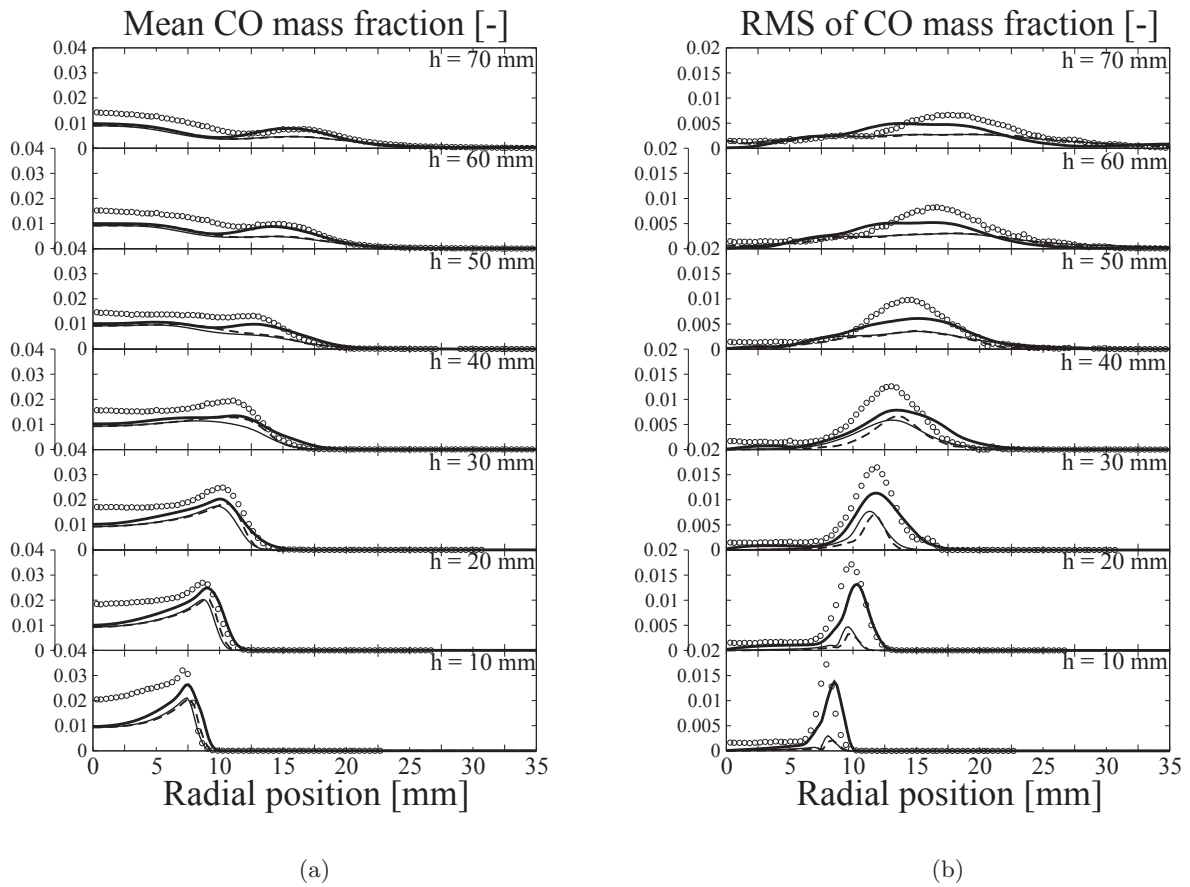


Figure 7.17: CO mass fraction statistics for CSWB5, radial profiles. Symbols: Experiment. LES: — azimuthal averaging coarse mesh, - - - single plane coarse mesh, — azimuthal averaging refined mesh.

that below 30 mm combustion is predominantly premixed type with occasional stratification occurring at a frequency controlled by the intersection of mixing layer vortices for both the cases. Frequency spectrum of a probe placed on the shear layer of the inner jet and the outer jet is shown in Fig. 7.27 which reveals a frequency of around 2300 Hz. For a given height, the curves are flatter for CSWB9 showing a higher probability for several equivalence ratios to exist at a given height than observed in CSWB5. This is expected since the stratification ratio of CSWB9 is higher than CSWB5. In spite of the minor differences in both cases evidently the flame undergoes combustion at lean mixtures and also experiences stratification especially at heights above 30 mm. The span of the equivalence ratio could be considered as a representative degree of stratification.

But as seen in literature [74], a complementary parameter that can be looked at is the gradient of equivalence ratio across the flame. A comparison of the probability distribution of the mean gradients of equivalence ratio at heights ranging from 40 mm - 70 mm for the CSWB5

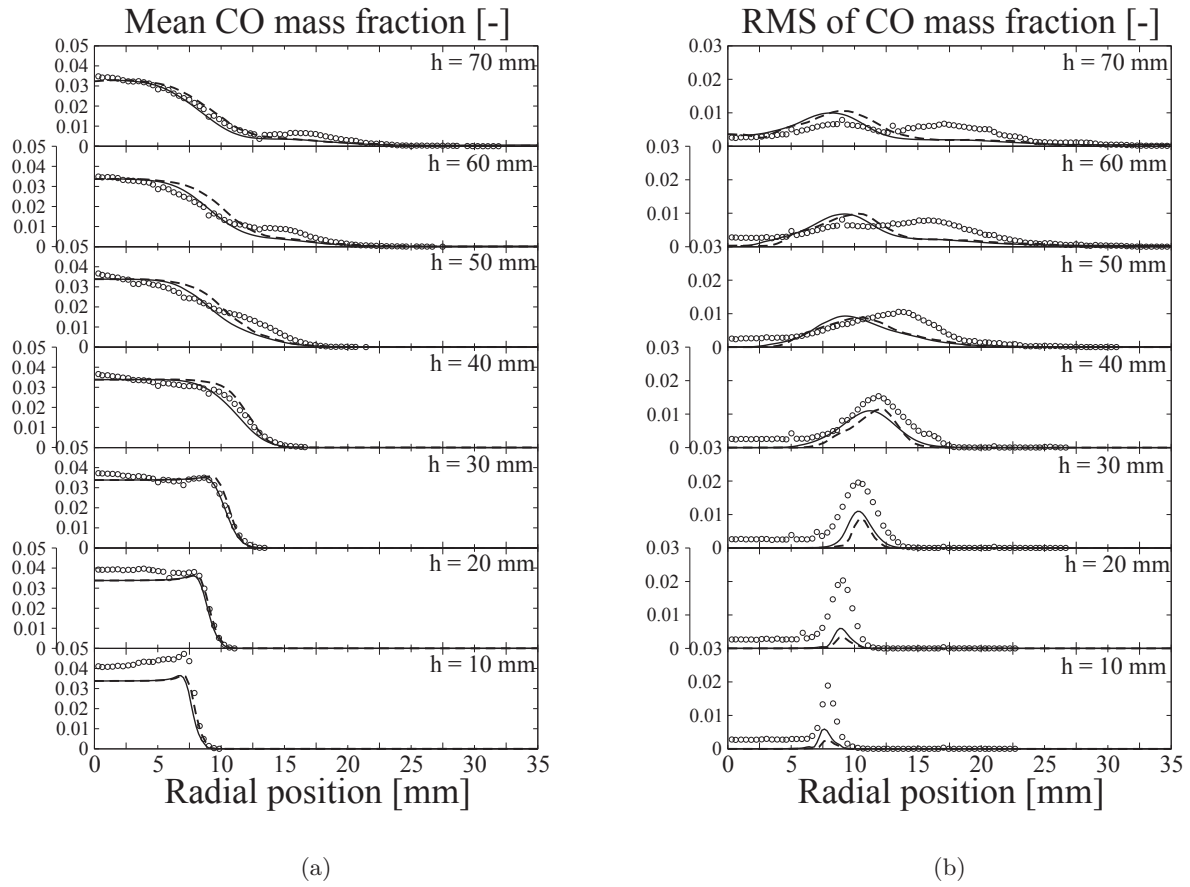


Figure 7.18: CO mass fraction statistics for CSWB9, radial profiles. Symbols: Experiment. LES: — azimuthal averaging, - - - single plane.

and CSWB9 cases are shown in Fig. 7.28. Since up to 30 mm, the flame is in the premixed regime the gradients are zero and not shown here. The plots show that at distances 40 mm and 50 mm from the burner exit, the mean gradient of equivalence ratio is higher for the CSWB9 than CSWB5 case. It should be recalled that these locations fall in the zone where the mixing and reaction zones intersect and maximum stratification is found. The plots show an expected trend again since the global stratification ratio for CSWB9 is higher and consequently a higher gradient is expected to exist. However, going downstream at locations 70 mm and 80 mm the mean gradients become comparable for both the cases. This is due to the higher turbulence levels leading to higher mixing and the gradients being dissipated.

Similar to the thermal flame thickness, a mixing layer thickness can be defined from the resolved quantities on the LES mesh as

$$\delta_\phi = \left(\frac{\phi^{max} - \phi^{min}}{|\nabla\phi|^{max}} \right) \quad (7.2)$$

Then for the CSWB5 case at 40 mm, considering the fact that $\phi^{max} = 1.0$, $\phi^{min} = 0.5$ and the

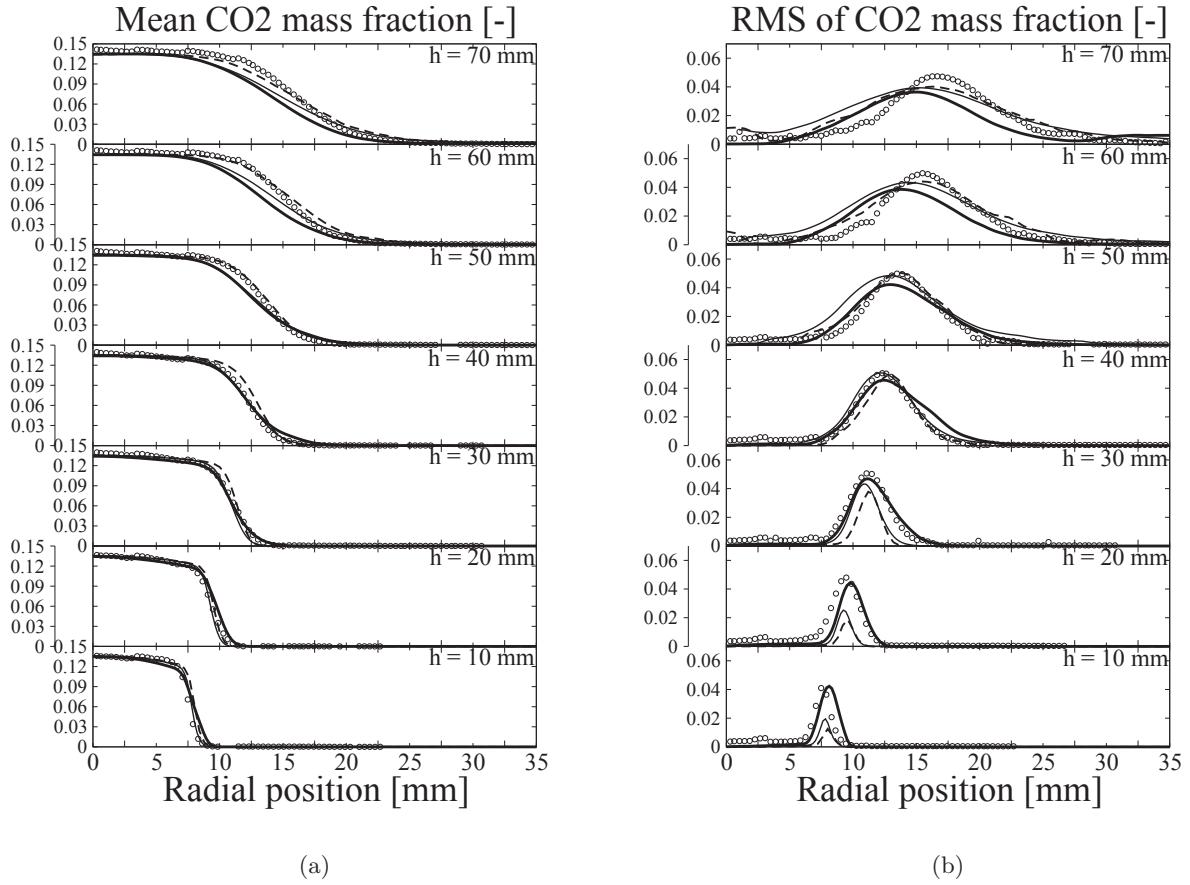


Figure 7.19: CO₂ mass fraction statistics for CSWB5, radial profiles. Symbols: Experiment. LES: — azimuthal averaging coarse mesh, - - - single plane coarse mesh, — azimuthal averaging refined mesh.

most probable value for $|\nabla\phi| \approx 200 \text{ m}^{-1}$ (from Fig. 7.28) an estimate of δ_ϕ can be obtained as 2.5 mm. This is an order of magnitude higher than the typical reaction layer thickness of the laminar flame for the stoichiometric mixture which is around 0.1 mm. Similarly for the CSWB9 case at 40 mm, taking $\phi^{max} = 1.125$, $\phi^{min} = 0.375$ and $|\nabla\phi|^{max} \approx 300 \text{ m}^{-1}$ we obtain $\delta_\phi \approx 2.5 \text{ mm}$ which again is around much larger than the reaction zone thickness. Due to the much larger scales of stratification compared to the flame thickness, it might explain the validity of the premixed flamelet hypothesis to simulate this configuration owing to a quasi-homogeneous propagation of the flame locally.

Premixed, diffusion and partially premixed regimes

To delineate between the possible flame structures and combustion regimes, hybrid flamelet equations were discussed in the literature [93, 229]. These equations employ three scalar dissipation rates, namely $\chi_Z = D_Z|\nabla Z|^2$, the mixture fraction dissipation rate, $\chi_{Y_c} = D_c|\nabla Y_c|^2$, the

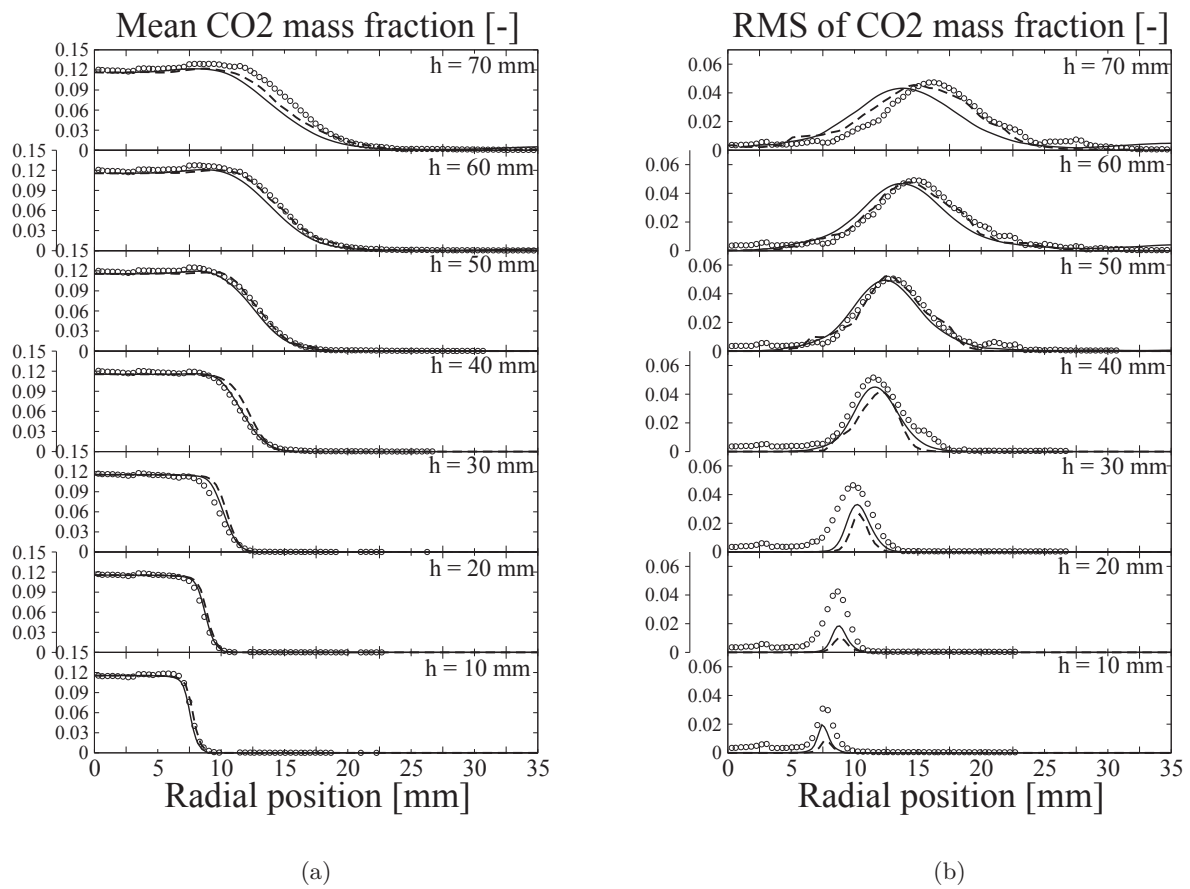


Figure 7.20: CO₂ mass fraction statistics for CSWB9, radial profiles. Symbols: Experiment. LES: — azimuthal averaging, - - - single plane.

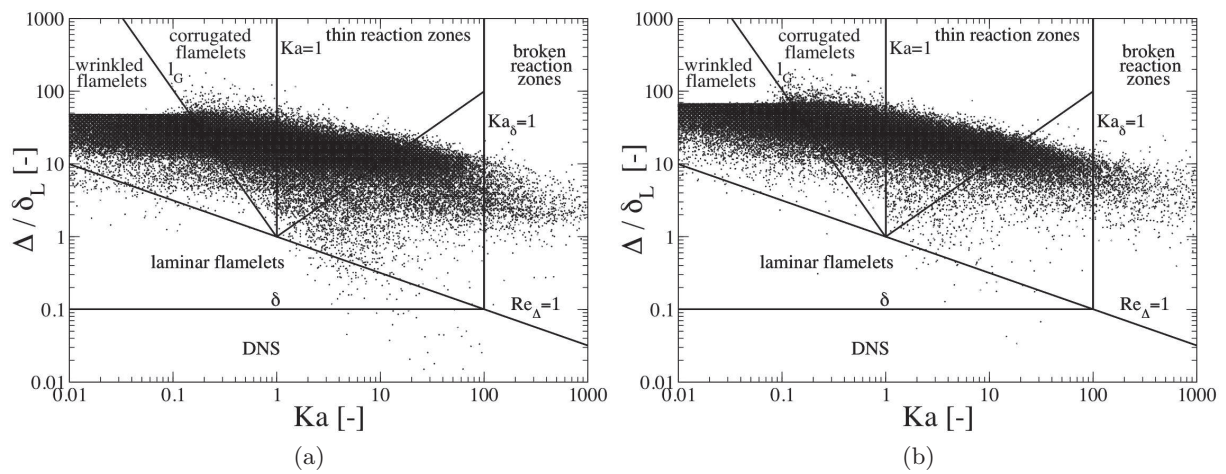


Figure 7.21: LES regime diagrams showing the distribution of flamelets in the computational domain a) CSWB5 b) CSWB9

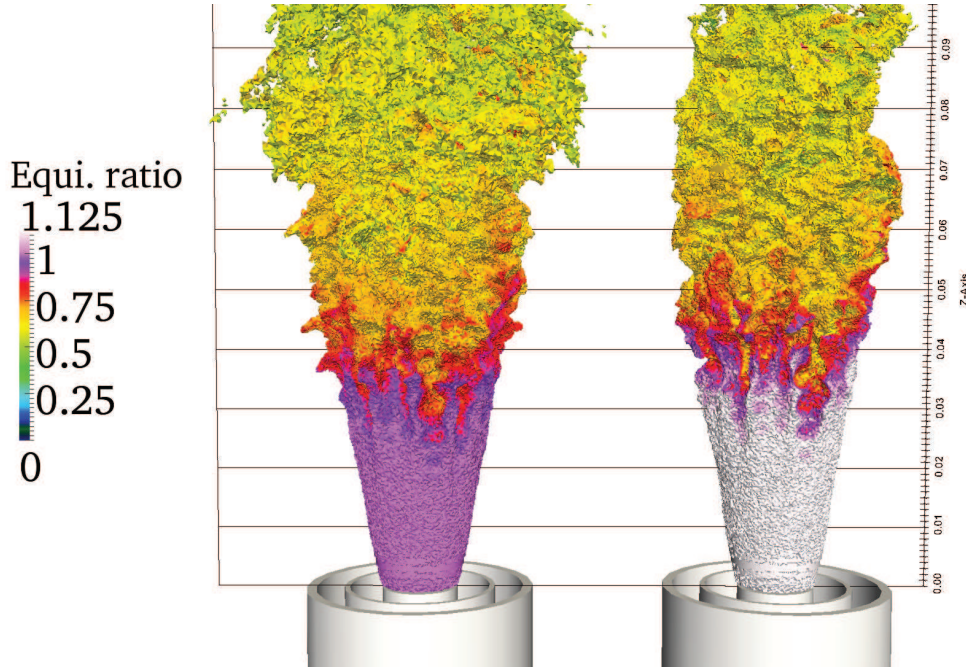


Figure 7.22: Instantaneous progress variable source term conditioned on the progress variable ($0.01 < \tilde{c} < 0.99$) colored by equivalence ratio. Left: CSWB5, Right: CSWB9. Every major division of the axis corresponds to 10 mm.

progress of reaction dissipation rate and $\chi_{Z,Y_c} = D_{Zc} \nabla Z \cdot \nabla Y_c$, the cross scalar dissipation rate. Various levels of approximation exist in these hybrid flamelets, in which the evolution of every species mass fraction Y_i is expressed versus Y_c [184]. The steady unity Lewis and Schmidt numbers case is considered here to study the flame topology on the basis of the gradients orientation only. Within this context the balance equation for Y_i reads [93, 229]:

$$\frac{\partial Y_i}{\partial Y_c} = R^{DF} \frac{\partial^2 Y_i}{\partial Z^2} + R^{PF} \frac{\partial^2 Y_i}{\partial Y_c^2} + R^{PPF} \frac{\partial^2 Y_i}{\partial Y_c \partial Z} + \frac{\dot{\omega}_i}{\dot{\omega}_{Y_c}} \quad (7.3)$$

where the R^i coefficients scale as the inverse of Damköhler numbers: $R^{DF} = \chi_Z / \dot{\omega}_{Y_c}$, $R^{PF} = \chi_c / \dot{\omega}_{Y_c}$, $R^{PPF} = \chi_{Z,c} / \dot{\omega}_{Y_c}$.

When $R^{DF} > R^{PPF} > R^{PF}$ diffusion combustion is expected to control the behavior of the reaction zone, whereas for $R^{PF} > R^{PPF} > R^{DF}$ the flame is premixed controlled, other situations where R^{PPF} dominates would correspond to partially premixed cases. These ratios based on the LES resolved quantities (very weak level of scalar SGS fluctuations) are plotted at various locations along the axis of the stratified burner for the two cases in Figs. 7.29 and 7.30 (not all mesh points are shown). Up to 30 mm only premixed flamelets are observed with equivalence ratios associated with the inner jet value. Therefore R^{PF} is governed largely by the shape of the progress variable source term with some contribution from the local strain proportional to the scalar dissipation rate. From 30 mm - 40 mm where the mixing layer is believed to intersect the flame, some partially premixed flamelets start to appear even though

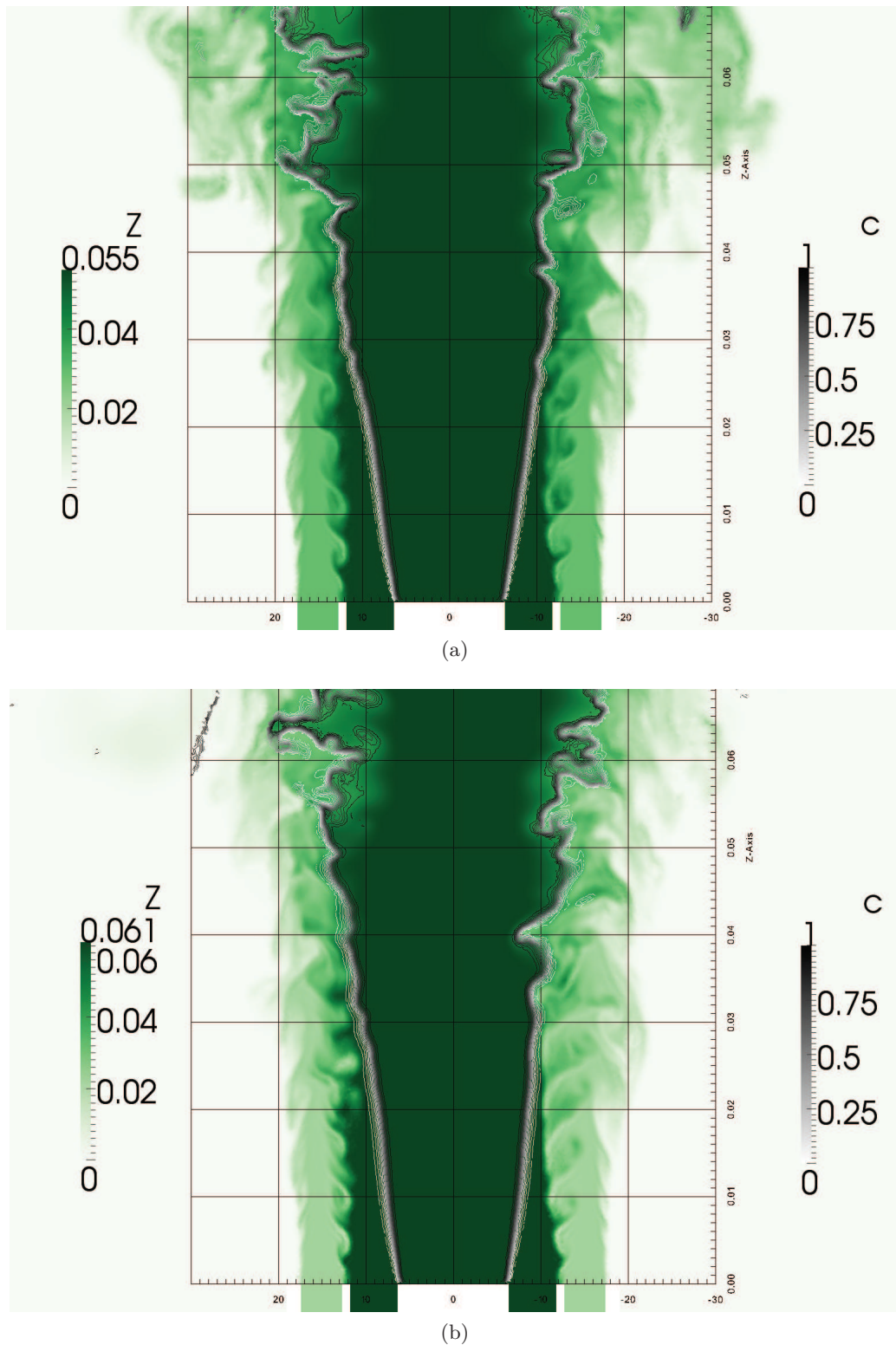


Figure 7.23: Intersection of the mixing layer and the flame a) CSWB5 b) CSWB9. Every major division of the axis corresponds to 10 mm.

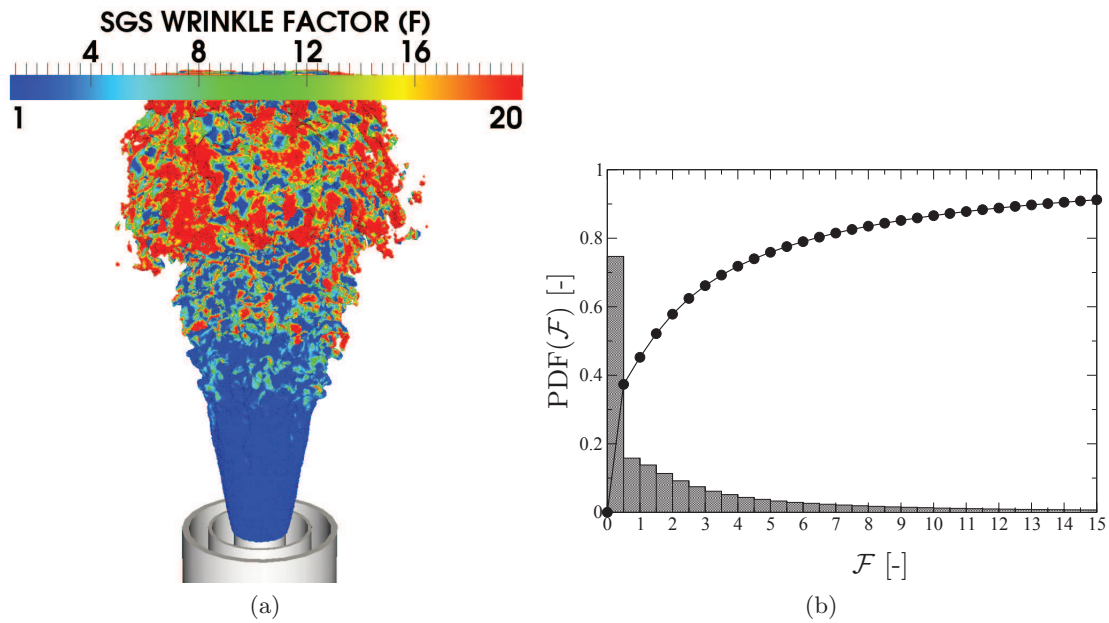


Figure 7.24: CSWB5 (a): Instantaneous source term colored by \mathcal{F} (Eq (4.22)). (b): PDF of \mathcal{F} computed over the mesh.

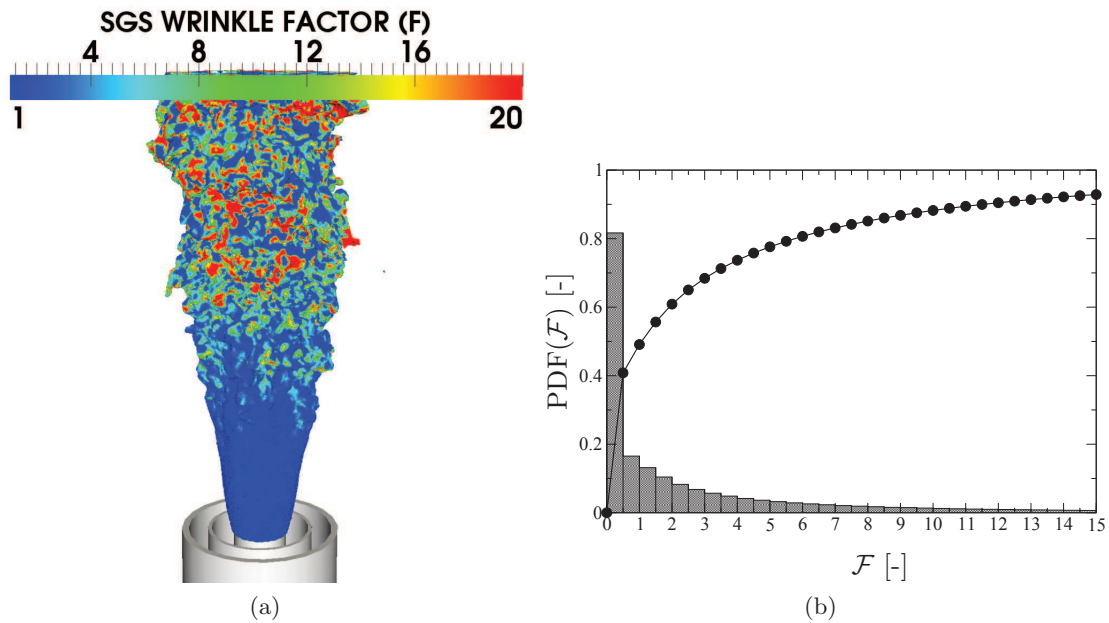


Figure 7.25: CSWB9 (a): Instantaneous source term colored by \mathcal{F} (Eq (4.22)). (b): PDF of \mathcal{F} computed over the mesh.

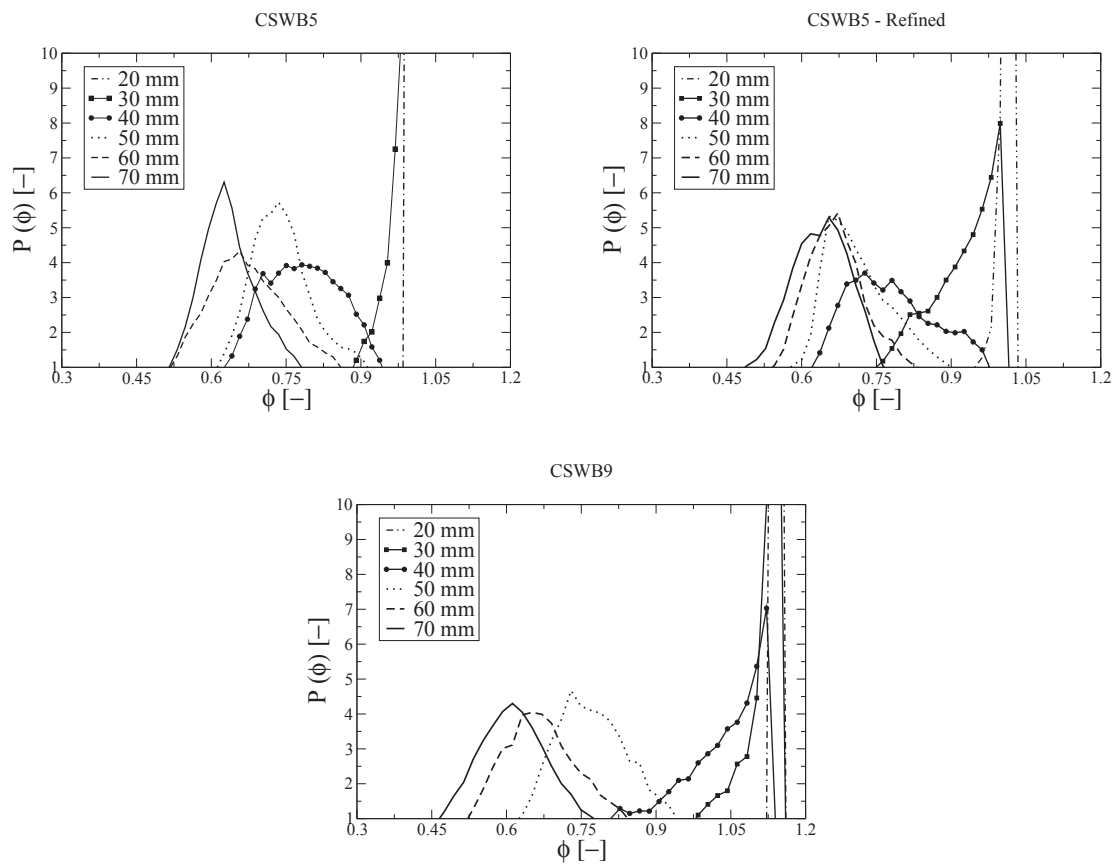


Figure 7.26: Probability distribution of equivalence ratio at different heights from the burner exit conditioned on the progress variable ($0.01 < \tilde{c} < 0.99$)

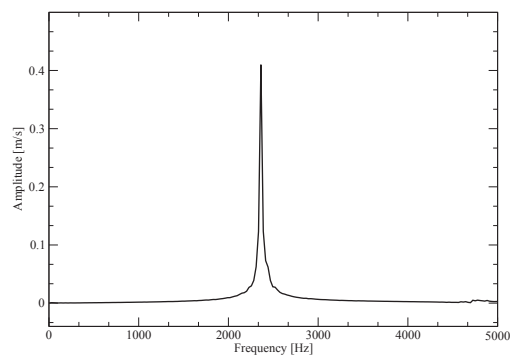


Figure 7.27: Frequency spectra of the axial velocity of a probe place in the shear layer of the inner and outer jet

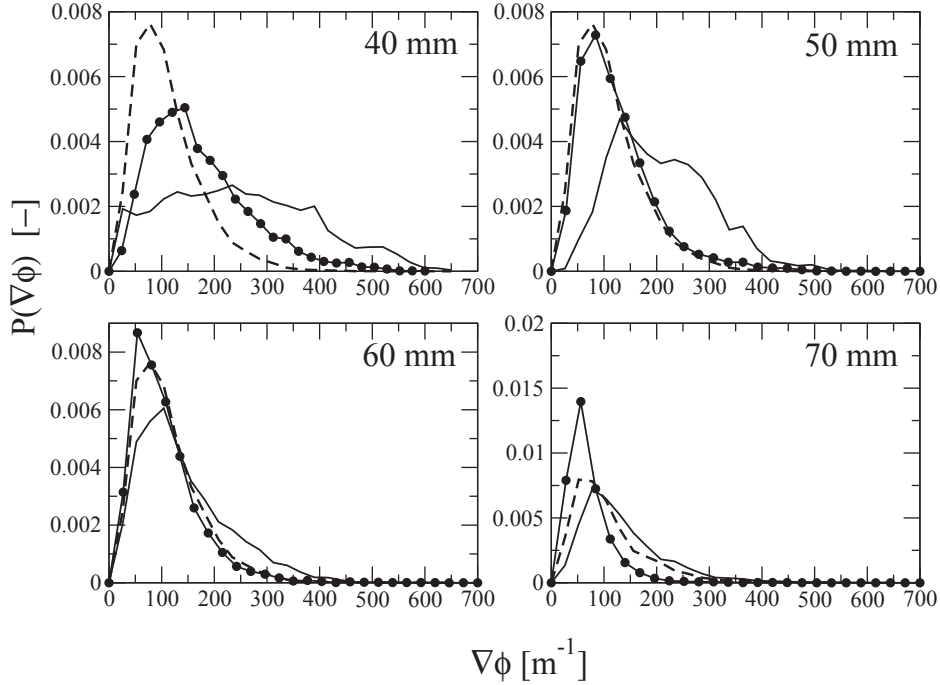


Figure 7.28: Probability distribution of instantaneous gradient of equivalence ratio as a function of equivalence ratio gradient at different heights for CSWB5 and CSWB9 conditioned on progress variable ($0.01 < \tilde{c} < 0.99$). Lines with circles: CSWB5 coarse mesh, Dashed line: CSWB5 refined mesh. Line: CSWB9 coarse mesh

premixed mode is the dominant one. Finally, between 40 - 70 mm, varying equivalence ratios are encountered by the flame and hence for R^{PF} points are observed everywhere with no specific trend of evolution which was observed at locations close to the burner (0 - 30 mm). In addition, in this zone of the flame, the number of points exhibiting non-negligible values for R^{PPF} increases. This is more pronounced in the highly stratified case CSWB9. In both cases, the diffusion flame regime is observed to be negligible. This leads us to the conclusion that downstream of this burner the reaction zones are in fact composed of almost independent collection of premixed flames at various equivalence ratios.

Focussing on the weak partially premixed burning mode observed, R^{PPF} used in Eq. 7.3 is indirectly controlled by the alignment of the flame and mixing vectors which will be discussed in the next section.

Alignment of the flame and mixing vectors

Stratified flames could be defined as back supported or front supported depending on the alignment of the flame propagation direction with the mixture fraction gradient (See § 2.3). In a

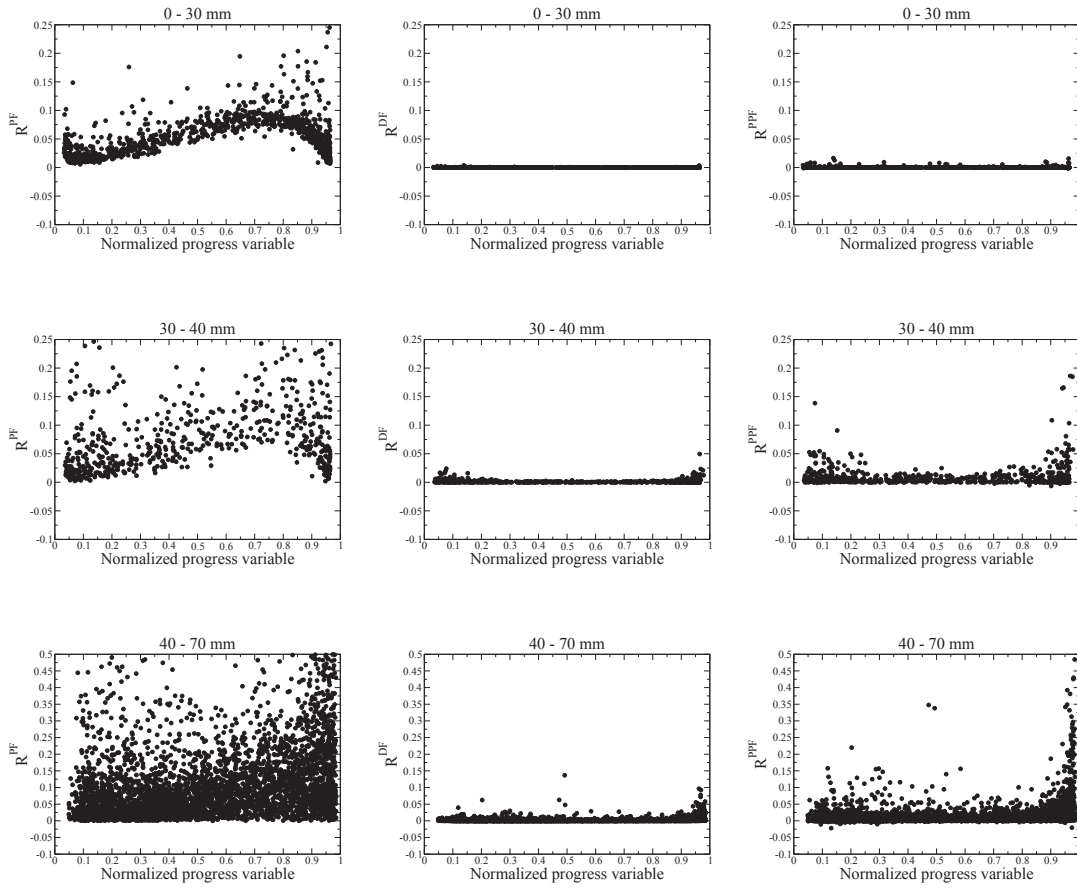


Figure 7.29: CSWB5 flamelets. Left: Premixed flamelets. Middle: Diffusion flamelets. Right: Partially premixed flamelets

back supported flame, the direction of propagation is from a rich mixture to a leaner zone and the vice versa for the front supported flames. Mathematically, we can define the orientation of the flame propagation and the mixture fraction gradient vector to identify these modes as

$$\theta = \cos^{-1} \left(\frac{\nabla \tilde{c} \cdot \nabla \tilde{Z}}{|\nabla \tilde{c}| |\nabla \tilde{Z}|} \right) \quad (7.4)$$

such that $\theta = 0^\circ$ denotes pure back supported flames and $\theta = 180^\circ$ denotes complete front supported combustion. Figure 7.31 shows the normalized number distribution of the angle, $P(\theta)$ versus θ from an instantaneous data and the time averaged data, both are shown to measure the impact of the resolved LES fluctuations on flame topology.

For the instantaneous case, the more probabilistic value of the angle observed for both CSWB5 and CSWB9 is around 20° which means that the combustion is predominantly back supported. In these low turbulent flames, this can be inferred also from the mean values. The instantaneous and time averaged data yield almost the same probability trends indeed, with

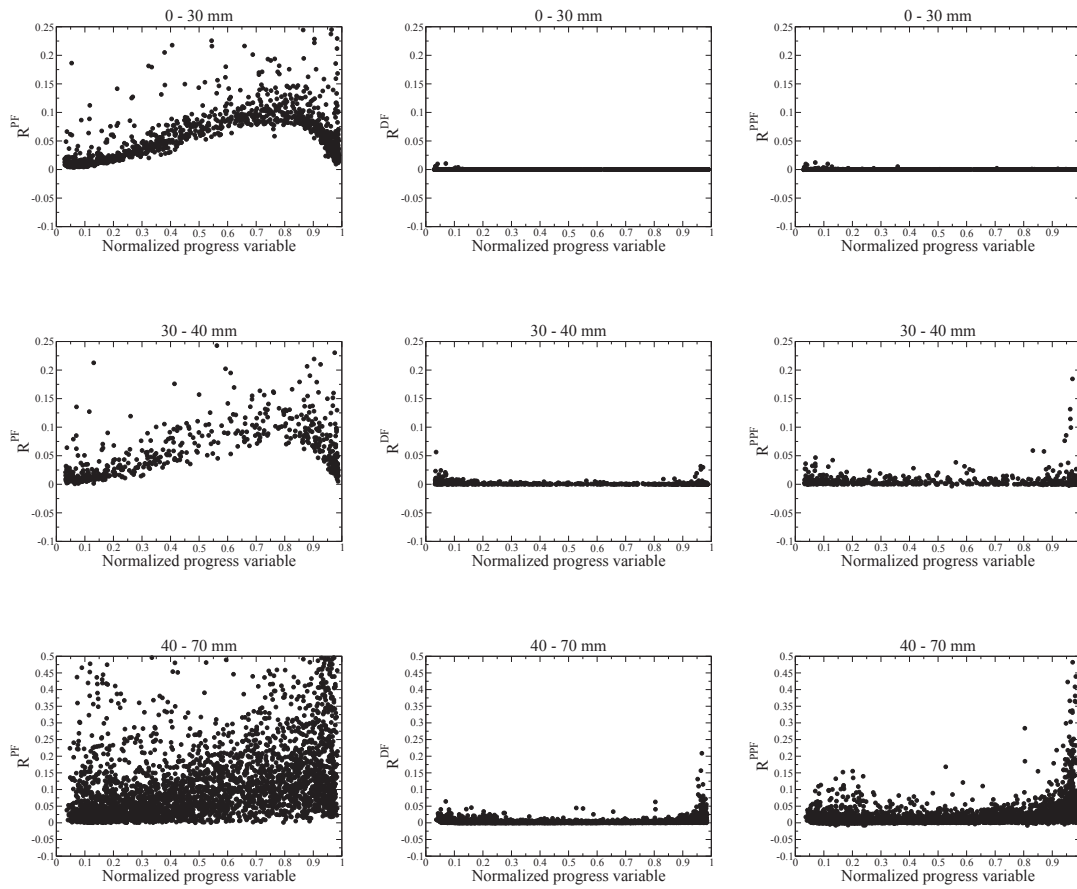


Figure 7.30: CSWB9 flamelets. Left: Premixed flamelets. Middle: Diffusion flamelets. Right: Partially premixed flamelets

small deviations observed, except in the most turbulent zones at 30 mm and 40 mm where the flame intersects the mixing layer. There, the mean values lead to a slightly wider θ distribution indicating front supported combustion. At downstream locations, the mean flame starts to align itself to the mixture fraction gradient as seen in Fig. 7.23 where the flame can be seen to follow the shear layer closely.

7.4 Summary and conclusions of CSWB5 and CSWB9 simulations

Large eddy simulation of the two stratified non-swirling configurations of the Cambridge swirl burner was reported.

The differential diffusion effect leading to the increase of mixture fraction in the recirculation one was observed for the stratified cases as well. However, the extent of this accumulation was

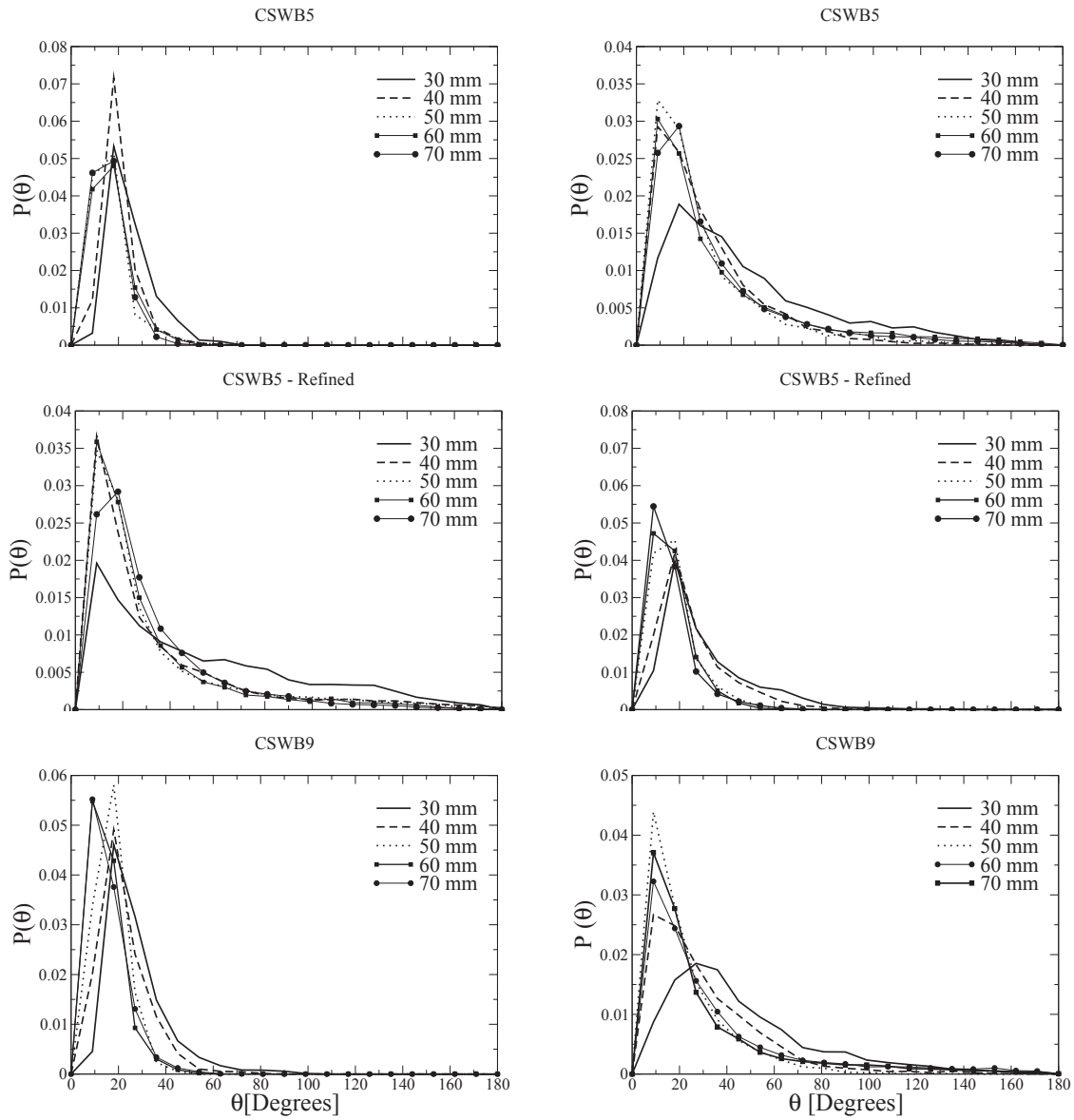


Figure 7.31: Probability distribution plot of θ as a function of θ conditioned over progress variable ($0.01 < \tilde{c} < 0.99$). Left: From instantaneous data. Right: From time averaged data

found to reduce from the CSWB1 case to the CSWB9 case. The accumulation of carbon atoms is present in the recirculation zone for all the cases which is in the form of CO for the stratified cases whereas CO₂ accumulation is dominant in the CSWB1 configuration.

The temperature statistics showed an over prediction in the recirculation zone compared to the experiments. This is believed to be due to the heat losses present at the bluff body walls which are not accounted in the model. The RMS profiles for the velocity and scalars in the flame zone close to the burner exit were under predicted on the coarse mesh in comparison to the refined mesh simulation which recovers the right level of fluctuations. A possible reason is the damping of the higher fluctuations by the larger filter width on the coarse mesh.

A multi-dimensional flamelet composition analysis at the resolved scales of the LES for the two stratified cases showed a dominant premixed mode of combustion with some level of partially premixed flamelets but no diffusion controlled combustion. It was also found that the combustion is composed of predominantly back supported flames with the flame tending to align parallel to the mixture stratification.

The reasonable predictions show that when the scale of mixing is much larger than the flame thickness, a quasi-homogeneous propagation is expected to happen and a premixed flamelet could be a good representation.

Conclusions and Perspectives 8

8.1 Conclusions

The main contributions and conclusions of this thesis work are summarized below:

- (i) A turbulent combustion modeling strategy for Large Eddy Simulation based on a filtered laminar flame probability density function (FLF-PDF) was presented. In this subgrid scale closure when the flame wrinkling is unresolved, the flame filter size is not fixed a priori but depends on the level of scalar unresolved fluctuations, calibrated using scalar variances. By solving four balance equations, this approach perfectly reproduces the signal of a laminar flame to which a Gaussian Favre filter was applied, the flame being solved over a coarse grid; both one-dimensional and two-dimensional Bunsen test cases were performed to validate the model. Then, the discussed approach was applied to the simulation of the Cambridge burner studied by Prof. Hochgreb and co-workers [3]. Three non-swirling configurations were studied namely, the lean premixed case (CSWB1) and the two stratified configurations (CSWB5 and CSWB9).
- (ii) The 3D LES of the Cambridge burner showed significant re-laminarisation effects for all the three configurations studied. As a consequence, flamelet model with presumed Beta-PDF (PCM-FPI), which relies heavily on the scalar dissipation rate closure based on the turbulent viscosity was found to have difficulties in predicting the proper laminar flame behaviour in these zones. A modified scalar dissipation rate closure was however found to improve the prediction. With a switching model based on FLF-PDF, the flow resolved regions gave an overall good agreement with the experimental statistics emphasizing the requirement of preserving the laminar flame invariants on a coarse mesh in combustion model. In addition, the burner simulation showed the presence of asymmetry, rendering the comparison of experiments and simulations relying only on 1D profiles difficult.
- (iii) Measurements of this burner had shown the presence of significant differential diffusion leading to accumulation of carbon atoms in the recirculation zone. Consequently, a mixture fraction definition using Bilger's formula evaluated from the measured species was also found to reflect the accumulation. Therefore, a differential diffusion modeling strategy to capture the accumulation of mixture fraction in the recirculation zone behind the bluff-body was also proposed and tested during this work. The LES analysis showed that the difference in residence times across the flame is a good marker of this differential diffusion

effect. Subsequently, a global differential diffusion number based on the residence times was proposed to quantify the differential diffusion effect and determine the presence of this phenomena in burners.

- (iv) The average velocity statistics were found to be well captured in all the three cases as well as in the non-reacting flow. The fluctuations were however under predicted in the flame zone on a coarse mesh, which could be associated to the damping of fluctuations by a larger filter on the coarse mesh. A refined mesh simulation in the stratified case was able to recover the fluctuations emphasizing this fact.
- (v) The predicted temperature in the recirculation zone was close to the equilibrium value and higher than those observed in the measurements. This deviation from the prediction is believed to be due to the heat losses present at the bluff body walls which are not accounted in the model. Similarly, a small over prediction of the velocity is also seen in the recirculation zone possibly arising from the heat loss. The temperature fluctuations followed a trend similar to that of the velocity.
- (vi) The species profiles showed interesting trends. Accumulation of carbon atoms in the recirculation zone was visible in the CO and CO₂ profiles for all the three cases studied. This accumulation was in the form of CO for the stratified cases whereas CO₂ accumulation was dominant in the fully premixed configuration. It could be argued that the leaner premixed mixture in the CSWB1 case ensures sufficient oxygen to oxidize the accumulated CO to CO₂ leading to this particular observation. In the flame zone, simulations could not predict the CO profiles in average and fluctuations, which could be considered as a limitation of the flamelet hypothesis. The flamelet hypothesis however gave good prediction of the mean CH₄ and CO₂ mass fractions as seen in the case of temperature also.
- (vii) Analysis of the stratified simulations showed that when the scale of mixing is much larger than the flame thickness, a quasi-homogeneous propagation is expected to happen and a premixed flamelet could be a good representation. The overall good agreement with the experiments shows that the non-swirling premixed and stratified configurations of this burner can be well described by retaining a flamelet hypothesis as observed by Sweeney et al. [3] also. A hybrid premixed/diffusion flamelet analysis at the resolved scales of the LES for the two stratified cases did not reveal a staged combustion in contrast to the literature. The experimentalists also have not reported the presence of a diffusion controlled combustion in this burner. It was also found that the combustion is composed of predominantly back supported flames with the flame tending to align parallel to the mixture fraction stratification.

8.2 Perspectives

Future developments for this thesis work is envisaged in the following directions.

1. Inclusion of heat loss effects in the model could be an immediate extension to this work. As seen in this stratified burner and others [48], modeling heat loss effects [238, 239] is important to improve the prediction of the scalar and velocity fields.
2. Towards improving the model in the wrinkling resolved regime, a variable filter width as a function of the local mesh resolution could be considered. Implementing this improvement might not be straight forward on an unstructured mesh since the characteristic filter size defined from the computational cell volume as $\mathcal{V}^{1/3}$ need not be smooth, resulting in numerical instability. A smoother metric of the LES characteristic filter size could be considered based on the edge size or by filtering the characteristic LES mesh size for ensuring numerical stability. On a structured mesh, introducing the variable filter size is assumed to be easier owing to their much smoother variation.
3. Scalar dissipation rate modeling is an important ingredient of this approach as well as in other PDF based models. An improved model for scalar dissipation rate which can account for the proper laminar flame propagation can avoid shifting between the two models and overcome the uncertainties involved in determining the subgrid velocity fluctuations. In addition, from the point of view of stratified and non-premixed combustion, cross scalar dissipation rates also need to be accounted.
4. Comparison of numerical results are normally made to unfiltered data (or data filtered at the measurement resolution level) of the experiments. Since in this model, when the SGS mixture fraction fluctuations are resolved, a deconvolution can be performed to get back the unfiltered scalar data. This information can be used to compare the experimental and numerical results on the same filter basis.
5. An improvement of the differential diffusion modeling strategy proposed here can be made by tabulating the scalars as a function of Z_d which is varying in the premixed flame rather than using a fixed inlet Z of a laminar premixed flame. This is similar in spirit to the approach used by Regele et al. [186] to account for thermo-diffusive instabilities in laminar H_2 flames. However, with the present model proposed in this work, a constant Lewis number assumption need not be used which was used by Regele et al.
6. Explicit LES filter which commutes with the derivative operator and is a normalized low pass filter in physical space can be used directly to presume the PDF of the scalars as well. By following the same approach mentioned in the work, filtered chemical tables can be generated for these PDFs also. This will allow both the momentum and the scalar equation closures to be based on the same characteristic filter width which is not the case in models like PCM-FPI coupled with implicit LES filtering.

Derivation of progress variable diffusivity

A

The diffusivity D_{Y_c} of the progress variable has an important role in combustion modeling and need to be determined correctly. The value of D_{Y_c} can be derived from the conservation equations as below.

For a reacting species Y_i , the steady conservation equation can be written in terms of propagation and reaction term as

$$\nabla \cdot (\rho(\mathbf{u} + \mathbf{V}_i + \mathbf{V}_a)Y_i) = \rho\dot{\omega}_i \quad (\text{A.1})$$

where \mathbf{V}_i is the diffusive velocity of the species. \mathbf{V}_a is the correction velocity which appears to ensure mass conservation. An expression for the corrective velocity \mathbf{V}_a can be obtained by summing the general transport Eq. A.1 over all the species. The corrective velocity, \mathbf{V}_a is then obtained as

$$\mathbf{V}_a = - \sum_{i=1}^{N_{sp}} \mathbf{V}_i Y_i \quad (\text{A.2})$$

where N_{sp} is the number of species.

The diffusive velocity \mathbf{V}_i in terms of molar fraction can be expressed as

$$\mathbf{V}_i = -D_i \frac{\nabla X_i}{X_i} \quad (\text{A.3})$$

where D_i is the molecular diffusivity of species Y_i obtained from a Curtiss and Hirschfelder approximation. It is useful to express the diffusive velocity as a function of mass fraction. Rewriting the diffusive velocity in terms of mass fraction,

$$\mathbf{V}_i = -D_i \frac{\nabla(Y_i \bar{W})}{Y_i \bar{W}} \quad (\text{A.4})$$

The mass fraction to molar fraction conversion can be carried out as

$$Y_i = X_i \frac{W_i}{\bar{W}} \quad (\text{A.5})$$

where W_i is the molecular weight of individual species and \bar{W} is the molar mass of the mixture.

If we define the progress variable as $Y_c = \sum_{k=1}^K \alpha_k Y_k$, a linear combination of mass fractions of certain species, then the transport equation for Y_c can be obtained from general transport Eq. A.1 after multiplying by appropriate coefficients and adding them as

$$\sum_{k=1}^K \nabla \cdot (\rho(\mathbf{u}\alpha_k Y_k + \alpha_k \mathbf{V}_k Y_k + \alpha_k \mathbf{V}_a Y_k)) = \sum_{k=1}^K (\rho\alpha_k \dot{\omega}_k) \quad (\text{A.6})$$

Using the definition of Y_c , the equation can be re-written and rearranged as

$$[\nabla \cdot (\rho \mathbf{u} Y_c) - \rho \dot{\omega}_{Y_c}] = -[\nabla \cdot (\rho \mathbf{V}_a Y_c + \sum_{k=1}^K \alpha_k \mathbf{V}_k Y_k)] \quad (\text{A.7})$$

The term on the LHS is equal to the diffusive term of Y_c transport equation. Therefore,

$$\nabla \cdot (\rho D_{Y_c} \nabla Y_c) = -[\nabla \cdot (\rho(\mathbf{V}_a Y_c + \sum_{k=1}^K \alpha_k \mathbf{V}_k Y_k))] \quad (\text{A.8})$$

Setting the constraint that the terms inside the derivative operator to be equal on either sides, one can finally arrive at

$$D_{Y_c} = -\frac{1}{\nabla Y_c} (\mathbf{V}_a Y_c + \sum_{k=1}^K \alpha_k \mathbf{V}_k Y_k) \quad (\text{A.9})$$

For e.g. if we define $Y_c = Y_{CO} + Y_{CO_2}$, [A.9](#) can be expressed as below

$$D_{Y_c} = -\frac{1}{\nabla Y_c} (\mathbf{V}_a Y_c + \mathbf{V}_{CO} Y_{CO} + \mathbf{V}_{CO_2} Y_{CO_2}) \quad (\text{A.10})$$

Method of tabulation for FLF-PDF

B

The main step in filtered tabulated chemistry is to determine for a given (\tilde{c}^*, S_c^*) combination, the value of the Favre filtered scalar $\tilde{\phi}(\tilde{c}^*, S_c^*)$ and store it in a look up table.

The FLF-PDF in the (\tilde{c}, S_c) space is simply a Gaussian Favre filter in (x, Δ) space. Therefore, to perform the Gaussian Favre filter operation, a physical space location \tilde{x}^{Δ^*} and a filter width Δ^* requires to be determined such that the laminar flame solution profile of c at location \tilde{x}^{Δ^*} , filtered with a Gaussian Favre filter of filter width Δ^* , yields (\tilde{c}^*, S_c^*) . In other words, $\tilde{\phi}(\tilde{c}^*, S_c^*) = \tilde{\phi}(\tilde{x}^{\Delta^*}, \Delta^*)$. Therefore for tabulation, the value $\tilde{x}^{\Delta}(\tilde{c}^*, S_c^*)$ and $\Delta(\tilde{c}^*, S_c^*)$ need to be determined. Since the flame signal involves a non-linear relation between the species and the physical space coordinate, finding an analytical expression for $\tilde{x}^{\Delta}(\tilde{c}^*, S_c^*)$ and $\Delta(\tilde{c}^*, S_c^*)$ is not straightforward. Hence, an interpolation technique is used to construct the look up table. In order to calculate $\tilde{x}^{\Delta}(\tilde{c}^*, S_c^*)$ and $\Delta(\tilde{c}^*, S_c^*)$, the following steps are pursued:

1. For a given mixture fraction, the Favre filtered progress variable, $\tilde{c}(\tilde{x}^{\Delta}, \Delta)$ is determined for a large number of filter widths so that it covers the full range of S_c values. \tilde{x}^{Δ} denotes the x -position where the \tilde{c} -value is found for the filter of size Δ and was used to define the

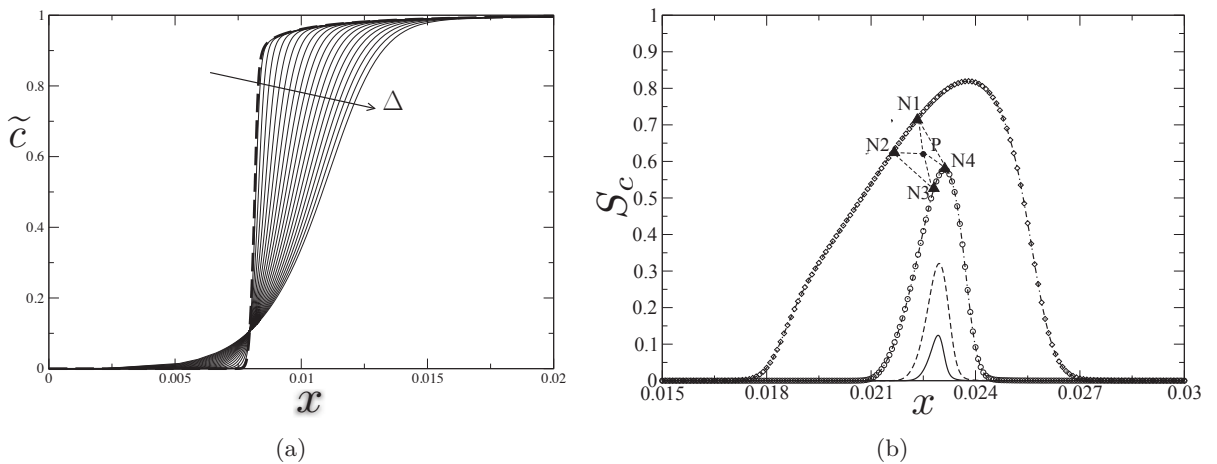


Figure B.1: Laminar premixed methane air flame at $\phi = 0.75$. (a) Filtered \tilde{c} profiles at different filter widths (b) S_c profiles for different filter widths. — $\Delta = 5\delta_L$, -- $10\delta_L$, -o- $20\delta_L$, -·◇- $50\delta_L$.

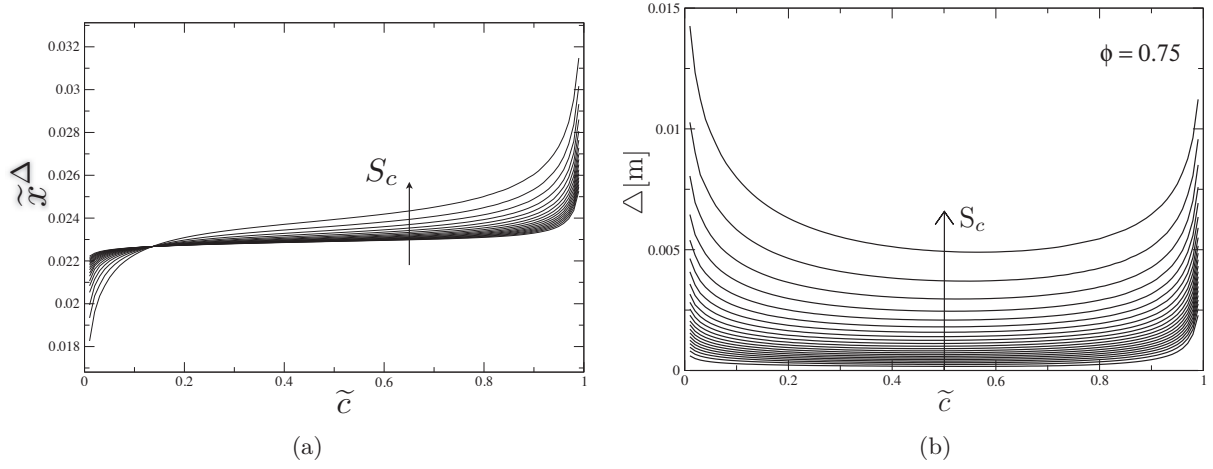


Figure B.2: Quantities obtained by numerical interpolation. (a) $\tilde{x}^\Delta = \tilde{x}^\Delta(\tilde{c}, S_c)$. (b) $\Delta = \Delta(\tilde{c}, S_c)$.

FLF-PDF in Eq. (4.5). Plots of $\tilde{c}(\tilde{x}^\Delta, \Delta)$ and $S_c(\tilde{x}^\Delta, \Delta)$ for four different filter widths are shown in Fig. B.1a and Fig. B.1b respectively.

- The next step is to determine the combination $(\tilde{x}^{\Delta*}, \Delta^*)$, which corresponds to a desired (\tilde{c}^*, S_c^*) . For every filtered profile of the progress variable, we can identify a combination of two points in \tilde{x}^Δ such that \tilde{c}^* is bounded by them. Now, for these set of points if we also impose the condition that S_c^* is also bounded as well by these points, we end up identifying four points finally which surround (\tilde{c}^*, S_c^*) . To summarize, four points $(\tilde{x}_i^\Delta, \Delta_i)$ are identified such that both \tilde{c}^* and S_c^* are bounded by them, where $i = 1, 4$ denotes the four neighbours. Figure B.1b gives a representation of the desired point (\tilde{c}^*, S_c^*) and the four neighbouring points. It should be noted that Fig. B.1b is just an illustration and in the actual situation interpolation is performed between very closely located points. Once the four neighbours are identified, $\tilde{x}^{\Delta*}$ can be calculated from an inverse distance weighting method as

$$\tilde{x}^{\Delta*} = \sum_{i=0}^4 \frac{W_i(\tilde{c}_i, S_{c_i}) x_i}{\sum_{j=0}^4 W_j(\tilde{c}_i, S_{c_i})} \quad (\text{B.1})$$

where

$$W_i(\tilde{c}_i, S_{c_i}) = \frac{1}{d_i} \quad (\text{B.2})$$

and d_i is the distance between (\tilde{c}^*, S_c^*) and (\tilde{c}_i, S_{c_i}) expressed as

$$d_i = \sqrt{(\tilde{c}^* - \tilde{c}_i)^2 + (S_c^* - S_{c_i})^2} \quad (\text{B.3})$$

A similar procedure is adopted to evaluate the corresponding filter width Δ^* as well. Plots of $\tilde{x}^\Delta(\tilde{c}, S_c)$ and $\Delta(\tilde{c}, S_c)$ obtained by the method of interpolation described above are shown in Figs. B.2a and B.2b.

3. Once $(\tilde{x}^{\Delta^*}, \Delta^*)$ is determined any filtered scalar $\tilde{\phi}(\tilde{c}^*, S_c^*)$ can be evaluated by considering $\phi(\tilde{x}^{\Delta^*})$ and performing a Favre filtering with a filter width Δ^* . $\phi(\tilde{x}^{\Delta^*})$ is the value of the scalar at any physical location and is determined from the unfiltered laminar flame solution by using a 3 point lagrangian polynomial interpolation.

Using this procedure, a look-up table of $\tilde{\phi}(\tilde{c}^*, S_c^*)$ is built and then accessed during the simulations, one-dimensional flame filtering is thus not needed during the LES runs.

List of Publications



C.1 Journal

1. S. Nambully, P. Domingo, V. Moureau, L. Vervisch. A Filtered-Laminar-Flame PDF sub-grid scale closure for LES of premixed turbulent flames: Part I: Formalism and application to a bluff-body burner with differential diffusion. *Combustion and Flame*, submitted.
2. S. Nambully, P. Domingo, V. Moureau, L. Vervisch. A Filtered-Laminar-Flame PDF sub-grid scale closure for LES of premixed turbulent flames: Part II: Application to a stratified bluff-body burner. *Combustion and Flame*, submitted.

C.2 Conferences

1. G. Godel, S. Nambully, P. Domingo, V. Moureau, and L. Vervisch. Uncertainty analysis in NO_x prediction: Impact of SGS scalar variance estimation in LES using presumed PDF. In *European Combusting Meeting, Cardiff, UK*. British section of the Combustion Institute, March 2011.
2. S. Nambully, P. Domingo, V. Moureau, and L. Vervisch. Modeling differential diffusion in large eddy simulation of a bluff body stabilized premixed weakly-turbulent flame. In *TNF, Eleventh International Workshop on Measurement and Computation of Turbulent Flames*, 64–65, 2012.
3. S. Nambully, P. Domingo, V. Moureau, and L. Vervisch. Modeling differential diffusion in large eddy simulation of a bluff body stabilized premixed weakly-turbulent flame. In *Turbulence, Heat and Mass Transfer 7*. Begell House Inc, 2012.

References

- [1] N. W. M. Ko, W. T. Chan, The inner regions of annular jets, *Journal of Fluid Mechanics* 93 (03) (1979) 549–584. [viii](#), [10](#), [11](#)
- [2] L. Blum, Flow field and turbulence measurements in different non-reacting and reacting flow configurations, Ph.D. thesis, Swiss Federal Institute of Technology, Zurich (2005). [viii](#), [10](#), [11](#)
- [3] M. S. Sweeney, S. Hochgreb, M. J. Dunn, R. S. Barlow, The structure of turbulent stratified and premixed methane/air flames I: Non-swirling flows, *Combustion and Flame* 159 (9) (2012) 2896–2911. [6](#), [13](#), [15](#), [26](#), [69](#), [127](#), [128](#)
- [4] R. S. Barlow, M. J. Dunn, M. S. Sweeney, S. Hochgreb, Effects of preferential transport in turbulent bluff-body-stabilized lean premixed CH₄/air flames, *Combustion and Flame* 159 (8) (2012) 2563–2575. [6](#), [31](#), [65](#)
- [5] C. Del Taglia, Numerical investigation of the non-reacting unsteady flow behind a disk stabilized burner with large blockage, Ph.D. thesis, Swiss Federal Institute of Technology (2002). [10](#), [12](#)
- [6] T. W. Davies, J. M. Beer, Flow in the wake of bluff-body flame stabilizers, *Symposium (International) on Combustion* 13 (1) (1971) 631–638. [10](#)
- [7] D. F. G. Durao, J. H. Whitelaw, Velocity characteristics of the flow in the near wake of a disk, *Journal of Fluid Mechanics* 85 (02) (1978) 369–385. [11](#), [12](#)
- [8] K. Li, S. Richard, A study of cold and combusting flow around bluff-body combustors, *Combustion Science and Technology* 52 (4-6) (1987) 173–206. [11](#), [12](#)
- [9] R. Huang, C. Lin, Velocity field of a bluff-body wake, *Journal of Wind Engineering and Industrial Aerodynamics* 85 (1) (2000) 31–45. [12](#)
- [10] H. J. Sheen, W. J. Chen, S. Y. Jeng, T. L. Huang, Correlation of swirl number for a radial-type swirl generator, *Experimental thermal and fluid science* 12 (4) (1996) 444–451. [12](#)
- [11] M. Vanierschot, E. Van den Bulck, Influence of swirl on the initial merging zone of a turbulent annular jet, *Physics of fluids* 20 (2008) 105–104. [12](#)

- [12] T. Frania, C. Hirsch, Measurements of the turbulent flow field generated by a single annular jet, in: XVI National Conference on Fluid Mechanics, Waplewo, Poland, 2004. [12](#)
- [13] F. Schmitt, B. Hazarika, C. Hirsch, LDV measurements of the flow field in the nozzle region of a confined double annular burner, *Journal of Fluids Engineering* 123 (2) (2001) 228–236. [12](#)
- [14] S. B. Pope, J. H. Whitelaw, The calculation of near-wake flows, *Journal of Fluid Mechanics* 73 (1) (1976) 9–32. [12](#)
- [15] M. Leschziner, W. Rodi, Calculation of annular and twin parallel jets using various discretization schemes and turbulence-model variations, *Journal of Fluids Engineering* 103 (2) (1981) 352–361. [12](#)
- [16] J. J. McGuirk, A. Taylor, J. H. Whitelaw, The assessment of numerical diffusion in upwind difference calculations of turbulent recirculating flows, *Turbulent Shear Flows* 3 1 (1982) 206–224. [12](#)
- [17] D. F. G. Durao, J. C. F. Pereira, Calculation of isothermal turbulent three-dimensional free multijet flows, *Applied Mathematical Modelling* 15 (7) (1991) 338–350. [12](#)
- [18] K. Akselvoll, P. Moin, Large-eddy simulation of turbulent confined coannular jets, *Journal of Fluid Mechanics* 315 (1996) 387–411. [12](#)
- [19] B. V. Johnson, J. C. Bennett, Statistical characteristics of velocity, concentration, mass transport, and momentum transport for coaxial jet mixing in a confined duct, *Journal of Engineering for Gas Turbines and Power* 106 (1) (1984) 121–128. [12](#)
- [20] P. Jochmann, A. Sinigersky, M. Hehle, O. Schäfer, R. Koch, H.-J. Bauer, Numerical simulation of a precessing vortex breakdown, *International Journal of Heat and Fluid Flow* 27 (2) (2006) 192 – 203. [12](#)
- [21] B. Wegner, A. Maltsev, C. Schneider, A. Sadiki, A. Dreizler, J. Janicka, Assessment of unsteady RANS in predicting swirl flow instability based on LES and experiments, *International Journal of Heat and Fluid Flow* 25 (3) (2004) 528–536. [12](#)
- [22] D. D, S. A, M. J. J, D. M, Comparison of Unsteady Reynolds Averaged Navier–Stokes and Large Eddy Simulation computational fluid dynamics methodologies for air swirl fuel injectors, *Journal of Engineering for Gas Turbines and Power* 131 (1) (2009) 011502. [12](#)
- [23] M. Garcia-Villalba, J. Frohlich, W. Rodi, Identification and analysis of coherent structures in the near field of a turbulent unconfined annular swirling jet using large eddy simulation, *Physics of fluids* 18 (5). [12](#)

- [24] X. Lu, S. Wang, H. Sung, S. Hsieh, V. Yang, Large-eddy simulations of turbulent swirling flows injected into a dump chamber, *Journal of Fluid Mechanics* 527 (1) (2005) 171–195. [12](#)
- [25] S. McIlwain, A. Pollard, Large eddy simulation of the effects of mild swirl on the near field of a round free jet, *Physics of Fluids* 14 (2) (2002) 653–661. [12](#)
- [26] C. Pierce, P. Moin, Progress-variable approach for large-eddy simulation of non-premixed turbulent combustion, *Journal of Fluid Mechanics* 504 (1) (2004) 73–97. [12](#), [42](#), [43](#)
- [27] J. P. Longwell, Flame stabilization by bluff bodies and turbulent flames in ducts, *Symposium (International) on Combustion* 4 (1) (1953) 90–97. [13](#)
- [28] E. A. de Zubay, A study of flame stability based on reaction rate theory, *American Society of Mechanical Engineers*. [13](#)
- [29] D. B. Spalding, Mixing and chemical reaction in steady confined turbulent flames, *Symposium (International) on Combustion* 13 (1) (1971) 649–657. [13](#)
- [30] E. E. Zukoski, F. Marble, Experiments concerning the mechanism of flame blowoff from bluff bodies, Tech. rep., Caltech (1983). [13](#)
- [31] M. Barrere, A. Mestre, Flame stabilization in supersonic combustion, *La Recherche Aerospaciale(English Edition)* (1) (1988) 1–13. [13](#)
- [32] A. H. Lefebvre, Gas turbine combustion, CRC, 1999. [13](#)
- [33] D. R. Ballal, A. H. Lefebvre, The structure and propagation of turbulent flames, *Proceedings of the Royal Society of London. A. Mathematical and Physical Sciences* 344 (1637) (1975) 217–234. [13](#)
- [34] A. H. Lefebvre, R. Reid, The influence of turbulence on the structure and propagation of enclosed flames, *Combustion and Flame* 10 (4) (1966) 355–366. [13](#)
- [35] A. H. Lefebvre, A. Ibrahim, N. C. Benson, Factors affecting fresh mixture entrainment in bluff-body stabilized flames, *Combustion and Flame* 10 (3) (1966) 231–239. [13](#)
- [36] I. Porumbel, Large Eddy Simulation of premixed and partially premixed combustion, Ph.D. thesis, Georgia Institute of Technology (2006). [13](#)
- [37] R. Knikker, D. Veynante, J. C. Rolon, C. Meneveau, Planar laser-induced fluorescence in a turbulent premixed flame to analyze Large Eddy simulation models, in: Proceedings of the International Symposium on Turbulence, Heat and Mass Transfer, 2000. [13](#)
- [38] A. Sjunnesson, S. Olovsson, B. Sjoblom, Validation rig- A tool for flame studies, in: International Symposium on Air Breathing Engines, 10 th, Nottingham, England, 1991, pp. 385–393. [13](#)

- [39] S. Chaudhuri, B. M. Cetegen, Blowoff characteristics of bluff-body stabilized conical premixed flames in a duct with upstream spatial mixture gradients and velocity oscillations, *Combustion Science and Technology* 181 (4) (2009) 555–569. [13](#)
- [40] R. Balachandran, B. O. Ayoola, C. F. Kaminski, A. P. Dowling, E. Mastorakos, Experimental investigation of the nonlinear response of turbulent premixed flames to imposed inlet velocity oscillations, *Combustion and Flame* 143 (1) (2005) 37–55. [13](#)
- [41] S. A. Husain, Analysis of blowoff scaling of bluff body stabilized flames, Ph.D. thesis, Georgia Institute of Technology (2008). [13](#)
- [42] S. J. Shanbhogue, Dynamics of perturbed exothermic bluff-body flow-fields, ProQuest, 2008. [13](#)
- [43] A. R. Masri, R. W. Bilger, Turbulent diffusion flames of hydrocarbon fuels stabilized on a bluff body, *Symposium (International) on Combustion* 20 (1) (1985) 319–326. [13](#)
- [44] B. B. Dally, D. F. Fletcher, A. R. Masri, Flow and mixing fields of turbulent bluff-body jets and flames, *Combustion Theory and Modelling* 2 (2) (1998) 193–219. [13](#), [14](#)
- [45] C. Schneider, A. Dreizler, J. Janicka, Fluid dynamical analysis of atmospheric reacting and isothermal swirling flows, *Flow, Turbulence and Combustion* 74 (2005) 103–127. [13](#), [19](#)
- [46] M. A. Gregor, F. Seffrin, F. Fuest, D. Geyer, A. Dreizler, Multi-scalar measurements in a premixed swirl burner using 1D Raman/Rayleigh scattering, *Proceedings of the Combustion Institute* 32 (2) (2009) 1739–1746. [13](#), [19](#)
- [47] M. S. Sweeney, S. Hochgreb, M. J. Dunn, R. S. Barlow, A comparative analysis of flame surface density metrics in premixed and stratified flames, *Proceedings of the Combustion Institute* 33 (1) (2011) 1419–1427. [13](#), [26](#), [27](#), [69](#), [71](#)
- [48] F. Seffrin, F. Fuest, D. Geyer, A. Dreizler, Flow field studies of a new series of turbulent premixed stratified flames, *Combustion and Flame* 157 (2) (2010) 384–396. [13](#), [15](#), [19](#), [24](#), [27](#), [129](#)
- [49] G. Lartigue, U. Meier, C. Berat, Experimental and numerical investigation of self-excited combustion oscillations in a scaled gas turbine combustor, *Applied thermal engineering* 24 (11) (2004) 1583–1592. [13](#), [21](#)
- [50] S. P. Nandula, R. W. Pitz, R. S. Barlow, G. J. Fiechtner, Rayleigh/Raman/LIF measurements in a turbulent lean premixed combustor, Tech. rep., Clemson Univ., SC (United States) (1995). [13](#), [14](#)

- [51] S. H. Kim, K. Y. Huh, Use of the conditional moment closure model to predict NO formation in a turbulent CH₄/H₂ flame over a bluff-body, *Combustion and flame* 130 (1-2) (2002) 94–111. [14](#)
- [52] K. Liu, S. B. Pope, D. A. Caughey, Calculations of bluff-body stabilized flames using a joint probability density function model with detailed chemistry, *Combustion and Flame* 141 (1) (2005) 89–117. [14](#)
- [53] T. S. Kuan, R. P. Lindstedt, Transported probability density function modeling of a bluff body stabilized turbulent flame, *Proceedings of the Combustion Institute* 30 (1) (2005) 767–774. [14](#)
- [54] B. Merci, D. Roekaerts, B. Naud, S. B. Pope, Comparative study of micromixing models in transported scalar PDF simulations of turbulent nonpremixed bluff body flames, *Combustion and flame* 146 (1) (2006) 109–130. [14](#)
- [55] M. Hossain, W. Malalasekera, A combustion model sensitivity study for CH₄/H₂ bluff-body stabilized flame, *Proceedings of the Institution of Mechanical Engineers, Part C: Journal of Mechanical Engineering Science* 221 (11) (2007) 1377–1390. [14](#)
- [56] V. Raman, H. Pitsch, R. O. Fox, Hybrid large-eddy simulation/Lagrangian filtered-density-function approach for simulating turbulent combustion, *Combustion and Flame* 143 (1) (2005) 56–78. [14](#)
- [57] V. Raman, H. Pitsch, Large-eddy simulation of a bluff-body-stabilized non-premixed flame using a recursive filter-refinement procedure, *Combustion and flame* 142 (4) (2005) 329–347. [14](#)
- [58] A. Kempf, R. P. Lindstedt, J. Janicka, Large-eddy simulation of a bluff-body stabilized nonpremixed flame, *Combustion and flame* 144 (1) (2006) 170–189. [14](#)
- [59] S. Navarro-Martinez, A. Kronenburg, LES–CMC simulations of a turbulent bluff-body flame, *Proceedings of the Combustion Institute* 31 (2) (2007) 1721–1728. [14](#)
- [60] W. Zhao, C. Zhang, C. Chen, Large eddy simulation of bluff-body stabilized flames using a multi-environment filtered density function model, *Proceedings of the Combustion Institute* 33 (1) (2011) 1347–1353. [14](#)
- [61] S. M. Cannon, B. S. Brewster, L. D. Smoot, PDF modeling of lean premixed combustion using in situ tabulated chemistry, *Combustion and flame* 119 (3) (1999) 233–252. [14](#)
- [62] W. Vicente, M. Salinas, E. Barrios, C. Dopazo, PDF modeling of CO and NO formation in lean premixed methane flames, *Combustion science and technology* 176 (4) (2004) 585–601. [14](#)

- [63] S. I. Möller, E. Lundgren, C. Fureby, Large eddy simulation of unsteady combustion, *Symposium (International) on Combustion* 26 (1) (1996) 241–248. [14](#)
- [64] E. Giacomazzi, V. Battaglia, C. Bruno, The coupling of turbulence and chemistry in a premixed bluff-body flame as studied by LES, *Combustion and Flame* 138 (4) (2004) 320–335. [14](#)
- [65] B. Manickam, S. P. R. Muppala, J. Franke, F. Dinkelacker, Evaluation of algebraic flame surface wrinkling model for bluff body stabilized flames and large-eddy simulation quality assessment for non-reacting and combusting flows, in: European Combusting Meeting, Vienna, Austria, 2009. [14](#)
- [66] V. K. Chakravarthy, S. Menon, Large Eddy Simulations of Confined Bluff Body Stabilized Highly Turbulent Premixed Flames, *FEDSM Paper 99 7798*. [15](#)
- [67] M. Boger, D. Veynante, Large eddy simulation of a turbulent premixed V-shaped flame, *Advances in Turbulence VIII* (2000) 449–452. [15](#)
- [68] V. Moureau, P. Domingo, L. Vervisch, From Large-Eddy Simulation to Direct Numerical Simulation of a lean premixed swirl flame: Filtered laminar flame-PDF modeling, *Combustion and Flame* 158 (7) (2011) 1340 – 1357. [15](#), [22](#), [51](#), [52](#), [59](#)
- [69] J. Galpin, A. Naudin, L. Vervisch, C. Angelberger, O. Colin, P. Domingo, Large-eddy simulation of a fuel-lean premixed turbulent swirl-burner, *Combustion and Flame* 155 (1–2) (2008) 247–266. [15](#)
- [70] S. Roux, G. Lartigue, T. Poinsot, U. Meier, C. Bérat, Studies of mean and unsteady flow in a swirled combustor using experiments, acoustic analysis and Large Eddy Simulations, *Combustion and Flame* 141 (2005) 40–54. [15](#)
- [71] B. Fiorina, R. Vicquelin, P. Auzillon, N. Darabiha, O. Gicquel, D. Veynante, A filtered tabulated chemistry model for LES of premixed combustion, *Combustion and Flame* 157 (3) (2010) 465–475. [15](#), [21](#), [51](#), [53](#), [55](#), [57](#)
- [72] G. Kuenne, A. Ketelheun, J. Janicka, LES modeling of premixed combustion using a thickened flame approach coupled with FGM tabulated chemistry, *Combustion and Flame* 158 (9) (2011) 1750–1767. [15](#), [19](#), [93](#)
- [73] M. Freitag, J. Janicka, Investigation of a strongly swirled unconfined premixed flame using LES, *Proceedings of the Combustion Institute* 31 (1) (2007) 1477 – 1485. [15](#)
- [74] G. Kuenne, F. Seffrin, F. Fuest, T. Stahler, A. Ketelheun, D. Geyer, J. Janicka, A. Dreizler, Experimental and numerical analysis of a lean premixed stratified burner using 1D Raman/Rayleigh scattering and large eddy simulation, *Combustion and Flame* 159 (8) (2012) 2669–2689. [15](#), [19](#), [26](#), [27](#), [107](#), [114](#)

- [75] C. M. Coats, Coherent structures in combustion, *Progress in Energy and Combustion Science* 22 (5) (1996) 427 – 509. 15
- [76] P. G. Mehta, M. C. Soteriou, Combustion heat release effects on the dynamics of bluff body stabilized premixed reacting flows, in: 41st Aerospace Sciences Meeting and Exhibit, 2003. 15
- [77] R. R. Erickson, M. C. Soteriou, The influence of reactant temperature on the dynamics of bluff body stabilized premixed flames, *Combustion and Flame* 158 (12) (2011) 2441 – 2457. 15
- [78] S. J. Shanbhogue, S. Husain, T. Lieuwen, Lean blowoff of bluff body stabilized flames: Scaling and dynamics, *Progress in Energy and Combustion Science* 35 (1) (2009) 98 – 120. 15
- [79] S. Fujii, K. Eguchi, A comparison of cold and reacting flows around a bluff-body flame stabilizer, *Journal of Fluids Engineering* 103 (2) (1981) 328–334. 16
- [80] T. Turanyi, Reduction of large reaction mechanisms, *New journal of chemistry* 14 (11) (1990) 795–803. 16
- [81] A. Tomlin, T. Turányi, M. Pilling, Mathematical tools for the construction, investigation and reduction of combustion mechanisms, *Comprehensive Chemical Kinetics* 35 (1997) 293–437. 16
- [82] T. Lu, K. L. Chung, A directed relation graph method for mechanism reduction, *Proceedings of the Combustion Institute* 30 (1) (2005) 1333 – 1341. 17
- [83] J. Warnatz, U. Maas, R. W. Dibble, *Combustion: physical and chemical fundamentals, modeling and simulation, experiments, pollutant formation*, Springer, 2006. 17
- [84] N. Peters, Numerical and asymptotic analysis of systematically reduced reaction schemes for hydrocarbon flames, *Numerical simulation of combustion phenomena* (1985) 90–109. 17
- [85] S. H. Lam, D. A. Goussis, The CSP method for simplifying kinetics, *International Journal of Chemical Kinetics* 26 (4) (1994) 461–486. 17
- [86] U. Maas, S. B. Pope, Simplifying chemical kinetics: Intrinsic low-dimensional manifolds in composition space, *Combustion and Flame* 88 (3–4) (1992) 239 – 264. 17
- [87] U. Maas, S. B. Pope, Implementation of simplified chemical kinetics based on intrinsic low-dimensional manifolds, *Symposium (International) on Combustion* 24 (1) (1992) 103 – 112. 17

- [88] U. Maas, V. Bykov, The extension of the reaction/diffusion manifold concept to systems with detailed transport models, *Proceedings of the Combustion Institute* 33 (1) (2011) 1253 – 1259. [17](#)
- [89] Z. Ren, S. B. Pope, The use of slow manifolds in reactive flows, *Combustion and Flame* 147 (4) (2006) 243 – 261. [17](#)
- [90] L. P. H. de Goey, J. A. van Oijen, H. Bongers, G. R. A. Groot, New flamelet based reduction methods: the bridge between chemical reduction techniques and flamelet methods, in: European Combustion Meeting, Orléans (France), 2003. [17](#)
- [91] O. Gicquel, N. Darabiha, D. Thévenin, Laminar premixed hydrogen/air counterflow flame simulations using flame prolongation of ILDM with differential diffusion, *Proceedings of the Combustion Institute* 28 (2) (2000) 1901 – 1908. [17](#)
- [92] J. A. V. Oijen, L. P. H. D. Goey, Modelling of Premixed Laminar Flames using Flamelet-Generated Manifolds, *Combustion Science and Technology* 161 (1) (2000) 113–137. [17](#)
- [93] P. D. Nguyen, L. Vervisch, V. Subramanian, P. Domingo, Multidimensional flamelet-generated manifolds for partially premixed combustion, *Combustion and Flame* 157 (1) (2010) 43–61. [17](#), [27](#), [116](#), [118](#)
- [94] O. Colin, F. Ducros, D. Veynante, T. Poinso, A thickened flame model for large eddy simulations of turbulent premixed combustion, *Physics of Fluids* 12 (7) (2000) 1843–1863. [19](#)
- [95] V. K. Chakravarthy, S. Menon, Subgrid modeling of turbulent premixed flames in the flamelet regime, *Flow, Turbulence and Combustion* 65 (2) (2000) 133–161. [19](#)
- [96] V. Sankaran, S. Menon, Subgrid combustion modeling of 3-d premixed flames in the thin-reaction-zone regime, *Proceedings of the Combustion Institute* 30 (1) (2005) 575–582. [19](#)
- [97] N. Peters, A. M. Kanury, Turbulent combustion, *Applied Mechanics Reviews* 54 (2001) B73. [19](#)
- [98] F. Marble, J. Broadwell, The coherent flame model for turbulent chemical reactions, Tech. rep., DTIC Document (1977). [19](#), [20](#)
- [99] E. R. Hawkes, R. S. Cant, Implications of a flame surface density approach to large eddy simulation of premixed turbulent combustion, *Combustion and Flame* 126 (3) (2001) 1617–1629. [19](#)
- [100] M. Boger, D. Veynante, H. Boughanem, A. Trouvé, Direct numerical simulation analysis of flame surface density concept for large eddy simulation of turbulent premixed combustion, *Symposium (International) on Combustion* 27 (1) (1998) 917–925. [19](#), [20](#)

- [101] O. Colin, A. Benkenida, C. Angelberger, 3d Modeling of Mixing, Ignition and Combustion Phenomena in Highly Stratified Gasoline Engines Modélisation 3D du mélange, de l'allumage et de la combustion dans les moteurs à essence fortement stratifiés, *Revue de L'Institut Français du Pétrole* 58 (1) (2003) 47–62. [19](#)
- [102] L. Vervisch, R. Hauguel, P. Domingo, M. Rullaud, Three facets of turbulent combustion modelling: DNS of premixed V-flame, LES of lifted non-premixed flame and RANS of jet flame, *Journal of turbulence* 5 (1) (2004) 4–4(1). [19](#), [23](#)
- [103] B. Thornber, R. W. Bilger, A. R. Masri, E. R. Hawkes, An algorithm for LES of premixed compressible flows using the Conditional Moment Closure model, *Journal of Computational Physics*. [19](#)
- [104] T. D. Butler, P. J. O'Rourke, A numerical method for two dimensional unsteady reacting flows, *Symposium (International) on Combustion* 16 (1) (1977) 1503–1515. [19](#)
- [105] P. J. O'Rourke, F. V. Bracco, Two scaling transformations for the numerical computation of multidimensional unsteady laminar flames, *Journal of Computational Physics* 33 (2) (1979) 185–203. [19](#)
- [106] J. P. L egier, T. Poinso, D. Veynante, Dynamically thickened flame LES model for premixed and non-premixed turbulent combustion, in: Proc. of the summer program, 2000, pp. 157–168. [19](#)
- [107] C. Angelberger, D. Veynante, F. Egolfopoulos, T. Poinso, Large eddy simulations of combustion instabilities in premixed flames, in: Proc. of the Summer Program, Center for Turbulence Research, Stanford, 1998, pp. 61–82. [19](#)
- [108] F. Charlette, C. Meneveau, D. Veynante, A power-law flame wrinkling model for LES of premixed turbulent combustion Part II: dynamic formulation, *Combustion and Flame* 131 (1–2) (2002) 181–197. [19](#), [21](#)
- [109] G. Wang, M. Boileau, D. Veynante, Implementation of a dynamic thickened flame model for large eddy simulations of turbulent premixed combustion, *Combustion and Flame* 158 (11) (2011) 2199–2213. [19](#)
- [110] F. A. Williams, Turbulent combustion, *The Mathematics of combustion* (1985) 97–131. [20](#)
- [111] H. Pitsch, A consistent level set formulation for large-eddy simulation of premixed turbulent combustion, *Combustion and Flame* 143 (4) (2005) 587–598. [20](#)
- [112] R. Knikker, D. Veynante, C. Meneveau, A priori testing of a similarity model for large eddy simulations of turbulent premixed combustion, *Proceedings of the Combustion Institute* 29 (2) (2002) 2105–2111. [20](#)

- [113] C. Nottin, R. Knikker, M. Boger, D. Veynante, Large eddy simulations of an acoustically excited turbulent premixed flame, *Proceedings of the Combustion Institute* 28 (1) (2000) 67–73. [20](#)
- [114] V. Moureau, B. Fiorina, H. Pitsch, A level set formulation for premixed combustion LES considering the turbulent flame structure, *Combustion and Flame* 156 (4) (2009) 801–812. [20](#)
- [115] M. C. Sebastien, J. P. Thierry, Flame stretch and the balance equation for the flame area, *Combustion Science and Technology* 70 (1-3) (1990) 1–15. [20](#)
- [116] S. B. Pope, The evolution of surfaces in turbulence, *International journal of engineering science* 26 (5) (1988) 445–469. [20](#)
- [117] K. N. C. Bray, The interaction between turbulence and combustion, *Symposium (International) on Combustion* 17 (1) (1979) 223–233. [20](#)
- [118] V. L. Zimont, Gas premixed combustion at high turbulence. Turbulent flame closure combustion model, *Experimental Thermal and Fluid Science* 21 (1) (2000) 179–186. [20](#)
- [119] C. Duwig, C. Fureby, Large eddy simulation of unsteady lean stratified premixed combustion, *Combustion and Flame* 151 (1–2) (2007) 85 – 103. [20](#), [21](#), [26](#), [27](#)
- [120] D. Veynante, T. Poinso, Reynolds averaged and large eddy simulation modeling for turbulent combustion, *New Tools in Turbulence Modelling* (1997) 105–140. [20](#)
- [121] F. C. Marincola, T. Ma, A. M. Kempf, Large eddy simulations of the Darmstadt turbulent stratified flame series, *Proceedings of the Combustion Institute* 34 (1) (2013) 1307 – 1315. [20](#)
- [122] P. Auzillon, B. Fiorina, R. Vicquelin, N. Darabiha, O. Gicquel, D. Veynante, Modeling chemical flame structure and combustion dynamics in LES, *Proceedings of the Combustion Institute* 33 (1) (2011) 1331–1338. [21](#), [55](#)
- [123] A. W. Vreman, J. A. Oijen, L. P. H. Goey, R. J. M. Bastiaans, Subgrid Scale Modeling in Large-Eddy Simulation of Turbulent Combustion Using Premixed Flamelet Chemistry, *Flow, Turbulence and Combustion* 82 (2009) 511–535. [22](#)
- [124] P. Domingo, L. Vervisch, S. Payet, R. Hauguel, DNS of a premixed turbulent V flame and LES of a ducted flame using a FSD-PDF subgrid scale closure with FPI-tabulated chemistry, *Combustion and Flame* 143 (4) (2005) 566–586. [23](#)
- [125] G. Lecocq, S. Richard, O. Colin, L. Vervisch, Hybrid presumed pdf and flame surface density approaches for Large-Eddy Simulation of premixed turbulent combustion. Part 2: Early flame development after sparking, *Combustion and Flame* 158 (6) (2011) 1215–1226. [23](#)

- [126] T. Kang, D. C. Kyritsis, A combined experimental/computational investigation of stratified combustion in methane-air mixtures, *Energy Conversion and Management* 48 (11) (2007) 2769–2774. [24](#)
- [127] T. Kang, D. C. Kyritsis, Departure from quasi-homogeneity during laminar flame propagation in lean, compositionally stratified methane-air mixtures, *Proceedings of the Combustion Institute* 31 (1) (2007) 1075–1083. [24](#), [25](#), [26](#)
- [128] E. S. Richardson, V. E. Granet, A. Eyssartier, J. H. Chen, Effects of equivalence ratio variation on lean, stratified methane-air laminar counterflow flames, *Combustion Theory and Modelling* 14 (6) (2010) 775–792. [24](#), [25](#), [26](#)
- [129] J. Hélie, A. Trouvé, Turbulent flame propagation in partially premixed combustion, *Symposium (International) on Combustion* 27 (1) (1998) 891–898. [25](#), [26](#)
- [130] D. C. Haworth, R. J. Blint, B. Cuenot, T. J. Poinso, Numerical simulation of turbulent propane-air combustion with nonhomogeneous reactants, *Combustion and Flame* 121 (3) (2000) 395–417. [25](#), [26](#), [108](#)
- [131] C. Jimenez, B. Cuenot, T. Poinso, D. Haworth, Numerical simulation and modeling for lean stratified propane-air flames, *Combustion and Flame* 128 (1-2) (2002) 1 – 21. [25](#), [26](#)
- [132] Y. Ra, Laminar flame propagation in a stratified charge, Ph.D. thesis, Massachusetts Institute of Technology (1999). [25](#)
- [133] C. Galizzi, D. Escudié, Experimental analysis of an oblique laminar flame front propagating in a stratified flow, *Combustion and flame* 145 (3) (2006) 621–634. [25](#)
- [134] O. Dégardin, B. Renou, A. M. Boukhalfa, Simultaneous measurement of temperature and fuel mole fraction using acetone planar induced fluorescence and Rayleigh scattering in stratified flames, *Experiments in Fluids* 40 (2006) 452–463. [25](#)
- [135] S. Balusamy, A. Cessou, B. Lecordier, Direct measurement of local instantaneous laminar burning velocity by a new PIV algorithm, *Experiments in Fluids* 50 (2011) 1109–1121. [25](#), [26](#)
- [136] A. P. D. Cruz, A. Dean, J. M. Grenda, A numerical study of the laminar flame speed of stratified methane/air flames, *Proceedings of the Combustion Institute* 28 (2) (2000) 1925 – 1932. [25](#)
- [137] Y. M. Marzouk, A. F. Ghoniem, H. N. Najm, Dynamic response of strained premixed flames to equivalence ratio gradients, *Proceedings of the Combustion Institute* 28 (2) (2000) 1859 – 1866. [25](#), [26](#)
- [138] E. S. Richardson, J. H. Chen, Application of PDF mixing models to premixed flames with differential diffusion, *Combustion and Flame* 159 (7) (2012) 2398 – 2414. [25](#), [31](#)

- [139] N. Pasquier, B. Lecordier, M. Trinite, A. Cessou, An experimental investigation of flame propagation through a turbulent stratified mixture, *Proceedings of the Combustion Institute* 31 (1) (2007) 1567–1574. 25, 26
- [140] R. Sankaran, H. G. Im, Dynamic flammability limits of methane/air premixed flames with mixture composition fluctuations, *Proceedings of the Combustion Institute* 29 (1) (2002) 77 – 84. 25
- [141] Y. Takagi, A new era in spark-ignition engines featuring high-pressure direct injection, *Symposium (International) on Combustion* 27 (2) (1998) 2055 – 2068. 25
- [142] F. Zhao, M. C. Lai, D. L. Harrington, Automotive spark-ignited direct-injection gasoline engines, *Progress in Energy and Combustion Science* 25 (5) (1999) 437 – 562. 25
- [143] T. Poinso, D. Veynante, A. Trouvé, G. Ruetsch, Turbulent flame propagation in partially premixed flames, *Proceedings of the Summer Program, Center for Turbulent Research, NASA Ames/Stanford University* (1996) 111. 26
- [144] W. J. S. Ramaekers, J. A. van Oijen, L. P. H. de Goey, Stratified turbulent Bunsen flames: flame surface analysis and flame surface density modelling, *Combustion Theory and Modelling* 16 (6) (2012) 943–975. arXiv:<http://www.tandfonline.com/doi/pdf/10.1080/13647830.2012.686172>. 26, 27
- [145] P. Auzillon, O. Gicquel, N. Darabiha, D. Veynante, B. Fiorina, A Filtered Tabulated Chemistry model for LES of stratified flames, *Combustion and Flame* 159 (8) (2012) 2704 – 2717. 26
- [146] C. Galizzi, D. Escudié, Experimental analysis of an oblique turbulent flame front propagating in a stratified flow, *Combustion and Flame* 157 (12) (2010) 2277–2285. 26
- [147] P. C. Vena, B. Deschamps, G. J. Smallwood, M. R. Johnson, et al., Flame front behaviour in a stratified iso-octane/air turbulent V-flame, *Proceedings of Combustion Institute, Canadian Section Spring Technical Meeting*. 26
- [148] P. Anselmo-Filho, S. Hochgreb, R. S. Barlow, R. S. Cant, Experimental measurements of geometric properties of turbulent stratified flames, *Proceedings of the Combustion Institute* 32 (2) (2009) 1763–1770. 26
- [149] V. Robin, A. Mura, M. Champion, Direct and indirect thermal expansion effects in turbulent premixed flames, *Journal of Fluid Mechanics* FirstView (2011) 1–34. 26
- [150] B. Renou, E. Samson, A. Boukhalfa, An experimental study of freely propagating turbulent propane/air flames in stratified inhomogeneous mixtures, *Combustion Science and Technology* 176 (11) (2004) 1867–1890. 26

- [151] A. Bonaldo, J. B. Kelman, Experimental annular stratified flames characterisation stabilised by weak swirl, *Combustion and Flame* 156 (4) (2009) 750 – 762. 26
- [152] P. Nguyen, P. Bruel, S. Reichstadt, An Experimental Database for Benchmarking Simulations of Turbulent Premixed Reacting Flows: Lean Extinction Limits and Velocity Field Measurements in a Dump Combustor, *Flow, Turbulence and Combustion* 82 (2009) 155–183. 27
- [153] E. Knudsen, H. Pitsch, Capabilities and limitations of multi-regime flamelet combustion models, *Combustion and Flame* 159 (1) (2012) 242–264. 27
- [154] D. Goodwin. Cantera: An object-oriented software toolkit for chemical kinetics, thermodynamics, and transport processes [online] (2009). 27, 51
- [155] M. Frenklach, H. Wang, M. Goldenberg, G. P. Smith, D. M. Golden, C. T. Bowman, R. K. Hanson, W. C. Gardiner, V. Lissianki, GRI 3.0, Tech. rep., Gas Research Institute (1995). 27
- [156] R. E. Mitchell, A. F. Sarofim, L. A. Clomburg, Partial equilibrium in the reaction zone of methane-air diffusion flames, *Combustion and Flame* 37 (0) (1980) 201 – 206. 27
- [157] R. W. Bilger, Reaction rates in diffusion flames, *Combustion and Flame* 30 (0) (1977) 277 – 284. 27
- [158] R. W. Bilger, S. H. Stårner, R. J. Kee, On reduced mechanisms for methane-air combustion in nonpremixed flames, *Combustion and Flame* 80 (2) (1990) 135–149. 27, 64
- [159] A. N. Lipatnikov, J. Chomiak, Molecular transport effects on turbulent flame propagation and structure, *Progress in Energy and Combustion Science* 31 (1) (2005) 1–73. 29
- [160] M. C. Drake, M. Lapp, C. M. Penney, S. Warshaw, B. W. Gerhold, Measurements of temperature and concentration fluctuations in turbulent diffusion flames using pulsed Raman spectroscopy, *Symposium (International) on Combustion* 18 (1) (1981) 1521–1531. 29
- [161] R. W. Bilger, S. H. Stårner, Differential diffusion effects on measurements in turbulent diffusion flames by the Mie scattering technique, *Flames, Lasers, and Reactive Systems* 1 (1983) 81–104. 29
- [162] A. R. Kerstein, R. W. Dibble, M. B. Long, B. Yip, K. Lyons, Measurement and computation of differential molecular diffusion in a turbulent jet, in: 7th Symposium on Turbulent Shear Flows, Volume 1, Vol. 1, 1989, p. 14. 29
- [163] R. W. Dibble, A. R. Kerstein, M. B. Long, B. Yip, K. Lyons, Measurement and Computation of Differential Molecular Diffusion in a Turbulent Jet, *Turbulence and Molecular Processes in Combustion* (1992) 303–310. 29

- [164] M. B. Long, S. H. Starner, R. W. Bilger, Differential Diffusion in Jets using Joint PLIF and Lorenz-Mie Imaging, *Combustion Science and Technology* 92 (4-6) (1993) 209–224. 29
- [165] L. L. Smith, R. W. Dibble, L. Talbot, R. S. Barlow, C. D. Carter, Laser Raman scattering measurements of differential molecular diffusion in nonreacting turbulent jets of H/CO mixing with air, *Physics of Fluids* 7 (1995) 1455. 29
- [166] A. R. Kerstein, M. A. Cremer, P. A. McMurtry, Scaling properties of differential molecular diffusion effects in turbulence, *Physics of Fluids* 7. 29
- [167] P. K. Yeung, S. B. Pope, Differential diffusion of passive scalars in isotropic turbulence, *Physics of Fluids A: Fluid Dynamics* 5 (1993) 2467. 29
- [168] V. Nilsen, G. Kosály, Differentially diffusing scalars in turbulence, *Physics of Fluids* 9 (1997) 3386. 29
- [169] P. K. Yeung, M. C. Sykes, P. Vedula, Direct numerical simulation of differential diffusion with Schmidt numbers up to 4.0, *Physics of Fluids* 12 (2000) 1601. 29
- [170] R. O. Fox, The Lagrangian spectral relaxation model for differential diffusion in homogeneous turbulence, *Physics of Fluids* 11 (1999) 1550. 29
- [171] A. R. G. Kronenburg, R. W. Bilger, Modelling Differential Diffusion in Nonpremixed Reacting Turbulent Flow: Model Development, *Combustion Science and Technology* 166 (1) (2001) 195–227. 29
- [172] R. W. Dibble, M. B. Long, Investigation of differential diffusion in turbulent jet flows using planar laser Rayleigh scattering, *Combustion and Flame* 143 (4) (2005) 644 – 649. 29
- [173] P. K. Yeung, Correlations and conditional statistics in differential diffusion: Scalars with uniform mean gradients, *Physics of Fluids* 10 (1998) 2621. 30
- [174] J. R. Saylor, K. R. Sreenivasan, Differential diffusion in low Reynolds number water jets, *Physics of Fluids* 10 (1998) 1135. 30
- [175] L. L. Smith, R. W. Dibble, L. Talbot, R. S. Barlow, C. D. Carter, Laser Raman scattering measurements of differential molecular diffusion in turbulent nonpremixed jet flames of H₂/CO₂ fuel, *Combustion and Flame* 100 (1–2) (1995) 153–160. 30
- [176] V. Bergmann, W. Meier, D. Wolff, W. Stricker, Application of spontaneous Raman and Rayleigh scattering and 2D LIF for the characterization of a turbulent CH₄/H₂/N₂ jet diffusion flame, *Applied Physics B* 66 (1998) 489–502. 30
- [177] R. S. Barlow, J. H. Frank, A. N. Karpetis, J. Y. Chen, Piloted methane/air jet flames: Transport effects and aspects of scalar structure, *Combustion and Flame* 143 (4) (2005) 433–449. 30

- [178] H. Pitsch, N. Peters, A Consistent Flamelet Formulation for Non-Premixed Combustion Considering Differential Diffusion Effects, *Combustion and Flame* 114 (1–2) (1998) 26 – 40. [30](#), [32](#)
- [179] H. Pitsch, Unsteady flamelet modeling of differential diffusion in turbulent jet diffusion flames, *Combustion and Flame* 123 (3) (2000) 358–374. [30](#)
- [180] R. McDermott, S. B. Pope, A particle formulation for treating differential diffusion in filtered density function methods, *Journal of Computational Physics* 226 (1) (2007) 947–993. [30](#)
- [181] C. J. Pope, R. A. Shandross, J. B. Howard, Variation of equivalence ratio and element ratios with distance from burner in premixed one-dimensional flames, *Combustion and Flame* 116 (4) (1999) 605 – 614. [30](#)
- [182] C. J. Pope, J. A. Milner, Variation of equivalence ratio and element ratios in low-pressure premixed flames of aliphatic fuels, Western Section of the Combustion Institute, Golden, Colorado, USA, 2000. [30](#)
- [183] J. C. Sutherland, P. J. Smith, J. H. Chen, Quantification of differential diffusion in non-premixed systems, *Combustion Theory and Modelling* 9 (2) (2005) 365–383. [30](#), [31](#)
- [184] G. Lodier, L. Vervisch, V. Moureau, P. Domingo, Composition-space premixed flamelet solution with differential diffusion for in situ flamelet-generated manifolds, *Combustion and Flame* 158 (10) (2011) 2009–2016. [31](#), [53](#), [118](#)
- [185] J. de Swart, R. Bastiaans, J. van Oijen, L. de Goey, R. Cant, Inclusion of Preferential Diffusion in Simulations of Premixed Combustion of Hydrogen/Methane Mixtures with Flamelet Generated Manifolds, *Flow, Turbulence and Combustion* 85 (2010) 473–511. [31](#)
- [186] J. D. Regele, E. Knudsen, H. Pitsch, G. Blanquart, A two-equation model for non-unity Lewis number differential diffusion in lean premixed laminar flames, *Combustion and Flame* 160 (2) (2013) 240–250. [31](#), [129](#)
- [187] J. Ferziger, M. Perić, Computational methods for fluid dynamics, Vol. 3, Springer Berlin etc, 1999. [33](#)
- [188] S. Klainerman, A. Majda, Compressible and incompressible fluids, *Communications on Pure and Applied Mathematics* 35 (5) (1982) 629–651. [35](#)
- [189] H. Kreiss, J. Lorenz, M. Naughton, Convergence of the solutions of the compressible to the solutions of the incompressible Navier-Stokes equations, *Advances in Applied Mathematics* 12 (2) (1991) 187–214. [35](#)
- [190] A. Majda, Compressible fluid flow and systems of conservation laws in several space variables, Vol. 53, Springer, 1984. [35](#)

- [191] T. Poinso, D. Veynante, Theoretical and numerical combustion, RT Edwards, Inc., 2005. 36
- [192] J. Hinze, Turbulence, 2nd Edition, McGraw-Hill, 1975. 37
- [193] H. Tennekes, J. Lumley, A first course in turbulence, MIT Press, 1972. 37
- [194] J. Smagorinsky, General circulation experiments with the primitive equations, *Monthly weather review* 91 (3) (1963) 99–164. 38, 72
- [195] M. Germano, U. Piomelli, P. Moin, W. Cabot, A dynamic subgrid-scale eddy viscosity model, *Physics of Fluids A: Fluid Dynamics* 3 (1991) 1760. 38, 57, 72
- [196] F. Nicoud, F. Ducros, Subgrid-Scale Stress Modelling Based on the Square of the Velocity Gradient Tensor, *Flow, Turbulence and Combustion* 62 (1999) 183–200. 39
- [197] S. Vantieghem, Numerical simulations of quasi-static magnetohydrodynamics using an unstructured finite volume solver: development and applications, Ph.D. thesis, Université Libre de Bruxelles (2011). 40
- [198] V. Moureau, G. Lartigue, Private communication (August 2011). 41
- [199] M. Kraushaar, Application of the compressible and low Mach number approaches to large eddy simulation of turbulent flows in aero-engines, Ph.D. thesis, Université de Toulouse (December 2011). 41, 46
- [200] G. Karypis, K. Schloegel, V. Kumar, Parmetis: Parallel graph partitioning and sparse matrix ordering library, *Version 1.0, Dept. of Computer Science, University of Minnesota*. 41
- [201] M. Malandain, N. Maheu, V. Moureau, Optimization of the deflated Conjugate Gradient algorithm for the solving of elliptic equations on massively parallel machines, *Journal of Computational Physics* 238 (0) (2013) 32 – 47. 41
- [202] J. Kim, P. Moin, Application of a fractional-step method to incompressible Navier-Stokes equations, *Journal of Computational Physics* 59 (2) (1985) 308–323. 42
- [203] A. Chorin, Numerical solution of the Navier-Stokes equations, *Math. Comp* 22 (104) (1968) 745–762. 42
- [204] C. Hirsch, Numerical computation of internal and external flows: the fundamentals of Computational Fluid Dynamics, Vol. 1, Butterworth-Heinemann, 2007. 45
- [205] A. W. Cook, W. H. Cabot, A high-wavenumber viscosity for high-resolution numerical methods, *Journal of Computational Physics* 195 (2) (2004) 594 – 601. 45

- [206] L. Quartapelle, V. Selmin, High-order Taylor-Galerkin methods for nonlinear multidimensional problems, *Finite Elements in Fluids* 76 (1993) 90. 46
- [207] G. Golub, C. Van Loan, Matrix computations, Vol. 3, Johns Hopkins University Press, 1996. 48
- [208] M. Malandain, N. Maheu, V. Moureau, Optimization of the deflated conjugate gradient algorithm for the solving of elliptic equations on massively parallel machines, *J. Comput. Phys. in press*. 48
- [209] G. P. Smith, D. M. Golden, M. Frenklach, N. W. Moriarty, B. Eiteneer, M. Goldenberg, C. Bowman, R. Hanson, S. Song, W. Gardiner Jr, et al., Gri-mech 3.0, URL: http://www.me.berkeley.edu/gri_mech. 51, 55
- [210] C. F. Curtiss, J. O. Hirschfelder, Transport properties of multicomponent gas mixtures, *Journal of Chemical Physics* 17 (1949) 550. 51, 55
- [211] V. Moureau, P. Domingo, L. Vervisch, D. Veynante, DNS Analysis of a $Re = 40,000$ swirl burner, *Proceedings of the Summer Program, Center for Turbulent Research, NASA Ames/Stanford University* (2010) 289–298. 55
- [212] A. Leboissetier, N. Okong’o, J. Bellan, Consistent large-eddy simulation of a temporal mixing layer laden with evaporating drops. Part 2. A posteriori modelling, *Journal of Fluid Mechanics* 523 (2005) 37–78. 57
- [213] N. A. Okong’o, J. Bellan, Consistent large-eddy simulation of a temporal mixing layer laden with evaporating drops. Part 1. Direct numerical simulation, formulation and a priori analysis, *Journal of Fluid Mechanics* 499 (2004) 1–47. 57
- [214] K. Bray, P. Libby, G. Masuya, J. Moss, Turbulence production in premixed turbulent flames, Taylor & Francis, 1981. 58
- [215] D. Veynante, A. Trouvé, K. N. C. Bray, T. Mantel, Gradient and counter-gradient scalar transport in turbulent premixed flames, *Journal of Fluid Mechanics* 332 (1997) 263–293. 58
- [216] C. Pera, J. Réveillon, L. Vervisch, P. Domingo, Modeling subgrid scale mixture fraction variance in LES of evaporating spray, *Combustion and Flame* 146 (4) (2006) 635–648. 58, 80
- [217] P. Sagaut, Large eddy simulation for incompressible flows: An Introduction, Springer, 2005. 58
- [218] R. Borghi, Turbulent combustion modelling, *Prog. Energy Combust. Sci.* 14 (1988) 245–292. 59

- [219] N. Peters, *Turbulent Combustion*, Cambridge University Press, 2000. 59
- [220] H. Pitsch, Large Eddy Simulation of Turbulent Combustion, *Annual Review of Fluid Mechanics* 38 (2006) 453–482. 59
- [221] A. Yoshizawa, Statistical theory for compressible turbulent shear flows, with the application to subgrid modeling, *Physics of Fluids* 29 (7) (1986) 2152–2164. 59, 73
- [222] V. Moureau, P. Domingo, L. Vervisch, Design of a massively parallel CFD code for complex geometries, *C.R. Mecanique* 339 (2-3) (2011) 141–148. 59
- [223] T. Poinso, T. Echekki, M. G. Mungal, A study of the laminar flame tip and implications for premixed turbulent combustion, *Combustion Science and Technology* 81 (1992) 45–73. 62
- [224] F. A. Williams, *Combustion theory*, The Benjamin/Cummings Publishing Company, Inc, 1985. 63
- [225] N. Enjalbert, P. Domingo, L. Vervisch, Mixing time-history effects in large eddy simulation of non-premixed turbulent flames: Flow-controlled chemistry tabulation, *Combustion and Flame* 159 (1) (2012) 336–352. 67
- [226] T. Passot, A. Pouquet, Numerical simulation of compressible homogeneous flows in the turbulent regime, *Journal of Fluid Mechanics* 181 (1987) 441–466. 72
- [227] S. Pope, Ten questions concerning the large-eddy simulation of turbulent flows, *New Journal of Physics* 6 (2004) 35. 73
- [228] Y. Shoshin, L. Tecce, J. Jarosinski, Experimental and Computational Study of Lean Limit Methane-Air Flame Propagating Upward in a 24 mm Diameter Tube, *Combustion Science and Technology* 180 (10-11) (2008) 1812–1828. 77, 99
- [229] P. Domingo, L. Vervisch, D. Veynante, Large-eddy simulation of a lifted methane jet flame in a vitiated coflow, *Combustion and Flame* 152 (3) (2008) 415–432. 80, 116, 118
- [230] G. Godel, S. Nambully, P. Domingo, V. Moureau, L. Vervisch, Uncertainty analysis in NO_x prediction: Impact of SGS scalar variance estimation in LES using presumed PDF, in: *European Combusting Meeting*, Cardiff, UK, British section of the Combustion Institute, 2011. 80
- [231] K. A. Kemenov, S. B. Pope, Molecular diffusion effects in LES of a piloted methane-air, *Combustion and Flame* 158 (2) (2011) 240 – 254. 80
- [232] A. Tyliczszak, E. Mastorakos, LES/CMC of blow-off in a liquid fueled swirl burner, *ICHMT DIGITAL LIBRARY ONLINE*. 80

- [233] A. Garmory, E. Mastorakos, Sensitivity analysis of LES-CMC predictions of piloted jet flames, *International Journal of Heat and Fluid Flow* (0) (2013) –. 80
- [234] C. D. Taglia, A. Moser, L. Blum, Spontaneous break of symmetry in unconfined laminar annular jets, *Journal of Fluids Engineering* 131 (8) (2009) 081202. 85, 86
- [235] C. D. Taglia, L. Blum, J. Gass, Y. Ventikos, D. Poulikakos, Numerical and experimental investigation of an annular jet flow with large blockage, *Journal of Fluids Engineering* 126 (3) (2004) 375–384. 85, 86
- [236] M. J. Dunn, R. S. Barlow, Effects of preferential transport and strain in bluff body stabilized lean and rich premixed CH₄/air flames, *Proceedings of the Combustion Institute* In press. 91
- [237] B. Fiorina, R. Baron, O. Gicquel, D. Thevenin, S. Carpentier, N. Darabiha, Modelling non-adiabatic partially premixed flames using flame-prolongation of ILDM, *Combustion Theory and Modelling* 7 (3) (2003) 449–470. 107
- [238] R. Mercier, P. Auzillon, V. Moureau, N. Darabiha, O. Gicquel, D. Veynante, B. Fiorina., Modeling flame stabilization by heat losses using Filtered Tabulated Chemistry for Large Eddy Simulation, in: TNF, Eleventh International Workshop on Measurement and Computation of Turbulent Flames, 2012, pp. 30–31. 107
- [239] P. Trisjono, K. Kleinheinz, H. Pitsch, Large eddy simulation of stratified and sheared flames of a premixed turbulent stratified flame burner using a flamelet model with heat loss, *Flow, Turbulence and Combustion* Under review. 107, 129
- [240] H. Pitsch, L. D. de Lageneste, Large-eddy simulation of premixed turbulent combustion using a level-set approach, *Proceedings of the Combustion Institute* 29 (2) (2002) 2001 – 2008. 110